

PHD THESIS

TESTING THE THREE MASSIVE
NEUTRINO PARADIGM
CONSTRAINTS ON NEUTRINO PROPERTIES AND INTERACTIONS FROM RECENT
EXPERIMENTAL DATA

JOÃO PAULO PINHEIRO

PHD ADVISORS:

PROF. DR. MARIA CONCEPCION GONZALEZ-GARCIA
PROF. DR. MICHELE MALTONI



UNIVERSITAT DE
BARCELONA

Testing the three massive neutrino paradigm

Constraints on Neutrino Properties and Interactions from Recent
Experimental Data

Memoria presentada para optar al grado de doctor por la Universidad de
Barcelona

(Programa de Doctorado en Física)

Autor: João Paulo Pinheiro
Directora: Prof. Dr. María Concepción González García
Co-Director: Prof. Dr. Michele Maltoni
Tutor: Prof. Dr. Joan Soto Rivera

Departament de Física Quàntica i Astrofísica
Institut de Ciències del Cosmos
Universitat de Barcelona



UNIVERSITAT DE
BARCELONA

Para Eudália, Ednólia, José, Anna e Arya.

Abstract

Neutrino physics stands at the intersection of particle physics, astrophysics, and nuclear physics, offering unique insights into phenomena beyond the Standard Model (BSM). This thesis presents a synthesis of phenomenological investigations organized around three interconnected pillars: the consolidation of the three-flavor oscillation paradigm, the exploration of the viability of new physics in light of the most up to date experimental data, and the precise determination of solar neutrino fluxes. By integrating diverse methodologies from global oscillation fits to astrophysical flux calculations and novel BSM constraints this work demonstrates how distinct analytical frameworks converge to test the limits of neutrino physics.

This thesis starts with two introductory chapters to set the state of the art of the discussion. In Chapter 2, we introduce the basic elements of the Standard Model and its extension to include massive neutrinos, leptonic mixing and the implied flavour transitions. In Chapter 3, we set the landscape of experimental results which will be included in the rest of this thesis. We make special emphasis in Borexino phases II and III and NOvA experiments, with details of the statistical analysis of each experiment, which is an original contribution of the author to the collaboration.

The first pillar establishes the three-flavor oscillation framework through a comprehensive global analysis of neutrino data from solar, atmospheric, reactor, and accelerator experiments. In Chapter 4 we present an updated determination of mixing angles (θ_{12} , θ_{13} , θ_{23}) and mass-squared differences (Δm_{21}^2 , Δm_{31}^2), resolving tensions between datasets and quantifying persistent ambiguities in the neutrino mass ordering and θ_{23} octant. These analyses incorporate results up to September 2024, solidifying the overall robustness of the three-flavor paradigm, originally presented in Ref. [1].

The second pillar conducts a systematic investigation of BSM physics through recent experimental results, integrating terrestrial and astrophysical neutrino observations. Chapters 5 and 6 are dedicated to laying the ground for the theoretical framework of the studied BSMs and the experimental results, based on Refs. [2–4]. A unified analytical framework simultaneously addresses Non-Standard Interactions (NSI) with electrons and quarks, differentiating between non-standard matter effects and detection-process modifications. Precision data analysis from Borexino experiment constrains electron-coupled NSI parameters, with potential to exclude Large Mixing Angle-Dark (LMA-D) solutions through matter-enhanced oscillations. Complementary constraints on quark-coupled NSI emerge from COHERENT’s coherent elastic neutrino-nucleus scattering (CE ν NS) measurements, sensitive to nuclear recoil kinematics. The global analysis disentangles parameter degeneracies by combining oscillation data (solar, atmospheric, reactor, accelerator) with CE ν NS cross-section measurements, establishing distinct bounds on propagation and detection couplings. This synthesis demonstrates how solar neutrino observations primarily constrain flavor-diagonal electron interactions, while CE ν NS measurements probe universal quark couplings, with joint analyses excluding previously viable regions of NSI parameter space. The framework further distinguishes between light mediator scenarios through energy-dependent signatures in oscillation versus scattering datasets.

The third pillar advances solar neutrino physics through precision flux determinations by using updated measurements of pp-chain and CNO-cycle neutrinos to resolve fundamental ques-

tions in stellar astrophysics. Chapter 7 is dedicated to explain the state of the art of Standard Solar Models, the determination of solar fluxes and the incompatibility between the resolution of the gallium source experiment anomaly and solar neutrino data by means of a light sterile neutrino. It compiles the results from Refs. [5, 6]. By integrating the latest solar and non-solar neutrino data including the first direct detection of CNO-cycle neutrinos this analysis disentangles solar model uncertainties from oscillation parameters, constraining metallicity-dependent energy production mechanisms. The analysis aims to resolve tensions between high- and low-metallicity compositional scenarios predicted by different Standard Solar Models (SSM), while testing sterile neutrino explanations for the Gallium anomaly. Our analysis resulted in a statistical preference for SSM that predicts high-metallicity and systematic consistency checks demonstrate incompatibility between $3 + 1$ mixing parameters favored by Gallium experiments and those allowed by solar neutrino observations, irrespective of astrophysical or reactor flux assumptions. These results establish solar neutrinos as dual diagnostics of particle physics and stellar processes, linking precision flux measurements to both solar composition models and the limits of BSM scenarios.

The convergence of these distinct analytical threads oscillation parameter fits, BSM constraints, and astrophysical flux determinations forms the core contribution of this work. By rigorously testing the three-flavor framework while probing its boundaries, this thesis provides a blueprint for interdisciplinary neutrino physics. The synthesis of disparate datasets and theoretical approaches underscores the role of neutrinos as both messengers of astrophysical processes and laboratories for fundamental physics, guiding future experiments toward resolving outstanding questions in mass ordering, CP violation, and dark sector interactions.

Resum

Provant el paradigma dels tres neutrins massius. Restriccions sobre les propietats i interaccions dels neutrins a partir de dades experimentals recents.

La física de neutrins es troba a la intersecció entre la física de partícules, l'astrofísica i la física nuclear, oferint una visió única de fenòmens més enllà del Model Estàndard (BSM, per les seves sigles en anglès). Aquesta tesi presenta una síntesi d'investigacions fenomenològiques organitzades al voltant de tres pilars interconnectats: la consolidació del paradigma d'oscil·lació de tres sabors, l'exploració de la viabilitat de nova física a la llum de les dades experimentals més recents i la determinació precisa dels fluxos de neutrins solars. Mitjançant la integració de metodologies diverses des d'ajustos globals d'oscil·lació fins a càlculs de fluxos astrofísics i noves restriccions BSM aquest treball demostra com diferents marcs analítics convergeixen per provar els límits de la física de neutrins.

Aquesta tesi comença amb dos capítols introductoris per tal d'establir quin és l'estat del debat sobre el tema. Al Capítol 2 introduïm els elements bàsics del Model Estàndard i la seva extensió per incloure neutrins massius, la mescla leptònica i les transicions de sabor implicades. Al Capítol 3 descrivim l'espectre de resultats experimentals que s'inclouran en la resta de la tesi. Posem especial èmfasi en les fases II i III de Borexino i en l'experiment NOvA, amb detalls de l'anàlisi estadística de cada experiment, que constitueixen una contribució original de l'autor a la col·laboració.

El primer pilar estableix el marc d'oscil·lació de tres sabors mitjançant una anàlisi global exhaustiva de dades de neutrins solars, atmosfèrics, de reactors i d'acceleradors. Al Capítol 4 presentem una determinació actualitzada dels angles de mescla (θ_{12} , θ_{13} , θ_{23}) i les diferències de massa al quadrat (Δm_{21}^2 , Δm_{31}^2), resolent discrepàncies entre conjunts de dades i quantificant ambigüitats persistents en l'ordenació de masses dels neutrins i l'octant de θ_{23} . Aquestes anàlisis incorporen resultats fins a setembre de 2024, consolidant la robustesa general del paradigma de tres sabors, originalment presentat a la Ref. [1].

El segon pilar realitza una investigació sistemàtica de física BSM a través de resultats experimentals recents, integrant observacions de neutrins terrestres i astrofísics. Els Capítols 5 i 6 estan dedicats a establir les bases del marc teòric dels BSM estudiats i els resultats experimentals, basats en les Refs. [2–4]. Un marc analític unificat aborda simultàniament les Interaccions No Estàndard (NSI) amb electrons i quarks, diferenciant entre efectes de matèria no estàndard i modificacions en el procés de detecció. L'anàlisi de dades de precisió de l'experiment Borexino constreny els paràmetres NSI acoblats a electrons, amb el potencial d'excloure solucions LMA-D (Large Mixing Angle-Dark) mitjançant oscil·lacions amplificades per matèria. Restriccions complementàries sobre NSI acoblats a quarks provenen de mesures de dispersió coherent elàstica neutrí-nucli ($\text{CE}\nu\text{NS}$) de COHERENT, sensibles a la cinemàtica de retrocés nuclear. L'anàlisi global

destrua degeneracions de paràmetres combinant dades d'oscil·lació (solars, atmosfèriques, de reactors, d'acceleradors) amb mesures de secció eficient $CE\nu NS$, establint límits diferencials per als acoblaments de propagació i detecció. Aquesta síntesi demostra com les observacions de neutrins solars restringeixen principalment les interaccions electòniques diagonals en sabor, mentre que les mesures $CE\nu NS$ exploren acoblaments universals amb quarks, amb anàlisis conjuntes que exclouen regions prèviament viables de l'espai de paràmetres NSI. El marc distingeix a més entre escenaris de mediadors lleugers mitjançant signatures dependents de l'energia en conjunts de dades d'oscil·lació versus dispersió.

El tercer pilar anticipa la física de neutrins solars mitjançant determinacions precises de fluxos, utilitzant mesures actualitzades de neutrins de la cadena pp i el cicle CNO per resoldre qüestions fonamentals en astrofísica estel·lar. El Capítol 7 s'encarrega d'explicar quina és la situació més recent dels Models Solars Estàndard (SSM), la determinació de fluxos solars i la incompatibilitat entre la resolució de l'anomalia de l'experiment de font de gal·li i les dades de neutrins solars mitjançant un neutrí estèril lleuger. Recopila els resultats de les Refs. [5, 6]. Integrant les últimes dades de neutrins solars i no solarsincloent la primera detecció directa de neutrins del cicle CNO aquesta anàlisi deslliga les incerteses dels models solars dels paràmetres d'oscil·lació, restringint mecanismes de producció d'energia dependents de la metal·licitat. L'anàlisi pretén resoldre tensions entre escenaris de composició d'alta i baixa metal·licitat predits per diferents SSM, mentre prova explicacions basades en neutrins estèrils per a l'anomalia del Gal·li. La nostra anàlisi va resultar en una preferència estadística pels SSM que prediuen alta metal·licitat, i les comprovacions de consistència sistemàtica demostren incompatibilitat entre els paràmetres de mescla $3 + 1$ afavorits pels experiments de Gal·li i els permesos per les observacions de neutrins solars, independentment de suposicions astrofísiques o de fluxos de reactors. Aquests resultats estableixen els neutrins solars com a diagnòstics duals de física de partícules i processos estel·lars, vinculant mesures precises de fluxos amb models de composició solar i límits d'escenaris BSM.

La convergència d'aquests perspectives analítiques diferents ajustos de paràmetres d'oscil·lació, restriccions BSM i determinacions de fluxos astrofísics forma la contribució central d'aquest treball. En provar rigorosament el marc de tres sabors mentre s'exploren els seus límits, aquesta tesi proporciona un pla per a la física interdisciplinària de neutrins. La síntesi de conjunts de dades i enfocaments teòrics dispars subratlla el paper dels neutrins tant com a missatgers de processos astrofísics com a laboratoris per a física fonamental, guiant experiments futurs cap a la resolució de qüestions pendents en ordenació de masses, violació de CP i interaccions del sector fosc.

PARAULES CLAU: Física de partícules(2203.08), Física Teòrica(2203.10), Astronomia y Astrofísica(2503.00).

Contents

Abstract	iii
Resum	v
List of publications	xi
List of abbreviations	xiii
1 Introduction	1
2 Electroweak theory and the neutrino mass	4
2.1 Electroweak theory of Massless Neutrinos	4
2.1.1 The Electroweak Lagrangian	5
2.1.2 Neutrino interactions	7
2.1.3 The number of neutrinos species	8
2.2 Introducing Neutrino Masses	8
2.2.1 Dirac Neutrinos	8
2.2.2 Majorana Neutrinos	10
2.2.3 Minimal gauge invariant neutrino mass	10
2.2.4 Leptonic Mixing and CP Violation	11
2.3 Neutrino flavour Oscillations	12
2.4 Flavour Transitions in Matter	14
2.4.1 Matter potentials	15
2.4.2 Modified Evolution	17
2.4.3 Solar neutrinos: MSW effect	18
2.5 Neutrino Mass Scale and Neutrino Mass Ordering	21
3 Experimental Inputs	23
3.1 Solar Neutrinos	24
3.1.1 Simulation of Borexino Phase II and III spectra	27
3.2 Atmospheric Neutrinos	36
3.3 Reactor Neutrinos	38
3.4 Accelerator Neutrinos	40
3.4.1 Long-Baseline (LBL) Experiments	41
3.4.2 Simulation of Nova	41
3.5 CEvNS	44
3.6 Gallium Source Experiments	45
3.7 Summary	46

4	Global analysis of Three neutrino oscillations	48
4.1	Global analysis	49
4.2	Status of neutrino mass ordering, leptonic CP violation, and θ_{23}	53
4.2.1	Updates from T2K and NOvA	53
4.2.2	Effects from $\nu_\mu/\bar{\nu}_\mu$ versus $\bar{\nu}_e$ disappearance	55
4.2.3	Sensitivity to the neutrino mass ordering	58
4.3	Updates in the “12” sector	60
4.4	Projections on neutrino mass scale observables	62
4.5	Summary	64
5	Three neutrino oscillations with new interactions: Formalism	66
5.1	Non-Standard Interactions - Formalism	66
5.1.1	Neutrino oscillations in the presence of NSI	69
5.1.2	Neutrino detection cross sections in the presence of NSI	76
5.2	New Physics scenarios of neutrino interactions	79
5.2.1	Neutrino Magnetic-Moments	79
5.2.2	Models with light scalar, pseudoscalar, and vector mediators	80
5.3	New pseudoscalar interactions in neutrino propagation	81
5.3.1	Monopole-dipole potential: Mathematical formulation	82
5.4	Summary	85
6	Three neutrino oscillations with new interactions: Analysis	87
6.1	Confronting new interactions with electrons with Borexino data	87
6.1.1	Non-Standard Interactions with electrons - Results	88
6.1.2	Neutrino magnetic moment	92
6.1.3	Light vector mediators	92
6.1.4	Light scalar and pseudoscalar mediators	94
6.2	Constraining NSI with electrons and quarks with global oscillation data	95
6.2.1	Simulation details	95
6.2.2	New constraints on NSI with electrons	97
6.2.3	Updated constraints on NSI with quarks	99
6.2.4	Constraints on NSI with quarks and electrons: effective NSI in the Earth	102
6.2.5	Present status of the LMA-D solution	105
6.3	Constraining Monopole-Dipole interactions with global oscillation data	107
6.3.1	Bounds from solar antineutrino constraints	110
6.4	Summary	111
7	Determination of the Solar Neutrino Fluxes and addressing Gallium Anomaly	115
7.1	Determination of solar neutrino fluxes	115
7.1.1	Solar Neutrino Fluxes: State of the Art	115
7.1.2	Analysis framework	117
7.1.3	New determination of solar neutrino fluxes	120
7.1.4	Examination of the determination of the CNO fluxes	125
7.1.5	Comparison with Standard Solar Models	128
7.2	Confronting the gallium anomaly with solar neutrino data	130
7.2.1	Results	132
7.3	Summary	138

8	Conclusion	139
A		144
A.1	Assumed true values for the MO test	144
B		145
B.1	Allowing free normalizations for the three CNO fluxes	145
C		149
C.1	Derivation of the scalar-pseudoscalar potential	149

List of publications

The original contents of this thesis are based on the following publications:

- P. Coloma, M. C. Gonzalez-Garcia, M. Maltoni, **J. P. Pinheiro**, S. Urrea, “Constraining new physics with Borexino Phase-II spectral data”, *J. High Energ. Phys.* **07** (2022) 138
- P. Coloma, M. C. Gonzalez-Garcia, M. Maltoni, **J. P. Pinheiro**, S. Urrea, “Global constraints on non-standard neutrino interactions with quarks and electrons”, *J. High Energ. Phys.* **08** (2023) 032
- M. C. Gonzalez-Garcia, M. Maltoni, **J. P. Pinheiro**, A. M. Serenelli, “Status of Direct Determination of Solar Neutrino Fluxes after Borexino”, *J. High Energ. Phys.* **02** (2024) 064
- S. Ansarifard, M. C. Gonzalez-Garcia, M. Maltoni, **J. P. Pinheiro**, “Solar neutrinos and leptonic spin forces”, *J. High Energ. Phys.* **07** (2024) 172
- I. Esteban, M. C. Gonzalez-Garcia, M. Maltoni, I. Martinez-Solar, **J. P. Pinheiro**, T. Schwetz, “NuFit-6.0: Updated global analysis of three-flavor neutrino oscillations”, *J. High Energ. Phys.* **12** (2025) 216
- M. C. Gonzalez-Garcia, M. Maltoni, **J. P. Pinheiro**, “Solar Model Independent Constraints on the Sterile Neutrino Interpretation of the Gallium Anomaly”, *Phys. Lett. B* **862** (2025) 139297

The following publications have been developed in parallel to the content of this thesis, although they have not been included in this dissertation:

- **J. P. Pinheiro**, C. A. S. Pires, “Vacuum stability and spontaneous violation of the lepton number at a low-energy scale in a model for light sterile neutrinos”, *Phys. Rev. D* **102** (2020) 015015
- **J. P. Pinheiro**, C. A. S. Pires, F. Queiroz, Y. Villamizar, “Confronting the inverse seesaw mechanism with the recent muon $g - 2$ result”, *Phys. Lett. B* **823** (2021) 136764
- **J. P. Pinheiro**, C. A. S. Pires, “On the Higgs spectra of the 3-3-1 model”, *Phys. Lett. B* **833** (2022) 137584
- **J. P. Pinheiro**, C. A. S. Pires, “On the Higgs spectra of the 3-3-1 model with the sextet of scalars engendering the type II seesaw mechanism”, *Nucl. Phys. B* **993** (2023) 116293

- A. Doff, **J. P. Pinheiro**, C. A. S. Pires, “Exploring solutions to the muon $g - 2$ anomaly in a THDM-like model under flavor constraints”, *arXiv:2405.05839* [hep-ph]
- D. Bečirević, F. Jaffredo, **J. P. Pinheiro**, O. Sumensari, “Lepton flavor violation in exclusive $b \rightarrow d\ell_i\ell_j$ and $b \rightarrow s\ell_i\ell_j$ decay modes”, *Phys. Rev. D* **110** (2024) 075004
- J. Gehrlein, P. A. N. Machado, **J. P. Pinheiro**, “Constraining non-standard neutrino interactions with neutral current events at long-baseline oscillation experiments”, *JHEP* **05** (2025) 065
- A. Doff, **J. P. Pinheiro**, C. A. S. Pires, “Leptoquark-induced radiative masses for active and sterile neutrinos within the framework of the 3-3-1 model”, *Phys. Lett. B* **863** (2025) 139375
- P. Escalona, **J. P. Pinheiro**, A. Doff, C. A. S. Pires “Meson Mixing Bounds on Z' Mass in the Alignment Limit: Establishing the Phenomenological Viability of the 331 Model”, *arXiv:2503.14653* [hep-ph]

List of abbreviations

BSM	Beyond the Standard Model
CEνNS	Coherent elastic neutrino-nucleus scattering
CP	Charge Parity
CC NSI	Charged Current Non-Standard Interactions
ESS	European Spallation Source
IO	Inverted ordering
LBL	Long baseline
NC NSI	Neutral Current Non-Standard Interactions
NO	Normal ordering
NP	New Physics
NSI	Non-Standard Interactions
QF	Quenching Factor
SBL	Long baseline
SM	Standard Model
SNS	Spallation Neutron Source
SSM	Standard Solar Model

Chapter 1

Introduction

There are many ways to start the discussion of the Standard Model and the role of neutrinos in it. In this thesis, I choose to begin with a chronological one. Neutrinos are essential to understand all radioactivity phenomena. As described in detail in [7], in 1896 Henri Becquerel started to methodologically explore the interaction of Uranium with different materials. He was intrigued by this “magical” behavior of Uranium crystals that spontaneously emit x-rays from it, discovered by Wilhelm Röntgen in 1895. He thought that this strange material would absorb energy emitted by the Sun and after it, releases it in the form of x-rays. In his diary [7], he wrote that one day was very cloudy and he wrapped black paper around photographic plates together with uranium salt and placed it inside the drawer of his laboratory, away from sunlight. One day after, to his surprise, he noticed that the plates had been exposed, indicating that the Uranium salts emitted radiation spontaneously, without the need for exposure to light. And how such discovery is associated with neutrinos? Let us advance a little bit on time.

According to the book “From X rays to quarks”[8] written by Emilio Segrè, just after Becquerel’s discovery, experimentalists coupled electric and magnetic field generator machines in order to separate the content of the energy released. After applying the fields, three different group of particles were identified: α particles, a positively charged beam without penetration properties which could be reflected by a thin paper; X rays, that are not deflected by electric fields and have good penetration in some materials, but scatter with bones and metals; and β particles. These could be positively or negatively charged, with a stronger penetration property than α particles.

In 1914, James Chadwick observed that the primary beta spectrum is continuum[8]. This means that, for example, a Thorium-234 decays into protactinium-234 and a beta particle. From a simple two-body decay, using conservation of energy, the beta particle should be monochromatic!

After different interpretations of the strange experimental result, it appears the genius idea of Wolfgang Pauli in his famous letter for the “Radioactives”[9]. There, he suggested “I have hit upon a desperate remedy to save the exchange theorem of statistics and the law of conservation of energy. Namely, the possibility that there could exist in the nuclei electrically neutral particles, that I wish to call neutrons, which have spin 1/2 and obey the exclusion principle ... The continuous spectrum would then become understandable by the assumption that in decay, a neutron is emitted in addition to the electron such that the sum of the energies of the neutron and electron is constant. Now the question that has to be dealt with is which forces act on the neutrons?...” With this the *neutrino* was born into the theoretical physics.

In fact, some years after Pauli’s letter, Chadwick discovered a neutral spin 1/2 particle, heavy, that participates in the radioactive interactions. He named it neutron. But this

neutron was not the light emitted state postulated by Pauli. In 1934, Enrico Fermi [9, 10] renamed the light neutral emitted state as *neutrino* and he wrote down the first field theoretical form of an interaction involving the neutron, the proton, electron and neutrino fields that would describe weak interactions. Schematically

$$\mathcal{H}_{\text{weak}}^{CC} = \frac{4G_F}{\sqrt{2}} \left[J^\mu(x) J_\mu(x) \right], \quad (1.1)$$

such that $J^\mu(x)$ represents the charged current (CC)

$$J_\mu(x) \sim \bar{p}\gamma_\mu n + \bar{\ell}\gamma_\mu \nu \quad (1.2)$$

As we will see below the Lorentz structure proposed by Fermi was not quite correct. Also we now know that the fundamental interaction can be described not in terms of hadrons like protons and neutrons, but quarks.

Still from the interaction described above, it was possible to write the decay of a neutron into a proton, an electron and an electron antineutrino as:

$$n(udd) \rightarrow p(uud) + e^- + \bar{\nu}_e \quad (1.3)$$

unraveling the fundamental understanding of all radioactive phenomena.

After all our discussion, we are able to describe all physics behind what happened to Becquerel on that cloudy day. It is well known that Uranium is a heavy element whose atomic nucleus is unstable, making it radioactive. It undergoes radioactive decay processes involving the emission of subatomic particles. The uranium nucleus emits an α particle, which consists of 2 protons and 2 neutrons (a helium nucleus).

The most common material studied by Becquerel was Uranium-238 (^{238}U). It typically decays into thorium-234 (^{234}Th):



Thorium-234 (^{234}Th), produced via alpha decay, undergoes beta decay to form protactinium-234 (^{234}Pa):



In this process, a neutron in the nucleus decays into a proton, emitting an electron (β^-) and an electron antineutrino ($\bar{\nu}_e$). After alpha or beta decay, the daughter nucleus is often left in an excited state, releasing its excess energy as gamma radiation.

The Inverse Beta Decay Experiment

The existence of free neutrinos was confirmed through the inverse beta decay experiment conducted by Frederick Reines and Clyde Cowan in 1956 [11]. They observed the reaction:

$$\bar{\nu}_e + p \rightarrow e^+ + n, \quad (1.4)$$

where an electron antineutrino ($\bar{\nu}_e$) interacts with a proton to produce a positron (e^+) and a neutron. This experiment was conducted using a nuclear reactor as a source of antineutrinos and a detector consisting of a liquid scintillator to capture the positrons and neutrons. The detection of the positron and neutron provided direct evidence for the existence of neutrinos and validated Fermi's theory of weak interactions, which will be described below.

The inverse beta decay experiment confirmed the reality of neutrinos, which had been postulated by Pauli. The success of this experiment also demonstrated the power of neutrino detection techniques, which have since become essential tools in studying weak interactions and neutrino properties.

Parity Violation and the V-A Structure

The structure of weak interactions was further clarified by the discovery of parity violation. In 1956, Chien-Shiung Wu and collaborators conducted an experiment involving the beta decay of cobalt-60 nuclei, which demonstrated that weak interactions violate parity symmetry (P) [12]. This means that weak interactions are not invariant under spatial inversion. The experiment measured the angular distribution of electrons emitted from polarized cobalt-60 nuclei and found an asymmetry in the emission relative to the nuclear spin direction. This asymmetry indicated that the weak force distinguishes between left-handed and right-handed systems, a clear violation of parity symmetry[9].

The violation of parity was a profound discovery, as it revealed that the weak interaction is intrinsically chiral. This led to the formulation of the $V - A$ (vector minus axial-vector) structure of the weak currents, proposed by Marshak and Sudarshan and independently by Feynman and Gell-Mann[9]. The $V - A$ structure implies that the weak interaction couples only to left-handed particles and right-handed antiparticles. Mathematically, the weak current J^μ is then expressed as:

$$J_\mu(x) = \bar{u}\gamma_\mu P_L d + \bar{\ell}\gamma_\mu P_L \nu \quad (1.5)$$

where the left and right chirality projection operators are defined as

$$P_L = \frac{1}{2}(1 - \gamma_5), \quad P_R = \frac{1}{2}(1 + \gamma_5). \quad (1.6)$$

The P_L in Eq. (1.5) ensures that only the left-handed components of the fermion fields participate in weak CC interactions. This chiral nature of the weak force is a fundamental feature that distinguishes it from other interactions, such as electromagnetism and the strong force, which are parity-conserving.

Despite its successes, the $V - A$ theory faced several theoretical and experimental challenges. From a theoretical point of view, the four-fermion interaction described by the $V - A$ theory is non-renormalizable. This means that calculations at high energies or short distances lead to infinities that cannot be systematically removed, making the theory inconsistent as a fundamental description of weak interactions. At the same time, at high energies, the cross-section for weak processes predicted by the $V - A$ theory grows without bound, violating unitarity. And since the $V - A$ theory is effective, it does not explain the mechanism by which weak interactions are mediated. Unlike electromagnetism, which is mediated by the photon, the four-fermi theory lacks a corresponding gauge boson.

These issues pointed to the need for a deeper theory that could address the shortcomings of the $V - A$ framework. This led to the development of the **Standard Model (SM)** of particle physics.

Chapter 2

Electroweak theory and the neutrino mass

2.1 Electroweak theory of Massless Neutrinos

The Standard Model (SM) of the elementary particles, proposed by Weinberg, Glashow and Salam [13–15] is the most precisely tested fundamental theory with predictions matching observations to 10^{-11} accuracy [16]. In this thesis, we will not go into all the details of the SM. We are going to focus on the Electroweak sector the aspects which are directly associated with neutrinos.

The Standard Model is a gauge theory constructed under the gauge symmetry principle which states that the laws of physics arise as a consequence of invariance under local (aka gauge) transformations of some symmetry group [17]. In these constructions the interactions are mediated by spin-one particles, called gauge bosons, in correspondence with the generators of the gauge group.

How is this machinery associated with neutrinos? To make a gauge theory comprehending the neutrino interactions one must first find a gauge symmetry group that is compatible with what we know of those interactions, in particular it must violate parity [18] and mediate $V - A$ interactions between the left-handed neutrinos and electrons so the mediator must be electrically charged. This can be achieved with a symmetry group $SU(2)$ transforming only the left-handed fields, hence labeled $SU(2)_L$ ([19]).

More technically, the general way to interpret the 4-fermion interaction is via the exchange of the gauge boson associated with the $T^\pm \propto T^1 \pm iT^2$ generators of the group $SU(2)_L$, denoted as \hat{W}^\pm , which transforms ν_L into ℓ_L (and quark u_L into quark d_L) and vice versa. This $SU(2)_L$ group is further combined with $U(1)_Y$, a *hypercharge* symmetry group, with Y related to the electric charge Q through the third generator T_3 of $SU(2)_L$ as [20]

$$Q = T_3 + \frac{Y}{2}. \quad (2.1)$$

The resulting *electroweak* unified theory has four generators and predicts the existence of three gauge bosons, W^\pm and Z^0 , as well as the photon, all of which have been experimentally confirmed [21].

The Standard Model (SM) consists then of three generations of fermions, and four gauge bosons. In addition, the model also contains a fundamental scalar, the Higgs boson, needed for spontaneous symmetry breaking and mass generation. We list their transformation properties under the gauge group $SU(2)_L \times U(1)_Y$ [22] in Table 2.1. We notice that the table does not contain a right-handed neutrino, ν_R , because such a state

would be a total singlet of the gauge interactions: as seen from Eq. (2.1), its hypercharge, charge, colour and weak-isospin would all be zero.

Particle	$SU(2)_L$	Y	Q	Type
$Q_{L,i} \equiv \begin{pmatrix} u_L \\ d_L \end{pmatrix}, \begin{pmatrix} c_L \\ s_L \end{pmatrix}, \begin{pmatrix} t_L \\ b_L \end{pmatrix}$	Doublet	$+\frac{1}{3}$	$u : +\frac{2}{3}, d : -\frac{1}{3}$	Quarks
u_R, c_R, t_R	Singlet	$+\frac{4}{3}$	$+\frac{2}{3}$	Quarks
d_R, s_R, b_R	Singlet	$-\frac{2}{3}$	$-\frac{1}{3}$	Quarks
$L_{L,i} \equiv \begin{pmatrix} \nu_{eL} \\ e_L \end{pmatrix}, \begin{pmatrix} \nu_{\mu L} \\ \mu_L \end{pmatrix}, \begin{pmatrix} \nu_{\tau L} \\ \tau_L \end{pmatrix}$	Doublet	-1	$\nu : 0, e : -1$	Leptons
e_R, μ_R, τ_R	Singlet	-2	-1	Leptons
$\phi \equiv \begin{pmatrix} G^+ \\ \frac{v+h+iG_0}{\sqrt{2}} \end{pmatrix}$	Doublet	$+1$	$G^+ : +1, h, G_0 : 0$	Higgs

Table 2.1: Quantum numbers for the different representations of the gauge group, associated to the Higgs boson and the fermions belonging to each family in the SM. Fermion families are ordered attending to their masses: the third one is the most massive, while the first one contains the lightest fermions.

2.1.1 The Electroweak Lagrangian

The electroweak Lagrangian constructed with the matter contents of Table 2.1 and the gauge symmetry group $SU(2)_L \times U(1)_Y$ can be written as:

$$\mathcal{L}_{\text{EW}} = \mathcal{L}_{\text{Gauge}} + \mathcal{L}_{\text{Fermion}} + \mathcal{L}_{\text{Higgs}} + \mathcal{L}_{\text{Yukawa}}, \quad (2.2)$$

where each term is defined as follows:

- $\mathcal{L}_{\text{Gauge}}$ → Describes the kinetic terms for the gauge fields and their self-interactions.
- $\mathcal{L}_{\text{Fermion}}$ → Represents the interactions between fermions and gauge bosons.
- $\mathcal{L}_{\text{Higgs}}$ → Encodes the dynamics of the Higgs field and its interactions with itself and with gauge bosons, leading to spontaneous symmetry breaking and the generation of the gauge boson masses.
- $\mathcal{L}_{\text{Yukawa}}$ → Describes the interaction between the Higgs field and fermions, leading to their mass generation.

Gauge Field Lagrangian

$$\mathcal{L}_{\text{Gauge}} = -\frac{1}{4}W_{\mu\nu}^a W^{a,\mu\nu} - \frac{1}{4}B_{\mu\nu} B^{\mu\nu}, \quad (2.3)$$

with $W_{\mu\nu}^a$ and $B_{\mu\nu}$ are the field strength tensors of $SU(2)_L$ and $U(1)_Y$, respectively. These terms describe the dynamics of the gauge bosons.

Fermion Lagrangian

The fermions are organized into doublets under $SU(2)_L$ and singlets under $U(1)_Y$ and there are three families of each fermion. The interaction terms are given by:

$$\mathcal{L}_{\text{Fermion}}^{\psi} = \sum_{\text{generations}} \bar{\psi}_L i\gamma^{\mu} \left(\partial_{\mu} - ig\frac{\tau^a}{2}W_{\mu}^a - ig'\frac{Y}{2}B_{\mu} \right) \psi_L + \bar{\psi}_R i\gamma^{\mu} \left(\partial_{\mu} - ig'\frac{Y}{2}B_{\mu} \right) \psi_R, \quad (2.4)$$

where g and g' are the gauge couplings and $\tau^a/2$.

Higgs Lagrangian and Spontaneous Symmetry Breaking

The Higgs mechanism introduces a scalar doublet under $SU(2)_L$, which will induce the breaking of the gauge symmetry as

$$SU(2)_L \times U(1)_Y \rightarrow U(1)_{em},$$

where $U(1)_{em}$ represents the electromagnetic interaction. This mechanism gives mass to the weak bosons (W^\pm, Z^0) while leaving the photon massless, consistent with experimental observations.

The Higgs field ϕ is introduced as a complex scalar doublet under $SU(2)_L$:

$$\phi = \begin{pmatrix} \phi^+ \\ \phi^0 \end{pmatrix}. \quad (2.5)$$

Its Lagrangian is:

$$\mathcal{L}_{\text{Higgs}} = (D_\mu \phi)^\dagger (D^\mu \phi) - V(\phi), \quad (2.6)$$

where D_μ is the covariant derivative:

$$D_\mu = \partial_\mu - ig \frac{\tau^a}{2} W_\mu^a - ig' \frac{Y}{2} B_\mu, \quad (2.7)$$

and the potential $V(\phi)$ is:

$$V(\phi) = \mu^2 \phi^\dagger \phi + \lambda (\phi^\dagger \phi)^2. \quad (2.8)$$

When $\mu^2 < 0$, the Higgs field acquires a vacuum expectation value (VEV):

$$\langle \phi \rangle = \frac{1}{\sqrt{2}} \begin{pmatrix} 0 \\ v \end{pmatrix}.$$

Quantizing above this ground state induces the spontaneous breaking of $SU(2)_L \times U(1)_Y \rightarrow U(1)_{em}$ and it generates masses for the gauge bosons:

$$M_W = \frac{gv}{2}, \quad M_Z = \frac{\sqrt{g^2 + g'^2}v}{2}, \quad M_\gamma = 0,$$

where W^\pm, Z^0 , and the photon (γ) are the resulting physical mass eigenstate gauge bosons. The photon remains massless, corresponding to the unbroken $U(1)_{em}$ symmetry.

Yukawa interaction

The Yukawa interactions in the Standard Model describe the coupling between fermions and the Higgs field and they are responsible for generating their masses after spontaneous electroweak symmetry breaking. The Yukawa Lagrangian is expressed as:

$$\mathcal{L}_{\text{Yukawa}} = - \sum_{\text{generations}} y^u \bar{Q}_L \tilde{\phi} u_R + y^d \bar{Q}_L \phi d_R + y^e \bar{L}_L \phi e_R + \text{h.c.} \quad (2.9)$$

where y^f represents the Yukawa coupling matrices, which are generally complex and non-diagonal, and $\tilde{\phi} = i\sigma_2 \phi^*$ is the conjugate of the ϕ scalar doublet field. After the Higgs

field acquires a vacuum expectation value (VEV), the Yukawa interactions lead to the fermion mass terms:

$$m_f = \frac{y^f v}{\sqrt{2}} \quad (2.10)$$

For the quark sector, the Higgs spontaneously generates masses for both up- and down-quarks via their couplings to ϕ and $\tilde{\phi}$, while for the leptonic sector, there is mass generated by the Higgs only for the electrically charged leptons, while neutrinos are massless as the SM does not contain the ν_R field needed to construct the required Yukawa interaction which would generate a neutrino mass. This was totally consistent with all experimental results at the time when the model was constructed. The first robust experimental evidence for neutrino mass came from the observation of neutrino oscillations by the Super-Kamiokande experiment in 1998 [23]. In the next section, we will discuss how to extend the SM to include massive neutrinos and their implications.

A final remark in this subsection concerns the structure of the Yukawa matrices y^f . The non-diagonal nature of the Yukawa matrices enables flavour mixing between different generations of fermions. This phenomenon was first observed in the oscillations of neutral mesons, such as K^0 - \bar{K}^0 , B^0 - \bar{B}^0 , and D^0 - \bar{D}^0 systems. However, this is not the case for leptons because no Yukawa term can be built for the neutrinos. As a consequence, the SM with the particle contents of Table 2.1 has a global accidental symmetry which implies that together with the total baryon number, each of the lepton flavours (and therefore the total lepton number) is conserved.

2.1.2 Neutrino interactions

Since neutrinos are neutral particles, in the SM they interact at tree-level exclusively through the weak interactions, which can be classified into two main types:

- **Charged current interactions (CC):** These interactions are mediated by the exchange of W^\pm bosons and involve transitions between neutrinos and their corresponding charged lepton

$$\mathcal{L}_{\text{CC}} = -\frac{g}{\sqrt{2}} \left(\bar{\ell}_L \gamma^\mu \nu_L W_\mu^- + \text{h.c.} \right), \quad (2.11)$$

where g is the weak coupling constant, ℓ_L represents the left-handed charged lepton, and ν_L denotes the left-handed neutrino. Charged current interactions allow for the identification of neutrino *flavour* through the observation of the associated charged lepton. We label those neutrinos as $(\nu_e, \nu_\mu, \nu_\tau)$. CC interactions are essential in experiments involving neutrino scattering off nuclei, where the detection of electrons, muons, or tau leptons signals the presence of electron, muon, or tau neutrinos, respectively.

- **Neutral current interactions (NC):** Neutral current interactions are mediated by the exchange of the Z^0 boson as

$$\mathcal{L}_{\text{NC}} = -\frac{g}{2 \cos \theta_W} \bar{\nu}_L \gamma^\mu \nu_L Z_\mu + \text{h.c.}, \quad (2.12)$$

where θ_W is the Weinberg angle. Unlike charged current interactions, NC processes are flavour-blind, meaning they provide limited information about the specific neutrino flavour involved. However, they contribute to neutrino-nucleon scattering and play a vital role in understanding the total neutrino flux in detectors.

Both types of interactions underpin the core mechanisms through which neutrinos are detected in a variety of experimental setups, from large underground detectors to particle accelerators and astrophysical observatories. Their precise measurement offers valuable information on neutrino masses, mixing angles, and potential physics beyond SM (BSM).

2.1.3 The number of neutrinos species

The discovery of the Z boson and subsequent precision measurements at LEP (Large Electron-Positron Collider) in the 1990s provided critical insights into the EW sector of the SM. The Z boson mediates neutral current interactions and can decay into fermion-antifermion pairs, including neutrinos [24–26]. The total decay width of the Z boson, Γ_Z , is determined by summing the partial widths for its decay into all possible fermions:

$$\Gamma_Z = \sum_f \Gamma(Z \rightarrow f\bar{f}). \quad (2.13)$$

Each partial width depends on the number of fermion generations and their couplings to the Z , which are specified by the SM:

$$\Gamma(Z \rightarrow f\bar{f}) \propto N_c^f \cdot (g_V^2 + g_A^2), \quad (2.14)$$

where N_c^f is the color factor ($N_c = 3$ for quarks, $N_c = 1$ for leptons), and g_V and g_A are the vector and axial couplings of the fermion to the Z boson.

An important result of LEP was the precise determination of the invisible decay width of the Z boson, Γ_{inv} . In the SM Γ_{inv} is due to the decay of the Z boson into neutrinos. Since the SM predicts that each generation of neutrinos contributes equally to the decay mode, one gets:

$$\Gamma_{\text{inv}} = \Gamma(Z \rightarrow \nu\bar{\nu})N_\nu = \frac{G_F M_Z^3}{12\pi\sqrt{2}}N_\nu, \quad (2.15)$$

where N_ν is the number of neutrino species. LEP measured Γ_{inv} precisely resulting in [24–26]:

$$N_\nu = 2.984 \pm 0.008, \quad (2.16)$$

consistent with three active neutrino flavours (ν_e, ν_μ, ν_τ) as predicted by the SM.

Hence, this measurement is fundamental for us to state that there are only three *active* neutrinos (those that participate in the weak interactions). If there are more neutrinos, they must be *sterile i.e.*, they do not participate in the weak interactions).

2.2 Introducing Neutrino Masses

As we will discuss in the next chapter in detail, neutrino oscillation experiments have shown beyond doubt that neutrinos are massive and the SM as described above needs to be extended to account for this. In this section we will introduce the simplest SM extensions with massive neutrinos and the generation of lepton flavour mixing.

2.2.1 Dirac Neutrinos

The *apparently* minimal way to extend the SM and generate neutrino masses is by introducing three right-handed neutrinos (RHNs), ν_{Ri} . As mentioned above, they are singlets of the SM group and for that reason they are often referred to as *sterile* neutrinos. The

introduction of three RHNs allows for a new Yukawa interaction, similar to those for up-type quarks:

$$\mathcal{L} \supset -y_{ij}^\nu \bar{L}_i \tilde{\phi} \nu_{Rj} + \text{h.c.}, \quad (2.17)$$

After spontaneous symmetry breaking, this interaction generates the following *Dirac* neutrino mass term:

$$\mathcal{L}_D = -M_D \bar{\nu}_{L_i} \nu_{R_j} + \text{h.c.}, \quad (2.18)$$

with

$$M_D = \frac{v}{\sqrt{2}} y_{ij}. \quad (2.19)$$

being a 3×3 matrix.

The three neutrino mass eigenstates are obtained by diagonalizing M_D via unitary transformations:

$$\nu_L^D = V_L^{\nu\dagger} \nu_L, \quad \nu_R^D = V_R^{\nu\dagger} \nu_R, \quad (2.20)$$

where $\nu_{R,L}^D$ represent the mass eigenstates and $\nu_{R,L}$ the flavour eigenstates. The diagonalization condition is:

$$V_L^{\nu\dagger} M_D V_R^\nu = M_D^{\text{diag}}. \quad (2.21)$$

We call the massive neutrino states in this scenario *Dirac* neutrinos.

Several comments are in order

- In this case total lepton number is still conserved since one can assign opposite lepton number to ν^D and its charge conjugate

$$\nu^{Dc} \equiv C \nu^{D\dagger}, \quad (2.22)$$

(here C is the charge conjugate matrix for spinors) because they are two distinct states.

But as we will argue below, in this scenario the conservation of total lepton number is not longer accidental but it has been implicitly *imposed* by adding only the term in Eq. (2.17) and not additional terms involving only the RHN's which, being purely singlets of the gauge group, would be equally allowed by the gauge symmetry.

- As we will see in Chapter 4 global analyses of neutrino experimental data [27] robustly indicate sub-eV masses for neutrinos. For Dirac neutrinos, the Yukawa couplings in eq. (2.19) must be of order $|y^\nu| \lesssim 10^{-12}$, significantly smaller than those for other fermions ($|y^{\text{other fermions}}| \gtrsim 10^{-6}$). This raises a naturalness question: *Why are neutrinos so light compared to other fermions?* This question remains unresolved in this minimal scenario. While this thesis will not dive deeply into extended scenarios, it is worth noting that introducing new particles into the SM can generate Dirac neutrino masses with Yukawa couplings larger than 10^{-6} [10].
- Dirac neutrinos predict a non-zero magnetic moment proportional to their mass:

$$\mu_\nu = \frac{3eG_F m_\nu}{8\pi^2 m_e}, \quad (2.23)$$

where m_e is the electron mass. This allows interactions with external electromagnetic fields, though heavily suppressed by the small neutrino mass.

2.2.2 Majorana Neutrinos

A Majorana neutrino is a fermion that is its own antiparticle, implying that the neutrino field satisfies the condition:

$$\nu^M = \nu^{M^c} = C\overline{\nu^M}^T, \quad (2.24)$$

In the minimal extension of the SM there are three Majorana neutrinos which are mass eigenstates of a mass term built out of the three left-handed states and their charge conjugate

$$\mathcal{L}_M = -\frac{1}{2}M_M \left(\overline{(\nu_L)^c} \nu_L + \overline{\nu_L} (\nu_L)^c \right), \quad (2.25)$$

such that M_M represents a 3×3 Majorana mass which is a symmetric matrix by construction and the diagonalization condition now reads

$$V^{\nu\dagger} M_M V^{\nu*} = M_M^{\text{diag}} \quad (2.26)$$

so the mass eigenstates verify

$$\nu_L^M = V^{\nu\dagger} \nu_L, \quad \nu_R^M = V^*(\nu_L)^C. \quad (2.27)$$

We notice that in this case total lepton violated as the Majorana mass term Eq. (2.25) has total lepton number ± 2 .

But most importantly Eq. (2.25) violates gauge invariance and therefore can only be understood as a low energy effective operator generated by some beyond the standard model physics as we will discuss next.

2.2.3 Minimal gauge invariant neutrino mass

Once we include m right-handed neutrinos the most general form of the renormalizable gauge invariant mass term which can be built is

$$\mathcal{L}_m = -\overline{\nu}_R M_D \nu_L - \frac{1}{2} \overline{\nu}_R^c M_R \nu_R + \text{h.c.}, \quad (2.28)$$

where M_D is $m \times 3$ matrix and M_R is a $m \times m$ symmetric matrix. In general this scenario leads to $3 + m$ massive Majorana neutrinos with

$$\nu^M = V^{\nu\dagger} \vec{\nu}, \quad (2.29)$$

where $\vec{\nu} = (\vec{\nu}_L, \vec{\nu}_R^C)^T$ contains the $3+m$ weak-eigenstate neutrinos.

Two interesting limiting cases are:

- $M_R \gg M_D$. In this case diagonalization leads to three states which are much lighter than the other m with an effective Majorana mass

$$m_\nu \simeq -M_D M_R^{-1} M_D^T. \quad (2.30)$$

The three light states are Majorana neutrinos combination of the 3 active neutrinos with projections over the right-handed states suppressed as $M_D M_R^{-1}$.

This is the so-called see-saw mechanism [28–31] in which the light neutrino masses are suppressed by the scale of M_R , which can be as high as the Grand Unified Theory (GUT) scale, thus naturally explaining why neutrino masses are orders of magnitude smaller than the masses of other fermions.

- Some s number of the eigenvalues of M_R is not large compared to those of M_D . In this case the spectrum contains $3+s$ light neutrino states and $m-s$ heavy neutrinos. All of them are Majorana. These are the scenarios usually named in the literature of light sterile neutrino models.

2.2.4 Leptonic Mixing and CP Violation

The charged current introduced in Eq. (2.11) describes the interaction between the gauge boson W^\pm and the leptons in the weak (or flavour) basis $\alpha = e, \mu, \tau$. In the absence of any new physics in the charged lepton sector, it is always possible to identify the three flavour charged lepton states with the states of well defined mass. But in that basis, as we have seen, the massive neutrinos will still be a superposition of the weak eigenstates so for massive leptons the CC lagrangian reads

$$\mathcal{L}_{CC} = - \sum_{\alpha} \sum_k \frac{g}{\sqrt{2}} \left(U_{\alpha k} \bar{\ell}_{\alpha L} \gamma^{\mu} \nu_{kL} W_{\mu}^{-} + \text{h.c.} \right), \quad (2.31)$$

where ν_k is a neutrino with definite mass. In the most general case with N massive neutrinos the *leptonic mixing matrix* U will be a $3 \times N$ matrix which verifies $U \times U^{\dagger} = I_{3 \times 3}$ but in general $U^{\dagger} U \neq I_{N \times N}$ and in this basis it can be identify with the upper 3 lines of the V^{ν} (V_L^{ν}) matrix diagonalizing the neutrino mass matrix for the case of Majorana (Dirac) neutrinos after the non-physical phases have been absorbed in the definition of the mass eigenstates which depends if neutrinos are Dirac or Majorana particles. Following Chapter 4 of [32] one finds that for Majorana [Dirac] neutrinos the U matrix contains a total of $6(N - 2)$ [$5N - 11$] real parameters, of which $3(N - 2)$ are angles and $3(N - 2)$ [$2N - 5$] can be interpreted as physical phases. So for a given N number of massive neutrinos

$$U^{\text{Maj}} = U^{\text{Dirac}} \times P_{\text{Maj}} \quad (2.32)$$

where P_{Maj} is a diagonal matrix containing the additional $N - 1$ phases.

For most of this thesis we will be studying scenarios with three light states; in this case, the U matrix contains 3 mixing angles plus 1 phase if neutrinos are Dirac and 3 if they are Majorana. It can be parametrized as

$$U \equiv \begin{pmatrix} U_{e1} & U_{e2} & U_{e3} \\ U_{\mu1} & U_{\mu2} & U_{\mu3} \\ U_{\tau1} & U_{\tau2} & U_{\tau3} \end{pmatrix} = \begin{pmatrix} 1 & 0 & 0 \\ 0 & c_{23} & s_{23} \\ 0 & -s_{23} & c_{23} \end{pmatrix} \begin{pmatrix} c_{13} & 0 & s_{13} e^{-i\delta_{\text{CP}}} \\ 0 & 1 & 0 \\ -s_{13} e^{i\delta_{\text{CP}}} & 0 & c_{13} \end{pmatrix} \begin{pmatrix} c_{12} & s_{12} & 0 \\ -s_{12} & c_{12} & 0 \\ 0 & 0 & 1 \end{pmatrix} \times P_{\text{Maj}} \quad (2.33)$$

where $c_{ij} = \cos \theta_{ij}$ and $s_{ij} = \sin \theta_{ij}$ and the three mixing angle θ_{ij} can be taken with generality to be in the first quadrant $0 \leq \theta_{ij} \leq \pi/2$ and the phases to be all between 0 and 2π . $P_{\text{Maj}} = I$ for Dirac neutrinos while for Majorana neutrinos contains the additional two phases

$$P_{\text{Maj}} = \begin{pmatrix} 1 & 0 & 0 \\ 0 & e^{i\alpha_{21}/2} & 0 \\ 0 & 0 & e^{i\alpha_{31}/2} \end{pmatrix}, \quad (2.34)$$

The presence of complex phases in the leptonic mixing matrix opens up the possibility of CP violation in the leptonic sector. For three Dirac or Majorana neutrinos one can build a basis independent quantity that directly measures the presence of leptonic CP violation: the Jarlskog invariant J_{CP} defined as:

$$J_{\text{CP}} = \text{Im}(U_{e1} U_{\mu2} U_{e2}^* U_{\mu1}^*). \quad (2.35)$$

which in the parametrization of the leptonic mixing matrix above reads

$$J_{\text{CP}} = \frac{1}{8} \sin 2\theta_{12} \sin 2\theta_{23} \sin 2\theta_{13} \cos \theta_{13} \sin \delta_{\text{CP}}. \quad (2.36)$$

From the expression above, if $\delta = 0$ or π , $J_{\text{CP}} = 0$ and there is no CP violation. A non-zero value of J_{CP} implies CP violation in the neutrino sector.

As for the additional Majorana phases they cannot be measured in conventional neutrino oscillation experiments because they do not affect oscillation probabilities, as will be described below. However, they can be probed through neutrinoless double-beta decay ($0\nu\beta\beta$), a rare nuclear process that violates lepton number by two units. In the minimal scenario with three massive Majorana neutrinos the decay rate depends on the so-called *effective Majorana mass*:

$$m_{ee} = \left| \sum_i U_{ei}^2 m_i \right| = \left| m_1 c_{12}^2 c_{13}^2 + m_2 s_{12}^2 c_{13}^2 e^{i\alpha_1} + m_3 s_{13}^2 e^{i(\alpha_2 - 2\delta_{\text{CP}})} \right|, \quad (2.37)$$

where m_i are the neutrino masses. The phases α_1 and α_2 affect the interference terms in $m_{\beta\beta}$, making it possible to constrain them experimentally.

2.3 Neutrino flavour Oscillations

Neutrino flavour oscillations is the phenomenon by which a neutrino produced in a flavour eigenstate α after traveling some distance can be detected as a neutrino with flavour β which could be different from α .

More quantitatively a neutrino with flavour α and momentum \mathbf{p} , created in a vertex via a charged current interaction process, is described by the flavour state:

$$|\nu_\alpha\rangle = \sum_i U_{\alpha i}^* |\nu_i\rangle. \quad (2.38)$$

expressed as a superposition of the mass eigenstates $|\nu_i\rangle$, which will have energy $E_i = \sqrt{|\mathbf{p}|^2 + m_i^2}$.

After a time t the state will have evolved as

$$|\nu_\alpha(t)\rangle = \sum_\beta \left(\sum_i U_{\alpha i}^* \exp(-iE_i t) U_{\beta i} \right) |\nu_\beta\rangle. \quad (2.39)$$

The probability of detecting it as neutrino of flavour β at time t is then

$$P_{\alpha \rightarrow \beta}(t) = |\langle \nu_\beta | \nu_\alpha(t) \rangle|^2 = \left| \sum_i U_{\beta i} U_{\alpha i}^* e^{-iE_i t} \right|^2. \quad (2.40)$$

In the ultrarelativistic limit, the energy E_i can be approximated by:

$$E_i \approx p + \frac{m_i^2}{2E}, \quad (2.41)$$

where p is the neutrino momentum, and E is its energy. This approximation is known as the *equal momentum assumption* [32]. Furthermore in this limit $t = L/c$ where L is the distance traveled by the neutrino at time t (called *light-ray approximation*[32]). With

this one can write

$$\begin{aligned}
 P_{\nu_\alpha \rightarrow \nu_\beta}(L, E) &= \left| \sum_i U_{\beta i} U_{\alpha i}^* e^{-i \frac{m_i^2 L}{2E}} \right|^2 = \sum_{k,j} U_{\alpha k}^* U_{\beta j}^* U_{\alpha j} U_{\beta k} \exp\left(-i \frac{\Delta m_{kj}^2 t}{2E}\right) \\
 &= \sum_i |U_{\alpha i}|^2 |U_{\beta i}|^2 + 2 \sum_{i < j} \text{Re}(U_{\alpha i} U_{\beta i}^* U_{\alpha j}^* U_{\beta j}) \cos\left(\frac{\Delta m_{ij}^2 L}{2E}\right) \\
 &\quad + 2 \sum_{i < j} \text{Im}(U_{\alpha i} U_{\beta i}^* U_{\alpha j}^* U_{\beta j}) \sin\left(\frac{\Delta m_{ij}^2 L}{2E}\right) \\
 &= \delta_{\alpha\beta} - 4 \sum_{i < j} \text{Re}(U_{\alpha i} U_{\beta i}^* U_{\alpha j}^* U_{\beta j}) \sin^2\left(\frac{\Delta m_{ij}^2 L}{4E}\right) \\
 &\quad + 2 \sum_{i < j} \text{Im}(U_{\alpha i} U_{\beta i}^* U_{\alpha j}^* U_{\beta j}) \sin\left(\frac{\Delta m_{ij}^2 L}{2E}\right) \tag{2.42}
 \end{aligned}$$

where $\Delta m_{ij}^2 = m_i^2 - m_j^2$. The probability in Eq. (2.42) presents an oscillatory behaviour with wavelengths

$$\lambda_{ij}^{\text{vac}} = \frac{4\pi E}{|\Delta m_{ij}^2|} \simeq 4.5 \text{ km} \frac{E/\text{GeV}}{|\Delta m_{ij}^2|/\text{eV}^2} \tag{2.43}$$

The probabilities described in Eq. (2.42) are categorized into two types. When $\alpha = \beta$, we call it survival probabilities (or disappearance probabilities). However, when $\alpha \neq \beta$, we call it transition probabilities (or appearance probabilities).

For the case of antineutrinos the derivation is the same with the change $U \rightarrow U^*$ oscillation.

$$\begin{aligned}
 P_{\bar{\alpha} \rightarrow \bar{\beta}}(L, E) &= \delta_{\alpha\beta} - 4 \sum_{i < j} \text{Re}(U_{\alpha i} U_{\beta i}^* U_{\alpha j}^* U_{\beta j}) \sin^2\left(\frac{\Delta m_{ij}^2 L}{4E}\right) \\
 &\quad - 2 \sum_{i < j} \text{Im}(U_{\alpha i} U_{\beta i}^* U_{\alpha j}^* U_{\beta j}) \sin\left(\frac{\Delta m_{ij}^2 L}{2E}\right) \tag{2.44}
 \end{aligned}$$

so if the last term is non zero it is possible to have different probabilities for neutrinos and antineutrinos and the leptonic CP violation can be experimentally established. It is also clear that for this to occur it is required that $\alpha \neq \beta$ and to have at least three massive neutrinos involved in the oscillation so that the U matrix contains some complex phase. For the case of three massive neutrinos unitarity relates all the combinations in the last term of the probabilities with the Jarlskog invariant defined in Eq. (2.35)

From these expressions we also see that the oscillation probabilities are the same for Dirac or Majorana neutrinos since the matrix P_{Maj} (see Eq. (2.32)) cancels in both Eq. (2.42) and Eq. (2.44).

In real experiments, neutrino beams are not monoenergetic and furthermore detectors have finite energy resolution and sometimes the distance traveled is also not fixed. Consequently experiments measure an average of the oscillation probability over some range of energy and sometimes also distance. Therefore there are three different characteristic regimes:

- $L \ll \lambda_{ij}^{\text{vac}}$: in this case, oscillations do not have enough time to develop and the experiment is basically not sensitive to either the mass splittings or the mixing angles.
- $L \sim \lambda_{ij}^{\text{vac}}$: in this, case the experiment can be sensitive to both Δm_{ij}^2 and the leptonic mixing matrix elements.

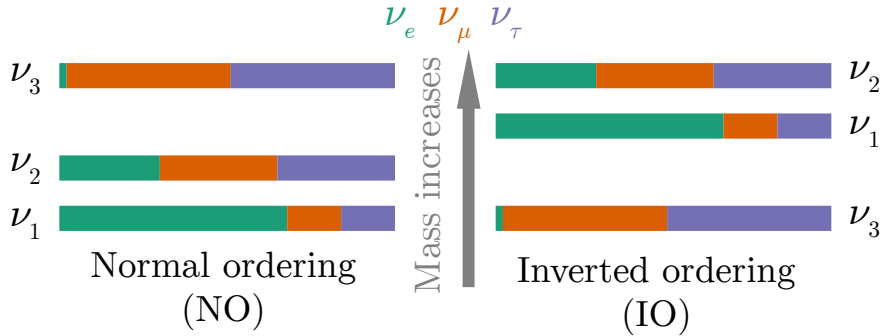


Figure 2.1: Convention for the numbering of mass eigenstates and possible orderings (NO in left, IO in right). The colours indicate the amount of mixing between mass and flavour eigenstates as obtained from the global analysis of neutrino oscillation experiments as we will describe and quantify in Chapters 3 and 4

- $L \gg \lambda_{ij}^{\text{vac}}$: in this case, the oscillation phase goes through many cycles. So when averaging over the energy or distance $\sin^2 \frac{\Delta m_{ij}^2 L}{4E} \sim \frac{1}{2}$, the experiment still provides information on the leptonic mixing matrix elements but not on the mass splittings.

Most experimental set ups are restricted to some range of neutrino energies and/or distances. Consequently they are mostly sensitive to oscillations driven by one particular Δm^2 and the results can be approximately understood in terms of oscillation probabilities derived with two neutrino massive states. In that case, there is an angle dominantly controlling the observable oscillation amplitude and a mass difference dominantly controlling the observable frequency and both Eqs. (2.42) and (2.44) become

$$P_{\alpha\beta} = \delta_{\alpha\beta} - (2\delta_{\alpha\beta} - 1) \sin^2 2\theta \sin^2 \frac{\Delta m^2 L}{4E}. \quad (2.45)$$

In this case, the oscillation probability is symmetric under the exchange $\theta \leftrightarrow \frac{\pi}{2} - \theta$ and/or $\Delta m^2 \leftrightarrow -\Delta m^2$. Furthermore, there is no physical CP violation in this limit. More-than-two neutrino mixing as well as matter effects break all these symmetries.

Let us make a final comment about the signs of the mass splittings which are physical in neutrino oscillations. As seen above for the case of two massive neutrinos there is a total degeneracy between the octact of the mixing angle and the sign of the mass splitting. For three massive neutrinos and in the convention that we are using for the physical range of the mixing angles ($0 \leq \theta_{ij} \leq \pi/2$) and the CP phase $0 \leq \delta \leq 2\pi$ one of the mass splittings, here Δm_{21}^2 , is by convention positive while the splitting Δm_{31}^2 can be positive or negative. We refer to these two signs as the *neutrino mass ordering*. So we have two possible orderings

- Normal ordering: $m_1 < m_2 < m_3$
- Inverted ordering: $m_3 < m_1 < m_2$.

diagrammatically shown in Fig.2.1.

2.4 Flavour Transitions in Matter

When neutrinos propagate through matter, their oscillation behaviour is modified by coherent forward elastic scattering and incoherent scattering with the matter that is

crossing by, described by the Mikheev-Smirnov-Wolfenstein (MSW) effect. However, the incoherent contribution is substantially smaller than the coherent one in regular scenarios (not too dense $N \gg N_A/\text{cm}^3$ or too energetic $E_\nu \gg 1 \text{ TeV}$)[32, 33]. For the cases studied in this thesis, none of them are considered.

Forward scattering occurs when a neutrino interacts with particles in a medium but continues moving in nearly the same direction as before the interaction. Unlike incoherent scattering, where the neutrino's direction changes significantly, forward scattering preserves the neutrino's momentum almost entirely. This process is coherent because the medium remains unchanged after the interaction. The scattered neutrino waves overlap and interfere with the unscattered waves, creating a combined effect [33]. Since the medium doesn't "remember" the interaction, the scattered waves add up constructively, enhancing the overall effect. This coherence allows us to describe the medium's influence on neutrinos using an effective potential, which depends on the density and composition of the matter[34].

It is not the goal of this thesis to develop the most general formalism for the evolution of neutrinos in matter. We will just briefly comment about how one could derive the matter potential from the QFT formalism (following [32, 33]) and from that, how the matter potential could change the oscillation pattern of neutrinos due to cross matter regions for the relevant physical cases studied in this thesis.

2.4.1 Matter potentials

Following [32, 33], we derive the effective potential for electron neutrinos propagating in a medium composed of electrons, protons, and neutrons starting with the relevant low-energy Hamiltonian describing neutrino interactions is given by:

$$H_W = \frac{G_F}{\sqrt{2}} \left[J^{(+)\alpha}(x) J_\alpha^{(-)}(x) + \frac{1}{4} J^{(N)\alpha}(x) J_\alpha^{(N)}(x) \right], \quad (2.46)$$

where the J_α 's are the standard fermionic currents:

$$J_\alpha^{(+)}(x) = \bar{\nu}_e(x) \gamma_\alpha (1 - \gamma_5) e(x), \quad (2.47)$$

$$J_\alpha^{(-)}(x) = \bar{e}(x) \gamma_\alpha (1 - \gamma_5) \nu_e(x), \quad (2.48)$$

$$J_\alpha^{(N)}(x) = \bar{\nu}_e(x) \gamma_\alpha (1 - \gamma_5) \nu_e(x) - \bar{e}(x) \left[\gamma_\alpha (1 - \gamma_5) - 4 \sin^2 \theta_W \gamma_\alpha \right] e(x) \\ + \bar{p}(x) \left[\gamma_\alpha (1 - g_A^{(p)} \gamma_5) - 4 \sin^2 \theta_W \gamma_\alpha \right] p(x) - \bar{n}(x) \gamma_\alpha (1 - g_A^{(n)} \gamma_5) n(x) \quad (2.49)$$

Here, $g_A^{(n,p)}$ are the axial couplings for neutrons and protons, respectively, and θ_W is the Weinberg angle. For simplicity, we focus on the CC interactions, which dominate the effective potential for ν_e .

The effective CC Hamiltonian due to electrons in the medium is:

$$H_{CC}^{(e)} = \frac{G_F}{\sqrt{2}} \int d^3 p_e f(E_e, T) \\ \times \langle \langle e(s, p_e) | \bar{e}(x) \gamma_\alpha (1 - \gamma_5) \nu_e(x) \bar{\nu}_e(x) \gamma_\alpha (1 - \gamma_5) e(x) | e(s, p_e) \rangle \rangle \\ = \frac{G_F}{\sqrt{2}} \bar{\nu}_e(x) \gamma_\alpha (1 - \gamma_5) \nu_e(x) \\ \times \int d^3 p_e f(E_e, T) \langle \langle e(s, p_e) | \bar{e}(x) \gamma_\alpha (1 - \gamma_5) e(x) | e(s, p_e) \rangle \rangle, \quad (2.50)$$

where s is the electron spin, p_e is its momentum, and $f(E_e, T)$ is the energy distribution function of the electrons in the medium, assumed to be homogeneous and isotropic. The

distribution function is normalized as:

$$\int d^3 p_e f(E_e, T) = 1. \quad (2.51)$$

The notation $\langle\langle \dots \rangle\rangle$ denotes averaging over electron spinors and summing over all electrons in the medium. Coherence implies that the spin and momentum of the initial and final electrons are the same.

Expanding the electron fields $e(x)$ in plane waves, we find:

$$\begin{aligned} \langle e(s, p_e) | \bar{e}(x) \gamma^\alpha (1 - \gamma_5) e(x) | e(s, p_e) \rangle = \\ \frac{1}{V} \langle e(s, p_e) | \bar{u}_s(p_e) a_s^\dagger(p_e) \gamma^\alpha (1 - \gamma_5) a_s(p_e) u_s(p_e) | e(s, p_e) \rangle, \end{aligned} \quad (2.52)$$

such that V is a volume normalization factor. The averaging gives:

$$\frac{1}{V} \langle\langle e(s, p_e) | a_s^\dagger(p_e) a_s(p_e) | e(s, p_e) \rangle\rangle = N_e(p_e) \frac{1}{2} \sum_s, \quad (2.53)$$

where $N_e(p_e)$ is the number density of electrons with momentum p_e . Assuming the medium has equal numbers of spin-up and spin-down electrons, we obtain:

$$\begin{aligned} \langle\langle e(s, p_e) | \bar{e}(x) \gamma^\alpha (1 - \gamma_5) e(x) | e(s, p_e) \rangle\rangle &= N_e(p_e) \frac{1}{2} \sum_s \bar{u}_s(p_e) \gamma^\alpha (1 - \gamma_5) u_s(p_e) \\ &= N_e(p_e) \frac{p_e^\alpha}{E_e}. \end{aligned} \quad (2.54)$$

Isotropy implies that $\int d^3 p_e \vec{p}_e f(E_e, T) = 0$, so only the p^0 term contributes upon integration. Substituting Eq. (2.54) into Eq. (2.50), we obtain:

$$H_{CC}^{(e)} = \frac{G_F N_e}{\sqrt{2}} \bar{\nu}_e(x) \gamma_0 (1 - \gamma_5) \nu_e(x), \quad (2.55)$$

where N_e is the electron number density at position x . The effective potential for ν_e induced by its charged current interactions with electrons in matter is then:

$$V_{CC} = \langle \nu_e | \int d^3 x H_{CC}^{(e)} | \nu_e \rangle = \sqrt{2} G_F N_e. \quad (2.56)$$

For $\bar{\nu}_e$, the sign of V_{CC} is reversed. This potential can also be expressed in terms of the matter density ρ :

$$V_{CC} = \sqrt{2} G_F N_e \simeq 7.6 Y_e \frac{\rho}{10^{14} \text{ g/cm}^3} \text{ eV}, \quad (2.57)$$

where $Y_e = \frac{N_e}{N_p + N_n}$ is the relative number density of electrons.

For ν_μ and ν_τ , $V_{CC} = 0$ in these media, while the neutral current potential V_{NC} generated by the fermions f in the medium is the same for all neutrino flavour and can be derived similarly [32, 33] and reads:

$$N_e, \quad V_{NC}^f = \sqrt{2} G_F N_f g_V^f, \quad (2.58)$$

with $g_V^p = -g_V^e$ and $g_V^n = -\frac{1}{2}$. For neutral matter, $N_p = N_n$, so the overall NC potential can be written as:

$$V_{NC}^{\text{total}} = -\frac{\sqrt{2}}{2} G_F N_n. \quad (2.59)$$

Altogether the potential for NC and CC that an active neutrino ν_α with $\alpha = e, \mu, \tau$ feels in a dense medium can be written as:

$$V_\alpha = \sqrt{2}G_F \left(N_e \delta_{\alpha e} - \frac{1}{2} N_n \right), \quad (2.60)$$

while for sterile neutrinos $V_s = 0$.

2.4.2 Modified Evolution

Altogether the total Hamiltonian governing the neutrino evolution in a dense medium can be written as the sum of its free Hamiltonian (here call H_{vac}) and an effective potential generated by the matter

$$H_M = H_{\text{vac}} + V \quad (2.61)$$

where V is the matter potential, given by Eq.(2.60).

The Schrödinger equation for a neutrino ensemble in the flavour basis can be then written in matrix form as

$$i \frac{d}{dt} |\nu(t)\rangle = H_M |\nu(t)\rangle = (U \Delta_M U^\dagger + V) |\nu(t)\rangle, \quad (2.62)$$

where allowing in general for the presence of light sterile neutrinos $\Delta_M = \text{diag}(0, \Delta m_{21}^2, \Delta m_{31}^2, \Delta m_{41} \dots)/2E$ and $V = \sqrt{2}G_F \text{diag}(N_e(x), 0, 0, N_n/2, \dots)$, after extracting a diagonal term $\left(p + \frac{m_\nu^2}{2E_\nu} + V_{\text{NC}} \right) \times I$, which does not contribute to the oscillation probabilities.

In general Eq. (2.62) is difficult to solve analytically except for the case when the neutrino is traveling through a region with constant matter density. In this case the oscillation probabilities can be recasted as Eqs. (2.42) and (2.44) with the substitutions

$$\Delta m_{ij}^2 \rightarrow \Delta \mu_{ij}^2, \quad U_{\alpha i} \rightarrow \tilde{U}_{\alpha i} \quad (2.63)$$

where

$$U \Delta_M U^\dagger \pm V = \tilde{U} \Delta_\mu \tilde{U}^\dagger \quad (2.64)$$

for neutrinos and antineutrinos respectively.

This is a valid approximation for neutrinos traveling through the crust of the Earth as it is the case in accelerator neutrinos at long baselines.

When the density of the matter crossed by the neutrino changes along its trajectory one can always solve the evolution equation numerically by discretizing the evolution in layers sufficiently thin so that the potential can be assumed constant in each layer. Schematically, within a layer of thickness L_j the evolution matrix \mathcal{U}_j , which relates the initial and final neutrino states, takes the form:

$$\mathcal{U}(L_i)_j = \exp \left(-i H_{M_j} L_i \right), \quad (2.65)$$

and can be evaluated numerically. The total evolution matrix is given by the product of the evolution matrices for each layer

$$\mathcal{U}_{\text{total}} = \mathcal{U}_n(L_n) \mathcal{U}_{n-1}(L_{n-1}) \cdots \mathcal{U}_1(L_1), \quad (2.66)$$

and the transition probability between flavors α and β is then:

$$P_{\nu_\alpha \rightarrow \nu_\beta} = |\langle \nu_\beta | \mathcal{U}_{\text{total}} | \nu_\alpha \rangle|^2. \quad (2.67)$$

It is also possible to find approximate analytical solutions for the evolution equation in non-uniform matter density under some simplifying conditions. A particularly illuminating example is the evolution in the Sun which we discuss next. For the sake of concreteness we are focusing in the evolution of three active neutrino ensemble.

2.4.3 Solar neutrinos: MSW effect

We are going to solve the evolution of the 3 neutrino ensemble in the solar matter. The first approximation which we will use is that the largest mass splitting, here $|\Delta m_{31}| \gg \Delta m_{21}^2$ (as we mentioned above $\Delta m_{21}^2 >$ by convention) and that $|\Delta m_{31}^2|/(2E)$ is always much larger than the matter potential in any point in the evolution. With these assumptions, only the first two mass eigenstates are dynamical. Since physical quantities have to be independent of the parametrization of the mixing matrix, we choose a parametrization that makes analytical expressions particularly simple in this case. We write $U = OU_{12}$, where $O = R_{23}R_{13}$ is real while U_{12} is a complex rotation by angle θ_{12} and phase δ , such that O is given by:

$$O = \begin{pmatrix} c_{13} & 0 & s_{13} \\ -s_{13}s_{23} & c_{23} & c_{13}s_{23} \\ -s_{13}c_{23} & -s_{23} & c_{13}c_{23} \end{pmatrix}, \quad U_{12} = \begin{pmatrix} c_{12} & s_{12}e^{-i\delta} & 0 \\ -s_{12}e^{i\delta} & c_{12} & 0 \\ 0 & 0 & 1 \end{pmatrix}. \quad (2.68)$$

With this definitions it is possible to rewrite Eq. (2.62) as:

$$H_M = O\tilde{H}O^\dagger \quad \text{with} \quad \tilde{H} = U_{12}\Delta U_{12}^\dagger + O^\dagger V O. \quad (2.69)$$

Defining

$$|\hat{\nu}\rangle = O^\dagger|\nu\rangle \quad (2.70)$$

and taking the limit $|\Delta m_{3l}^2| \rightarrow \infty$ for $l = 1, 2$, the matrix \tilde{H} takes the effective block-diagonal form:

$$\tilde{H} \approx \begin{pmatrix} H^{(2)} & \mathbf{0} \\ \mathbf{0} & \frac{\Delta m_{31}^2}{2E_\nu} \end{pmatrix} \quad (2.71)$$

and $H^{(2)} = H_{\text{vac}}^{(2)} + H_{\text{mat}}^{(2)}$ with

$$H_{\text{vac}}^{(2)} = \frac{\Delta m_{21}^2}{4E_\nu} \begin{pmatrix} -\cos 2\theta_{12} & \sin 2\theta_{12} e^{i\delta} \\ \sin 2\theta_{12} e^{-i\delta} & \cos 2\theta_{12} \end{pmatrix}, \quad (2.72)$$

$$H_{\text{mat}}^{(2)} = \frac{\sqrt{2}}{2}G_F \left[N_e(x) \begin{pmatrix} c_{13}^2 & 0 \\ 0 & -c_{13}^2 \end{pmatrix} \right]. \quad (2.73)$$

The state $|\hat{\nu}\rangle_3$ decouples from $|\hat{\nu}\rangle_1$ and $|\hat{\nu}\rangle_2$. Hence, such a state will have the following differential equation:

$$i \frac{d}{dx} |\hat{\nu}(x)\rangle_3 = \frac{1}{2E_\nu} \Delta m_{31}^2 |\hat{\nu}(x)\rangle_3, \quad (2.74)$$

that has the simple solution:

$$|\hat{\nu}(x)\rangle_3 = \exp\left(-i \frac{\Delta m_{31}^2 x}{2E_\nu}\right) |\hat{\nu}(0)\rangle_3. \quad (2.75)$$

Now, by combining Eqs. (2.72) and (2.73) it is possible to write the evolution equation for the states $|\hat{\nu}(x)\rangle_1$ and $|\hat{\nu}(x)\rangle_2$ as:

$$i \frac{d}{dx} \begin{pmatrix} |\hat{\nu}(x)\rangle_1 \\ |\hat{\nu}(x)\rangle_2 \end{pmatrix} = \frac{1}{4E_\nu} \begin{pmatrix} -\cos 2\theta_{12} \Delta m_{12}^2 + A c_{13}^2 & \sin 2\theta_{12} \Delta m_{12}^2 e^{i\delta} \\ \sin 2\theta_{12} \Delta m_{12}^2 e^{-i\delta} & + \cos 2\theta_{12} \Delta m_{12}^2 - A c_{13}^2 \end{pmatrix} \begin{pmatrix} |\hat{\nu}(x)\rangle_1 \\ |\hat{\nu}(x)\rangle_2 \end{pmatrix}, \quad (2.76)$$

with $A = A(x) = 2\sqrt{2}G_F N_e(x)E_\nu = VE_\nu$. Eq. 2.76 can be rewritten as:

$$i \frac{d}{dx} \begin{pmatrix} |\hat{\nu}(x)\rangle_1 \\ |\hat{\nu}(x)\rangle_2 \end{pmatrix} = \frac{1}{4E_\nu} \begin{pmatrix} -\cos 2\theta_M(x)\Delta m_M^2(x) & \sin 2\theta_M(x)\Delta m_M^2(x) \\ \sin 2\theta_M(x)\Delta m_M^2(x) & +\cos 2\theta_M(x)\Delta m_M^2(x) \end{pmatrix} \begin{pmatrix} |\hat{\nu}(x)\rangle_1 \\ |\hat{\nu}(x)\rangle_2 \end{pmatrix}, \quad (2.77)$$

where we have dropped the phase δ which produces no effects in a two-neutrino framework, and

$$\Delta m_M^2(x) = \sqrt{(\cos 2\theta_{12}\Delta m_{12}^2 - Ac_{13}^2)^2 + (\sin 2\theta_{12}\Delta m_{12}^2)^2} \quad (2.78)$$

$$\cos 2\theta_M(x) = \frac{\cos 2\theta_{12}\Delta m_{12}^2 - Ac_{13}^2}{\Delta m_M^2(x)} \quad \text{and} \quad \sin 2\theta_M(x) = \frac{\sin 2\theta_{12}\Delta m_{12}^2}{\Delta m_M^2(x)} \quad (2.79)$$

are the effective mass splitting and mixing angle in matter at position x , The instantaneous Hamiltonian eigenstates at position x are

$$|\hat{\eta}\rangle = U_M(x)|\hat{\nu}\rangle, \quad \text{such that} \quad U_M(x) = \begin{pmatrix} \cos \theta_M(x) & \sin \theta_M(x) \\ -\sin \theta_M(x) & \cos \theta_M(x) \end{pmatrix} \quad (2.80)$$

and in terms of these states the equation 2.77 reads

$$iU_M(x) \frac{d}{dx} \left(U_M^\dagger(x) \begin{pmatrix} |\hat{\eta}(x)\rangle_1 \\ |\hat{\eta}(x)\rangle_2 \end{pmatrix} \right) = \frac{1}{4E_\nu} \begin{pmatrix} -\Delta m_M^2(x) & 0 \\ 0 & \Delta m_M^2(x) \end{pmatrix} \begin{pmatrix} |\hat{\eta}(x)\rangle_1 \\ |\hat{\eta}(x)\rangle_2 \end{pmatrix}, \quad (2.81)$$

which after some algebra results into the evolution equation for the instantaneous mass eigenstates

$$i \frac{d}{dx} \begin{pmatrix} |\hat{\eta}(x)\rangle_1 \\ |\hat{\eta}(x)\rangle_2 \end{pmatrix} = \frac{1}{4E_\nu} \begin{pmatrix} -\Delta m_M^2(x) & -4E_\nu i \frac{d\theta_M(x)}{dx} \\ 4E_\nu i \frac{d\theta_M(x)}{dx} & \Delta m_M^2(x) \end{pmatrix} \begin{pmatrix} |\hat{\eta}(x)\rangle_1 \\ |\hat{\eta}(x)\rangle_2 \end{pmatrix}. \quad (2.82)$$

This evolution equation is non-diagonal which means that the instantaneous mass eigenstates are not the eigenstates of the evolution, *i.e.*, the evolution is a priori not adiabatic. The non-diagonal terms in Eq. (2.82) are proportional to the change of density on the way of neutrinos. We define the adiabaticity parameter¹

$$\gamma \equiv \frac{\Delta m_M^2(x)}{4E_\nu \left| \frac{d\theta_M(x)}{dx} \right|} = \frac{(\Delta m_M^2(x))^2}{4\sqrt{2}G_F E_\nu^2 \sin 2\theta_M(x) c_{13}^2 \left| \frac{dN_e(x)}{dx} \right|}. \quad (2.83)$$

When $\gamma \gg 1$ for all x , we can neglect the off-diagonal terms in Eq.(2.82), and this is called the adiabatic approximation [35, 36]. The adiabaticity condition implies that transitions between the eigenstates $|\hat{\eta}\rangle_1$ and $|\hat{\eta}\rangle_2$ are suppressed, and the evolution of the system is governed by the separate propagation of each eigenstates. This condition is satisfied when the electron number density $N_e(x)$ varies sufficiently slowly along the neutrino's path compared to the characteristic oscillation wavelength in vacuum as is the case for solar neutrinos propagating through the Sun.

The Sun produces $|\nu_e\rangle$'s which from Eq. (2.70) are

$$|\nu_e\rangle = \cos \theta_{13} |\hat{\nu}\rangle_1 + \cos \theta_{13} |\hat{\nu}\rangle_3 \quad (2.84)$$

¹The Standard Solar Model (SSM) describes the Sun's electron density as

$$N_e(r) = N_e(0) \exp(-r/r_0),$$

for $0.1 \leq r/R_\odot \leq 0.9$, where $N_e(0) = 245 N_A/\text{cm}^3$ and $r_0 = 10.54 R_\odot$. This profile aids in analyzing resonance adiabaticity, characterized by the parameter γ_R .

and $|\hat{\nu}\rangle_1$ is a superposition of the matter eigenstates $|\hat{\eta}\rangle_1$ and $|\hat{\eta}\rangle_2$ at the production point x_0 :

$$|\nu_1\rangle = \cos\theta_M(x_0)|\hat{\eta}(x_0)\rangle_1 + \sin\theta_M(x_0)|\hat{\eta}(x_0)\rangle_2. \quad (2.85)$$

As the neutrino propagates adiabatically, the $|\hat{\eta}(x)\rangle_i$ (and $|\hat{\nu}\rangle_3$) evolve independently, and the state at a later point x can be written as:

$$|\nu(x)\rangle_1 = \cos\theta_M(x_0)e^{-i\phi_1(x)}|\hat{\eta}(x)\rangle_1 + \sin\theta_M(x_0)e^{-i\phi_2(x)}|\hat{\eta}(x)\rangle_2, \quad (2.86)$$

where $\phi_1(x)$ and $\phi_2(x)$ are the accumulated phases of the eigenstates $|\hat{\eta}\rangle_1$ and $|\hat{\eta}\rangle_2$, respectively. These phases are given by:

$$\phi_i(x) = (-1)^{i+1} \int_{x_0}^x \frac{\Delta m_M^2(x')}{4E_\nu} dx', \quad i = 1, 2. \quad (2.87)$$

At the detection point x_f , the neutrino state is projected back onto the flavour eigenstate $|\nu_e\rangle$. The survival probability $P_{\hat{\nu}_1 \rightarrow \hat{\nu}_1}$ is then given by the squared overlap of the evolved state with the initial state:

$$\begin{aligned} P_{\hat{\nu}_1 \rightarrow \hat{\nu}_1} &= |\langle \hat{\nu}_1 | \nu(x_f) \rangle|^2 = \cos^2\theta_M(x_0)\cos^2\theta_M(x_f) + \sin^2\theta_M(x_0)\sin^2\theta_M(x_f) \\ &+ \frac{1}{2}\sin 2\theta_M(x_0)\sin 2\theta_M(x_f)\cos(\phi_2(x_f) - \phi_1(x_f)). \end{aligned} \quad (2.88)$$

For the case of solar neutrinos the detection occurs in vacuum (or very low density), where the effective mixing angle $\theta_M(x_f)$ reduces to the vacuum mixing angle θ_{12} . The distance between the neutrino source and the detector is huge, the phase of the cosine is very large averaging it to zero, $\cos(\phi_2(x_f) - \phi_1(x_f)) \rightarrow 0$, the survival probability simplifies to:

$$\begin{aligned} \langle P_{\hat{\nu}_1 \rightarrow \hat{\nu}_1} \rangle &\simeq \cos^2\theta_M(x_0)\cos^2\theta_{12} + \sin^2\theta_M(x_0)\sin^2\theta_{12} = \frac{1}{2} + \frac{1}{2}\cos 2\theta_M(x_0)\cos 2\theta_{12} \\ &\equiv \langle P_{\nu_e \rightarrow \nu_e} \rangle^{2\nu} \end{aligned} \quad (2.89)$$

Including the projection over the third state one gets

$$\langle P_{\nu_e \rightarrow \nu_e} \rangle^{3\nu} = \cos^4\theta_{13}\langle P_{\nu_e \rightarrow \nu_e} \rangle^{2\nu} + \sin^4\theta_{13}. \quad (2.90)$$

The MSW effect

From Eqs.(2.79) and (2.78) we find that the mixing angle in matter is

$$\tan 2\theta_M = \frac{\sin 2\theta_{12}}{\cos 2\theta_{12} - \frac{c_{13}^2 V(x) E_\nu}{\Delta m_{21}^2}}. \quad (2.91)$$

So when

$$V(x) = 2\sqrt{2}G_F N_e(x) = \frac{\Delta m_{21}^2}{2E_\nu c_{13}^2} \cos 2\theta_{12}, \quad (2.92)$$

$\tan 2\theta_M$ changes sign and the mixing angle becomes $\theta_M = \pi/4$ irrespective of its value in vacuum. We call this the resonant condition.

Since $\Delta m_{21}^2 > 0$ by convention, this condition can be satisfied for electron neutrinos propagating through matter with a sufficiently high electron density N_e if $\cos 2\theta_{12} > 0$. This is, if the mixing angle θ_{12} lies in the first octant, $\theta_{12} < \frac{\pi}{4}$ the resonance condition is

met for neutrinos (rather than antineutrinos), as the matter potential V has the opposite sign for antineutrinos. At resonance, the mixing angle in matter is $\theta_M = \pi/4$.

For solar neutrinos, which are produced in the core of the Sun as electron neutrinos (ν_e), the electron density is very high, causing the effective mixing angle $\theta_{M,0}$ to initially be close to $\pi/2$ ($\sin 2\theta_M(x_0) \rightarrow -1$). As the neutrinos propagate outward through the Sun, the electron density decreases and θ_M evolves toward its vacuum value θ_{12} . If the evolution is adiabatic the resulting survival probability becomes

$$\langle P_{\nu_e \rightarrow \nu_e} \rangle^{2\nu} = \frac{1}{2} - \frac{1}{2} \cos 2\theta_{12} = \sin^2 \theta_{12} . \quad (2.93)$$

This is the MSW effect.

2.5 Neutrino Mass Scale and Neutrino Mass Ordering

Because of its quantum-interference nature, mass-induced flavor oscillations are sensitive to the phase differences induced by the mass-squared splitting Δm_{ij}^2 and to misalignment between the detection and propagation eigenstates, *i.e.*, to the leptonic mixing matrix elements $U_{\alpha j}$. They are, however, insensitive to overall shifts of the energy levels, and hence they cannot provide information on the absolute mass scale of the neutrinos other than the obvious lower bound on the masses of the heaviest states involved in the oscillations.

The most model-independent information on the neutrino mass, rather than on mass differences, is obtained from kinematic studies of reactions in which a neutrino or an antineutrino is involved. In the presence of mixing, the most relevant constraint comes from the study of the end point ($E \sim E_0$) of the electron spectrum in Tritium beta decay ${}^3\text{H} \rightarrow {}^3\text{He} + e^- + \bar{\nu}_e$. This spectrum can be effectively described by a single parameter, m_{ν_e} , if for all neutrino states $E_0 - E \gg m_i$:

$$m_{\nu_e}^2 \equiv \frac{\sum_i m_i^2 |U_{ei}|^2}{\sum_i |U_{ei}|^2} = \sum_i m_i^2 |U_{ei}|^2 , \quad (2.94)$$

where the second equality holds if unitarity is assumed. The most recent result on the kinematic search for neutrino mass in tritium decay is from KATRIN [37], which sets an upper limit $m_{\nu_e} < 0.45$ eV at 90% CL.

Direct information on neutrino masses can also be obtained from neutrinoless double beta decay $(A, Z) \rightarrow (A, Z + 2) + e^- + e^-$. This process violates lepton number by two units, hence in order to induce the $0\nu\beta\beta$ decay, neutrinos must be Majorana particles. In particular, if the only effective lepton number violation at low energies is induced by a Majorana mass term for neutrinos, the rate of $0\nu\beta\beta$ decay is proportional to the *effective Majorana mass of ν_e* :

$$m_{ee} = \left| \sum_i m_i U_{ei}^2 \right|. \quad (2.95)$$

Currently the strongest bound on $0\nu\beta\beta$ decay lifetimes are obtained with Germanium ($T_{1/2}^{0\nu} > 1.8 \times 10^{26}$ yr) by GERDA [38] and with Xenon ($T_{1/2}^{0\nu} > 3.8 \times 10^{26}$ yr) by KamLAND-Zen [39]. Depending on the assumed nuclear matrix elements, these correspond to 90% CL limits of $m_{ee} \lesssim 0.079\text{--}0.180$ eV [38] and $m_{ee} \lesssim 0.028\text{--}0.122$ eV [39], respectively.

Finally, neutrino masses also have effects in cosmology. In general, cosmological data mostly gives information on the sum of the neutrino masses, $\sum m_\nu$, while it has very little to say on their mixing structure and on the ordering of the mass states. At present, no positive evidence of the cosmological effect of a non-zero neutrino mass has been observed,

which results into upper bounds on $\sum m_\nu$ in the range of $\sum m_\nu \lesssim 0.04\text{--}0.3$ eV (see, *e.g.*, Refs. [40, 41] and references therein for post-DESI [42] global analyses) depending on, *e.g.*, the cosmological data included in the analysis, assumptions on the cosmological model, the statistical approach, the treatment of systematics, or parameter priors.

Within the 3ν -mixing scenario, for each mass ordering, the values of these observables can be directly predicted in terms of the parameters determined in the global oscillation analysis and a single mass scale, which is usually taken to be the lightest neutrino mass m_0 . In addition, the prediction for m_{ee} also depends on the unknown Majorana phases:

$$m_{\nu e} = \sqrt{m_1^2 c_{13}^2 c_{12}^2 + m_2^2 c_{13}^2 s_{12}^2 + m_3^2 s_{13}^2}, \quad (2.96)$$

$$m_{ee} = \left| m_1 c_{13}^2 c_{12}^2 e^{2i(\alpha_1 - \delta_{\text{CP}})} + m_2 c_{13}^2 s_{12}^2 e^{2i(\alpha_2 - \delta_{\text{CP}})} + m_3 s_{13}^2 \right|, \quad (2.97)$$

$$\sum m_\nu = m_1 + m_2 + m_3, \quad (2.98)$$

$$\text{with } \begin{cases} \text{NO: } m_1 = m_0, & m_2 = \sqrt{m_0^2 + \Delta m_{21}^2}, & m_3 = \sqrt{m_0^2 + \Delta m_{3\ell}^2}, \\ \text{IO: } m_3 = m_0 & m_2 = \sqrt{m_0^2 - \Delta m_{3\ell}^2}, & m_1 = \sqrt{m_0^2 - \Delta m_{3\ell}^2 - \Delta m_{21}^2}. \end{cases} \quad (2.99)$$

where, following the convention adopted by the NuFIT group, we denote by $\Delta m_{3\ell}^2$ the mass-squared splitting with the largest absolute value for the given mass ordering (that is, $\Delta m_{3\ell}^2 \equiv \Delta m_{31}^2 > 0$ for NO, and $\Delta m_{3\ell}^2 \equiv \Delta m_{32}^2 < 0$ for IO).

Chapter 3

Experimental Inputs

Building on the theoretical foundation of neutrino oscillations including the leptonic mixing matrix, matter effects, and oscillation probabilities derived in Chapter 2— this chapter examines the experimental methodologies that have empirically validated and refined these concepts. Neutrino oscillations are dominantly probed with neutrinos that can be classified according to their sources as solar, atmospheric, reactor, and accelerator neutrinos. Each source exploits specific baseline-to-energy ratios (L/E) and detection techniques to isolate different terms in the oscillation probability, enabling precision measurements of some mass splittings and mixing angles.

In this chapter we will briefly describe the main features of these experiments and their results, which will be employed in the coming chapters to test different forms of new physics. Most quantitative details are provided for the two experiments for which this thesis has contributed most in their simulation and analysis: Borexino and NOvA.

In Section 3.1, we present the results obtained with solar neutrinos. Solar neutrino experiments Homestake, Gallex-GNO, Super-Kamiokande, SNO, and Borexino have shown that ν_e 's produced in the Sun's interior undergo matter-enhanced flavour transitions via the MSW mechanism. In the framework of 3ν mixing they mostly provide information on Δm_{21}^2 and θ_{12} . At the end of Sec. 3.1 we present the details of Borexino Phase II and III data analyses, illustrating the interplay between spectral decomposition, systematic uncertainty modeling (e.g., energy scale corrections and background correlations), and statistical methods (e.g., χ^2 minimization and data analysis).

Section 3.2 focuses on atmospheric neutrinos, generated by cosmic ray interactions on Earth's atmosphere. The experiments Super-Kamiokande and IceCube utilize their wide energy range (MeVTeV) and baselines (1012,700 km) to observe oscillations of ν_μ 's which are dominated by the 3ν mixing parameters $|\Delta m_{32}^2|$ and θ_{23} . Section 3.3 describes reactor neutrino experiments, which leverage controlled $\bar{\nu}_e$ fluxes from nuclear fission to measure θ_{13} and $|\Delta m_{32}^2|$ (Daya Bay) and Δm_{21}^2 and θ_{12} (KamLAND). Section 3.4 explores accelerator-based long-baseline experiments (NOvA, T2K), where high-intensity ν_μ and $\bar{\nu}_\mu$ beams enable studies of both ν_μ disappearance as well as $\nu_\mu \rightarrow \nu_e$ and $\bar{\nu}_\mu \rightarrow \bar{\nu}_e$ transitions and offer a direct test to leptonic CP violation. In the end of Section 3.4, we present detailed studies of NOvA systematic uncertainty modeling (e.g., energy scale corrections and background correlations), and statistical methods (e.g., χ^2 minimization and data analysis).

We conclude this chapter by examining two types of experiments that challenge our current understanding of the standard neutrino paradigm. Section 3.6 addresses the persistent discrepancy observed in gallium-based neutrino detection experiments, where measured electron neutrino (ν_e) interaction rates from radioactive sources systematically fall below SM predictions—a phenomenon known as the gallium anomaly. In Section 3.5

we explore another important class of experiments that bounds BSM physics: Coherent Elastic Neutrino-Nucleus Scattering (CE ν NS). Recent precision measurements of this neutral-current process have established new constraints on neutrino-quark coupling parameters, bounding new physics that could add any contribution to the SM predictions.

3.1 Solar Neutrinos

The Sun is a powerful source of neutrinos, originating from nuclear fusion processes within its core. As we will see in the coming chapters, studying these neutrinos provides information on both particle physics and solar physics. The fusion proceeds through two primary pathways:

- **Proton-Proton (pp) Chain:** This is the dominant fusion process in the Sun. It consists of several branches

- **pp:** This is the dominant branch and proceeds as follows

1. $p + p \rightarrow d + e^+ + \nu_e$ ($E_\nu \leq 0.42$ MeV)
2. $p + d \rightarrow {}^3\text{He} + \gamma$
3. ${}^3\text{He} + {}^3\text{He} \rightarrow {}^4\text{He} + 2p$

- **${}^7\text{Be}$:** Second in energy production

1. ${}^3\text{He} + {}^4\text{He} \rightarrow {}^7\text{Be} + \gamma$
2. ${}^7\text{Be} + e^- \rightarrow {}^7\text{Li} + \nu_e$ ($E_\nu = 0.861$ MeV)
3. ${}^7\text{Li} + p \rightarrow 2 {}^4\text{He}$.

- **pep:**

$$p + e^- + p \rightarrow d + \nu_e \quad (E_\nu = 1.44 \text{ MeV}).$$

- **${}^8\text{B}$:** It is responsible for producing most of the high-energy solar neutrinos:

1. ${}^3\text{He} + {}^4\text{He} \rightarrow {}^7\text{Be} + \gamma$,
2. ${}^7\text{Be} + p \rightarrow {}^8\text{B} + \gamma$,
3. ${}^8\text{B} \rightarrow {}^8\text{Be}^* + e^+ + \nu_e$,
4. ${}^8\text{Be}^* \rightarrow 2 {}^4\text{He}$.

- **hep :** It produces the neutrinos of highest energy via

$${}^3\text{He} + p \rightarrow {}^4\text{He} + e^+ + \nu_e,$$

but has the lowest flux.

- **Carbon-Nitrogen-Oxygen (CNO) Cycle:** This process is less significant in the Sun but dominates in heavier stars. It uses carbon, nitrogen, and oxygen as catalysts to fuse hydrogen into helium, producing neutrinos in the process. Measuring

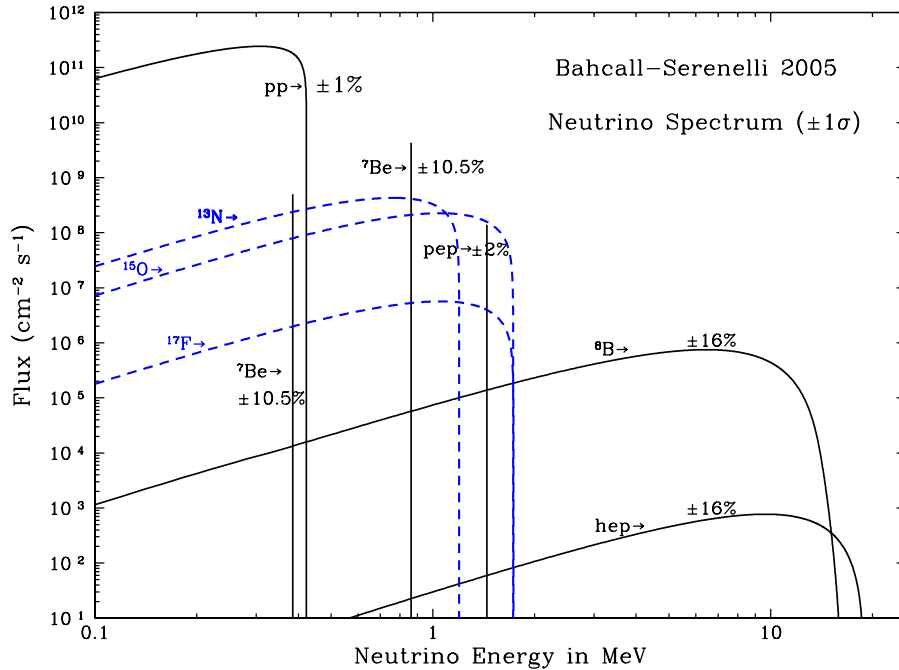


Figure 3.1: Neutrino fluxes predicted by the SSM[43] as a function of the neutrino energy. Figure extracted from [44].

precisely the flux of these neutrinos is essential to determine the abundance of heavy elements inside the Sun. The main reactions are:

1. $^{12}\text{C} + p \rightarrow ^{13}\text{N} + \gamma$
2. $^{13}\text{N} \rightarrow ^{13}\text{C} + e^+ + \nu_e \quad (E_\nu \leq 1.2 \text{ MeV})$
3. $^{13}\text{C} + p \rightarrow ^{14}\text{N} + \gamma$
4. $^{14}\text{N} + p \rightarrow ^{15}\text{O} + \gamma$
5. $^{15}\text{O} \rightarrow ^{15}\text{N} + e^+ + \nu_e \quad (E_\nu \leq 1.7 \text{ MeV})$
6. $^{15}\text{N} + p \rightarrow ^{12}\text{C} + ^4\text{He}$.

The resulting neutrino spectrum exhibits typical energies on the order of $\mathcal{O}(\text{MeV})$ as seen in Fig. 3.1. The precise computation of this spectrum requires detailed knowledge of the Sun's structure and evolution [43, 45]. Standard Solar Models (SSM), are mathematical representations used in astrophysics to describe the structure, composition, and evolution of the Sun. Over the years several SSM, able to describe the properties of the Sun and its evolution after entering the main sequence, have been constructed with increasing level of refinement [43, 46–53]. Such models are numerical calculations calibrated to match present-day surface properties of the Sun, and developed under the assumption that the Sun was initially chemically homogeneous and that mass loss is negligible at all moments during its evolution up to the present solar age $\tau_\odot = 4.57 \text{ Gyr}$. The calibration is done in order to satisfy the constraints imposed by the current solar luminosity L_\odot , radius R_\odot , and surface metal to hydrogen abundance ratio $(Z/X)_\odot$. Refinements introduced over the years include more precise observational and experimental information about the input parameters (such as nuclear reaction rates and the surface abundances of different elements), more accurate calculations of constituent quantities (such as radiative opacity and equation of state), the inclusion of new physical effects (such as element

diffusion), and the development of faster computers and more precise stellar evolution codes. The predictions of SSMs can be tested against the neutrino observations as we will quantify in Chapter 7.

The detection of solar neutrinos began in 1970 with the Homestake experiment [54], which employed radiochemical methods to observe neutrinos via inverse beta decay interactions in a chlorine-based target with a detection threshold of 0.814 MeV (so mostly sensitive to ${}^7\text{Be}$ and ${}^8\text{B}$ fluxes) and integrating the interaction of the neutrinos over time. This experiment provided the first direct evidence of solar neutrinos but revealed a significant discrepancy: the observed neutrino flux was approximately one-third of the flux predicted by the SSM. This inconsistency was termed the "solar neutrino problem". The second generation of radiochemical detectors SAGE [55] and Gallex/GNO [56] detect inverse beta decay interactions in a gallium-based target which had a much lower detection threshold of 0.233 MeV and was able to detect the most abundant flux of pp neutrinos. They also observed a deficit but it was $\sim 50\%$.

The Kamiokande experiment [57–59], a precursor to Super-Kamiokande, was a water Cherenkov detector located in Japan. Unlike the radiochemical experiments, Kamiokande was able to detect solar neutrinos in **real time** through elastic scattering of neutrinos with electrons ($\nu + e^- \rightarrow \nu + e^-$). This process produced Cherenkov light, enabling directional information that confirmed neutrinos originated from the Sun. Kamiokande observed a solar neutrino flux deficit of approximately 60% compared to SSM predictions. However, its higher energy threshold (~ 7.5 MeV) limited sensitivity to only ${}^8\text{B}$ neutrinos. While Kamiokande could not resolve the solar neutrino problem alone, its real-time detection capability and directional verification were essential for subsequent experiments like Super-Kamiokande and SNO, which identified neutrino flavour transitions as the solution. The Super-Kamiokande experiment [60–63], a water Cherenkov detector, measured solar neutrinos with improved precision and spectral resolution. By detecting Cherenkov radiation from relativistic electrons produced in neutrino interactions, Super-Kamiokande confirmed the deficit of high-energy solar neutrinos and determined the energy (in)dependence of the suppression. This spectral information provided critical evidence to establish the MSW effect as the mechanism behind the observations. Still because the radiochemical experiments detected only ν_e and the rate of ν_e interactions in water Cherenkov detectors is larger than that of ν_μ and ν_τ , these deficits could only be established through comparison with predictions of some SSM.

The Sudbury Neutrino Observatory (SNO) [64] resolved the solar neutrino problem conclusively and independently of the SSM. Using heavy water (D_2O), SNO simultaneously measured the flux of electron neutrinos (via charged-current interactions) and the total flux of all active neutrino flavours (via neutral-current interactions). The results showed that the total neutrino flux matched SSM predictions, while the electron neutrino flux remained suppressed. This confirmed that solar neutrinos undergo flavour transitions, with electron neutrinos transitioning to muon or tau neutrinos during propagation.

Ultimately all these results validated the neutrino flavour oscillation hypothesis with averaged oscillation in vacuum and MSW matter transition as dominant mechanisms depending on the neutrino energy. In a nut-shell in the Sun's high-density core (~ 150 g/cm³), the higher-energy solar neutrinos ($E \gtrsim 10$ MeV) undergo flavor conversion due to matter-enhanced oscillations as described Sec. 2.4. In a two-neutrino system the adiabatic transition aligns the produced ν_e with the heaviest matter eigenstate (ν_2^m), which exits the Sun as the vacuum mass eigenstate ν_2 , resulting in $P_{ee} \approx \sin^2 \theta \sim 0.31$ ($\theta \sim 34^\circ$), consistent with measurements from Homestake and SK/SNO. At low energies ($E \ll 1$ MeV), vacuum oscillations dominate: neutrinos propagate incoherently as mass

eigenstates (ν_1, ν_2) , and P_{ee} approaches $\cos^4 \theta + \sin^4 \theta = 1 - \frac{1}{2} \sin^2 2\theta \approx 0.57$ (in agreement with the Gallium experiments), reflecting the incoherent sum of probabilities for ν_1 and ν_2 to be detected as ν_e . The transition between these regimes is governed by the interplay of the solar matter potential ($V \sim 10^{-11}$ eV) and vacuum oscillation wavelength and requires $\Delta m_{21}^2 \sim 7.5 \times 10^{-5}$ eV². In the framework of 3ν mixing this effect is controlled by Δm_{21}^2 and θ_{12} with small corrections from θ_{13} as seen in Eq. (2.90). In summary

$$P_{ee} \approx \begin{cases} \cos^4 \theta_{13} \sin^2 \theta_{12} + \sin^4 \theta_{13} & \text{(high energy, adiabatic limit),} \\ \cos^4 \theta_{13} \left(1 - \frac{1}{2} \sin^2 2\theta_{12}\right) + \sin^4 \theta_{13} & \text{(low energy, vacuum limit).} \end{cases} \quad (3.1)$$

In the last decade Borexino [65], has significantly advanced solar neutrino research by utilizing liquid scintillator technology. It measures neutrinos through the process of elastic scattering with electrons, a method that allows for the detection of low-energy neutrinos with high sensitivity. This capability has been essential in observing solar neutrinos from all branches of the pp-chain. Most recently, Borexino reported also the detection of CNO neutrinos with a confidence level exceeding 6σ [66]. This measurement provides new insights into solar metallicity and confirms the dominant energy production mechanism in heavy stars. During my PhD, together with collaborators, we contributed important results on solar neutrinos. In the next section, we will describe our analysis and in next chapters we will present the main results obtained from this work.

3.1.1 Simulation of Borexino Phase II and III spectra

The Borexino experiment, located in Gran Sasso (Italy), played a crucial role in the precise measurement of solar neutrinos due to its remarkably low background noise (it's still playing; however, the experiment was discontinued recently). Phase I of the experiment was successful in the detection of ${}^7\text{Be}$, adding significantly to our understanding of the sun's energy generation [67]. Phase II of Borexino was characterized by strongly reduced internal ${}^{85}\text{Kr}$ and ${}^{210}\text{Bi}$ backgrounds, leading to the most precise measurement to date of ${}^7\text{Be}$ solar neutrinos and the first real-time detection of pp and pep neutrinos. In Phase III, the Borexino succeeded in measuring for the first time the CNO cycle by thermally stabilizing the detector, thus reducing the convection currents responsible for the diffusion of ${}^{210}\text{Bi}$ into the scintillator. A detailed description of our analysis of the full spectrum of the Phase-I [65, 67] and Phase-II [68] of Borexino can be found in Ref. [69] and Ref. [2] respectively. Here we document the details of our analysis of the Borexino Phase II (data collected between December 2011 and May 2016, corresponding to an exposure of 1291.51 days \times 71.3 tons) and Phase-III (data collected from January 2017 to October 2021, corresponding to a total exposure of 1431.6 days \times 71.3 tons), which we perform following closely the details presented by the collaboration in Refs. [68] and [66, 70], respectively.

As discussed in a previous section, Borexino detects interactions of solar neutrinos produced in the pp, pep, ${}^7\text{Be}$, and ${}^8\text{B}$ reactions of the pp-chain, as well as from all reactions in the CNO-cycle. The produced total flux is described by the differential spectrum:

$$\frac{d\phi_{\nu}^{\text{prod}}}{dE_{\nu}} = \sum_f \frac{d\phi_{\nu}^f}{dE_{\nu}}(E_{\nu}), \quad (3.2)$$

where E_{ν} is the neutrino energy and f refers to each of the main components of the solar neutrino flux (pp, pep, CNO, ${}^7\text{Be}$, and ${}^8\text{B}$). In their journey to the Earth the produced ν_e will change flavour and interact upon arrival via elastic scattering with the e^{-} of the detector. Thus, the expected number of solar neutrino events corresponding to N_h hits

is given by the convolution of the oscillated solar neutrino spectrum with the interaction cross section and the energy resolution function. Quantitatively we compute the solar neutrino signal S_i in the i -th bin (*i.e.*, with $N_h \in [N_{h,\min}^i, N_{h,\max}^i]$) as:

$$S_i = \int_{N_{h,\min}^i}^{N_{h,\max}^i} \int \frac{dS}{dT_e}(T_e) \frac{d\mathcal{R}}{dN_h}(T_e, N_h) dT_e dN_h. \quad (3.3)$$

Here, dS/dT_e is the differential distribution of neutrino-induced events as a function of recoil energy of the scattered electrons (T_e)

$$\frac{dS}{dT_e}(T_e) = \mathcal{F}_s \mathcal{N}_{\text{tgt}} \mathcal{T}_{\text{run}} \mathcal{E}_{\text{cut}} \int \frac{d\phi_\nu^{\text{prod}}}{dE_\nu}(E_\nu) \left[P_{e\alpha}(E_\nu) \frac{d\sigma^{\text{det}}}{dT_e}(\nu_\alpha) \right] dE_\nu \quad (3.4)$$

where $\mathcal{F}_s = 0.3572$ (0.6359) is the fraction for $s =$ “tagged” (“subtracted”) signal events, \mathcal{N}_{tgt} is the number of e^- targets (*i.e.*, the total number of electrons inside the fiducial volume of the detector, corresponding to 71.3 ton of scintillator for both phases), while $\mathcal{T}_{\text{run}}^{\text{II}} = 1291.51$ days and $\mathcal{T}_{\text{run}}^{\text{III}} = 1431.6$ days is the data taking time for phase II and III, respectively, and $\mathcal{E}_{\text{cut}} = 98.5\%$ is the overall efficiency for both phases. $P_{e\alpha}(E_\nu)$ is the transition probability between the flavours e and α , and $d\sigma^{\text{det}}(\nu_\alpha)/dT_e$ is the flavour dependent $\nu_\alpha - e^-$ elastic scattering detection cross section.

In addition, Eq. (3.3) includes the energy resolution function $d\mathcal{R}/dT_e$ for the detector, which gives the probability that an event with electron recoil energy T_e yields an observed number of hits N_h . We assume it follows a Gaussian distribution:

$$\frac{d\mathcal{R}}{dN_h}(T_e, N_h) = \frac{1}{\sqrt{2\pi} \sigma_h(T_e)} \exp \left[-\frac{1}{2} \left(\frac{N_h - \bar{N}_h(T_e)}{\sigma_h(T_e)} \right)^2 \right], \quad (3.5)$$

where \bar{N}_h is the expected value of N_h for a given true recoil energy T_e . We determine $\bar{N}_h(T_e)$ and $\sigma_h(T_e)$ via the calibration procedure described below.

The data from BXII contains background contributions from a number of sources. The main backgrounds come from radioactive isotopes in the scintillator ^{14}C , ^{11}C , ^{10}C , ^{10}Po , ^{10}Bi , ^{85}Kr , and ^6He . The collaboration identifies two additional backgrounds due to pile-up of uncorrelated events, and residual external backgrounds (see Ref. [68] for a complete description of these backgrounds).

Among the considered backgrounds, the one coming from ^{11}C is particularly relevant for the analysis. This isotope is produced in the detector by muons through spallation on ^{12}C . In Ref. [68] the collaboration uses a Three-Fold Coincidence (TFC) method to tag the ^{11}C events, which are correlated in space and time with a muon and a neutron. Thus, they divide the Phase II data set in two samples: one enriched (tagged) and one depleted (subtracted) in ^{11}C events. The separation of the solar neutrino signal (as well as most of the other backgrounds) into these two samples is uncorrelated from the number of hits N_h . Concretely, the tagged sample picks up 35.72% of the solar neutrino events, while the subtracted sample accounts for the remaining 64.28%.

Similarly to Phase-II, the main backgrounds of Phase-III come from radioactive isotopes in the scintillator ^{11}C , ^{210}Bi , ^{10}C , ^{210}Po and ^{85}Kr , extracted from Fig. 2(a) of Ref. [70] as well as the plot provided to us by the collaboration [71]. These figures show the best-fit normalization of the different background components as obtained by the collaboration, and we take them as our nominal background predictions. As for Phase II, the tagged sample of Phase III picks up about 35.72% of the solar neutrino events, while the subtracted sample accounts for the remaining 64.28%. The data and best fit

components for the spectrum of the subtracted sample are shown in Fig. 2(a) of Ref. [70]. The data points for this sample can also be found in the data release material in Ref. [72]. The corresponding information for the tagged sample was kindly provided to us by the Borexino collaboration [71].

In our analysis we include both sets of data, denoted in what follows by $s = \text{“tagged”}$ or “subtracted” . As for the background, we have read the contribution $B_{s,i}^c$ for each component c , in each bin i , and for each data set s from the corresponding lines in the two panels in Fig. 7 of Ref. [68]. Altogether the nominal number of expected events $T_{s,i}^0$ in some bin i of data sample s is the sum of the neutrino-induced signal and the background contributions:

$$T_{s,i}^0 = \sum_f S_{s,i}^f + \sum_c B_{s,i}^c, \quad (3.6)$$

where the index $f \in \{\text{pp}, {}^7\text{Be}, \text{pep}, \text{CNO}, {}^8\text{B}\}$ runs over the solar fluxes, while the index $c \in \{{}^{14}\text{C}, {}^{11}\text{C}, {}^{10}\text{C}, {}^{210}\text{Po}, {}^{210}\text{Bi}, {}^{85}\text{Kr}, {}^6\text{He}, \text{pile-up}, \text{ext}\}$ runs over the background components. In our calculation of $S_{s,i}^f$ we use the high-metallicity (HZ) solar model for simplicity.¹

Energy Calibration

The Borexino data fit is performed using the observed number of hits, N_h , as an estimator for the electron recoil energy, T_e . The energy resolution is modelled with a Gaussian function, parameterized by the mean number of hits $\bar{N}_h(T_e)$ and its width $\sigma_h(T_e)$. These parameters were derived in two steps:

1. The relation between \bar{N}_h and σ_h was calibrated using γ -ray source data. During our investigations, we discovered that each phase of Borexino has a particular way to relate \bar{N}_h and σ_h , particularly for the last two phases of the experiment.

For **Borexino Phase II**:

$$\sigma_h(\bar{N}_h) = 1.21974 + 1.31394\sqrt{\bar{N}_h} - 0.0148585\bar{N}_h. \quad (3.7)$$

And for the **Borexino Phase III**

$$\sigma_h(\bar{N}_h) = 1.21974 + 1.60121\sqrt{\bar{N}_h} - 0.014859\bar{N}_h. \quad (3.8)$$

2. A third-degree polynomial was used to model $\bar{N}_h(T_e)$ for reproducing solar neutrino spectra:

$$\bar{N}_h(T_e) = -8.065244 + 493.2560 \frac{T_e}{\text{MeV}} - 64.09629 \left(\frac{T_e}{\text{MeV}} \right)^2 + 4.146102 \left(\frac{T_e}{\text{MeV}} \right)^3. \quad (3.9)$$

Analysis of Borexino Phase II

Our statistical analysis is based on the construction of a χ^2 function based on the described experimental data, neutrino signal expectations and sources of backgrounds, as well as the effect of systematic uncertainties.

The analysis incorporates the concept of pulls, denoted as ξ_r , which are varied to minimize the χ^2 . A total of 27 pulls are included to account for uncertainties in background normalizations, detector performance, priors on solar fluxes, and energy shifts. Assuming

¹It should be noted that this is the model currently favoured by the CNO measurement at Borexino [66], albeit with a modest significance.

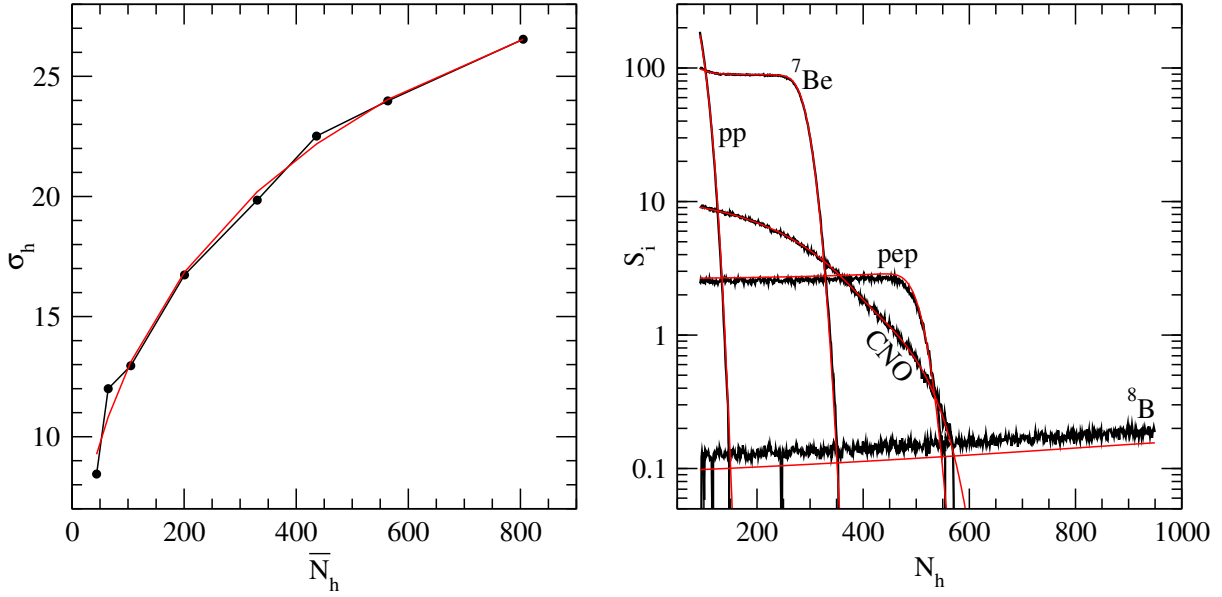


Figure 3.2: Left: our choice of the energy resolution function, based on the relation between σ_h and \bar{N}_h inferred from the upper panel of Fig. 22 of Ref.[68]. Right: our reconstruction of solar spectra after the optimization of the energy scale function.

a linear dependence of event rates on the pulls, the χ^2 minimization can be performed analytically if the χ^2 is Gaussian.

The Borexino collaboration, for Phase II, bins their data into 858 bins per sample, ranging from $N_h = 92$ to $N_h = 950$. However, this fine binning does not provide sufficient events per bin to ensure Gaussian statistics. To address this, we rebin the data using coarser bins. Specifically:

- The first 42 bins are grouped into sets of 2.
- The next 210 bins are grouped into sets of 5.
- The subsequent 260 bins are grouped into sets of 10.
- The final 346 bins are grouped into sets of 50.

This rebinning results in a total of 96 bins (k) for each data sample (s), ensuring sufficient events in each bin to guarantee Gaussian statistics. The resulting χ^2 function is given by:

$$\chi^2 = \min_{\vec{\xi}} \left[\sum_{s,k} \frac{[T_{s,k}(\vec{\xi}) - O_{s,k}]^2}{O_{s,k}} + \sum_r (\xi_r^{\text{unc}})^2 + \sum_{r,r'} (\Sigma^{-1})_{rr'} \xi_r^{\text{corr}} \xi_{r'}^{\text{corr}} \right], \quad (3.10)$$

where $O_{s,k}$ represents the observed number of events in bin k of sample s , and $T_{s,k}$ is the predicted number of events, incorporating systematic uncertainties:

$$T_{s,k}(\vec{\xi}) = T_{s,k}^0 + \sum_r D_{s,k}^r \xi_r. \quad (3.11)$$

Here $D_{s,k}^r$ represents the derivatives of the total event rates with respect to each pull.

The last two terms in Eq. (3.31) introduce Gaussian bias factors to account for prior constraints on specific pulls. The first term addresses pulls associated with uncorrelated

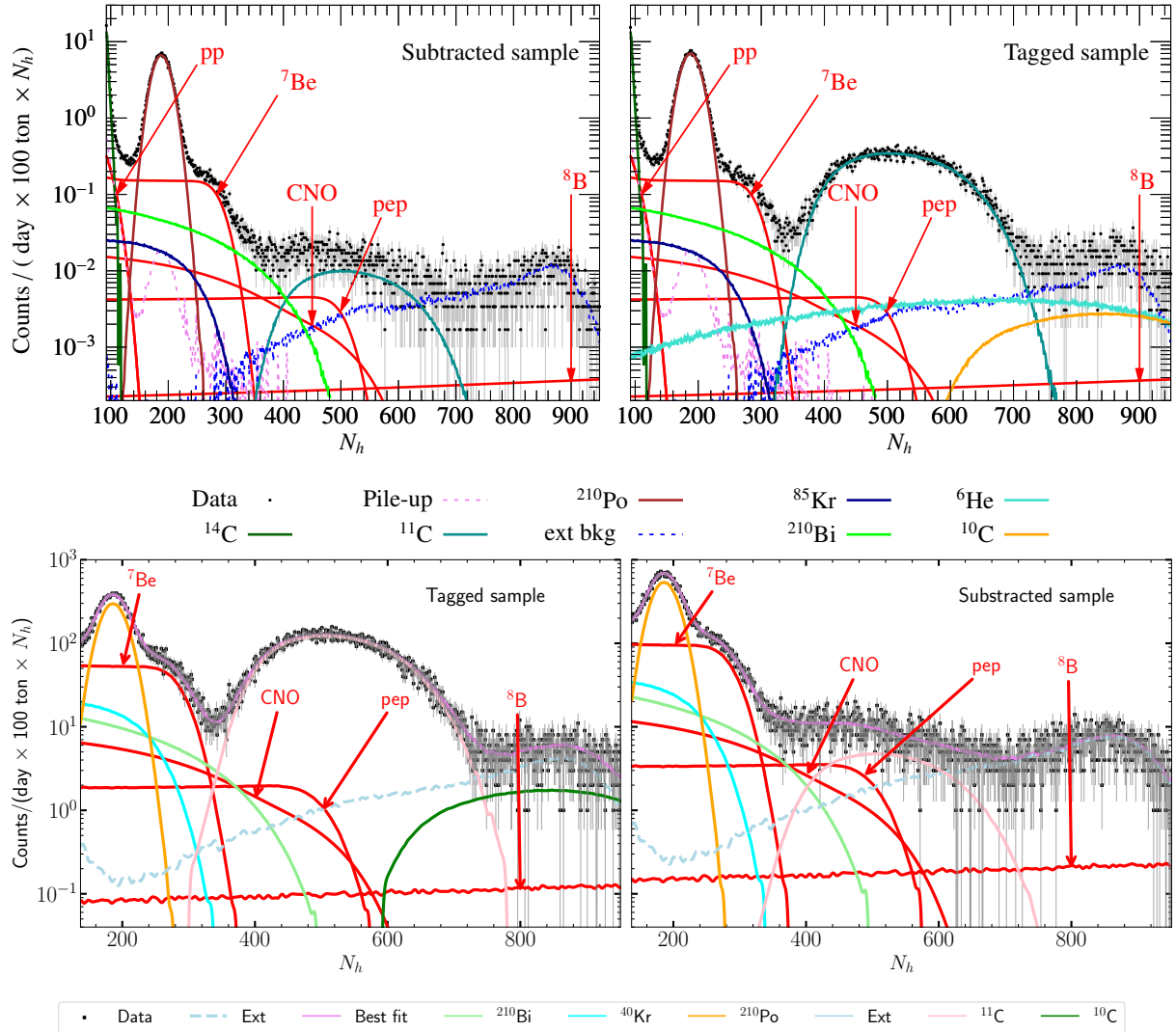


Figure 3.3: Spectrum for the best-fit normalizations of the different components obtained from our fit to the (**upper panel**) Borexino Phase II data for TFC-subtracted (left) and TFC-tagged events and (**lower panel**) Borexino Phase III data for TFC-subtracted (left) and TFC-tagged events.

(“unc”) uncertainties, while the second term addresses correlated (“corr”) uncertainties. In this context, Σ represents the covariance matrix for correlated uncertainties, detailed in the Appendix of [2].

Analysis of Borexino Phase-III spectrum

Our statistical analysis is based on the construction of a χ^2 function built with the described experimental data, neutrino signal expectations and sources of backgrounds. Following Refs. [66, 70] we leave the normalization of all the backgrounds as free parameters with the exception of ^{210}Bi . The treatment of this background is paramount to the positive evidence of CNO neutrinos. As described in [66], the extraction of the CNO neutrino signal from the Borexino data faces two significant challenges: the resemblance between spectra of CNO- ν recoil electrons and the ^{210}Bi β^- spectra, and their pronounced correlation with the pep- ν recoil energy spectrum. In order to surpass the first challenge,

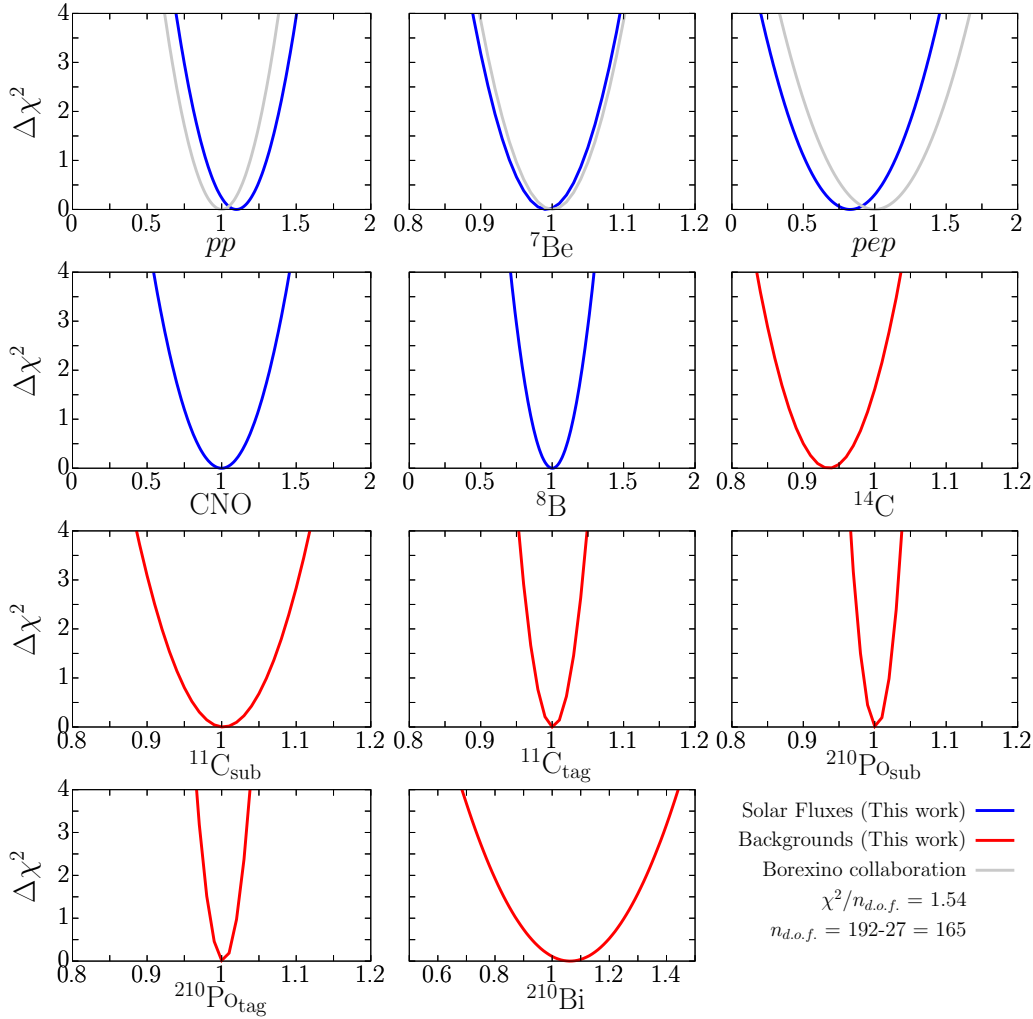


Figure 3.4: Dependence of our $\Delta\chi^2$ for the fit to the Borexino phase-II spectra on the normalization of the solar fluxes and the dominant backgrounds (normalized to the corresponding best fit normalizations of the fit of the Borexino collaboration in Ref.[68]). For comparison we show as light blue curves the corresponding results of the determination of solar fluxes in Ref.[68]) (see text for details).

the collaboration restricted the rate of ^{210}Bi for which it sets and upper limit [70]:

$$R(^{210}\text{Bi}) \leq (10.8 \pm 1.0) \text{ cpd}/100 \text{ t}, \quad (3.12)$$

while no constraint is imposed on its minimum value which is free to be as low as allowed by the fit (as long as it remains non-negative). In our analysis we implement this upper limit by constraining the corresponding normalization factor $f_{^{210}\text{Bi}}$ as

$$f_{^{210}\text{Bi}} \leq \left(1 \pm \frac{1.0}{10.8}\right), \quad (3.13)$$

With this we construct the χ_{BXIII}^2 as

$$\chi_{\text{BXIII}}^2 = \sum_{s,i} 2 \left[T_{s,i}^0 - O_{s,i} + O_{s,i} \log \left(\frac{O_{s,i}}{T_{s,i}^0} \right) \right] + \left(\frac{f_{^{210}\text{Bi}} - 1}{\sigma_{^{210}\text{Bi}}} \right)^2 \Theta(f_{^{210}\text{Bi}} - 1), \quad (3.14)$$

where $O_{s,i}$ is the observed number of events in bin i of sample s , and $\sigma_{^{210}\text{Bi}} = 1.0/10.8$, and $\Theta(x)$ is the Heaviside step function.

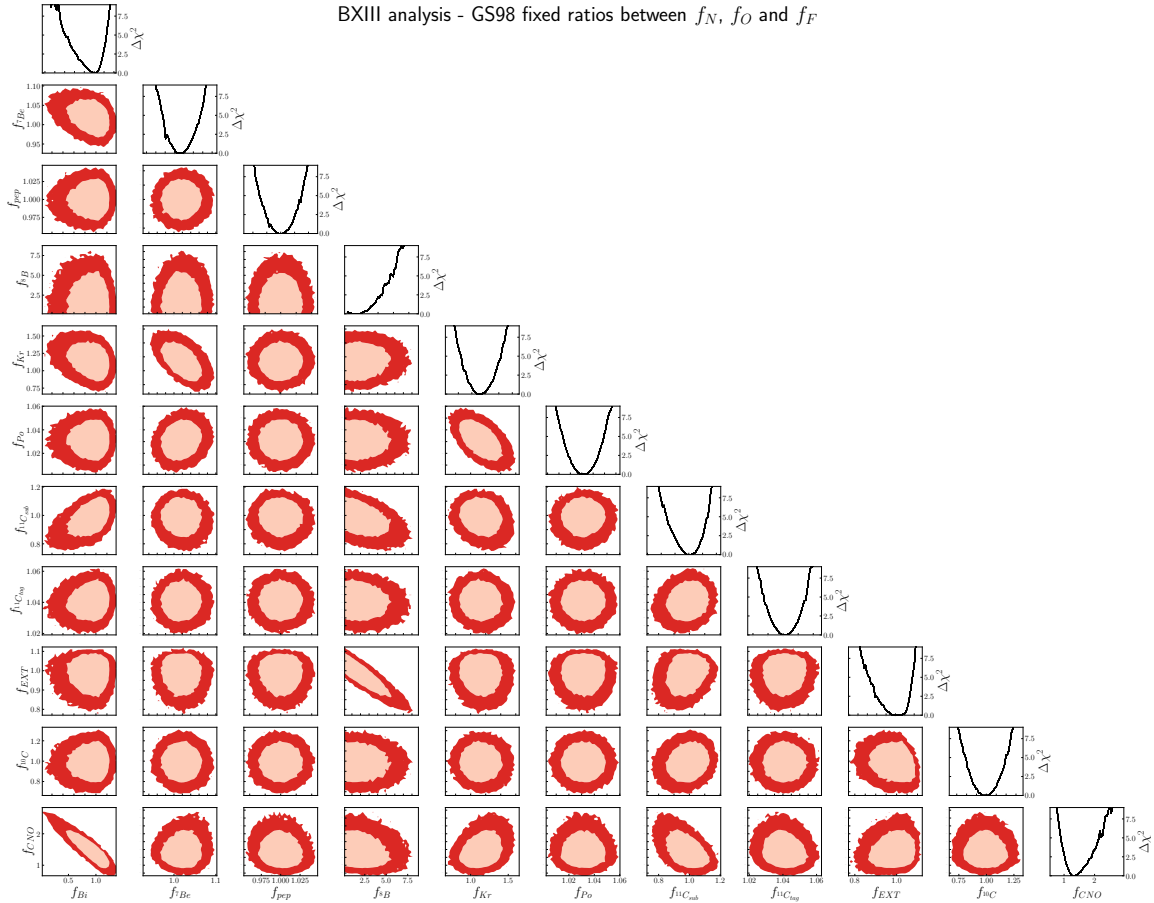


Figure 3.5: Constraints from our analysis of Borexino Phase-III spectra obtained with $\chi^2_{\text{BXIII, test}}$ in Eq. (3.15). Each panel shows a two-dimensional projection of the allowed multi-dimensional parameter space after minimization with respect to the undisplayed parameters. The regions correspond to 90% and 99% CL (2 d.o.f.). The curves in the right-most panels show the marginalized one-dimensional $\Delta\chi^2_{\text{BXIII, test}}$ for each of the parameters.

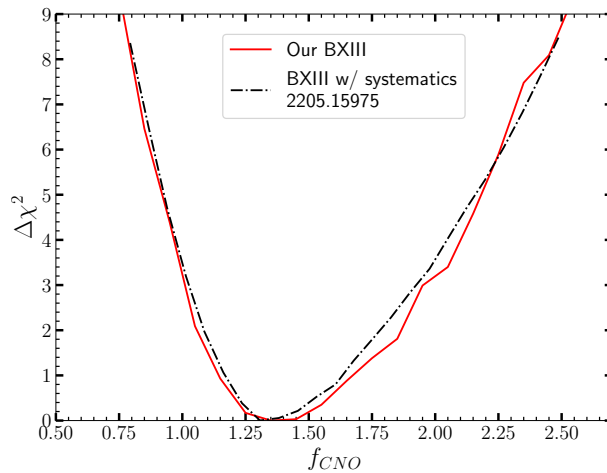


Figure 3.6: Dependence of $\Delta\chi^2$ of our fit to the Borexino Phase-III spectra on the common normalization of the CNO fluxes (red line). For comparison we plot (black dot-dashed line) the corresponding results in figure 2(b) of [70] for their “Fit w/ Systematics”, divided by the central value of the predicted CNO- ν rate of the B16-GS98 mode.

Constructed this way, χ_{BXIII}^2 depends on 16 parameters: the 3 oscillation parameters (Δm_{21}^2 , θ_{12} , θ_{13}), 6 solar flux normalizations (f_{Be} , f_{pep} , f_{N} , f_{O} , f_{F} , f_{B}) and 7 background normalizations (f_{Pb} , f_{Bi} , f_{Kr} , f_{C} , f_{ext} and two different factors $f_{\text{C}}^{\text{tag}}$ and $f_{\text{C}}^{\text{sub}}$ for the tagged and subtracted samples).

As a first validation of our χ^2 function we perform an analysis focused at reproducing the results on the solar neutrino fluxes found by the Borexino collaboration in Ref. [70], and in particular the positive evidence of CNO neutrinos. In this test fit we fix the three oscillation parameters to their best fit value ($\sin^2 \theta_{13} = 0.023$, $\sin^2 \theta_{12} = 0.307$, $\Delta m_{21}^2 = 7.5 \times 10^{-5}$), and following the procedure of the collaboration we assume a common normalization factor for the three CNO fluxes with respect to the SSM ($f_{\text{N}} = f_{\text{O}} = f_{\text{F}} \equiv f_{\text{CNO}}$). Furthermore, in order to break the pronounced correlation with the pep- ν recoil energy spectrum mentioned above, the collaboration introduced a prior for the pep neutrino signal flux following the SSM. Thus we define

$$\chi_{\text{BXIII,test}}^2 = \chi_{\text{BXIII}}^2 + \left(\frac{f_{\text{pep}} - 1}{\sigma_{\text{pep}}} \right)^2 \quad (3.15)$$

with $\sigma_{\text{pep}} = 0.04/2.74$ (for concreteness we choose the B16-GS98 model for this prior). The ${}^7\text{Be}$ and ${}^8\text{B}$ fluxes are left completely free.

The results of this 11-parameter fit are shown in Figs. 3.5 and 3.6. In Fig. 3.5 we plot the allowed ranges and correlations for the parameters. Notice that in this figure all parameters are normalized to the best fit values obtained by the corresponding analysis of the Borexino collaboration, hence a value of “1” means perfect agreement. We observe a strong correlation between the normalization of the CNO fluxes f_{CNO} and the ${}^{210}\text{Bi}$ background. This is expected because, as mentioned before, the spectrum of CNO neutrinos and that of the ${}^{210}\text{Bi}$ background are similar. Still, the two spectra are different enough so that, under the assumption of the upper bound on the ${}^{210}\text{Bi}$ background, the degeneracy gets broken enough to lead to a positive evidence of CNO neutrinos in an amount compatible with the prediction of the SSMs.

A quantitative comparison with the results of the collaboration is shown in Fig. 3.6 where we plot the dependence of our marginalized $\Delta\chi^2$ on the common CNO flux normalization, f_{CNO} , together with that obtained by the collaboration as extracted from Figure 2(b) of Ref. [70] (labeled “Fit w/ Systematics” in that figure).² Altogether, these figures show that our constructed event rates and the best-fit normalization of the CNO flux reproduce with very good accuracy those of the fit performed by the collaboration.

Analysis with Correlated Integrated Directionality Method

In a very recent work [73] the Borexino collaboration has presented a combined analysis of their three phases making use of the Correlated and Integrated Directionality (CID) method, which aims to enhance the precision of the determination of the flux of CNO neutrinos. In a nut-shell, the CID method exploits the sub-dominant Cherenkov light in the liquid scintillator produced by the electrons scattered in the neutrino interaction. These Cherenkov photons retain information of the original direction of the incident neutrino, hence they can be used to enhance the discrimination between the solar neutrino signal and the radioactive backgrounds.

Effectively, the CID analysis results into a determination of the total number of solar neutrinos detected within a restricted range of N_h which corresponds to $0.85 \text{ MeV} <$

²Figure 2(b) of Ref. [70] shows their $\Delta\chi^2$ as a function of the CNO- ν event rate which we divide by the central value of the expected rate in the B16-GS98 model to obtain the black dot-dashed curve in Fig. 3.6.

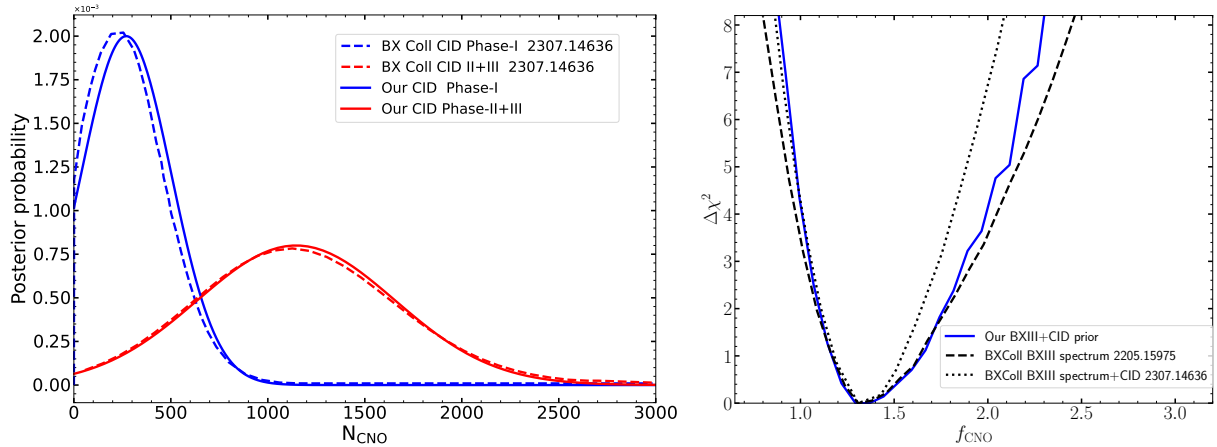


Figure 3.7: Left: CID posterior probabilities for the number for Phase-I and Phase-II+III of CNO- ν events after constraining pep and ^8B neutrino events to their SSM expectation. Right: Dependence of $\Delta\chi^2$ on the CNO flux normalization from our fit to the Borexino Phase-III spectra combined with the CID constraint (blue line) compared to that obtained by the Borexino collaboration (dotted black line). For comparison we also show the result without CID information (dashed black line).

$T_e < 1.3$ MeV for Phase-I and 0.85 MeV $< T_e < 1.29$ MeV for Phase-II+III. In this range the dominant contribution comes from CNO, pep and some ^8B . The increased fiducial volume for this analysis brings the exposures to 740.7 days $\times 104.3$ ton $\times 55.77\%$ for Phase-I and 2888.0 days $\times 94.4$ ton $\times 63.97\%$ for Phase-II+III. The resulting number of solar neutrinos detected is $N_{\text{obs}}^{\text{P-I}} = 643_{-224}^{+235}(\text{stat})_{-30}^{+37}(\text{sys})$ for Phase-I and $N_{\text{obs}}^{\text{P-II+III}} = 2719_{-494}^{+518}(\text{stat})_{-83}^{+85}(\text{sys})$ for Phase-II+III. After subtracting the expected SSM contribution from pep and ^8B the Borexino collaboration obtains the posterior probability distributions for the number of CNO neutrinos shown in Fig. 9 of Ref. [73] (which we reproduce in the left panel in Fig. 3.7). Furthermore, since this new directional information is independent of the spectral information, the collaboration proceeded to combine these two priors on N_{CNO} with the their likelihood for the Borexino Phase-III spectral analysis. This resulted in a slightly stronger dependence of the combined likelihood on the CNO- ν rate shown in their Fig. 12 (which we reproduce in the right panel in Fig. 3.7).

In order to account for the CID information in our analysis we try to follow as closely as possible the procedure of the collaboration. With the information provided on the covered energy range and exposures for the CID analysis, we integrate our computed spectra of solar neutrino events in each phase to derive the corresponding total number of expected events in Phase-I and Phase-II+III. We then subtract the SSM predictions for pep and ^8B neutrinos from the observed number of events to derive an estimate for CNO neutrinos in in Phase-I and Phase-II+III, and construct a simple Gaussian $\chi^2(N_{\text{CNO}})$ for Phase-Y (Y=I or II+III)

$$\chi_{\text{CID,P-Y}}^2(N_{\text{CNO}}) = \left(\frac{N_{\text{obs}}^{\text{P-Y}} - N_{\text{SSM,pep}}^{\text{P-Y}} - N_{\text{SSM},^8\text{B}}^{\text{P-Y}} - N_{\text{CNO}}}{\sigma_{\text{P-Y}}} \right)^2 \quad (3.16)$$

where in $\sigma_{\text{P-Y}}$ we add in quadrature the symmetrized statistical and systematic uncertainties in the number of observed events.

We plot in the left panel in Fig. 3.7 our inferred probability distributions $P_{\text{P-Y}}(N_{\text{CNO}}) \propto \exp[-\chi_{\text{P-Y}}^2/2]$ compared to those from Borexino in Fig. 9 of Ref. [73]. As seen in the figure our simple procedure reproduces rather well the results of the collaboration for the Phase-II+III but only reasonably for Phase-I. This may be due to differences in the reanalysis

of the Phase-I data by the collaboration in the CID analysis compared to their spectral analysis of 2011. Our simulations of the Phase-I event rates are tuned to their 2011 and there is not enough information in Ref. [73] to deduce what may have changed. Thus we decide to introduce in our analysis the CID prior for the Phase-II+III data but not for Phase-I.

We then combine the CID from Phase-II+III and Phase-III spectral information as

$$\chi_{\text{CID+BXIII,test}}^2 = \chi_{\text{BX-III}}^2 + \left(\frac{f_{\text{pep}} - 1}{\sigma_{\text{pep}}} \right)^2 + \chi_{\text{CID,P-II+III}}^2. \quad (3.17)$$

A quantitative comparison with the results of the collaboration for this combined CID + Phase-III spectrum analysis is shown in the right panel of Fig. 3.7 where we plot the dependence of our marginalized $\Delta\chi^2$ on the CNO flux normalization after including the CID information compared to that obtained by the collaboration in Fig. 12 of Ref. [73]. As seen in the figure, we reproduce well the improved sensitivity for the lower range of the CNO flux normalization but our constraints are more conservative in the higher range, though they still represent an improvement over the spectrum-only analysis.

Altogether, after all these tests and validations we define the χ^2 for the full Borexino analysis as

$$\begin{aligned} \chi_{\text{BX}}^2(\vec{\omega}_{\text{osc}}, \vec{\omega}_{\text{flux}}) = & \chi_{\text{BXI}}^2(\vec{\omega}_{\text{osc}}, \vec{\omega}_{\text{flux}}) + \chi_{\text{BXII}}^2(\vec{\omega}_{\text{osc}}, \vec{\omega}_{\text{flux}}) \\ & + \chi_{\text{BXIII}}^2(\vec{\omega}_{\text{osc}}, \vec{\omega}_{\text{flux}}) + \chi_{\text{CID,P-II+III}}^2(\vec{\omega}_{\text{osc}}, \vec{\omega}_{\text{flux}}). \end{aligned} \quad (3.18)$$

with $\chi_{\text{BXIII}}^2(\vec{\omega}_{\text{osc}}, \vec{\omega}_{\text{flux}})$ and $\chi_{\text{CID,P-II+III}}^2(\vec{\omega}_{\text{osc}}, \vec{\omega}_{\text{flux}})$ in Eqs. (3.14) and (3.16), respectively. We finish by noticing that the inclusion of the CID information is not enough to break the large degeneracy between the ^{13}N and ^{210}Bi contributions to the spectra discussed in the previous section.

3.2 Atmospheric Neutrinos

Atmospheric neutrinos are produced by the interactions of cosmic rays with atomic nuclei in the Earth's atmosphere. Cosmic rays, which are primarily composed of high-energy protons and heavier nuclei, originate from astrophysical sources such as supernovae, active galactic nuclei, and other high-energy phenomena in the universe. When these cosmic rays collide with atmospheric nuclei (mainly nitrogen and oxygen), they produce a cascade of secondary particles, including pions (π), kaons (K), and other mesons. The subsequent decays of these unstable particles generate atmospheric neutrinos. For example, the charged pions then decay into muons and muon neutrinos:

$$\begin{aligned} \pi^\pm & \rightarrow \mu^\pm + \frac{\nu_\mu}{\bar{\nu}_\mu} \\ \mu^\pm & \rightarrow e^\pm + \frac{\bar{\nu}_\mu + \nu_e}{\nu_\mu + \bar{\nu}_e} \end{aligned} \quad (3.19)$$

Similar decay chains occur for kaons and heavier mesons contributing to the flux of atmospheric neutrinos. As a result, atmospheric neutrinos consist of a mixture of electron neutrinos, muon neutrinos, and their corresponding antineutrinos. The relative abundance of these neutrino flavors depends on the energy of the primary cosmic rays and the altitude at which the interactions occur. Atmospheric neutrinos span a wide range of energies, from MeV to TeV scales, making them a valuable probe for studying neutrino

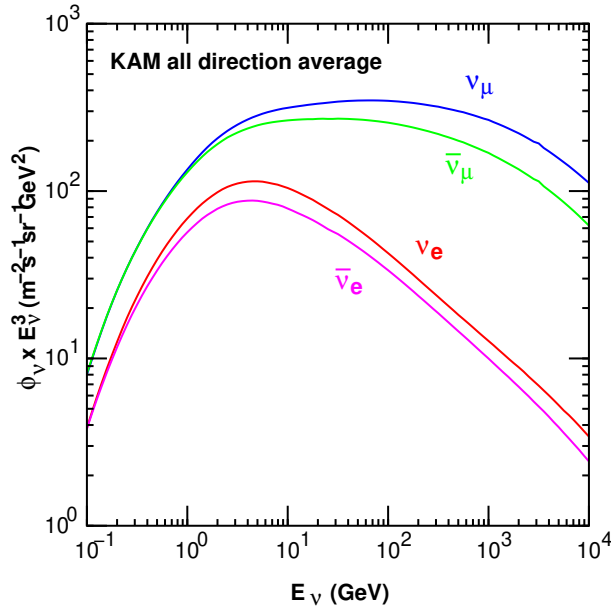


Figure 3.8: Atmospheric neutrino flux at the Super-Kamiokande site, averaged over all directions and over one year. Extracted from Ref. [74].

oscillations and other fundamental properties of neutrinos. A realistic representation of the atmospheric neutrinos is provided in Fig. 3.8.

The study of atmospheric neutrinos has been realized by large-scale detectors such as Super-Kamiokande [75, 76] and most recently IceCube [77, 78]. Super-Kamiokande is a water Cherenkov detector located in Japan. It played a pivotal role in the study of the discovery of neutrino oscillations. By measuring the zenith angle dependence of the atmospheric neutrino flux, Super-Kamiokande provided conclusive evidence that muon neutrinos oscillate into tau neutrinos as they travel through the Earth. As seen in Fig. 3.9, Super-Kamiokande data reveals a zenith-angle-dependent $\nu_\mu/\bar{\nu}_\mu$ deficit, increasing with baseline L (e.g., upward-going neutrinos traversing Earth), consistent with the survival probability:

$$P_{\mu\mu} = 1 - \sin^2 2\theta \sin^2 \left(\frac{\Delta m^2 L}{4E} \right), \quad (3.20)$$

where θ and Δm^2 parametrize $\nu_\mu \rightarrow \nu_\tau$ oscillations. No $\nu_e/\bar{\nu}_e$ appearance or disappearance is observed, and matter effects are negligible (no sensitivity to θ 's octant or Δm^2 's sign). Higher-energy neutrinos (e.g., “UpThrough” or “Multi-GeV” samples) show reduced disappearance due to the L/E dependence. In the three-flavor framework, this corresponds to $\theta_{23} \sim 45^\circ$ and $|\Delta m_{32}^2| \sim 2.5 \times 10^{-3} \text{ eV}^2$, which is much larger than the mass splitting observed in solar neutrinos.

IceCube, located at the South Pole, utilizes a cubic kilometer of Antarctic ice as a detection medium and it also detects neutrinos through the Cherenkov radiation emitted by secondary particles produced in neutrino interactions. These two experiments still collect data, most recent results are the IceCube's IC24 configuration corresponding to 9.3-year dataset [80, 81] and the combined results from Super-Kamiokande's SK1-5 phases [75, 76].

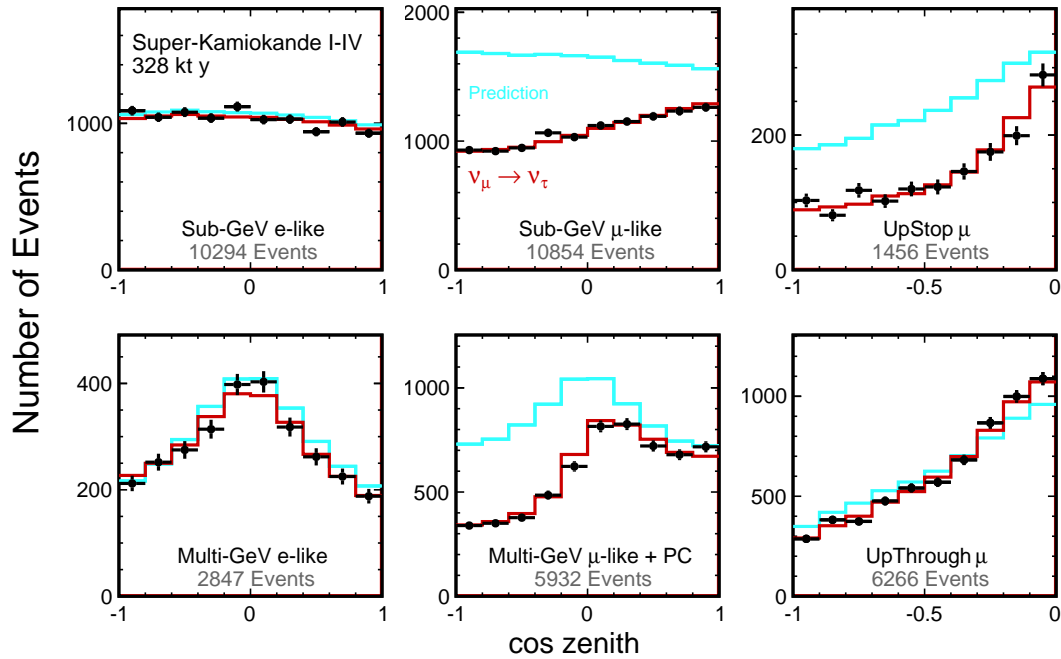


Figure 3.9: Zenith-angle distribution of Super-Kamiokande neutrino events, comparing data (points) to expectations without (blue) and with (red) oscillations. A clear $\nu_\mu/\bar{\nu}_\mu$ disappearance is observed, enhanced for upward-going neutrinos. Events are categorized as Sub-GeV (< 1.33 GeV), Multi-GeV (> 1.33 GeV), or up-going muons (“UpStop”/“UpThrough” from rock interactions, the latter involving higher-energy neutrinos). Figure extracted from [79].

3.3 Reactor Neutrinos

Reactor neutrinos are electron antineutrinos ($\bar{\nu}_e$) produced by power reactors. Nuclear reactors are powerful sources of neutrinos generated in the β decay processes in the fission of ^{235}U , ^{238}U , ^{239}Pu , and ^{241}Pu

$$n \rightarrow p + e^- + \bar{\nu}_e, \quad (3.21)$$

resulting in $\bar{\nu}_e$ with energies in the range $E_{\bar{\nu}_e} \approx 1\text{--}10$ MeV, with flux represented in Fig.3.10. These antineutrinos are emitted isotropically and can be detected in liquid scintillator detectors through the inverse beta decay process:

$$\bar{\nu}_e + p \rightarrow n + e^+. \quad (3.22)$$

From Eq (2.44) we find that the survival probability of $\bar{\nu}_e$ in 3ν mixing reads:

$$P_{\bar{\nu}_e \rightarrow \bar{\nu}_e} = 1 - c_{13}^4 \sin^2 2\theta_{12} \sin^2 \left(\frac{\Delta m_{21}^2 L}{4E} \right) - \sin^2 2\theta_{13} \left[c_{12}^2 \sin^2 \left(\frac{\Delta m_{31}^2 L}{4E} \right) + s_{12}^2 \sin^2 \left(\frac{\Delta m_{32}^2 L}{4E} \right) \right]. \quad (3.23)$$

where the dominant terms depend on the baseline of the experiment. According to that they can be classified as follows:

Short-Baseline (SBL) Reactor Experiments

For baselines $L = \mathcal{O}(10\text{--}100\text{ m})$, these experiments are not sensitive to the standard three-neutrino oscillation framework. Oscillations at such short baselines would indicate

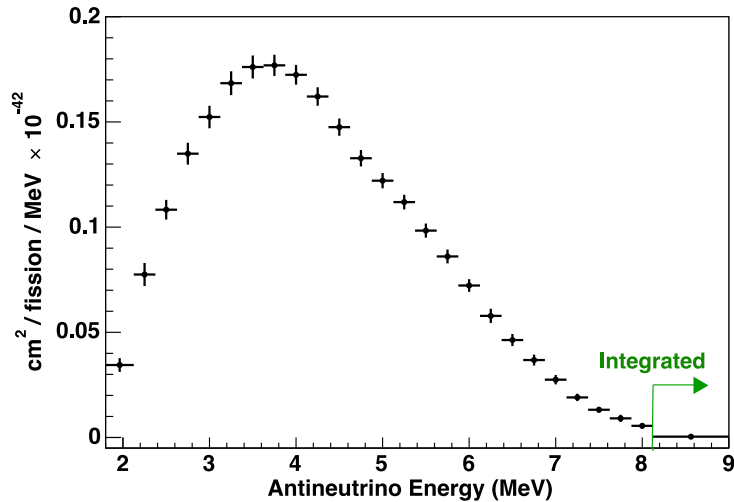


Figure 3.10: Reactor $\bar{\nu}_e$ spectrum, as measured by the Daya Bay collaboration [82].

the existence of a new, sterile neutrino species. Examples include:

- Early experiments: Bugey-3 [83], Goesgen [84], ILL [85],
- Recent experiments: NEOS [86], DANSS [87], PROSPECT [88], STEREO [89].

Medium-Baseline (MBL) Reactor Experiments

For baselines $L = \mathcal{O}(1 \text{ km})$, these experiments are sensitive to Δm_{31}^2 and θ_{13} . Examples include:

- Early experiments: CHOOZ [90], Palo Verde [91],
- Recent experiments: Daya Bay [92–94], RENO [95], Double Chooz [96].

Among the experiments listed, Daya Bay experiment was the most important in the determination of θ_{13} by observing $\bar{\nu}_e$ disappearances at different baselines. Located near the Daya Bay Nuclear Power Plant in China, the experiment has six 20-ton gadolinium-doped liquid scintillator detectors that registered the IBD reactions resulting from the interaction of reactor antineutrinos with protons. In 2012, the Daya Bay collaboration announced the discovery of a non-zero value of θ_{13} with more than 5σ significance, a significant milestone in neutrino physics. The results from the Daya Bay experiment [93, 94] are critical because a non-zero θ_{13} is a necessary condition for the investigation of CP violation in the lepton sector by future LBL neutrino experiments. Their measurement of $|\Delta m_{31}^2|$, complementary to that of atmospheric (and long-baseline) experiments is also an essential input for the determination of the neutrino mass ordering as we will see in the next chapter.

Long-Baseline (LBL) Reactor Experiments

For baselines $L = \mathcal{O}(100 \text{ km})$, these experiments are sensitive to Δm_{21}^2 , θ_{12} , and θ_{13} , similar to solar neutrino experiments. Until now, there is only one experiment of this type, called Kamioka Liquid Scintillator Antineutrino Detector (KamLAND) [97], located in the Kamioka mine. KamLAND detects antineutrinos from multiple reactors across Japan and South Korea, with baselines ranging from 80 km to 800 km and an effective baseline of 180 km. Data from KamLAND confirm the oscillation of neutrinos in vacuum

with parameters as observed in solar neutrino experiments. In terms of precision it outperforms solar neutrino measurements in constraining Δm_{21}^2 . In the very near future the forthcoming experiment JUNO (presently under advanced construction) will observe neutrinos at about $L = \mathcal{O}(50 \text{ km})$ baseline, measuring the solar parameters Δm_{21}^2 and θ_{12} with unprecedented precision while also aiming at a complete determination of Δm_{31}^2 in both magnitude and sign.

3.4 Accelerator Neutrinos

In accelerator-based experiments, a high-energy proton beam collides with a target composed of a light material. These collisions produce mesons such as π , K , and heavier mesons (depending on the energy of the incoming proton beam) which then decay producing neutrinos and antineutrinos in a way similar to the chain in Eq.(3.19). In the accelerator beam line after the target, there is a vacuum space known as the decay pipe, allowing these mesons to decay in-flight into neutrinos. Following the decay pipe, a heavy material, called the dump, is used to stop all remaining particles. In the dump, mesons decay predominantly at rest, ensuring that only neutrinos survive beyond this point. Furthermore, a magnetic field can be used to discard negative or positive pions, generating a beam of muon neutrinos or antineutrinos, respectively. This allows exploring matter effects and CP violation, that affect differently neutrinos and antineutrinos.

Accelerator-produced neutrinos have typical energies $\mathcal{O}(\sim \text{GeV})$. The orientation of the detector with respect to the beam can be exploited to enhance the beam in a narrow range of energies.

Based on the distance between the neutrino source and the detector, accelerator experiments are categorized as Short-Baseline (SBL) or Long-Baseline (LBL):

- **Short-Baseline (SBL):** Baselines on the order of $0.01 - 1 \text{ km}$.
- **Long-Baseline (LBL):** Baselines in the range $100 - 1300 \text{ km}$.

SBL accelerator experiments are not sensitive to the standard three-neutrino oscillation framework. Oscillations at such short baselines would indicate the existence of a new, sterile neutrino species. In the context of 3ν analysis they play a critical role in constraining systematic uncertainties in neutrino-nucleus interactions.

In brief, generically accelerator neutrino experiments typically employ two detectors:

- **Near Detector (ND):** Positioned a few hundred meters from the target to measure the unoscillated flux and reduce energy-dependent systematic uncertainties. These detectors are also themselves capable of studies of SBL physics.
- **Far Detector (FD):** Placed hundreds of kilometers from the target to measure neutrino oscillations. Combined with the ND, they form the usual structure of LBL experiments.

The number of neutrino events of flavour α , N_{ν_α} , observed at each detector can be approximated as:

$$N_{\nu_\beta} \sim \phi_{\nu_\mu} \times P_{\nu_\mu \rightarrow \nu_\alpha} \times \sigma_{\nu_\beta}, \quad (3.24)$$

where ϕ_{ν_μ} is the neutrino flux, $P_{\nu_\mu \rightarrow \nu_\alpha}$ is the oscillation probability, and σ_{ν_β} is the cross-section for neutrinos of flavour β . The oscillation probability can be extracted using:

$$P_{\nu_\mu \rightarrow \nu_\beta} \simeq \frac{N_\beta^{\text{far}}}{N_\mu^{\text{near}}} \cdot \frac{\phi_{\nu_\mu}^{\text{near}}}{\phi_{\nu_\mu}^{\text{far}}} \cdot \frac{\sigma_{\nu_\mu}}{\sigma_{\nu_\beta}}. \quad (3.25)$$

This method reduces systematic uncertainties related to flux and cross-sections. As mentioned above, far Detectors can be placed on-axis (aligned with the beam) or off-axis (displaced from the beam line). Off-axis configurations reduce background but also decrease neutrino flux. Another method that accelerators use to reduce systematic effects is by studying separately two types of events: Neutral Current (NC) and Charged Current (CC) interactions. CC events, where the neutrino transfers its flavor (e.g., $\nu_\mu \rightarrow \mu^-$), are used to directly measure oscillations. NC events, which are flavor-blind (e.g., $\nu_x + N \rightarrow \nu_x + X$), provide a flux normalization sample, as their rate is unaffected by oscillations. By comparing NC rates between near and far detectors, experiments constrain flux and cross-section uncertainties, isolating true oscillation signals in CC channels.

3.4.1 Long-Baseline (LBL) Experiments

As mentioned above, in an LBL experiment neutrinos are detected after crossing distances of $\mathcal{O}(100 \text{ km})$. The most important experiments in this field are the NuMI Off-Axis ν_e Appearance (NOvA) experiment [98, 99], the Tokai-to-Kamioka (T2K) experiment [100–102] and MINOS [103, 104].

- **MINOS [103, 104]:** Used the 120 GeV NUMI beam at Fermilab. The far detector was located 735 km away, on-axis and underground to mitigate cosmic ray backgrounds.
- **NOvA [98, 99]:** NOvA is a second-generation long-baseline neutrino experiment at Fermilab [99] with a detection baseline of 810 km. Below we give more details of our simulation and analysis of NOvA.
- **T2K [100–102]:** Utilizes the muon neutrino beam at the J-PARC facility in Tokai, which is then directed (off-axis) towards the Super-Kamiokande detector located 295 km away.

In these experiments, neutrinos traverse a nearly constant layer of matter, enabling the study of matter effects. The dominant contributions to the $\nu_\mu/\bar{\nu}_\mu$ (disappearance probability-**dis**) $P_{\mu\mu}$ in 3ν scenario is

$$P_{\mu\mu} \approx 1 - \sin^2 2\theta_{23} \sin^2 \left(\frac{\Delta m_{32}^2 L}{4E} \right) + (\text{subdominant } \Delta m_{21}^2 \text{ terms}). \quad (3.26)$$

For $\nu_e/\bar{\nu}_e$ (appearance probability-**app**) $P_{\mu e}$:

$$P_{\mu e} = \sin^2 \theta_{23} \sin^2 2\theta_{13} \frac{\sin^2 \Delta (1 - A)}{(1 - A)^2} \pm \alpha \cos \theta_{13} \sin 2\theta_{13} \sin 2\theta_{23} \sin 2\theta_{12} \\ \times \cos(\Delta + \delta_{CP}) \frac{\sin \Delta A \sin \Delta (1 - A)}{A (1 - A)} + \text{other terms } \mathcal{O}(\alpha^2) \quad (3.27)$$

where $\Delta = \Delta m_{31}^2 \frac{L}{4E_\nu}$, $\alpha \equiv \Delta m_{21}^2 / \Delta m_{31}^2$, and the + (−) sign correspond to ν ($\bar{\nu}$). Matter effects ($A \propto \pm \sqrt{2} G_F n_e$, + for ν , − for $\bar{\nu}$) induce a $\sim 510\%$ correction in NOvA due to its longer baseline. They enhance (suppress) $P_{\mu e}$ for normal (inverted) mass ordering. T2K, on the contrary, is largely vacuum-dominated making it more sensitive to δ_{CP} -driven $\nu/\bar{\nu}$ asymmetry.

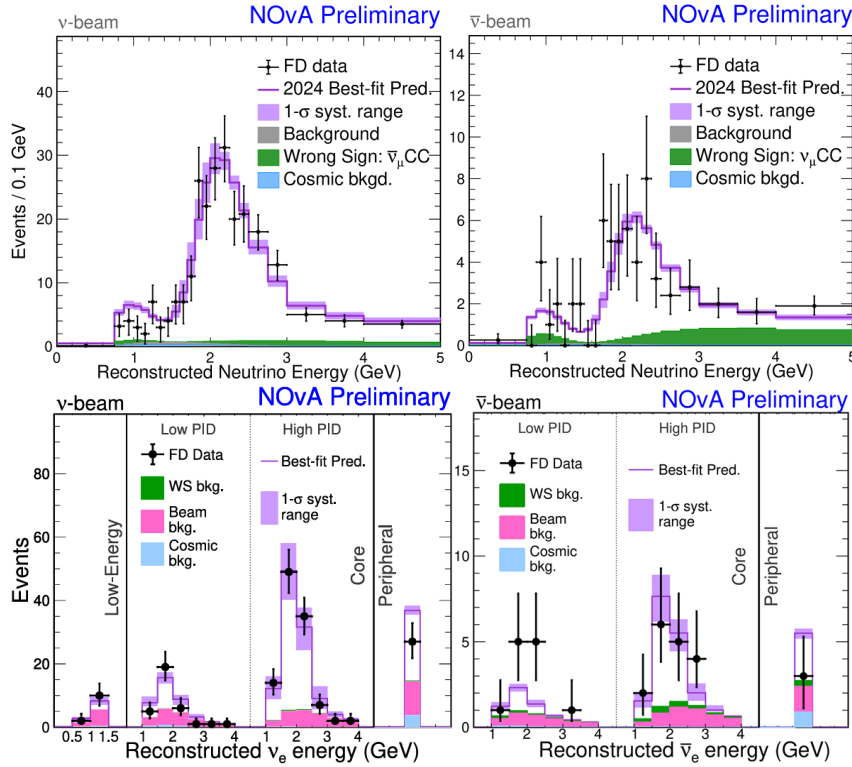


Figure 3.11: NOvA results as of June 2024 on ν_μ and $\bar{\nu}_\mu$ disappearance (upper panels) and ν_e and $\bar{\nu}_e$ appearance. The appearance events are classified in three bins from lowest to highest purity: Peripheral, Low PID, and High PID. Extracted from Ref.[98]

3.4.2 Simulation of Nova

Compared to the case of solar neutrinos, the analysis of NOvA is relatively simpler. Using the formalism for LBL described above for CC interactions, we will perform a χ^2 -analysis in order to obtain the confidence level regions for the oscillation parameters. In general, we define the number of expected events in a given energy bin i and for a given channel α ($\alpha \in \{\nu_\mu, \nu_e, \bar{\nu}_\mu, \bar{\nu}_e\}$). This can generically be calculated as

$$N_i^\alpha = N_{\text{bkg},i} + \int_{E_i}^{E_{i+1}} dE_{\text{rec}} \int_0^\infty dE_\nu R(E_{\text{rec}}, E_\nu) \varepsilon(E_\nu) \sum_\beta \frac{d\Phi^\beta}{dE_\nu} P_{\nu_\beta \rightarrow \nu_\alpha}(E_\nu) \sigma_\alpha(E_\nu), \quad (3.28)$$

where

- $N_{\text{bkg},i}$ is the number of background events in that bin. If there is a neutrino component in the background, its oscillation has to be consistently included.
- $[E_i, E_{i+1}]$ are the bin limits.
- E_{rec} is the reconstructed neutrino energy.
- E_ν is the true neutrino energy.
- $R(E_{\text{rec}}, E_\nu)$ is the energy reconstruction function: the probability to observe a reconstructed energy E_{rec} if the true neutrino energy is E_ν . We usually take it to be Gaussian, i.e.,

$$R(E_{\text{rec}}, E_\nu) = \frac{1}{\sqrt{2\pi}\sigma_E E_\nu} \exp\left[-\frac{1}{2\sigma_E^2} \left(\frac{E_\nu - E_{\text{rec}}}{E_\nu}\right)^2\right]. \quad (3.29)$$

That is, $\frac{E_\nu - E_{\text{rec}}}{E_\nu}$ is Gaussian-distributed around zero with standard deviation σ_E . The $\frac{1}{E_\nu}$ prefactor is for normalisation purposes.

- ε is the detection efficiency.
- $\frac{d\Phi^\beta}{dE_\nu}$ is the incident neutrino flux with flavour β .
- $P_{\nu_\beta \rightarrow \nu_\alpha}(E_\nu)$ is the $\nu_\beta \rightarrow \nu_\alpha$ transition probability, with the Earth's crust density assumed as constant at 2.76 g/cm^3 , with matter composed of equal proton and neutron densities.
- σ_α is the ν_α detector cross section.

The antineutrino channels are obtained by switching ν to $\bar{\nu}$. The incident flux of muon (anti)neutrinos, background events and energy resolutions are provided by the collaboration, extracting information from Ref. [98]. The scattering cross section between the neutrinos and nuclear targets (for the case of NOvA, Hydrocarbons) is provided by the collaboration, too.

The analysis procedure commenced with the unoscillated event distribution from a collaboration-provided benchmark point. Predictions were subsequently reweighted to match the official collaboration spectra through iterative adjustments of detection efficiencies, ensuring consistency with the expected oscillated event rates.

For the analyses, a priori there are three nuisance parameters associated to systematic uncertainties for each channel (**DIS** and **APP**): a signal normalisation factor $\eta_1 \equiv \eta_s$, a background normalisation factor $\eta_2 \equiv \eta_b$, and an absolute energy scale uncertainty $\eta_3 \equiv \rho$, all of them centred around 1. In that case, the prediction N_i^α for a given energy bin $[E_\nu^i, E_\nu^{i+1}]$ is given by

$$N_i^\alpha = \eta_b N_{\text{bkg},i} + \eta_s \int_{\rho E_i}^{\rho E_{i+1}} dE_{\text{rec}} \int_0^\infty dE_\nu R(E_{\text{rec}}, E_\nu) \varepsilon(E_\nu) \sum_\beta \frac{d\Phi^\beta}{dE_\nu} P_{\nu_\beta \rightarrow \nu_\alpha}(E_\nu) \sigma_\alpha(E_\nu), \quad (3.30)$$

The observed number of events per bin i and neutrino flavor α , n_i^α , as well as the nuisance parameters θ_j , are assumed to be independent. The χ^2 statistic can be written as (for each channel):

$$\chi_\alpha^2 = 2 \sum_i \left(n_i^\alpha + N_i^\alpha \ln \frac{n_i^\alpha}{N_i^\alpha} \right) + \sum_j \frac{(\eta_j - 1)^2}{\sigma_j^2}, \quad (3.31)$$

where the logarithmic term is taken to be zero if $n_i = 0$. σ_j are the systematic uncertainties of the nuisance parameters. These parameters were calibrated to replicate reported confidence intervals through χ^2 minimization. The statistical minimization employed a dual-methodology approach: Bayesian parameter estimation and evidence calculation were performed using the MULTINEST algorithm [105, 106], while frequentist optimization utilized the Nelder-Mead simplex implementation from the GNU Scientific Library (GSL) [107]. This hybrid strategy ensured robust convergence across parameter space landscapes while maintaining computational efficiency.

Using the $\nu/\bar{\nu}$ beam data and background estimates from Fig. 3.11, the framework simultaneously analysed appearance and disappearance channels. All oscillation parameters except Δm_{32}^2 , $\sin^2 \theta_{23}$, and δ_{CP} were fixed to central values from Ref. [1]. The resulting confidence contours (Fig. 3.12) demonstrate qualitative agreement with NOvA's official

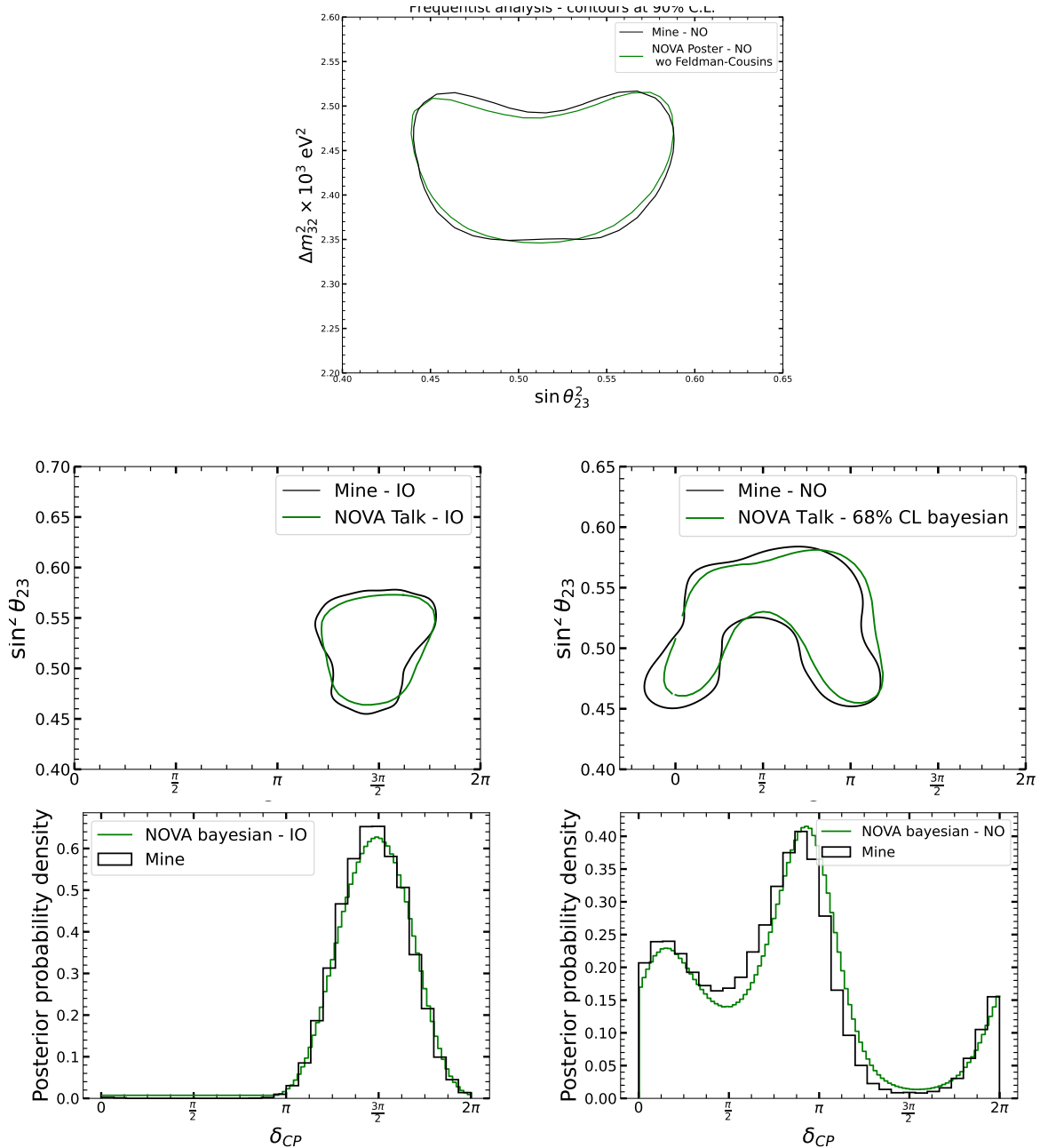


Figure 3.12: Validation of our simulation of NOvA. Each figure represents in green the information released by the collaboration in Ref. [98] while in black the corresponding results obtained with our simulations.

results, with residual quantitative discrepancies attributable to approximations in energy scale systematics and efficiency modeling. The framework’s robustness was further verified through spectrum morphology checks at best-fit parameter values.

3.5 CEνNS

Coherent Elastic Neutrino-Nucleus Scattering (CEνNS) is a neutral-current weak interaction process where low-energy neutrinos scatter elastically off entire atomic nuclei. The coherence condition, satisfied when the momentum transfer $|q| \ll 1/R$ (with R being

the nuclear radius), enables constructive interference of scattering amplitudes from individual nucleons. This results in a cross-section enhancement proportional to the square of the neutron number N^2 , making heavy nuclei ideal targets. SM predicts the differential cross-section as:

$$\frac{d\sigma_{\nu N}}{dT} \approx \frac{G_F^2 M}{4\pi} [N - (1 - 4\sin^2\theta_W)Z]^2 \left(1 - \frac{MT}{2E_\nu^2}\right) |F_{\text{weak}}(q)|^2, \quad (3.32)$$

where G_F is the Fermi coupling constant, M the nuclear mass, T the nuclear recoil energy, E_ν the neutrino energy, and N (Z) the neutron (proton) number. $F_{\text{weak}}(q)$ is the weak nuclear form factor and is dominated by neutron contributions. The recoil energies (sub-keV to keV) and low neutrino fluxes at suitable sources posed significant detection challenges until the COHERENT collaboration's landmark 2017 observation using a 14.6 kg CsI[Na] scintillator at the Spallation Neutron Source (SNS) [108], forty-three years after Freedman's theoretical proposal [109].

Spallation sources like SNS provide pulsed π^+ -decay-at-rest neutrinos with energies $\lesssim 50$ MeV, satisfying the coherence condition while enabling background suppression via timing cuts. In addition to spallation sources, CE ν NS is also searched for in experiments using electron antineutrinos from nuclear reactors, including TEXONO [110], GeN [111], CONNIE [112], MINER [113], Ricochet [114], ν -cleus [115], RED-100 [116], NEON [117], CONUS [118], and NCC-1701 at Dresden-II [119]. To date, most reactor-based experiments have not yet achieved definitive CE ν NS detection. The exception is the NCC-1701 experiment at the Dresden-II reactor, which reported an event spectrum with a low-energy excess in its first published data [119], consistent with SM CE ν NS predictions. Recently, the collaboration released updated results with increased exposure, observing CE ν NS with *strong* to *very strong* statistical preference (relative to a background-only hypothesis) in a Bayesian framework, depending on the assumed quenching factor [120].

CE ν NS processes provide unique nuclear structure insights through sensitivity to neutron distributions, inaccessible via electromagnetic probes [121], constraints on non-standard neutrino interactions (NSI) [122], neutrino electromagnetic properties [123], sterile neutrinos [124], and hidden-sector particles [125].

3.6 Gallium Source Experiments

It is almost two decades since the so-called *Gallium Anomaly* [126, 127] became a standing puzzle in neutrino physics. In general terms, the anomaly accounts for the deficit of the event rate measured in Gallium source experiments with respect to the expectation. It was originally observed in the calibration of the gallium solar-neutrino detectors GALLEX [56, 128] and SAGE [129, 130] with radioactive ^{51}Cr and ^{37}Ar sources:



Using the detection cross section as predicted by Bahcall [131], the average ratio of observed vs predicted rates was found to be $R_{\text{GALLEX+SAGE}} = 0.88 \pm 0.05$ [130], which represented a 2.4σ statistically significant deficit. Most interestingly the Gallium Anomaly has been recently rechecked by the BEST experiment [132, 133], which placed the ^{51}Cr radioactive source at the center of a concentric two-zone gallium target (thus effectively probing two distinctive neutrino path lengths, of about 0.5 m and 1.1 m). In both zones they observe consistent deficits of $R_{\text{in}} = 0.79 \pm 0.05$ and $R_{\text{out}} = 0.77 \pm 0.05$ [132, 133], so the current combined level of the deficit is $R_{\text{GALLEX+SAGE+BEST}} = 0.80 \pm 0.05$ [132, 133] promoting the statistical significance of the anomaly beyond 4σ .

Careful scrutiny [134, 135] of the neutrino capture cross sections and its uncertainties does not provide an explanation of the deficit, leaving open a possible effect in the neutrino propagation. The idea that ν_e may disappear during propagation from source to detector is no surprise nowadays, as the phenomenon of mass-induced neutrino flavour oscillations has been established beyond doubt (see for example the review in Ref. [136]) and the involved masses and mixing are being determined with increasing accuracy by the combined results of solar, reactor, atmospheric and long-baseline neutrino experiments (see Ref. [27] for the latest global analysis). Unfortunately, it is precisely such accuracy which puts in jeopardy the possible interpretation of the Gallium anomaly in terms of neutrino oscillations. Given the characteristic baseline $\mathcal{O}(\text{meter})$ of the GALLEX, SAGE, and BEST radioactive source experiments and their average neutrino energy $\mathcal{O}(\text{MeV})$, a $\Delta m^2 \gtrsim \mathcal{O}(\text{eV}^2)$ is required to produce visible effects, and this is more than two orders of magnitude larger than what is indicated by the global analysis. Hence at least a fourth massive state must be involved in the propagation of the neutrino ensemble with mass $m_4 \sim \mathcal{O}(\text{eV})$. This in turn requires the introduction of a fourth neutrino weak eigenstate, which must be an $SU(2)$ singlet to comply with the bounds from the Z invisible width [136]. This is how the light sterile neutrino scenario makes its entrance, but in order to explain the Gallium anomaly in such a way, the fourth state must significantly mix with the three standard neutrinos, $\sin^2 \theta \sim \mathcal{O}(10)\%$.

The problem is that such large mixing would impact heavily the oscillation signals included in the global analysis. This results in a strong tension between the sterile-neutrino interpretation of the Gallium anomaly and other neutrino data [137–139]. In particular solar neutrinos and reactor antineutrinos provide a clean test of the possible projection of ν_e and $\bar{\nu}_e$ on a $\mathcal{O}(\text{eV})$ massive state. Given the long baselines and the energies involved, the oscillations driven by $\Delta m^2 \sim \mathcal{O}(\text{eV}^2)$ are averaged in both solar and KamLAND experiments so they directly test the mixing relevant for the interpretation of the Gallium anomaly. The analyses presented in Refs. [138, 139] lead to 2σ bounds $\sin^2 \theta \lesssim 0.025\text{--}0.045$ of the corresponding mixing angle, clearly disfavoring the sterile oscillation interpretation of the Gallium anomaly. Alternative non-conventional scenarios have also been considered (see for example Refs. [140–144]), but they are nevertheless not free from severe tension with other data [145].

3.7 Summary

In this chapter we have briefly presented the neutrino oscillation experiments performed with neutrinos produced in the Sun (Sec. 3.1), in the atmosphere (Sec. 3.2), at nuclear reactors (Sec. 3.3) and at dedicated accelerator beams (Sec. 3.4). They have robustly confirmed the three-neutrino mixing scenario. For convenience we compile in Table 3.1 the different experiments which contribute to the determination of the 3ν oscillation parameters.

The global interpretation of this bulk of data is in the hands of phenomenological groups and in the next chapter we will present the results of the last analysis of NuFIT. Analysis of this data has also been used to constrain other forms of new physics as we will present in the subsequent chapters. Paramount to this type of work is the precise simulation of the experiments and the consistent statistical analysis of their data. On that front, the work in this thesis contains the original contributions to the analysis of the solar neutrino results from the phases-II and III of Borexino and of the accelerator neutrino experiment NOvA which have been described in detail in Secs. 3.1.1 and 3.4.2 respectively.

Experiment	Dominant	Important
Solar Experiments	θ_{12}	$\Delta m_{21}^2, \theta_{13}$
Reactor LBL (KamLAND)	Δm_{21}^2	θ_{12}, θ_{13}
Reactor MBL (Daya-Bay, Reno, D-Chooz)	$\theta_{13}, \Delta m_{31,32}^2 $	$\theta_{23}, \Delta m_{31,32}^2 , \theta_{13}, \delta_{\text{CP}}$
Atmospheric Experiments (SK, IC-DC)		
Accel LBL $\nu_\mu, \bar{\nu}_\mu$, Disapp (K2K, MINOS, T2K, NO ν A)	$ \Delta m_{31,32}^2 , \theta_{23}$	
Accel LBL $\nu_e, \bar{\nu}_e$ App (MINOS, T2K, NO ν A)	δ_{CP}	θ_{13}, θ_{23}

Table 3.1: Summary of experiments contributing to the present determination of the oscillation parameters in the 3ν framework (table taken from Ref. [79]).

We close this chapter with a short description of two additional experimental inputs which are also relevant to the work presented in the following chapters. In Section 3.5, we introduced CE ν NS measurements which we later on will employ in Sections 5.1.2 and 6.2 to bound new physics that could add any contribution to the SM predictions at the scattering level via neutral-current processes. In Section 3.6 we added the results from source experiments in gallium detectors which are a persistent puzzle that we will address in Section 7.2.

Chapter 4

Global analysis of Three neutrino oscillations

In Chapter 3, we discussed the role of the neutrino experiments in the determination of the oscillation parameters. Each experiment, including solar, atmospheric, reactor, and accelerator sources, is able to constrain a specific region of the parameter space. When performing a joint fit of all main experiments, it is expected that such analysis will yield the most stringent determination of the oscillation parameters, as free of degeneracies as presently possible. This is the main goal of a combined fit. The global analysis of neutrino oscillation data provides a comprehensive understanding of the flavor structure of leptons. While experimental collaborations like T2K and NOvA have made strides in combining their data [98], the primary responsibility for global phenomenological analyses still lies with groups like NuFIT[1]. Over the past decade, these studies have consistently shown that mass-driven oscillations between three neutrino states, characterized by different masses and mixing angles, explain the majority of experimental results. Subdominant effects, such as the mass ordering (MO), the maximality of θ_{23} , and leptonic CP violation, remain open questions and are the focus of upcoming experiments like JUNO, DUNE, and Hyper-Kamiokande.

The following chapter is dedicated to presenting the main results of the NuFIT collaboration after the Neutrino 2024 conference. It describes the joint analysis of the main experiments up to this moment. For solar neutrinos, we include constraints from Standard Solar Models [146] and experimental results from the chlorine experiment [147], Gallex/GNO [56] and SAGE [55], as well as spectral measurements from Super-Kamiokande (SK) phases 1 to 4 [60–63], SNO [64], and Borexino Phases I-III [67, 68, 70, 148]. Atmospheric neutrino data include IceCube/DeepCore measurements from IC19 (3-year) [77, 78] and IC24 (9.3-year) [80, 81], along with Super-Kamiokande (SK1-5) results [75, 76]. Reactor neutrino data incorporate KamLAND spectra [97], SNO+ results [149–151], Double Chooz spectral ratios [152], as well as extensive measurements from Daya Bay [93, 94] and Reno [153]. Finally, accelerator neutrino data include MINOS disappearance and appearance channels [103, 104], T2K ν_μ and ν_e appearance and disappearance measurements [100–102], and NOvA results for both neutrino and antineutrino modes [98, 99]. These datasets collectively provide a comprehensive picture of neutrino oscillation parameters.

	Normal Ordering (NO)		Inverted Ordering (IO)	
	bf $\pm 1\sigma$	3σ range	bf $\pm 1\sigma$	3σ range
IC19 wo SK atmospheric data ($\Delta\chi^2 = 0.6$ for NO)				
$\sin^2 \theta_{12}$	$0.307^{+0.012}_{-0.011}$	$0.275 \rightarrow 0.345$	$0.308^{+0.012}_{-0.011}$	$0.275 \rightarrow 0.345$
$\theta_{12}/^\circ$	$33.68^{+0.73}_{-0.70}$	$31.63 \rightarrow 35.95$	$33.68^{+0.73}_{-0.70}$	$31.63 \rightarrow 35.95$
$\sin^2 \theta_{23}$	$0.561^{+0.012}_{-0.015}$	$0.430 \rightarrow 0.596$	$0.562^{+0.012}_{-0.015}$	$0.437 \rightarrow 0.597$
$\theta_{23}/^\circ$	$48.5^{+0.7}_{-0.9}$	$41.0 \rightarrow 50.5$	$48.6^{+0.7}_{-0.9}$	$41.4 \rightarrow 50.6$
$\sin^2 \theta_{13}$	$0.02195^{+0.00054}_{-0.00058}$	$0.02023 \rightarrow 0.02376$	$0.02224^{+0.00056}_{-0.00057}$	$0.02053 \rightarrow 0.02397$
$\theta_{13}/^\circ$	$8.52^{+0.11}_{-0.11}$	$8.18 \rightarrow 8.87$	$8.58^{+0.11}_{-0.11}$	$8.24 \rightarrow 8.91$
$\delta_{CP}/^\circ$	177^{+19}_{-20}	$96 \rightarrow 422$	285^{+25}_{-28}	$201 \rightarrow 348$
$\frac{\Delta m_{21}^2}{10^{-5} \text{ eV}^2}$	$7.49^{+0.19}_{-0.19}$	$6.92 \rightarrow 8.05$	$7.49^{+0.19}_{-0.19}$	$6.92 \rightarrow 8.05$
$\frac{\Delta m_{3\ell}^2}{10^{-3} \text{ eV}^2}$	$+2.534^{+0.025}_{-0.023}$	$+2.463 \rightarrow +2.606$	$-2.510^{+0.024}_{-0.025}$	$-2.584 \rightarrow -2.438$
IC24 w SK atmospheric data ($\Delta\chi^2 = 6.1$ for IO)				
$\sin^2 \theta_{12}$	$0.308^{+0.012}_{-0.011}$	$0.275 \rightarrow 0.345$	$0.308^{+0.012}_{-0.011}$	$0.275 \rightarrow 0.345$
$\theta_{12}/^\circ$	$33.68^{+0.73}_{-0.70}$	$31.63 \rightarrow 35.95$	$33.68^{+0.73}_{-0.70}$	$31.63 \rightarrow 35.95$
$\sin^2 \theta_{23}$	$0.470^{+0.017}_{-0.013}$	$0.435 \rightarrow 0.585$	$0.550^{+0.012}_{-0.015}$	$0.440 \rightarrow 0.584$
$\theta_{23}/^\circ$	$43.3^{+1.0}_{-0.8}$	$41.3 \rightarrow 49.9$	$47.9^{+0.7}_{-0.9}$	$41.5 \rightarrow 49.8$
$\sin^2 \theta_{13}$	$0.02215^{+0.00056}_{-0.00058}$	$0.02030 \rightarrow 0.02388$	$0.02231^{+0.00056}_{-0.00056}$	$0.02060 \rightarrow 0.02409$
$\theta_{13}/^\circ$	$8.56^{+0.11}_{-0.11}$	$8.19 \rightarrow 8.89$	$8.59^{+0.11}_{-0.11}$	$8.25 \rightarrow 8.93$
$\delta_{CP}/^\circ$	212^{+26}_{-41}	$124 \rightarrow 364$	274^{+22}_{-25}	$201 \rightarrow 335$
$\frac{\Delta m_{21}^2}{10^{-5} \text{ eV}^2}$	$7.49^{+0.19}_{-0.19}$	$6.92 \rightarrow 8.05$	$7.49^{+0.19}_{-0.19}$	$6.92 \rightarrow 8.05$
$\frac{\Delta m_{3\ell}^2}{10^{-3} \text{ eV}^2}$	$+2.513^{+0.021}_{-0.019}$	$+2.451 \rightarrow +2.578$	$-2.484^{+0.020}_{-0.020}$	$-2.547 \rightarrow -2.421$

Table 4.1: Three-flavor oscillation parameters from our fit to global data for the two variants of the analysis described in the text. The numbers in the 1st (2nd) column are obtained assuming NO (IO), i.e., relative to the respective local minimum. Note that $\Delta m_{3\ell}^2 \equiv \Delta m_{31}^2 > 0$ for NO and $\Delta m_{3\ell}^2 \equiv \Delta m_{32}^2 < 0$ for IO.

4.1 Global analysis

We start by presenting the results of the NuFIT 6.0 global fit [27], which includes all data available up to September 2024. As is customary in the NuFIT releases since v4.0 [154], there are two versions of the analysis. They differ in the inclusion of some atmospheric neutrino data, for which there is not enough information for us to make an independent fit comparable to that performed by the collaborations. In NuFIT 6.0, this is the case for the atmospheric data from Super-Kamiokande phases 1-5 (SK-atm) and from the latest 9.3-year results from IceCube/DeepCore (IC24). For those, we use their tabulated χ^2 maps provided in Refs. [76] and [81], respectively, which we can combine with our global analysis of solar, reactor and LBL experiments. We note that for IceCube/DeepCore we have performed an independent fit of their previous 3-year atmospheric neutrino data sample [77, 78], which we do include in the version of the analysis without tabulated χ^2 maps. In what follows, we refer as «IC19 w/o SK-atm» to the analysis variant without tabulated χ^2 maps, and as «IC24 with SK-atm» to the one that includes the tabulated SK-atm and IC24 χ^2 maps instead of our 3-year IceCube/DeepCore analysis.

A selection of the results of our global fit are displayed in Fig. 4.1 (one-dimensional $\Delta\chi^2$ curves) and Fig. 4.2 (two-dimensional projections of confidence regions). In Table 4.1 we give the best-fit values as well as 1σ and 3σ confidence intervals for the oscillation parameters in both mass orderings, relative to the local best-fit points in each ordering. Additional figures and tables corresponding to this global analysis can be found in the NuFIT webpage [1].

With these results, we obtain the following 3σ relative precision of each parameter x , defined as $2(x^{\text{up}} - x^{\text{low}})/(x^{\text{up}} + x^{\text{low}})$, where x^{up} (x^{low}) is the upper (lower) bound on x

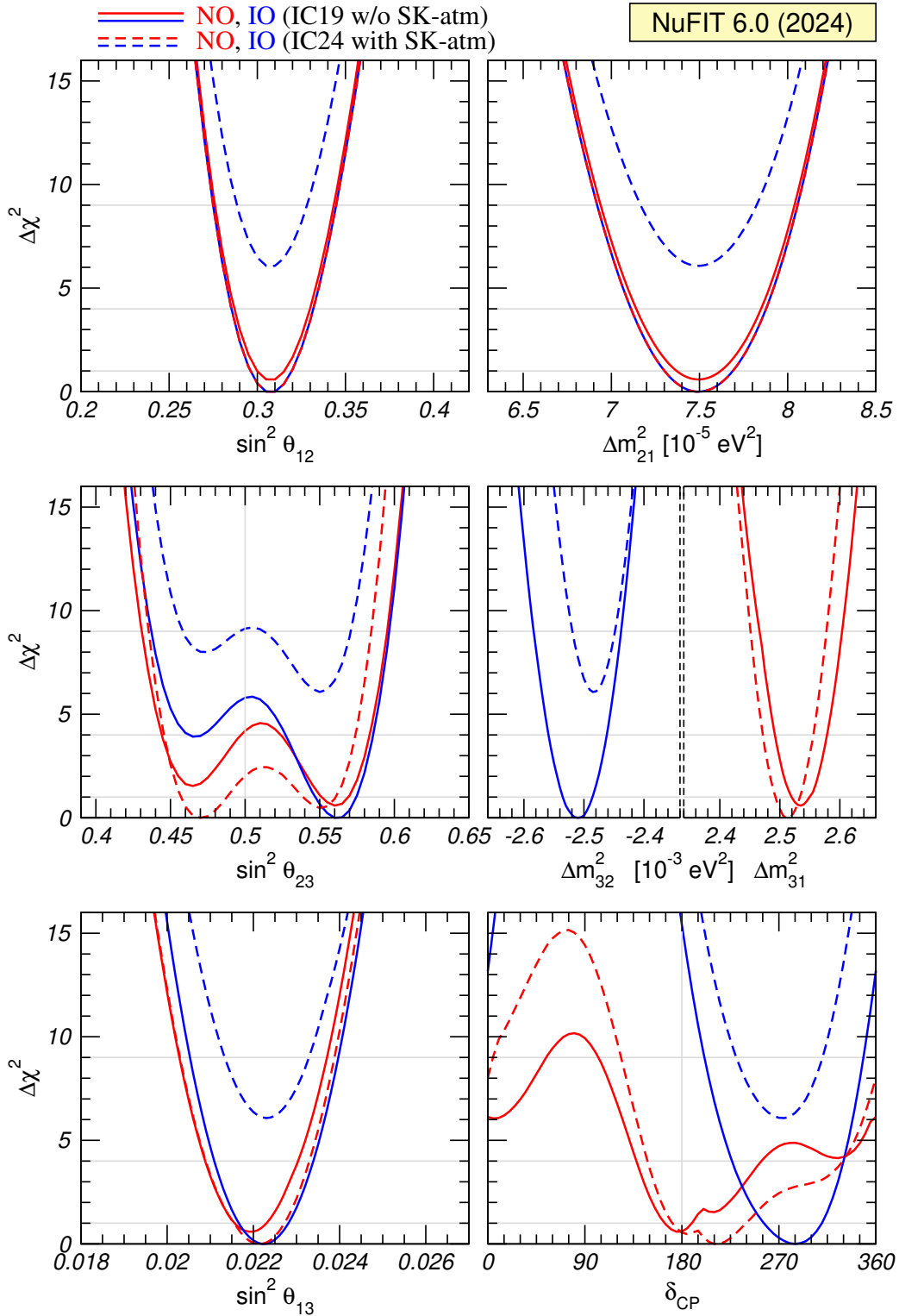


Figure 4.1: Global 3ν oscillation analysis. We show $\Delta\chi^2$ profiles minimized with respect to all undisplayed parameters. The red (blue) curves correspond to Normal (Inverted) Ordering. Solid and dashed curves correspond to the two variants of the analysis as described in the labels.

at the 3σ level:

$$\begin{aligned}
 \theta_{12} : 13\%, \quad \theta_{13} : \begin{cases} \text{NO} & 8.1\% [8.2\%], \\ \text{IO} & 7.8\% [7.9\%], \end{cases} \quad \theta_{23} : \begin{cases} \text{NO} & 21\% [19\%], \\ \text{IO} & 20\% [18\%], \end{cases} \\
 \Delta m_{21}^2 : 15\%, \quad |\Delta m_{3\ell}^2| : \begin{cases} \text{NO} & 5.6\% [5.1\%], \\ \text{IO} & 5.8\% [5.1\%], \end{cases} \quad \delta_{\text{CP}} : \begin{cases} \text{NO} & 100\% [98\%], \\ \text{IO} & 54\% [55\%], \end{cases}
 \end{aligned} \tag{4.1}$$

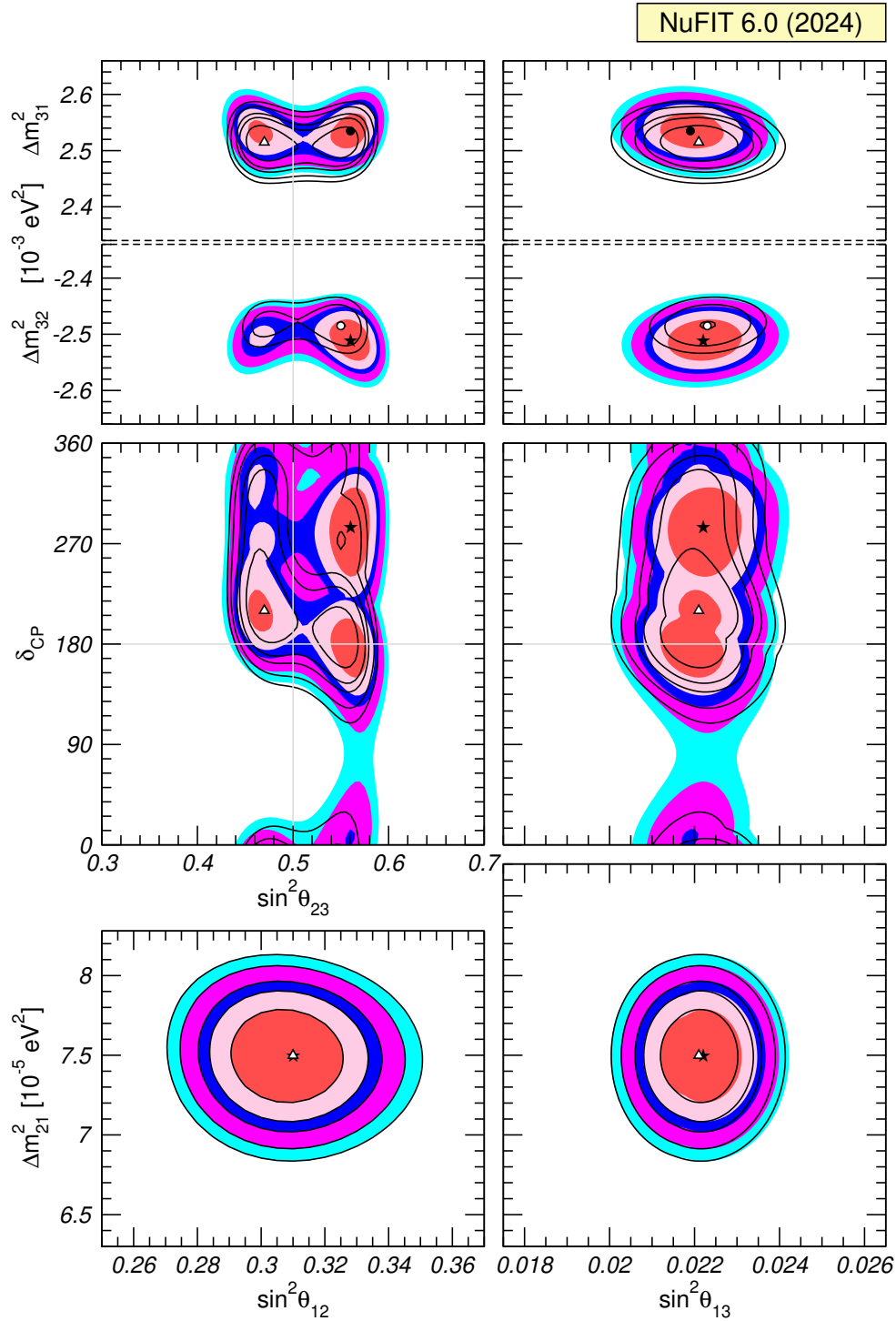


Figure 4.2: Global 3ν oscillation analysis. Each panel shows the two-dimensional projection of the allowed six-dimensional region after minimization with respect to the undisplayed parameters. The regions in the four lower panels are obtained from $\Delta\chi^2$ minimized with respect to the mass ordering. The different contours correspond to 1σ, 90%, 2σ, 99%, 3σ CL (2 dof). Colored regions (black contours) correspond to the variant with IC19 and without SK-atm (with IC24 and with SK-atm).

where the numbers between brackets show the impact of including IC24 and SK-atm. We note that given the non-Gaussianity of $\Delta\chi^2(\delta_{\text{CP}})$, the above estimated precision for δ_{CP} can only be taken as indicative, in particular for NO.

Altogether, we derive the following 3σ ranges on the magnitude of the elements of the leptonic mixing matrix (see Ref. [155] for details on how we derive the ranges and their correlations):

$$\begin{aligned}
 |U|_{3\sigma}^{\text{IC19 w/o SK-atm}} &= \begin{pmatrix} 0.801 \rightarrow 0.842 & 0.519 \rightarrow 0.580 & 0.142 \rightarrow 0.155 \\ 0.248 \rightarrow 0.505 & 0.473 \rightarrow 0.682 & 0.649 \rightarrow 0.764 \\ 0.270 \rightarrow 0.521 & 0.483 \rightarrow 0.690 & 0.628 \rightarrow 0.746 \end{pmatrix} \\
 |U|_{3\sigma}^{\text{IC24 with SK-atm}} &= \begin{pmatrix} 0.801 \rightarrow 0.842 & 0.519 \rightarrow 0.580 & 0.142 \rightarrow 0.155 \\ 0.252 \rightarrow 0.501 & 0.496 \rightarrow 0.680 & 0.652 \rightarrow 0.756 \\ 0.276 \rightarrow 0.518 & 0.485 \rightarrow 0.673 & 0.637 \rightarrow 0.743 \end{pmatrix}
 \end{aligned} \tag{4.2}$$

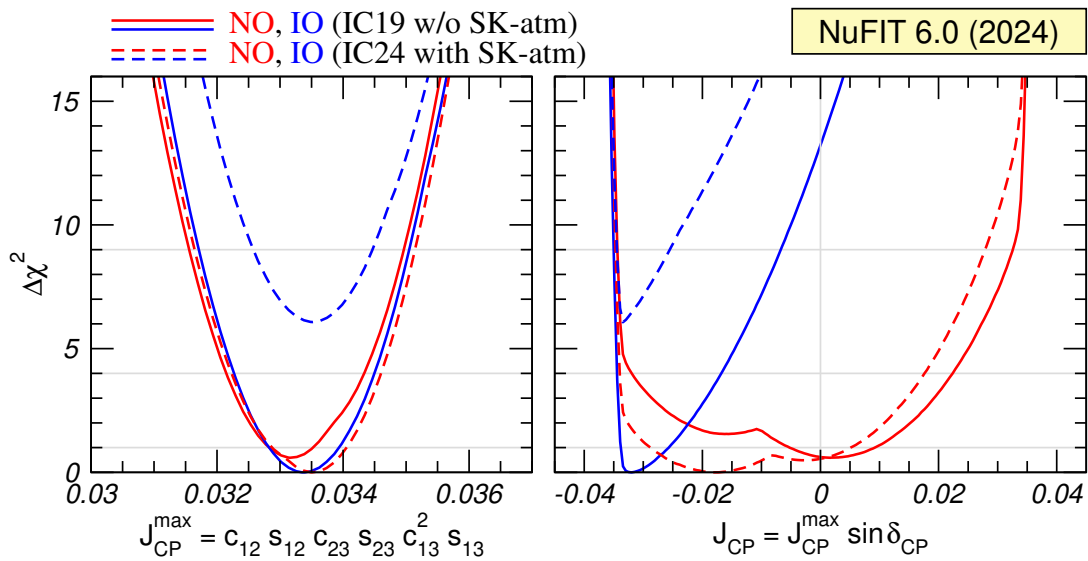


Figure 4.3: Dependence of the global $\Delta\chi^2$ function on the Jarlskog invariant. The red (blue) curves are for NO (IO). Solid (dashed) curves are for the «IC19 w/o SK-atm» («IC24 with SK-atm») $\Delta\chi^2$.

We quantify the presence of leptonic CP violation in vacuum in a convention-independent form in terms of the leptonic Jarlskog invariant in EQs.2.35 and 2.36. Its present determination is shown in Fig. 4.3. While the precise value of J_{CP} —and in particular its deviation from zero—is still highly uncertain, its maximum possible value $J_{\text{CP}}^{\text{max}}$ (which depends solely on the mixing angles and not on δ_{CP}) is now well determined:

$$J_{\text{CP}}^{\text{max}} = 0.0333 \pm 0.0007 (\pm 0.0017) \tag{4.3}$$

at 1σ (3σ) for both orderings. As for J_{CP} itself, the right panel of figure 4.3 shows that in NO the best-fit value $J_{\text{CP}}^{\text{best}} = 0.0017 (-0.018)$ (where the value in parenthesis corresponds to the analysis with IC24 and SK-atm) is only favored over CP conservation $J_{\text{CP}} = 0$ with $\Delta\chi^2 = 0.02$ (0.55). In contrast, in IO CP conservation is disfavored with respect to $J_{\text{CP}}^{\text{best}} = -0.032$ with $\Delta\chi^2 = 13$ (16), which corresponds to 3.6σ (4σ) when evaluated for 1 dof. Let us stress that J_{CP} is totally analogous to the invariant introduced in Ref. [156] for the description of CP-violating effects in the quark sector, presently determined to be $J_{\text{CP}}^{\text{quarks}} = (3.12_{-0.12}^{+0.13}) \times 10^{-5}$ [79].

4.2 Status of neutrino mass ordering, leptonic CP violation, and θ_{23}

4.2.1 Updates from T2K and NOvA

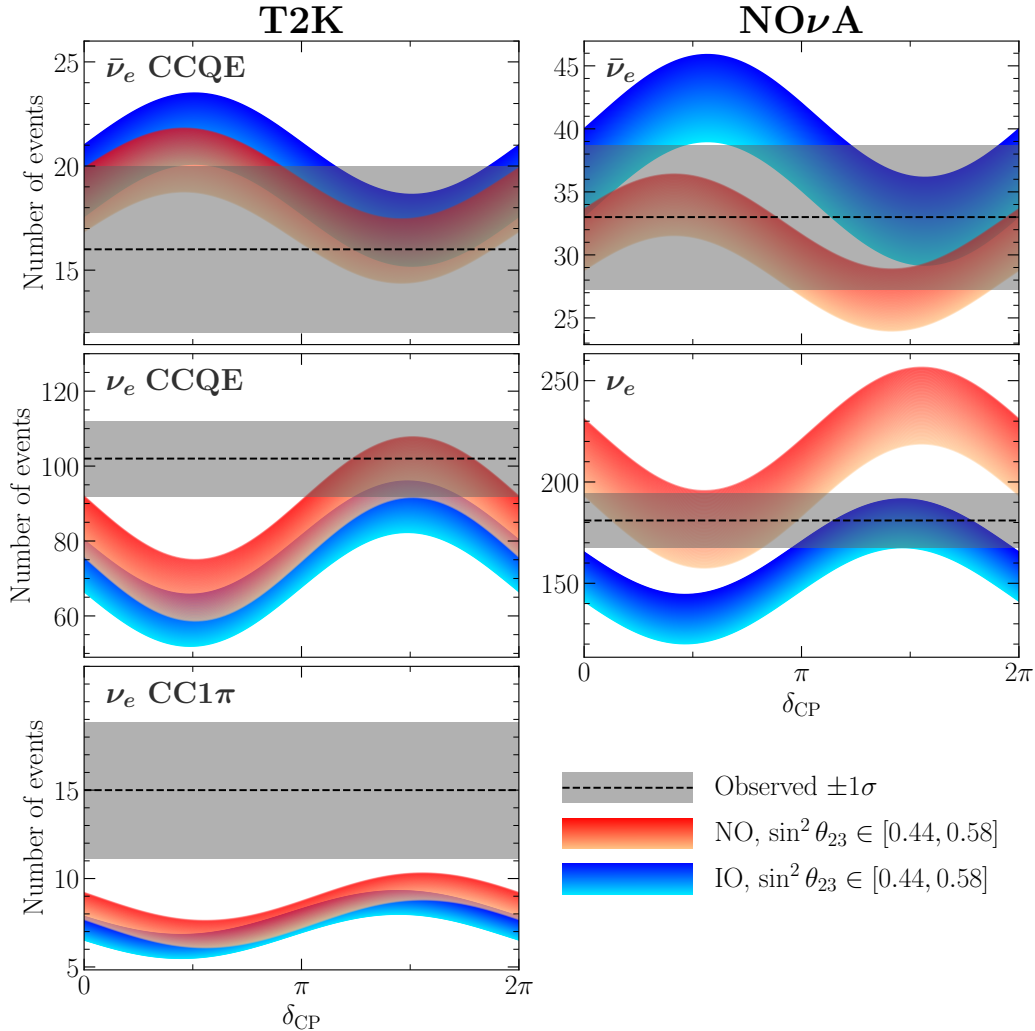


Figure 4.4: Predicted number of events as a function of δ_{CP} for the T2K (left) and NOvA (right) appearance data sets. $\sin^2 \theta_{23}$ varies between 0.44 and 0.58, where the lower-light (upper-dark) bound of the colored bands corresponds to 0.44 (0.58). Red (blue) bands correspond to NO (IO). For the other oscillation parameters we have adopted $\sin^2 \theta_{13} = 0.0222$, $|\Delta m_{3\ell}^2| = 2.5 \times 10^{-3} \text{ eV}^2$, $\sin^2 \theta_{12} = 0.32$, $\Delta m_{21}^2 = 7.5 \times 10^{-5} \text{ eV}^2$. The horizontal dashed lines show the observed number of events, with the $\pm 1\sigma$ statistical error indicated by the gray shaded band.

We analyze the latest data from T2K and NOvA presented at Neutrino 2024. Fig. 4.4 shows the predicted number of events as a function of δ_{CP} for varying $\sin^2 \theta_{23}$ and mass ordering, compared to observations. Predictions are based on numerical simulations, with approximate expressions from Refs. [154, 157] describing the general behavior:

$$N_{\nu_e} \approx \mathcal{N}_\nu \left[2s_{23}^2(1 + 2oA) - C' \sin \delta_{CP}(1 + oA) \right], \quad (4.4)$$

$$N_{\bar{\nu}_e} \approx \mathcal{N}_{\bar{\nu}} \left[2s_{23}^2(1 - 2oA) + C' \sin \delta_{CP}(1 - oA) \right], \quad (4.5)$$

	T2K (ν)			T2K ($\bar{\nu}$)	NOvA (ν)	NOvA ($\bar{\nu}$)
	CCQE	CC1 π	Sum			
\mathcal{N}	54	5	59	13	104	23
N_{obs}	102	15	117	16	181	33
$N_{\text{obs}} - N_{\text{bck}}$	81.6	12.5	94.2	10	117.3	19
$r = \frac{N_{\text{obs}} - N_{\text{bck}}}{\mathcal{N}}$	1.5 (1.6)	2.5 (2.4)	1.59 (1.65)	0.77 (0.61)	1.13 (1.14)	0.83 (0.83)

Table 4.2: Normalization coefficients \mathcal{N}_ν and $\mathcal{N}_{\bar{\nu}}$ for T2K and NOvA appearance samples. Numbers in parentheses correspond to NuFIT 5.0.

where $o \equiv \text{sgn}(\Delta m_{3\ell}^2)$. For T2K, $A \approx 0.05$, while for NOvA, $A = 0.1$ empirically. Setting the oscillation parameters to their global best-fit values, we get $C' \approx 0.28$. normalization constants $\mathcal{N}_{\nu,\bar{\nu}}$ are given in Table 4.2, along with observed events and backgrounds. The ratio $r \equiv N_{\nu_e,\bar{\nu}_e}/\mathcal{N} = (N_{\text{obs}} - N_{\text{bck}})/\mathcal{N}$ provides insights:

- T2K data shows $r > 1$ for neutrinos and $r < 1$ for antineutrinos, favoring $\delta_{\text{CP}} \simeq 3\pi/2$ in NO. This preference, present since early T2K results, remains significant in NuFIT 6.0, strongest in the CC1 π sample.
- NOvA antineutrino results ($r < 1$) are consistent with NO and $\delta_{\text{CP}} \simeq \pi/2$ or IO and $\delta_{\text{CP}} \simeq 3\pi/2$, slightly favoring NO.
- NOvA neutrino results, with 60% more statistics, show $r \sim 1$, compatible with NO and $\delta_{\text{CP}} \simeq \pi/2$ or IO and $\delta_{\text{CP}} \simeq 3\pi/2$, aligning with antineutrino results. NOvA shows only a mild NO preference.
- T2K and NOvA favor different δ_{CP} values in NO, making their combination better described by IO with $\delta_{\text{CP}} \simeq 3\pi/2$, a trend strengthened in NuFIT 6.0.

Fig. 4.5 shows the $\Delta\chi^2$ profiles as a function of δ_{CP} for T2K, NOvA, and their combination, including MBL reactor and IC atmospheric data analyzed in NuFIT 5.0 and NuFIT 6.0 (discussed in Sec. 4.2.2). The NOvA neutrino results disfavor NO and $\delta_{\text{CP}} \simeq 3\pi/2$ by $\Delta\chi^2 \approx 6$ (versus 3 in NuFIT 5.0). For IO, T2K and NOvA show a statistically stronger preference for $\delta_{\text{CP}} \simeq 3\pi/2$. This drives the LBL combination's preference for IO, with $\Delta\chi^2(\text{NO} - \text{IO}) \approx 3.2$ (versus 1.5 in NuFIT 5.0).

The two-dimensional regions for T2K and NOvA in the $(\delta_{\text{CP}}, \sin^2 \theta_{23})$ plane (Fig. 4.6) show better consistency for IO. Unlike NuFIT 5.0, the 1σ regions for NO do not overlap. The global fit projections (Fig. 4.7) closely resemble the T2K+NOvA combination, exhibiting correlations with the MO. For IO, $\delta_{\text{CP}} \simeq 270^\circ$ is highly preferred, whereas NO presents a more complex structure with multiple local minima. The θ_{23} octant degeneracy persists with $\Delta\chi^2 < 4$ for both MOs and data variants, with minima near $\sin^2 \theta_{23} \approx 0.56$ and 0.47.

Then, after the discussion of the absence of overlapping regions for NO, a natural question is how large is the tension between T2K and NOvA. Consistency among different data sets can be quantified with the parameter goodness-of-fit (PG) [158]. For a number N of different data sets i , each depending on n_i model parameters, and globally depending on n_{glob} parameters, it can be shown that the test statistic

$$\chi_{\text{PG}}^2 \equiv \chi_{\text{min, glob}}^2 - \sum_i^N \chi_{\text{min, } i}^2 = \min \left[\sum_i^N \chi_i^2 \right] - \sum_i \chi_{\text{min, } i}^2, \quad (4.6)$$

follows a χ^2 distribution with $n \equiv \sum_i n_i - n_{\text{glob}}$ degrees of freedom [158].

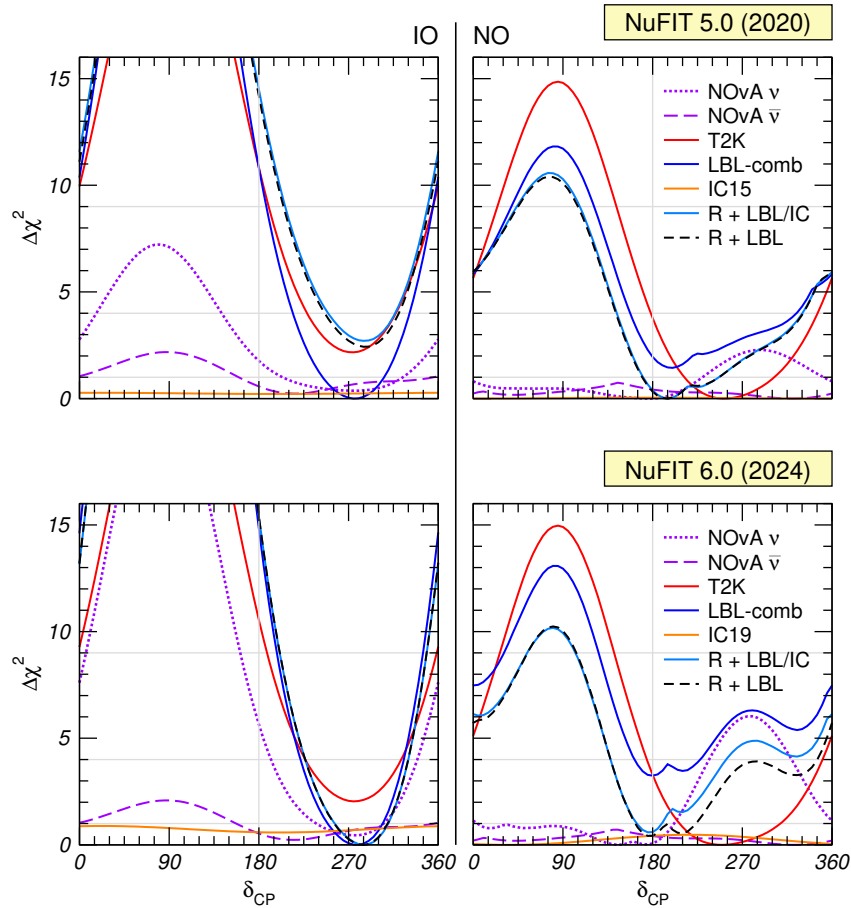


Figure 4.5: $\Delta\chi^2$ profiles as a function of δ_{CP} for different data sets and combinations as labeled in the figure. In the curves where the reactors R are not included in the combination we have fixed $\sin^2\theta_{13} = 0.0222$ as well as the solar parameters and minimized with respect to θ_{23} and $|\Delta m_{3\ell}^2|$. When the reactors are included θ_{13} is also marginalized. Left (right) panels are for IO (NO) and $\Delta\chi^2$ is shown with respect to the global best-fit point for each curve. Upper panels are for the NuFIT 5.0 data set, whereas lower panels correspond to the current update.

Applying this test to the full NOvA and T2K samples (including both appearance and disappearance data for neutrinos and antineutrinos) we obtain the values in Table 4.3. We carry out the analysis separately for each mass ordering, in all cases fixing Δm_{21}^2 and θ_{12} to their best fit. In the results reported in the upper part of the table θ_{13} is varied in the minimization, so $n_{\text{T2K}} = n_{\text{NOvA}} = n_{\text{glob=T2K+NOvA}} = 4$ (i.e., $\Delta m_{3\ell}^2$, θ_{23} , δ_{CP} , and θ_{13}). In the lower part θ_{13} is kept fixed to its best fit so $n_{\text{T2K}} = n_{\text{NOvA}} = n_{\text{glob=T2K+NOvA}} = 3$. From the table we read that, as expected, agreement is better in IO, where irrespective on θ_{13} the samples are compatible at the 0.5σ level or better. In NO, compatibility arises at 1.7σ (2.0σ) for free (fixed) θ_{13} . This is to be compared with the NuFIT 5.0 results of 1.4σ (1.7σ) respectively. We conclude that the tension between T2K and NOvA in NO has slightly strengthened with the new results, reaching at most the 2σ level.

4.2.2 Effects from $\nu_\mu/\bar{\nu}_\mu$ versus $\bar{\nu}_e$ disappearance

Figure 4.8 illustrates the determination of $\sin^2\theta_{23}$, $\sin^2\theta_{13}$, and $\Delta m_{3\ell}^2$ using different neutrino disappearance channels: $\nu_\mu/\bar{\nu}_\mu$ disappearance from long-baseline (LBL) accelerator and atmospheric data (left panel) and $\bar{\nu}_e$ disappearance from reactor experiments (right panel). The combination of these datasets demonstrates a strong synergy, as the global

Data sets	Normal Ordering			Inverted Ordering		
	χ^2_{PG}/n	p -value	$\#\sigma$	χ^2_{PG}/n	p -value	$\#\sigma$
T2K vs NOvA	7.9/4	0.093	1.7	2.3/4	0.67	0.42
T2K vs React	0.23/2	0.89	0.14	1.7/2	0.43	0.79
NOvA vs React	1.1/2	0.58	0.56	4.3/2	0.12	1.6
T2K vs NOvA vs React	8.6/6	0.20	1.3	6.0/6	0.42	0.80
(T2K & NOvA) vs React	0.76/2	0.68	0.41	3.4/2	0.18	1.3
T2K vs IC19	2.7/4	0.61	0.51	1.2/4	0.88	0.15
NOvA vs IC19	3.3/4	0.51	0.66	2.3/4	0.68	0.41
React vs IC19	2.1/2	0.35	0.93	0.88/2	0.64	0.84
NOvA vs T2K vs IC19	11/8	0.20	1.3	4.3/8	0.83	0.21
NOvA vs T2K vs React vs IC19	11.5/10	0.33	0.96	7.2/10	0.71	0.38
T2K vs NOvA	8.0/3	0.045	2.0	1.8/3	0.61	0.50
T2K vs NOvA vs React	8.3/4	0.081	1.7	4.1/4	0.39	0.85
(T2K & NOvA) vs React	0.25/1	0.62	0.50	2.0/1	0.16	1.4
T2K vs IC19	0.72/3	0.86	0.16	0.2/3	0.98	0.028
NOvA vs IC19	1.5/3	0.68	0.41	1.0/3	0.80	0.25
NOvA vs T2K vs IC19	9.3/6	0.16	1.4	2.4/6	0.88	0.15
NOvA vs T2K vs React vs IC19	9.4/7	0.22	1.2	4.5/7	0.72	0.36
NOvA vs T2K vs IC24	9.5/6	0.15	1.4	4.4/6	0.62	0.49
NOvA vs T2K vs React vs IC24	10/7	0.19	1.3	8.2/7	0.27	1.1

Table 4.3: Consistency test among different data sets, shown in the first column, assuming either normal or inverted ordering. “React” includes Daya-Bay, RENO and Double-Chooz. In the analyses above the horizontal line, θ_{13} is a free parameter, whereas below the line we have fixed $\sin^2 \theta_{13} = 0.0222$. See text for more details.

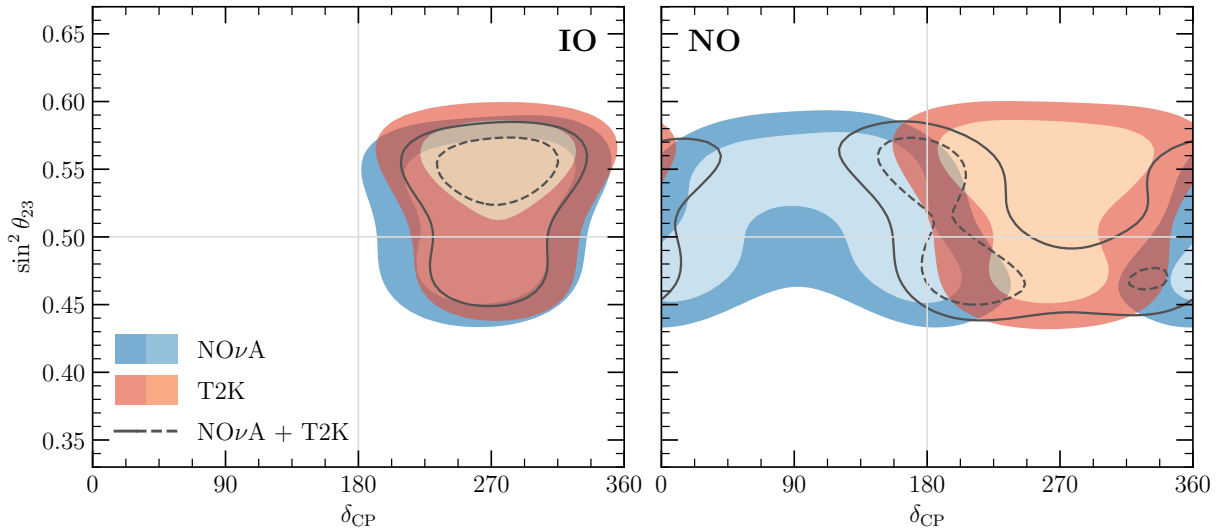


Figure 4.6: 1σ and 2σ allowed regions (2 dof) for T2K (red shading), NO ν A (blue shading) and their combination (black curves). Contours are defined with respect to the local minimum for IO (left) or NO (right). We fix $\sin^2 \theta_{13} = 0.0222$, $\sin^2 \theta_{12} = 0.31$, $\Delta m_{21}^2 = 7.5 \times 10^{-5} \text{ eV}^2$ and minimize with respect to $|\Delta m_{3\ell}^2|$.

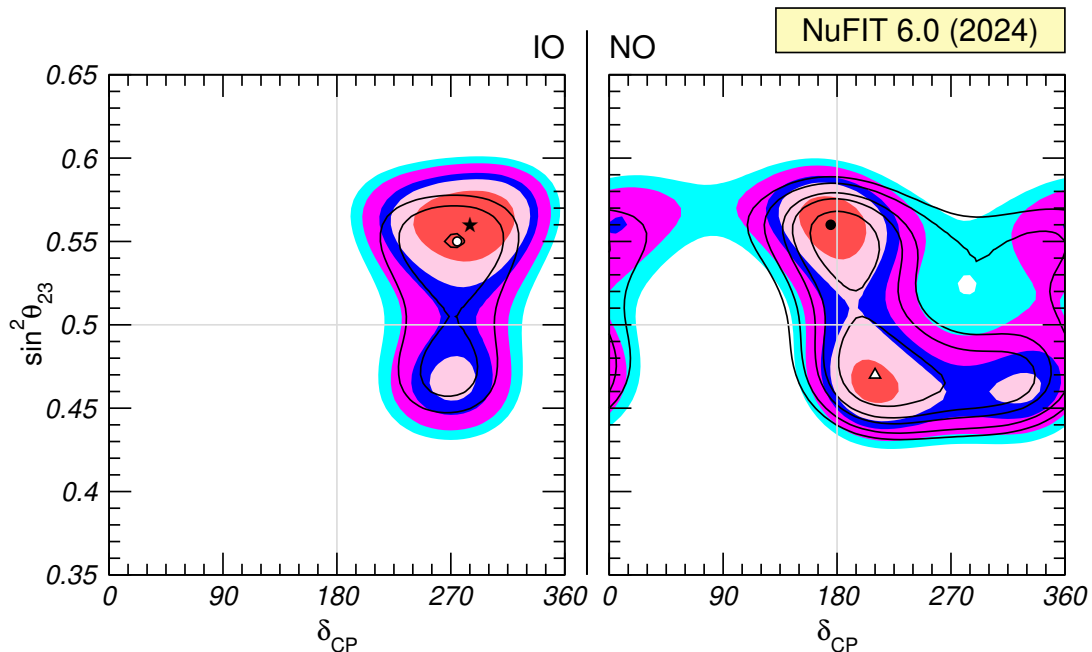


Figure 4.7: Two-dimensional projection of the allowed six-dimensional region from global data in the plane of $(\delta_{\text{CP}}, \sin^2 \theta_{23})$ for IO (left) and NO (right) after minimization with respect to the undisplayed parameters. Regions for both orderings are defined with respect to the global best-fit point. The different contours correspond to 1σ , 90%, 2σ , 99%, 3σ CL (2 dof). Colored regions (black contours) correspond to the variant with IC19 and without SK-atm (with IC24 and with SK-atm).

constraints are significantly tighter than those from individual experiments, indicating a high level of consistency (Table 4.3). The interplay between LBL and reactor data is particularly crucial for mass ordering (MO) determination, as these experiments provide complementary constraints [159, 160].

The χ^2 projections for $\Delta m_{3\ell}^2$ (Fig. 4.9) reveal different sensitivities to the mass or-

dering across datasets. While most individual datasets either show little sensitivity or slightly prefer normal ordering (NO), the combination of LBL accelerator data with IceCube atmospheric neutrinos (LBL/IC) favors inverted ordering (IO), primarily due to the tension between T2K and NOvA results. However, when LBL and reactor data are combined, they yield a preference for NO with $\Delta\chi_{\text{IO,NO}}^2 = -0.6$, effectively canceling out the preference for IO from T2K and NOvA.

Compatibility tests using the parameter goodness-of-fit (PG) method (Table 4.3) confirm a better agreement with NO when comparing the combined T2K and NOvA dataset with reactor data. However, this preference diminishes when T2K and NOvA are tested separately, reflecting their internal tension. Figure 4.9 also shows that the older IceCube dataset (IC19) has a negligible impact on MO determination due to its weak constraint on $|\Delta m_{3\ell}^2|$. In contrast, the more recent IceCube dataset (IC24), which includes 9.3 years of data [80, 81], significantly strengthens the preference for NO when combined with reactor data, leading to $\Delta\chi_{\text{IO,NO}}^2 \approx 4.5$. However, this result does not simply add to the previous $\Delta\chi_{\text{IO,NO}}^2 = -0.6$ from LBL and reactor data, as their interplay shifts the best-fit region, ultimately leading to an overall preference of $\Delta\chi_{\text{IO,NO}}^2 \approx 1.5$.

Super-Kamiokande atmospheric neutrino data [76] alone also favors NO with $\Delta\chi_{\text{IO,NO}}^2 \approx 5.7$. However, this preference appears to stem from a statistical fluctuation [75], as the data is not strongly conclusive for either ordering. Finally, when combining the IC24, Super-Kamiokande, and global fit data, the overall preference for NO increases to $\Delta\chi_{\text{IO,NO}}^2 \approx 6.1$ (Sec. 4.1). This suggests that, despite the conflicting trends among individual datasets, the global combination increasingly supports normal ordering.

4.2.3 Sensitivity to the neutrino mass ordering

To better understand how current global data constrains the neutrino mass ordering (MO), we analyze its sensitivity following the methodology in Ref. [161]. A widely used test statistic for this purpose is the χ^2 difference between the best-fit points for NO and IO, defined as

$$T \equiv \Delta\chi_{\text{IO,NO}}^2 = \chi_{\text{min,IO}}^2 - \chi_{\text{min,NO}}^2. \quad (4.7)$$

A positive value of T favors NO, while a negative value favors IO. As demonstrated in Refs. [161, 162], under certain conditions T follows a Gaussian distribution with mean $\pm T_0$ and standard deviation $2\sqrt{T_0}$. The value of T_0 is obtained by considering the expected event rates for the opposite MO:

$$\begin{aligned} T_0^{\text{NO}} &= \min_{\theta} \chi^2 [p_i(\text{IO}, \theta); p_i(\text{NO}, \theta^{\text{true}})], \\ T_0^{\text{IO}} &= \min_{\theta} \chi^2 [p_i(\text{NO}, \theta); p_i(\text{IO}, \theta^{\text{true}})]. \end{aligned} \quad (4.8)$$

Here, $p_i(o, \theta)$ represents the expected event number in bin i for ordering $o \in \{\text{NO}, \text{IO}\}$, and d_i is the observed event number. This approach ensures that T_0 is always positive, with its magnitude depending on the true values of the oscillation parameters θ^{true} , which we take as the best-fit points from Table 4.1.

Since IC24 and Super-Kamiokande data are provided as numerical χ^2 tables, we cannot apply this test directly to them. Thus, we perform the analysis using the dataset labeled «IC19 w/o SK-atm». The results for the global combination are

$$T_0^{\text{NO}} = 6.47, \quad T_0^{\text{IO}} = 4.85. \quad (4.9)$$

Figure 4.10 (bottom panel) shows the corresponding Gaussian distributions. Given the observed value $T_{\text{obs}} = -0.6$, we compute the probability (p -value) of obtaining a more

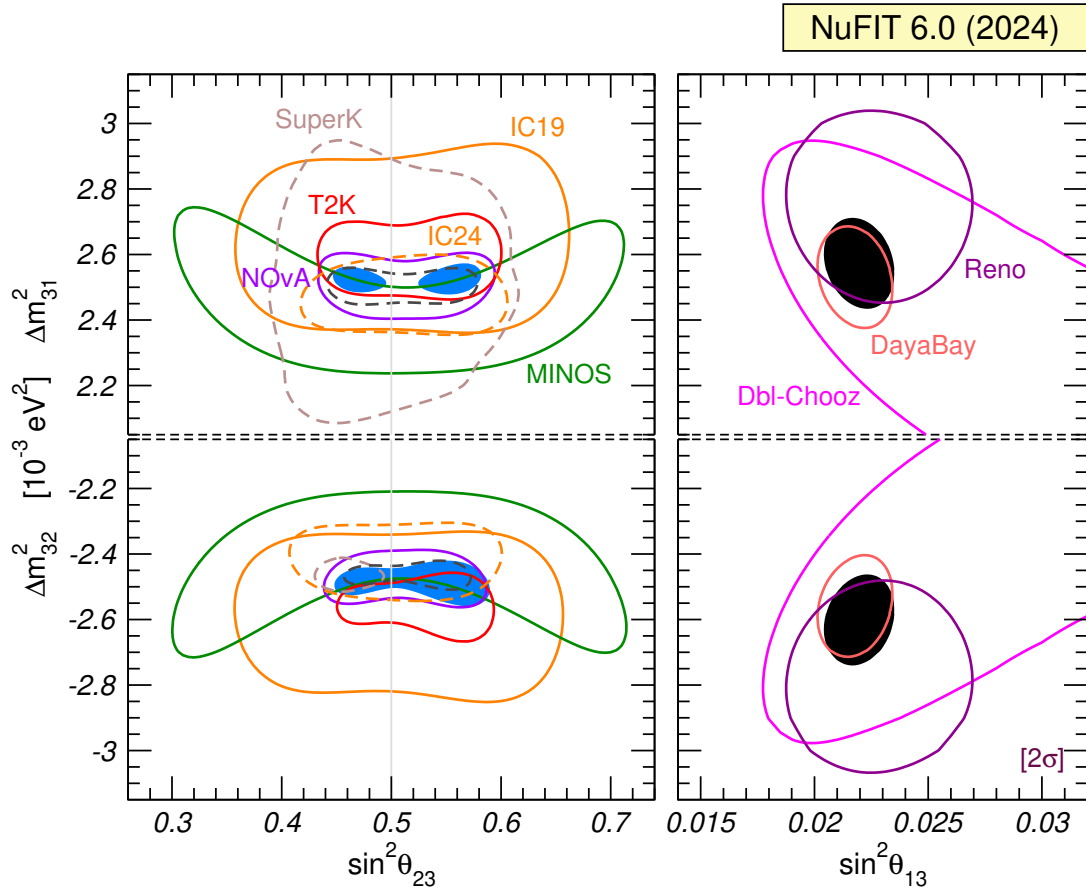


Figure 4.8: Confidence regions at 95.45% CL (2 dof) in the plane of $\sin^2 \theta_{23}$ ($\sin^2 \theta_{13}$) and $\Delta m_{3\ell}^2$ in the left (right) panels. For the left panels we use both appearance and disappearance data from MINOS (green), NOvA (purple) and T2K (red), as well as atmospheric data from IC (orange) and Super-Kamiokande (light-brown); the colored region corresponds to the combination of these accelerator data with IC19, whereas the black-dashed contour corresponds to the combination with IC24 and Super-Kamiokande. A prior on θ_{13} is included to account for the reactor constraint. The right panels show regions using data from Daya-Bay (pink), Double-Chooz (magenta), RENO (violet), and their combination (black regions). In all panels solar, KamLAND and SNO+ data are included to constrain Δm_{21}^2 and θ_{12} . Contours are defined with respect to the global minimum of the two orderings for each data set.

extreme result under each hypothesis:

$$\begin{aligned} \text{NO: } p_{\text{NO}} &= 8.2\%, \quad 91.8\% \text{ CL}, \quad 1.7\sigma, \\ \text{IO: } p_{\text{IO}} &= 16.7\%, \quad 83.3\% \text{ CL}, \quad 1.4\sigma. \end{aligned} \quad (4.10)$$

As $|T_{\text{obs}}| < 1$, the p -values for both orderings are similar, preventing a strong preference for either. Neither NO nor IO can be rejected at high significance, with both p -values remaining below 2σ . The slightly lower p_{NO} reflects the negative T_{obs} value.

The median sensitivity of the dataset, assuming T_{obs} follows the expected mean, gives

$$\begin{aligned} \text{NO: } p_{\text{NO}}^{\text{med}} &= 1.3\%, \quad 98.7\% \text{ CL}, \quad 2.5\sigma, \\ \text{IO: } p_{\text{IO}}^{\text{med}} &= 0.51\%, \quad 99.49\% \text{ CL}, \quad 2.8\sigma. \end{aligned} \quad (4.11)$$

This implies that, under ideal conditions, the dataset has a nominal sensitivity above 2.5σ to the MO. However, the observed T_{obs} lies between the peaks of the distributions due to competing trends in the data, weakening the rejection of either ordering.

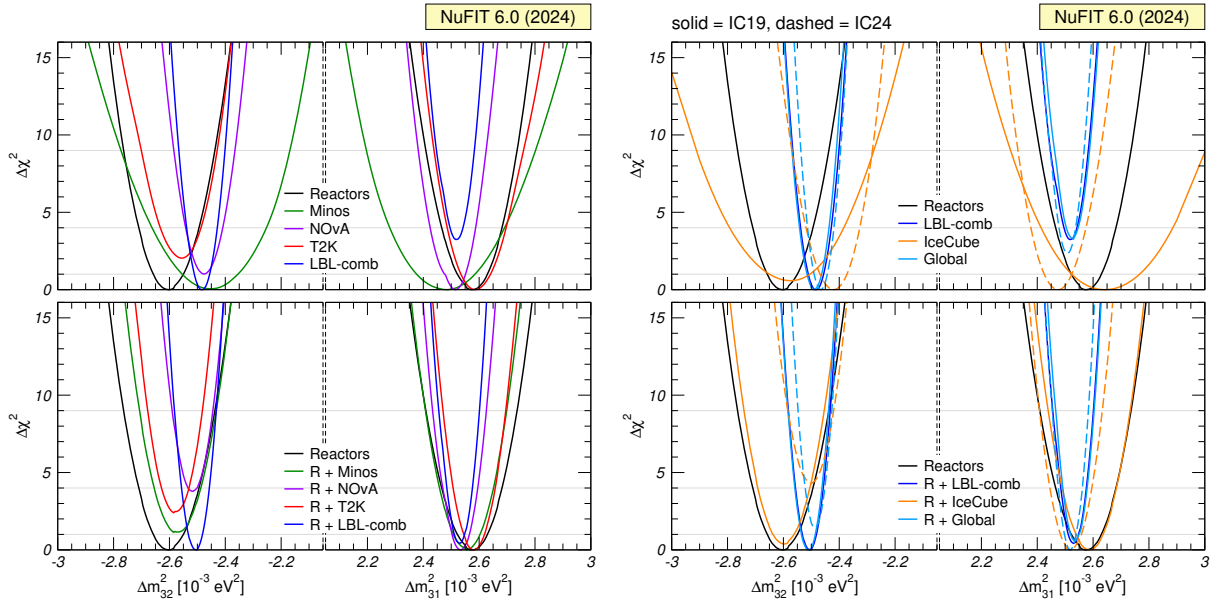


Figure 4.9: $\Delta\chi^2$ profiles as a function of $\Delta m_{3\ell}^2$ for different data sets and combinations as labeled in the figures. In the curves where the reactors R are not included in the combination we have fixed $\sin^2\theta_{13} = 0.0222$ as well as the solar parameters and minimized with respect to θ_{23} and δ_{CP} . When the reactors are included θ_{13} is also marginalized. $\Delta\chi^2$ is shown with respect to the global best-fit point (IO or NO) for each curve. The left set of panels visualizes the reactor/LBL combination, whereas in the right set of panels we are illustrating the impact of the IC19 or IC24 data sets.

To assess the likelihood of this result, the top panel of Fig. 4.10 shows the expected T_{obs} range with 68.27% (green) and 95.45% (yellow) probability for each ordering. The observed value $T_{\text{obs}} = -0.6$ lies well within the 1σ (2σ) range for IO (NO), confirming that it is not an unusual outcome for either scenario.

4.3 Updates in the “12” sector

The dominant constraints on the solar neutrino oscillation parameters, Δm_{21}^2 and θ_{12} , come from solar neutrino experiments and LBL reactor experiments at distances of $\mathcal{O}(100 \text{ km})$. Figure 4.11 compares the current determination of these parameters from the global solar analysis with that from LBL reactor data.

In the solar neutrino sector, several new data sets have been incorporated since NuFIT 5.0, including the full day-night spectrum from Super-Kamiokande phase IV [61], as well as the final spectra from Borexino phases II [68] and III [70]. Additionally, the solar neutrino flux predictions have been updated using the latest generation of Standard Solar Models (SSMs) [146].

For the past two decades, solar modeling has faced the so-called solar composition problem, which stems from differences in heavy element abundances. Earlier models used abundances from Ref. [163] (GS98), which predicted a higher metallicity and provided excellent agreement with helioseismology. However, more modern analyses [164] (AGSS09) yielded lower metallicity values, leading to discrepancies with helioseismology. Consequently, two versions of the Standard Solar Model were developed, one based on GS98 abundances and another on AGSS09 [52, 53, 165]. More recently, an updated AGSS09-based model (AAG21) [166] slightly increased the metallicity, while a separate

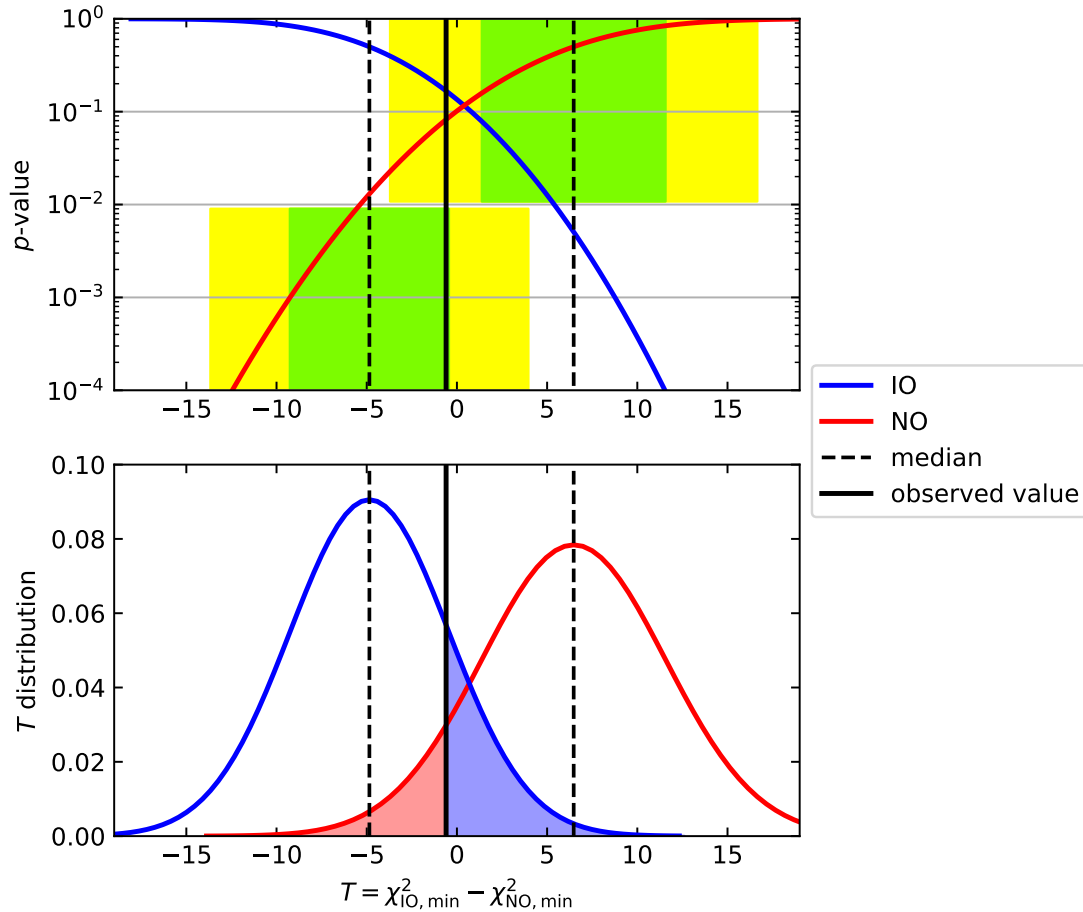


Figure 4.10: p -values (top) and distributions (bottom) for the test statistic $T = \chi_{\text{IO},\text{min}}^2 - \chi_{\text{NO},\text{min}}^2$ corresponding to the «IC19 w/o SK-atm» analysis, assuming true NO (red) or true IO (blue). The observed value $T_{\text{obs}} = -0.6$ is shown by the solid vertical black line. The corresponding median values are shown by the dashed vertical lines. The green and yellow bands in the top panel —vertically displaced to avoid graphical overlap— correspond to the 1σ and 2σ intervals for T assuming NO (upwards displaced bands) and IO (downwards displaced bands).

study (MB22) [167] found metallicity values closer to GS98. Importantly, MB22-based models align well with helioseismology observations, reinforcing their credibility.

Figure 4.11 compares the current determinations of Δm_{21}^2 and θ_{12} using solar data with two extreme solar model versions: one based on AAG21 and another on MB22-met abundances. While the overall determination of these parameters remains robust across models, the allowed parameter ranges especially at higher confidence levels vary slightly. Notably, a recent model-independent solar flux determination [5] shows better agreement with MB22 predictions, leading us to adopt MB22 as the reference model for NuFIT 6.0.

For reactor neutrino data, we have updated the predicted antineutrino fluxes at the KamLAND location to incorporate the latest Daya Bay measurements [94]. Furthermore, our analysis now includes the first results from the SNO+ experiment, combining 114 ton-years of data from its partial-fill phase [149] with the first 286 ton-years from its full-fill phase [150, 151]. The right panel of Fig. 4.11 displays the $\Delta\chi^2$ dependence on Δm_{21}^2 after marginalizing over θ_{12} (with $\sin^2\theta_{13} = 0.0222$ fixed). Although SNO+ is currently less precise than KamLAND, its best-fit value for Δm_{21}^2 is slightly higher. However, its impact on the global determination remains minor at this stage.

Looking ahead, as SNO+ accumulates more data, it will provide valuable insights into

the potential tension between solar and reactor determinations of Δm_{21}^2 . Presently, the best-fit Δm_{21}^2 from reactor experiments corresponds to $\Delta\chi_{\text{solar,MB22}}^2 = 2.5$, representing a slight increase over the $\Delta\chi_{\text{solar,GS98}}^2 = 1.3$ reported in NuFIT 5.0. To illustrate the effect of different data inputs, Fig. 4.11 also shows the solar analysis results without including Super-Kamiokandes day-night variation data (orange curve). Removing this information reduces the tension, bringing the agreement to $\Delta\chi^2 \sim 1.5$.

Overall, the latest updates lead to only minor shifts in the determination of solar neutrino oscillation parameters a $\sim 1\%$ increase in the best-fit value and a $\sim 10\%$ improvement in precision. These small variations reaffirm the robustness of the current results.

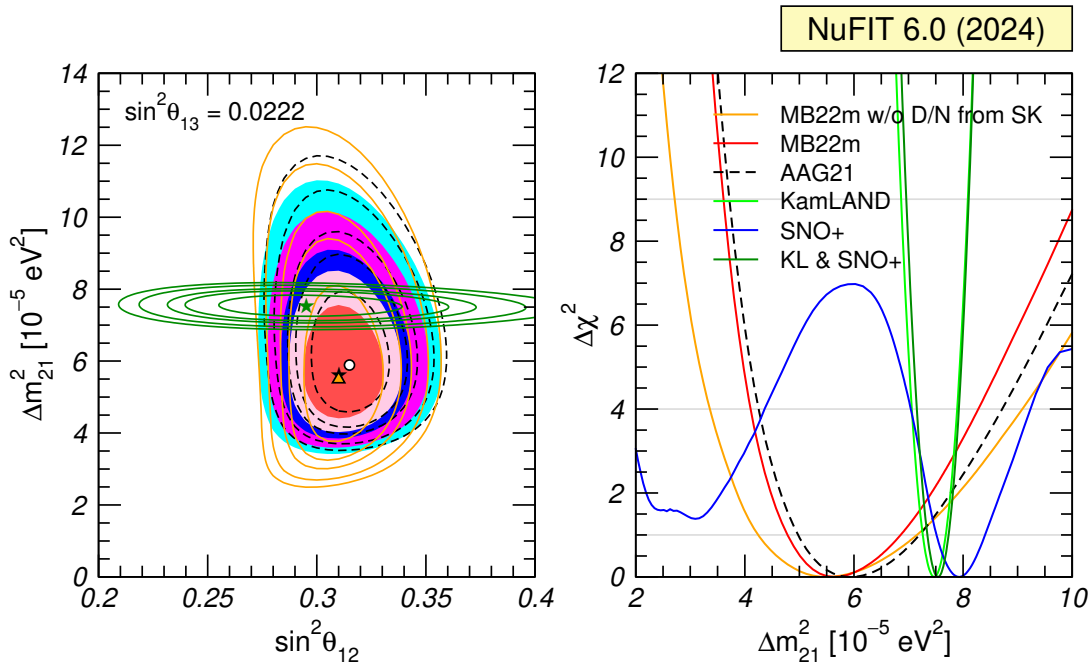


Figure 4.11: Left: Allowed parameter regions (at 1σ , 90%, 2σ , 99%, and 3σ CL for 2 dof) from the combined analysis of solar data for MB22-met model (full regions with best fit marked by black star) and AAG21 model (dashed void contours with best fit marked by a white dot), and for the analysis of the combination of KamLAND and SNO+ data (solid green contours with best fit marked by a green star) for fixed $\sin^2\theta_{13} = 0.0222$. For comparison we also show as orange contours the results obtained with the MB22-met model without including the results of the day-night variation in SK. Right: $\Delta\chi^2$ dependence on Δm_{21}^2 for the same four analyses after marginalizing over θ_{12} . In addition we show separately the results from KamLAND and SNO+.

4.4 Projections on neutrino mass scale observables

Neutrino oscillations arise from quantum interference effects, making them sensitive to mass-squared differences Δm_{ij}^2 and to the structure of the leptonic mixing matrix $U_{\alpha j}$. However, oscillations do not reveal the absolute neutrino mass scale, only setting a lower bound on the mass of the heaviest participating neutrino.

The most direct information on absolute neutrino masses comes from kinematic studies of processes involving neutrinos as discussed in Section 2.96. The most recent result from the KATRIN experiment [37] sets an upper limit of $m_{\nu_e} < 0.45$ eV at 90% CL. The most stringent limits on neutrinoless double beta decay come from Germanium-based

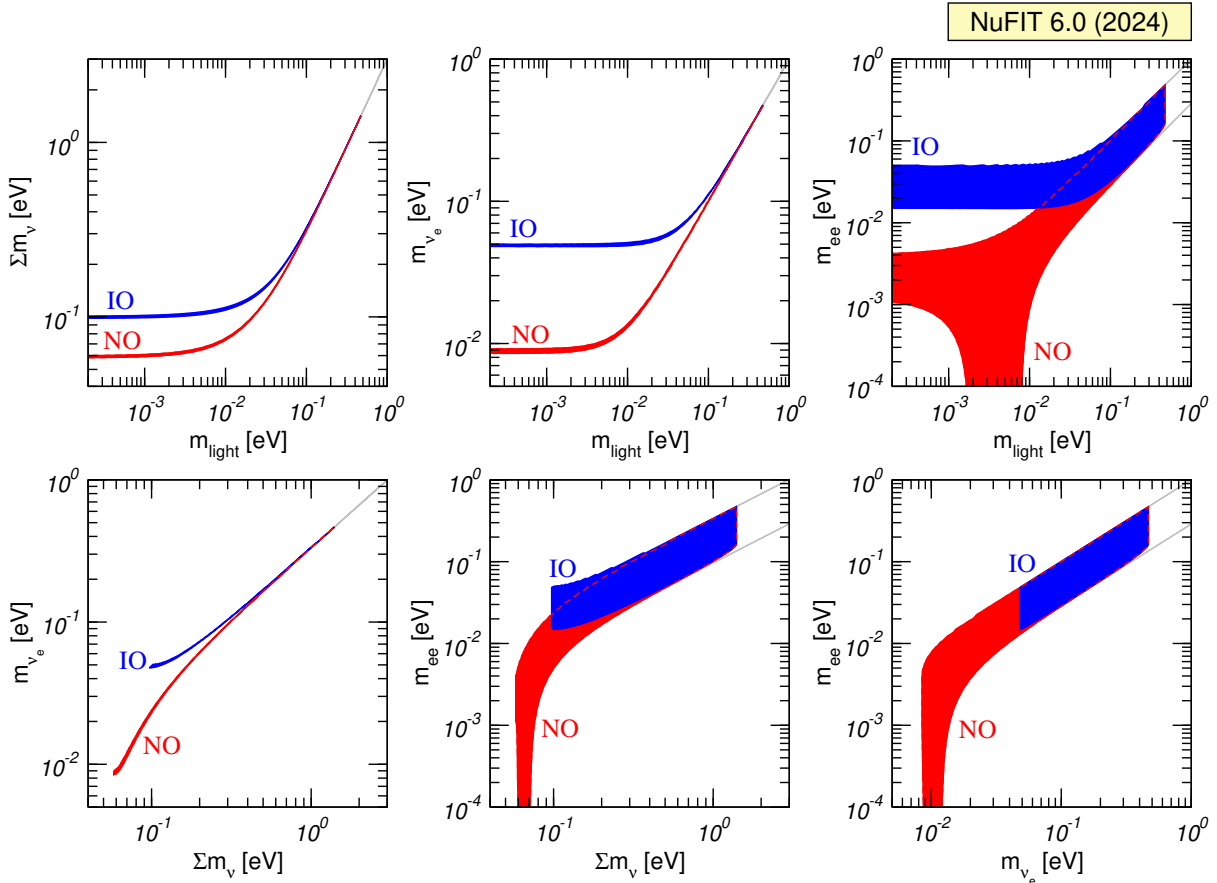


Figure 4.12: Upper: 95% CL allowed ranges of the three probes of the absolute neutrino mass $\sum m_\nu$, m_{ν_e} , m_{ee} as a function of the mass of the lightest neutrino obtained from projecting the results of the global analysis of oscillation data. The regions are defined with respect to the minimum for each ordering. Lower: Corresponding 95% CL allowed regions (for 2 dof) in the planes $(m_{\nu_e}, \sum m_\nu)$, $(m_{ee}, \sum m_\nu)$, and (m_{ν_e}, m_{ee}) .

GERDA [38], which sets $T_{1/2}^{0\nu} > 1.8 \times 10^{26}$ yr, and Xenon-based KamLAND-Zen [39], with $T_{1/2}^{0\nu} > 3.8 \times 10^{26}$ yr. Depending on the assumed nuclear matrix elements, these translate into limits of $m_{ee} \lesssim 0.079\text{--}0.180$ eV for GERDA and $m_{ee} \lesssim 0.028\text{--}0.122$ eV for KamLAND-Zen.

As already commented in Chapter 2, neutrino masses also leave an imprint in cosmology, primarily through their impact on the large-scale structure of the Universe. Cosmological constraints typically provide information on the sum of neutrino masses provided in EQ. 2.96, while being largely insensitive to the mass ordering or mixing angles. Current cosmological observations set upper limits in the range $\sum m_\nu \lesssim 0.04\text{--}0.3$ eV [40, 41], depending on the dataset used, the assumed cosmological model, and the statistical approach.

Figure 4.12 (upper panels) shows the 95% CL allowed regions for m_{ν_e} , m_{ee} , and $\sum m_\nu$ obtained from the NuFIT 6.0 global fit, plotted as a function of m_0 . The spread in m_{ee} predictions is due to the unknown Majorana phases. The figure compares constraints from oscillations alone (void regions) and from oscillations combined with the KATRIN limit (filled regions). The KATRIN result is included using a simple χ^2 function based on their measurement, $m_{\nu_e}^2 = -0.14^{+0.13}_{-0.15}$ eV, assuming Gaussian errors and Wilks' theorem.¹

¹This gives a 90% CL upper limit of $m_{\nu_e} \leq 0.35$ eV, which lies between the limits obtained with the Lohkov-

Since these observables are linked through the neutrino mass spectrum, knowing two of them allows in principle for constraints on the Majorana phases and/or the mass ordering [168, 169]. Figure 4.12 (lower panels) illustrates these correlations, showing that a strong constraint on any one parameter can provide valuable insights into the others [170].

The combined constraints from oscillation data and KATRIN at 95% CL are:

$$0.00085 \text{ eV} \leq m_{\nu_e} \leq 0.4 \text{ eV} \quad (\text{NO}), \quad 0.048 \text{ eV} \leq m_{\nu_e} \leq 0.4 \text{ eV} \quad (\text{IO}), \quad (4.12)$$

$$0.058 \text{ eV} \leq \sum m_\nu \leq 1.2 \text{ eV} \quad (\text{NO}), \quad 0.098 \text{ eV} \leq \sum m_\nu \leq 1.2 \text{ eV} \quad (\text{IO}). \quad (4.13)$$

For Majorana neutrinos, the corresponding m_{ee} limits are:

$$0 \leq m_{ee} \leq 0.41 \text{ eV} \quad (\text{NO}), \quad 0.015 \text{ eV} \leq m_{ee} \leq 0.41 \text{ eV} \quad (\text{IO}). \quad (4.14)$$

These results illustrate how complementary approaches—oscillations, direct kinematic searches, neutrinoless double beta decay, and cosmology—collectively constrain the absolute neutrino mass scale and mass ordering.

4.5 Summary

We have presented an updated global analysis of neutrino oscillation data available up to September 2024, as outlined in the introduction of this chapter. Our results are provided in two versions:

- **IC19 w/o SK-atm:** This dataset includes all data for which enough information is available to perform an independent and detailed fit.
- **IC24 with SK-atm:** This dataset incorporates numerical χ^2 tables provided by the IceCube and Super-Kamiokande collaborations, which are added to our own χ^2 analysis.

The global best-fit values, along with their 1σ and 3σ confidence ranges, are presented in Table 4.1. Our main findings can be summarized as follows:

- The parameters θ_{12} , θ_{13} , Δm_{21}^2 , and $|\Delta m_{3\ell}^2|$ remain very well constrained, with nearly Gaussian χ^2 distributions up to high confidence levels. Their relative uncertainties at 3σ are approximately 13%, 8%, 16%, and (5–6)%, respectively, showing strong stability across datasets.
- The mixing angle θ_{23} remains the least precisely determined, with a relative uncertainty of about 20% at 3σ . The well-known octant ambiguity persists, as both solutions ($\theta_{23} < 45^\circ$ and $\theta_{23} > 45^\circ$) have nearly degenerate χ^2 minima. There is a slight overall preference for the second octant ($\theta_{23} > 45^\circ$), except in NO for the «IC24 with SK-atm» dataset. However, for all dataset combinations and mass orderings, the alternative octant remains viable, with $\Delta\chi^2 < 4$ between the two minima.
- The determination of the CP-violating phase δ_{CP} strongly depends on the assumed mass ordering. For NO, the best-fit value is close to the CP-conserving scenario $\delta_{\text{CP}} \approx 180^\circ$, with $\Delta\chi^2 < 1$, making its profile highly non-Gaussian and dependent

Tkachov (0.45 eV) and Feldman-Cousins (0.31 eV) methods.

on the dataset variant and the θ_{23} octant. In contrast, for IO, the best-fit values for both data variants favor maximal CP violation at $\delta_{\text{CP}} \approx 270^\circ$, disfavoring CP conservation at 3.6σ (4σ) in the «IC19 w/o SK-atm» («IC24 with SK-atm») analysis.

- The mass ordering preference remains a subject of debate. The difference in χ^2 between IO and NO is found to be:

$$\Delta\chi_{\text{IO,NO}}^2 = -0.6 \quad (\text{IC19 w/o SK-atm}), \quad 6.1 \quad (\text{IC24 with SK-atm}). \quad (4.15)$$

The nearly indecisive result in the «IC19 w/o SK-atm» dataset arises from opposing trends in different experiments. The appearance data from T2K and NOvA exhibit a 2σ tension for NO, while they remain fully consistent for IO. However, the disappearance channels from accelerator and reactor experiments show better agreement with NO than IO, particularly in their determination of $|\Delta m_{3\ell}^2|$.

Despite a sensitivity estimate indicating that the «IC19 w/o SK-atm» dataset should have a median ability to reject NO (IO) at 2.5σ (2.8σ), the actual observed constraints are much weaker at only 1.7σ (1.4σ) due to competing trends in the data. The inclusion of IceCube (IC24) and Super-Kamiokande atmospheric data enhances the preference for NO, leading to the more decisive result of $\Delta\chi_{\text{IO,NO}}^2 = 6.1$ in the «IC24 with SK-atm» dataset.

Additionally, we provide updated constraints and correlations for parameters sensitive to the absolute neutrino mass, obtained from beta decay, neutrinoless double beta decay, and cosmological observations. These results, along with supplementary materials such as detailed figures and data tables, can be accessed on the NuFit webpage [1].

Chapter 5

Three neutrino oscillations with new interactions: Formalism

As established in Chapter 3, modern neutrino physics exploits four primary neutrino sources: solar, atmospheric, reactor, and accelerator-generated to probe oscillation phenomena through both charged-current (CC) and neutral-current (NC) interaction channels. While Chapter 4 demonstrated the precision achievable in standard three-flavor oscillation parameters through global analyses of multi-experiment data, the following chapters address a critical open question: *How do current experimental constraints limit beyond-Standard Model (BSM) scenarios affecting both neutrino propagation and detection?*

This chapter develops the theoretical formalism for Non-Standard Neutrino Interactions (NSI) and related BSM frameworks that modify neutrino dynamics. We focus on three complementary approaches:

1. Generic NSI-induced modifications to matter effects in neutrino propagation and detection (Section 5.1);
2. Heavy mediator scenarios altering detection cross-sections (Section 5.2);
3. Long-range monopole-dipole interactions mediated by ultra-light scalars (Section 5.3).

5.1 Non-Standard Interactions - Formalism

Generic BSM physics can be systematically incorporated via an effective field theory (EFT) approach. This involves constructing a hierarchy of gauge-invariant effective operators, ordered by their mass dimension and suppressed by powers of a high-energy NP scale Λ . Remarkably, neutrino masses emerge naturally in this construction through the sole dimension-five operator compatible with the SM gauge symmetry and field content. This observation places neutrino masses as the leading-order phenomenological signature of BSM physics. At the next order in the EFT expansion, dimension-six four-fermion operators dominate. Among these, operators involving neutrino fields induce non-standard modifications to neutrino interactions referred to as NSI which alter neutrino production, propagation, and detection processes. In this section, we specifically analyze NSI arising from dimension-six operators that generate purely vector or axial-vector couplings between neutrinos and matter fermions, as these interactions are most relevant for neutrino oscillation and scattering phenomenology (for recent works including additional operators with different Lorentz structures see for example Refs. [171–174]). Generically these can be classified in charged-current (CC) NSI

$$\mathcal{L}_{\text{NSI,CC}} = -2\sqrt{2}G_F \sum_{f,f',\alpha,\beta} \varepsilon_{\alpha\beta}^{ff',P} (\bar{\ell}_\alpha \gamma_\mu P_L \nu_\beta) (\bar{f} \gamma^\mu P f') + \text{h.c.}, \quad (5.1)$$

and neutral-current (NC) NSI

$$\mathcal{L}_{\text{NSI,NC}} = -2\sqrt{2}G_F \sum_{f,P,\alpha,\beta} \varepsilon_{\alpha\beta}^{f,P} (\bar{\nu}_\alpha \gamma^\mu P_L \nu_\beta) (\bar{f} \gamma_\mu P f). \quad (5.2)$$

In Eqs. (5.1) and (5.2), f and f' refer to SM charged fermions, ℓ denotes a SM charged lepton and P can be either a left-handed or a right-handed projection operator (P_L or P_R , respectively). Moreover, the normalization of the couplings is deliberately chosen to match that of the weak currents in the SM, so the values of $\varepsilon_{\alpha\beta}^{f,P}$ indicate the strength of the new interaction with respect to the Fermi constant, G_F . The corresponding vector and axial-vector combinations of NSI coefficients are defined as:

$$\varepsilon_{\alpha\beta}^{f,V} \equiv \varepsilon_{\alpha\beta}^{f,L} + \varepsilon_{\alpha\beta}^{f,R} \quad \text{and} \quad \varepsilon_{\alpha\beta}^{f,A} \equiv \varepsilon_{\alpha\beta}^{f,L} - \varepsilon_{\alpha\beta}^{f,R}. \quad (5.3)$$

Precise measurements of meson and muon decays place severe constraints on the possible strength of CC NSI (see for example Refs. [171, 175–177]). Conversely, NC NSI are much more difficult to probe directly, given the intrinsic difficulties associated with neutrino detection via neutral currents. A priori, the requirement of gauge invariance would generate similar operators in the charged lepton sector, in severe conflict with experimental observables [178, 179]. However, such bounds may be alleviated (or evaded) in NP models in which NC NSI are generated by exchange of neutral mediators with masses well below the EW scale (for a recent review on viable NSI models see, *e.g.*, Ref. [180]). It is in these scenarios that one can envision observable effects in present and future neutrino experiments. Several models have been proposed, involving new gauge symmetries and light degrees of freedom, that would give rise to relatively large NC NSI. These include, for example, models where the NSI are generated from the Z' boson associated to a new $U(1)'$ symmetry [181–188], radiative neutrino mass models involving new scalars [189], or models with leptoquarks [189–191]. Many of these extensions involve a gauge symmetry based on a combination of baryon and lepton quantum numbers, and would therefore induce equal NSI for up and down quarks. However, exceptions to this rule arise, for example, in models with leptoquarks where NSI may be only generated for down-quarks [189, 190]. Similarly it should be stressed that, while many of these models typically lead to diagonal NSI in lepton flavor space, this is not always the case and, depending on the particular extension, sizable off-diagonal NSI may also be obtained (see, *e.g.*, Refs. [183, 184, 187]). In order to derive constraints to such a wide landscape of models, the use of the effective operator approach advocated above is extremely useful. For bounds from oscillation data on $U(1)'$ models with diagonal couplings in flavor space, see Ref. [192].

In fact, some of the best model-independent bounds on NC NSI are obtained from global fits to oscillation data. These are affected by vector couplings involving fermions present in matter, $\varepsilon_{\alpha\beta}^{f,V}$ with $f \in \{u, d, e\}$, since they modify the effective matter potential [193, 194] felt by neutrinos as they propagate in a medium. In Ref. [195] such global analysis was performed in the context of vector NC NSI with either up or down quarks. In Ref. [196] the study was extended to account for the possibility vector NC NSI with up and down quarks simultaneously, under the restriction that the neutrino flavour structure of the NSI interactions is independent of the quark type. However, NSI with electrons were not considered.

One important effect of the presence of NSI [193, 197, 198] affecting the neutrino propagation in oscillation experiments is the appearance of a degeneracy leading to a qualitative change of the lepton mixing pattern. This was first observed in the context of solar neutrinos, for which the established standard MSW solution (discussed in Chapter

2), requires a mixing angle θ_{12} in the first octant, while with suitable NSI the data could be described by a mixing angle θ_{12} in the second octant, the so-called LMA-Dark (LMA-D) [199] solution. The origin of the LMA-D solution is a degeneracy in the oscillation probabilities due to a symmetry of the Hamiltonian describing neutrino evolution in the presence of NSI [195, 200–202]. Such degeneracy makes it impossible to determine the neutrino mass ordering by oscillation experiments alone [202] and therefore jeopardizes one of the main goals of the upcoming neutrino oscillation program. Although the degeneracy is not exact when including oscillation data from neutrino propagating in different environments, quantitatively the breaking is small and global fits show that the LMA-D solution is still pretty much allowed by oscillation data alone [195, 196]. A second important limitation of oscillation data is that it is only sensitive to differences in the potential felt by different neutrino flavours. Thus, oscillation data may be used to derive constraints on the differences between diagonal NC NSI parameters, but not on the individual parameters themselves.

To make the analysis feasible, the following simplifications are introduced:

- we assume that the neutrino flavour structure of the interactions is independent of the charged fermion properties;
- we further assume that the chiral structure of the charged fermion vertex is the same for all fermion types.

Under these hypotheses, we can factorize $\varepsilon_{\alpha\beta}^{f,P}$ as the product of three terms:

$$\varepsilon_{\alpha\beta}^{f,P} \equiv \varepsilon_{\alpha\beta} \xi^f \chi^P \quad (5.4)$$

where the matrix $\varepsilon_{\alpha\beta}$ describes the dependence on the neutrino flavour, the coefficients ξ^f parametrize the coupling to the charged fermions, and the terms χ^P account for the chiral structure of such couplings, normalized so that $\varepsilon_{\alpha\beta}^{f,L}$ ($\varepsilon_{\alpha\beta}^{f,R}$) corresponds to $\chi^L = 1/2$ and $\chi^R = 0$ ($\chi^R = 1/2$ and $\chi^L = 0$). With these assumptions the Lagrangian in Eq. (5.2) takes the form:

$$\mathcal{L}_{\text{NSI,NC}} = -2\sqrt{2}G_F \left[\sum_{\alpha,\beta} \varepsilon_{\alpha\beta} (\bar{\nu}_\alpha \gamma^\mu P_L \nu_\beta) \right] \left[\sum_{f,P} \xi^f \chi^P (\bar{f} \gamma_\mu P f) \right]. \quad (5.5)$$

Concerning the chiral structure of the charged fermion vertex, in this work we will consider either vector couplings ($\chi^L = \chi^R = 1/2$), or axial-vector couplings ($\chi^L = -\chi^R = 1/2$). The corresponding combinations of NSI coefficients are given in Eq. (5.3).

For what concerns the dependence of the NSI on the charged fermion type, we notice that ordinary matter is composed of electrons (e), up quarks (u) and down quarks (d), so that only the coefficients ξ^e , ξ^u and ξ^d are experimentally accessible. For vector NSI, since quarks are always confined inside protons (p) and neutrons (n), we may define (see, *e.g.*, Ref. [172]):

$$\xi^p = 2\xi^u + \xi^d, \quad \xi^n = 2\xi^d + \xi^u \quad (5.6)$$

so that $\varepsilon_{\alpha\beta}^{p,V} \equiv 2\varepsilon_{\alpha\beta}^{u,V} + \varepsilon_{\alpha\beta}^{d,V} = \varepsilon_{\alpha\beta} \xi^p (\chi^L + \chi^R)$ and $\varepsilon_{\alpha\beta}^{n,V} \equiv 2\varepsilon_{\alpha\beta}^{d,V} + \varepsilon_{\alpha\beta}^{u,V} = \varepsilon_{\alpha\beta} \xi^n (\chi^L + \chi^R)$. For axial-vector NSI, the correspondence between quark NSI and nucleon NSI is not that obvious: for example, for non-relativistic nucleons an axial-vector hadronic current would induce a change in the spin of the nucleon. In any case, it is clear that a simultaneous re-scaling of all $\{\xi^f\}$ by a common factor can be reabsorbed into a re-scaling of $\varepsilon_{\alpha\beta}$, so that only the direction of (ξ^e, ξ^u, ξ^d) – or, equivalently, (ξ^e, ξ^p, ξ^n) – is phenomenologically non-trivial. We parametrize such direction using spherical coordinates, in terms of a

“latitude” angle η and a “longitude” angle ζ , as an extension of the framework and notation introduced in Ref. [196] (see also Ref. [203]). Concretely, we define:

$$\xi^e = \sqrt{5} \cos \eta \sin \zeta, \quad \xi^p = \sqrt{5} \cos \eta \cos \zeta, \quad \xi^n = \sqrt{5} \sin \eta \quad (5.7)$$

or, in terms of the “quark” couplings:

$$\xi^u = \frac{\sqrt{5}}{3}(2 \cos \eta \cos \zeta - \sin \eta), \quad \xi^d = \frac{\sqrt{5}}{3}(2 \sin \eta - \cos \eta \cos \zeta) \quad (5.8)$$

Using this parametrization, the case of NSI with quarks analyzed in Ref. [196] correspond to the “prime meridian” $\zeta = 0$, with the pure up-quark and pure down-quark cases located at $\eta = \arctan(1/2) \approx 26.6^\circ$ and $\eta = \arctan(2) \approx 63.4^\circ$, respectively. The “poles” ($\eta = \pm 90^\circ$) correspond to NSI with neutrons, while NSI with protons lies on the “equator” ($\eta = \zeta = 0$). Finally, the pure electron case is also on the equator, at a right angle ($\zeta = \pm 90^\circ$) from the pure proton case. Notice that an overall sign flip of (ξ^e, ξ^u, ξ^d) is just a special case of re-scaling and produces no observable effect, hence it is sufficient to restrict both η and ζ to the $[-90^\circ, +90^\circ]$ range.

The presence of vector NC NSI will affect both neutrino propagation in matter and neutrino scattering in the detector, while axial-vector NC NSI only affect some of the interaction cross sections. Both propagation and interaction effects lead to a modification of the expected number of events which can be described by the generic expression [2]:

$$N_{\text{ev}} \propto \text{Tr} \left[\rho^{\text{det}} \sigma^{\text{det}} \right] \quad (5.9)$$

where ρ^{det} is the density matrix characterizing the flavour state of the neutrinos reaching the detector, while the *generalized* cross section σ^{det} is a matrix in flavour space containing enough information to describe the interaction of *any* neutrino configuration. The form of Eq. (5.9) is manifestly basis-independent and permits a separate description of propagation effects (encoded into ρ^{det}) and of the scattering process (contained in σ^{det}), while at the same time properly taking into account possible interference between them. Notice that both ρ^{det} and σ^{det} are hermitian matrices, which ensures that N_{ev} is real. Actually, Eq. (5.9) is invariant under the joint transformation:

$$\rho^{\text{det}} \rightarrow [\rho^{\text{det}}]^* \quad \text{and} \quad \sigma^{\text{det}} \rightarrow [\sigma^{\text{det}}]^* \quad (5.10)$$

whose implications will be discussed later on in this section.

5.1.1 Neutrino oscillations in the presence of NSI

In general, the evolution of the neutrino and antineutrino flavour state during propagation is governed by the Hamiltonian:

$$H^\nu = H_{\text{vac}} + H_{\text{mat}} \quad \text{and} \quad H^{\bar{\nu}} = (H_{\text{vac}} - H_{\text{mat}})^*, \quad (5.11)$$

where H_{vac} is the vacuum part which in the flavour basis has been defined in Chapter 2. Here $U_{\text{vac}} = O \cdot U_{12}$ denotes the three-lepton mixing matrix in vacuum, as defined in Eq. 2.68. The advantage of defining U_{vac} in this way rather than as in Eq. (2.33) is that the transformation $H_{\text{vac}} \rightarrow -H_{\text{vac}}^*$, whose relevance for the present work will be discussed below, can be implemented exactly (up to an irrelevant multiple of the identity) by the following transformation of the parameters:

$$\begin{aligned} \Delta m_{31}^2 &\rightarrow -\Delta m_{31}^2 + \Delta m_{21}^2 = -\Delta m_{32}^2, \\ \theta_{12} &\rightarrow \pi/2 - \theta_{12}, \\ \delta_{\text{CP}} &\rightarrow \pi - \delta_{\text{CP}} \end{aligned} \quad (5.12)$$

which does not spoil the commonly assumed restrictions on the range of the vacuum parameters ($\Delta m_{21}^2 > 0$ and $0 \leq \theta_{ij} \leq \pi/2$).

Concerning the matter part H_{mat} of the Hamiltonian which governs neutrino oscillations, if all possible operators in Eq. (5.2) are added to the SM Lagrangian we get:

$$H_{\text{mat}} = \sqrt{2}G_F N_e(x) \begin{pmatrix} 1 + \mathcal{E}_{ee}(x) & \mathcal{E}_{e\mu}(x) & \mathcal{E}_{e\tau}(x) \\ \mathcal{E}_{e\mu}^*(x) & \mathcal{E}_{\mu\mu}(x) & \mathcal{E}_{\mu\tau}(x) \\ \mathcal{E}_{e\tau}^*(x) & \mathcal{E}_{\mu\tau}^*(x) & \mathcal{E}_{\tau\tau}(x) \end{pmatrix} \quad (5.13)$$

where the “+1” term in the ee entry accounts for the standard contribution, and

$$\mathcal{E}_{\alpha\beta}(x) = \sum_{f=e,u,d} \frac{N_f(x)}{N_e(x)} \varepsilon_{\alpha\beta}^{f,V} \quad (5.14)$$

describes the non-standard part. Here $N_f(x)$ is the number density of fermion f as a function of the distance traveled by the neutrino along its trajectory. In Eq. (5.14) we have limited the sum to the charged fermions present in ordinary matter, $f = e, u, d$. Taking into account that $N_u(x) = 2N_p(x) + N_n(x)$ and $N_d(x) = N_p(x) + 2N_n(x)$, and also that matter neutrality implies $N_p(x) = N_e(x)$, Eq. (5.14) becomes:

$$\mathcal{E}_{\alpha\beta}(x) = \left(\varepsilon_{\alpha\beta}^{e,V} + \varepsilon_{\alpha\beta}^{p,V} \right) + Y_n(x) \varepsilon_{\alpha\beta}^{n,V} \quad \text{with} \quad Y_n(x) \equiv \frac{N_n(x)}{N_e(x)} \quad (5.15)$$

which shows that, from the phenomenological point of view, the propagation effects of NSI with electrons can be mimicked by NSI with quarks by means of a suitable combination of up-quark and down-quark contributions.

Since the matter potential can be determined by oscillation experiments only up to an overall multiple of the identity, each $\varepsilon_{\alpha\beta}^{f,V}$ matrix introduces 8 new parameters: two differences of the three diagonal real parameters (*e.g.*, $\varepsilon_{ee}^{f,V} - \varepsilon_{\mu\mu}^{f,V}$ and $\varepsilon_{\tau\tau}^{f,V} - \varepsilon_{\mu\mu}^{f,V}$) and three off-diagonal complex parameters (*i.e.*, three additional moduli and three complex phases). Under the assumption that the neutrino flavour structure of the interactions is independent of the charged fermion type, as described in Eq. (5.4), we get:

$$\begin{aligned} \mathcal{E}_{\alpha\beta}(x) &= \varepsilon_{\alpha\beta} \left[\xi^e + \xi^p + Y_n(x) \xi^n \right] (\chi^L + \chi^R) \\ &= \sqrt{5} \left[\cos \eta (\cos \zeta + \sin \zeta) + Y_n(x) \sin \eta \right] (\chi^L + \chi^R) \varepsilon_{\alpha\beta} \end{aligned} \quad (5.16)$$

so that the phenomenological framework adopted here is characterized by 10 matter parameters: eight related to the matrix $\varepsilon_{\alpha\beta}$ plus two directions (η, ζ) in the (ξ^e, ξ^p, ξ^n) space. Notice, however, that the dependence on ζ in Eq. (5.16) can be reabsorbed into a re-scaling of $\varepsilon_{\alpha\beta}$ by introducing a new effective angle η' :

$$\begin{aligned} \mathcal{E}_{\alpha\beta}(x) &= \sqrt{5} \left[\cos \eta' + Y_n(x) \sin \eta' \right] (\chi^L + \chi^R) \varepsilon'_{\alpha\beta} \\ \text{with} \quad \tan \eta' &\equiv \tan \eta / (\cos \zeta + \sin \zeta) \quad \text{and} \quad \varepsilon'_{\alpha\beta} \equiv \varepsilon_{\alpha\beta} \sqrt{1 + \cos^2 \eta \sin(2\zeta)}. \end{aligned} \quad (5.17)$$

This is a consequence of the fact that electron and proton NSI always appear together in propagation, as explained after Eq. (5.15). Indeed, η' is just a practical way to express the direction in the $(\xi^e + \xi^p, \xi^n)$ plane. For $\zeta = 0$, which is the case studied in Ref. [196], one trivially recovers $\eta' = \eta$ and $\varepsilon'_{\alpha\beta} = \varepsilon_{\alpha\beta}$. Furthermore, for $\zeta = -45^\circ$ one gets $\xi^e + \xi^p = 0$, so that NSI effects in oscillations depend solely on the neutron coupling ξ^n . This would be the case, for example, in models where the Z' does not couple directly to matter

fermions, and NSI are generated through $Z - Z'$ mass mixing (see the related discussion in Ref. [186]). In fact, in this case, the specific value of η becomes irrelevant as long as it is different from zero (since Eq. (5.17) always yields $\eta' = \pm 90^\circ$ in this case), while for the special point where $\eta = 0$ and $\zeta = -45^\circ$ NSI completely cancel from oscillations. It should be stressed, however, that this only applies to *oscillations*: the implications of NSI for neutrino scattering described in Sec. 5.2 will still depend non-trivially on η .

LMA-D solution

An important piece of the discussion of NSI is about the LMA-Dark solution. Neutrino transition probabilities remain invariant – and more generically the density matrix ρ^{det} undergoes complex conjugation, as described in Eq. (5.10) – if the Hamiltonian $H^\nu = H_{\text{vac}} + H_{\text{mat}}$ is transformed as $H^\nu \rightarrow -(H^\nu)^*$. This requires a simultaneous transformation of both the vacuum and the matter terms. The transformation of H_{vac} is described in Eq. (5.12) and involves a change in the octant of θ_{12} , as well as a change in the neutrino mass ordering (*i.e.*, the sign of Δm_{31}^2), which is why it has been called “generalized mass-ordering degeneracy” in Ref. [202]. As for H_{mat} we need:

$$\begin{aligned} [\mathcal{E}_{ee}(x) - \mathcal{E}_{\mu\mu}(x)] &\rightarrow -[\mathcal{E}_{ee}(x) - \mathcal{E}_{\mu\mu}(x)] - 2, \\ [\mathcal{E}_{\tau\tau}(x) - \mathcal{E}_{\mu\mu}(x)] &\rightarrow -[\mathcal{E}_{\tau\tau}(x) - \mathcal{E}_{\mu\mu}(x)], \\ \mathcal{E}_{\alpha\beta}(x) &\rightarrow -\mathcal{E}_{\alpha\beta}^*(x) \quad (\alpha \neq \beta), \end{aligned} \tag{5.18}$$

see Refs. [195, 201, 202]. As seen in Eqs. (5.14), (5.15) and (5.16) the matrix $\mathcal{E}_{\alpha\beta}(x)$ depends on the chemical composition of the medium, which may vary along the neutrino trajectory, so that in general the condition in Eq. (5.18) is fulfilled only in an approximate way. The degeneracy becomes exact in the following two cases:¹

- if the effective NSI coupling to neutrons vanishes, so that $\varepsilon_{\alpha\beta}^{n,V} = 0$ in Eq. (5.15). In terms of fundamental quantities this occurs when $\varepsilon_{\alpha\beta}^{u,V} = -2\varepsilon_{\alpha\beta}^{d,V}$, *i.e.*, the NSI couplings are proportional to the electric charge of quarks. In our parametrization this corresponds to the “equator” $\eta = 0$ for arbitrary ζ , as shown in Eq. (5.16);
- if the neutron/proton ratio $Y_n(x)$ is constant along the entire neutrino propagation path. This is certainly the case for reactor and long-baseline experiments, where only the Earth’s mantle is involved, and to a good approximation also for atmospheric neutrinos, since the differences in chemical composition between mantle and core can safely be neglected in the context of NSI [200]. In this case the matrix $\mathcal{E}_{\alpha\beta}(x)$ becomes independent of x and can be regarded as a new phenomenological parameter, as we will describe in Sec. 5.1.1.

Further details on the implications of this degeneracy for different classes of neutrino experiments (solar, atmospheric, *etc.*) is provided below in the corresponding section.

Matter potential in atmospheric and long-baseline neutrinos

As discussed in Ref. [200], in the Earth the neutron/proton ratio $Y_n(x)$ which characterizes the matter chemical composition can be taken to be constant to very good approximation. The PREM model [204] fixes $Y_n = 1.012$ in the Mantle and $Y_n = 1.137$ in the Core, with

¹Strictly speaking, Eq. (5.18) can be satisfied exactly for *any* matter chemical profile $Y_n(x)$ if $\varepsilon_{\alpha\beta}^{n,V}$ and $\varepsilon_{\alpha\beta}^{e,V} + \varepsilon_{\alpha\beta}^{p,V}$ are allowed to transform independently of each other. This possibility, however, is incompatible with the factorization constraint of Eq. (5.4), so it will not be discussed here.

an average value $Y_n^\oplus = 1.051$ all over the Earth. Setting therefore $Y_n(x) \equiv Y_n^\oplus$ in Eqs. (5.14) and (5.15) we get $\mathcal{E}_{\alpha\beta}(x) \equiv \varepsilon_{\alpha\beta}^\oplus$ with:

$$\varepsilon_{\alpha\beta}^\oplus = \varepsilon_{\alpha\beta}^{e,V} + \left(2 + Y_n^\oplus\right)\varepsilon_{\alpha\beta}^{u,V} + \left(1 + 2Y_n^\oplus\right)\varepsilon_{\alpha\beta}^{d,V} = \left(\varepsilon_{\alpha\beta}^{e,V} + \varepsilon_{\alpha\beta}^{p,V}\right) + Y_n^\oplus\varepsilon_{\alpha\beta}^{n,V}. \quad (5.19)$$

If we impose quark-lepton factorization as in Eq. (5.16) we get:

$$\begin{aligned} \varepsilon_{\alpha\beta}^\oplus &= \sqrt{5} \left[\cos \eta (\cos \zeta + \sin \zeta) + Y_n^\oplus \sin \eta \right] (\chi^L + \chi^R) \varepsilon_{\alpha\beta} \\ &= \sqrt{5} \left[\cos \eta' + Y_n^\oplus \sin \eta' \right] (\chi^L + \chi^R) \varepsilon'_{\alpha\beta}. \end{aligned} \quad (5.20)$$

In other words, within this approximation the analysis of atmospheric and LBL neutrinos holds for any combination of NSI with up, down or electrons and it can be performed in terms of the effective NSI couplings $\varepsilon_{\alpha\beta}^\oplus$, which play the role of phenomenological parameters. In particular, the best-fit value and allowed ranges of $\varepsilon_{\alpha\beta}^\oplus$ are independent of η and ζ , while the bounds on $\varepsilon_{\alpha\beta}$ simply scale as $[\cos \eta (\cos \zeta + \sin \zeta) + Y_n^\oplus \sin \eta]$. Moreover, it is immediate to see that for $\eta' = \arctan(-1/Y_n^\oplus) \approx -43.6^\circ$, with η' defined in Eq. (5.17), the contribution of NSI to the matter potential vanishes, so that no bound on $\varepsilon_{\alpha\beta}$ can be derived from atmospheric and LBL data in such case. This would be approximately the case, for example, for $U(1)'$ models associated to the combination $B - 2L_e + \alpha L_\mu - \beta L_\tau$ and, consequently, oscillation bounds are significantly relaxed for this type of models [185].

Following the approach of Ref. [200], the matter Hamiltonian H_{mat} , given in Eq. (5.13) after setting $\mathcal{E}_{\alpha\beta}(x) \equiv \varepsilon_{\alpha\beta}^\oplus$, can be parametrized in a way that mimics the structure of the vacuum term:

$$H_{\text{mat}} = Q_{\text{rel}} U_{\text{mat}} D_{\text{mat}} U_{\text{mat}}^\dagger Q_{\text{rel}}^\dagger \quad \text{with} \quad \begin{cases} Q_{\text{rel}} = \text{diag} \left(e^{i\alpha_1}, e^{i\alpha_2}, e^{-i\alpha_1 - i\alpha_2} \right), \\ U_{\text{mat}} = R_{12}(\varphi_{12}) R_{13}(\varphi_{13}) \tilde{R}_{23}(\varphi_{23}, \delta_{\text{NS}}), \\ D_{\text{mat}} = \sqrt{2} G_F N_e(x) \text{diag}(\varepsilon_\oplus, \varepsilon'_\oplus, 0) \end{cases} \quad (5.21)$$

where $R_{ij}(\varphi_{ij})$ is a rotation of angle φ_{ij} in the ij plane and $\tilde{R}_{23}(\varphi_{23}, \delta_{\text{NS}})$ is a complex rotation by angle φ_{23} and phase δ_{NS} . Note that the two phases α_1 and α_2 included in Q_{rel} are not a feature of neutrino-matter interactions, but rather a relative feature of the vacuum and matter terms. In order to simplify the analysis we impose that two eigenvalues of H_{mat} are equal, $\varepsilon'_\oplus = 0$. This assumption is justified since, as shown in Ref. [205], in this case strong cancellations in the oscillation of atmospheric neutrinos occur, and this is precisely the situation in which the weakest constraints can be placed. Setting $\varepsilon'_\oplus \rightarrow 0$ implies that the φ_{23} angle and the δ_{NS} phase disappear from neutrino oscillations, so that the effective NSI couplings $\varepsilon_{\alpha\beta}^\oplus$ can be parametrized as:

$$\begin{aligned} \varepsilon_{ee}^\oplus - \varepsilon_{\mu\mu}^\oplus &= \varepsilon_\oplus (\cos^2 \varphi_{12} - \sin^2 \varphi_{12}) \cos^2 \varphi_{13} - 1, \\ \varepsilon_{\tau\tau}^\oplus - \varepsilon_{\mu\mu}^\oplus &= \varepsilon_\oplus (\sin^2 \varphi_{13} - \sin^2 \varphi_{12} \cos^2 \varphi_{13}), \\ \varepsilon_{e\mu}^\oplus &= -\varepsilon_\oplus \cos \varphi_{12} \sin \varphi_{12} \cos^2 \varphi_{13} e^{i(\alpha_1 - \alpha_2)}, \\ \varepsilon_{e\tau}^\oplus &= -\varepsilon_\oplus \cos \varphi_{12} \cos \varphi_{13} \sin \varphi_{13} e^{i(2\alpha_1 + \alpha_2)}, \\ \varepsilon_{\mu\tau}^\oplus &= \varepsilon_\oplus \sin \varphi_{12} \cos \varphi_{13} \sin \varphi_{13} e^{i(\alpha_1 + 2\alpha_2)}. \end{aligned} \quad (5.22)$$

As further simplification, in order to keep the fit manageable we assume real NSI, which we implement by choosing $\alpha_1 = \alpha_2 = 0$ and $-\pi/2 \leq \varphi_{ij} \leq \pi/2$, and also restrict $\delta_{\text{CP}} \in \{0, \pi\}$. It is important to note that with these approximations the formalism for atmospheric and

long-baseline data is CP-conserving; we will go back to this point when discussing the experimental results included in the fit. In addition to atmospheric and LBL experiments, important information on neutrino oscillation parameters is provided also by reactor experiments with a baseline of about 1 km. Due to the very small amount of matter crossed, both standard and non-standard matter effects are completely irrelevant for these experiments, so that neutrino propagation depends only on the vacuum parameters.

Matter potential for solar and KamLAND neutrinos

For the study of propagation of solar and KamLAND neutrinos one can work in the one mass dominance approximation, $\Delta m_{31}^2 \rightarrow \infty$ (the same approach of Chapter 2). In this limit the neutrino evolution can be calculated in an effective 2×2 model described by the Hamiltonian $H_{\text{eff}} = H_{\text{vac}}^{\text{eff}} + H_{\text{mat}}^{\text{eff}}$ (similarly to Eqs. 2.72 and 2.73), with:

$$H_{\text{vac}}^{\text{eff}} = \frac{\Delta m_{21}^2}{4E_\nu} \begin{pmatrix} -\cos 2\theta_{12} & \sin 2\theta_{12} e^{i\delta_{\text{CP}}} \\ \sin 2\theta_{12} e^{-i\delta_{\text{CP}}} & \cos 2\theta_{12} \end{pmatrix}, \quad (5.23)$$

$$H_{\text{mat}}^{\text{eff}} = \sqrt{2}G_F N_e(x) \left[\frac{c_{13}^2}{2} \begin{pmatrix} 1 & 0 \\ 0 & -1 \end{pmatrix} + [\xi^e + \xi^p + Y_n(x)\xi^n] (\chi^L + \chi^R) \begin{pmatrix} -\varepsilon_D & \varepsilon_N \\ \varepsilon_N^* & \varepsilon_D \end{pmatrix} \right], \quad (5.24)$$

where we have imposed the quark-lepton factorization of Eq. (5.16). The coefficients ε_D and ε_N are related to the original parameters $\varepsilon_{\alpha\beta}$ by the following relations:

$$\begin{aligned} \varepsilon_D &= c_{13}s_{13} \text{Re}(s_{23}\varepsilon_{e\mu} + c_{23}\varepsilon_{e\tau}) - (1 + s_{13}^2) c_{23}s_{23} \text{Re}(\varepsilon_{\mu\tau}) \\ &\quad - \frac{c_{13}^2}{2} (\varepsilon_{ee} - \varepsilon_{\mu\mu}) + \frac{s_{23}^2 - s_{13}^2 c_{23}^2}{2} (\varepsilon_{\tau\tau} - \varepsilon_{\mu\mu}), \end{aligned} \quad (5.25)$$

$$\varepsilon_N = c_{13} (c_{23}\varepsilon_{e\mu} - s_{23}\varepsilon_{e\tau}) + s_{13} [s_{23}^2 \varepsilon_{\mu\tau} - c_{23}^2 \varepsilon_{\mu\tau}^* + c_{23}s_{23} (\varepsilon_{\tau\tau} - \varepsilon_{\mu\mu})]. \quad (5.26)$$

Denoting by S_{eff} the 2×2 unitary matrix obtained integrating H_{eff} along the neutrino trajectory, the full density matrix ρ^{det} introduced in Eq. (5.9) can be written as:

$$\rho_{\alpha\beta}^{\text{det}} = c_{13}^2 [A_{\alpha\beta} P_{\text{osc}} + B_{\alpha\beta} P_{\text{int}} + iC_{\alpha\beta} P_{\text{ext}}] + D_{\alpha\beta} \quad (5.27)$$

where the effective probabilities P_{osc} , P_{int} and P_{ext} are given by

$$P_{\text{osc}} \equiv |S_{21}^{\text{eff}}|^2, \quad P_{\text{int}} \equiv \text{Re}(S_{11}^{\text{eff}} S_{21}^{\text{eff}*}), \quad P_{\text{ext}} \equiv \text{Im}(S_{11}^{\text{eff}} S_{21}^{\text{eff}*}), \quad (5.28)$$

and the numerical coefficients $A_{\alpha\beta}$, $B_{\alpha\beta}$, $C_{\alpha\beta}$ and $D_{\alpha\beta}$ are defined as

$$\begin{aligned} A_{\alpha\beta} &\equiv O_{\alpha 2} O_{\beta 2} - O_{\alpha 1} O_{\beta 1}, & B_{\alpha\beta} &\equiv O_{\alpha 1} O_{\beta 2} + O_{\alpha 2} O_{\beta 1}, \\ C_{\alpha\beta} &\equiv O_{\alpha 1} O_{\beta 2} - O_{\alpha 2} O_{\beta 1}, & D_{\alpha\beta} &\equiv \sum_{i=\text{all}} O_{\alpha i} O_{\beta i} |O_{ei}|^2. \end{aligned} \quad (5.29)$$

with $O = R_{23}(\theta_{23})R_{13}(\theta_{13})$. Unlike in Ref. [196] where NSI did *not* affect the scattering process and only the ρ_{ee}^{det} entry (which depends exclusively on P_{osc}) was required, a rephasing of S_{eff} now produces visible consequences as it affects P_{int} and P_{ext} . Moreover, ν_μ and ν_τ are no longer indistinguishable as their scattering amplitude may be different under NSI, so that the θ_{23} angle acquires relevance. Hence, for each fixed value of η and ζ the density matrix ρ^{det} for solar and KamLAND neutrinos depends effectively on eight quantities: the four real oscillation parameters θ_{12} , θ_{13} , θ_{23} and Δm_{21}^2 , the real ε_D and

complex ε_N matter parameters, and the CP phase δ_{CP} . As stated in Sec. 5.1.1 in this work we will assume real NSI, implemented here by setting $\delta_{\text{CP}} \in \{0, \pi\}$ and considering only real values for ε_N .

Unlike in the Earth, the matter chemical composition of the Sun varies substantially along the neutrino trajectory, and consequently the potential depends non-trivially on the specific combinations of $(\xi^e + \xi^p)$ and ξ^n couplings – *i.e.*, on the value of η' as determined by the (η, ζ) parameters. This implies that the generalized mass-ordering degeneracy is not exact, except for $\eta = 0$ (in which case the NSI potential is proportional to the standard MSW potential and an exact inversion of the matter sign is possible). However the transformation described in Eqs. (5.12) and (5.18) still results in a good fit to the global analysis of oscillation data for a wide range of values of η' , and non-oscillation data are needed to break this degeneracy [202].

Departures from adiabaticity in presence of NSI

When computing neutrino evolution in the Sun, it is often assumed that it takes place in the adiabatic regime, as this considerably simplifies the calculation, as discussed in Chapter 2. While this is the case for neutrino oscillations within the LMA solution with a standard matter potential, it is worthwhile asking if the inclusion of NP effects (such as NSI) can lead to non-adiabatic transitions. If this were the case, it would require special care and may lead to interesting new phenomenological consequences. This possibility has been largely overlooked in the literature, where most studies of NSI in the Sun assume adiabatic transitions.

Let us consider the two-neutrino case, with a matter potential that depends on the position x along the neutrino path inside the Sun. In the instantaneous mass basis, the Hamiltonian can be written as:

$$i \frac{d}{dx} \begin{pmatrix} \tilde{\nu}_1 \\ \tilde{\nu}_2 \end{pmatrix} = \begin{pmatrix} -\Delta_m(x) & -i\theta'_m(x) \\ i\theta'_m(x) & \Delta_m(x) \end{pmatrix} \begin{pmatrix} \tilde{\nu}_1 \\ \tilde{\nu}_2 \end{pmatrix} \quad (5.30)$$

where $\theta_m(x)$ and $\Delta_m(x)$ refer to the mixing angle and oscillation frequency in the presence of matter effects, and $\theta'(x) \equiv d\theta(x)/dx$. In this basis, transitions between $\tilde{\nu}_1 \leftrightarrow \tilde{\nu}_2$ are negligible as long as the off-diagonal terms $\theta'_m(x)$ are small compared to the diagonal entries $\Delta_m(x)$ in Eq. (5.30). This leads to the adiabaticity condition discussed in Eq. (2.83). Neutrino transitions will be adiabatic if this condition is satisfied along all points in the neutrino trajectory. Of course, this argument is general and may be applied both in the standard case and in the presence of NP. In the present work neutrino propagation is described by the effective 2×2 Hamiltonian H_{eff} introduced in Eqs. (5.23) and (5.24). Assuming $\delta_{\text{CP}} = 0$ and real NSI, so that H_{eff} is traceless and real with $H_{11}^{\text{eff}} = -H_{22}^{\text{eff}}$ and $H_{12}^{\text{eff}} = H_{21}^{\text{eff}}$, we can write:

$$\theta_m(x) \equiv \frac{1}{2} \arctan \left[H_{12}^{\text{eff}}(x) / H_{22}^{\text{eff}}(x) \right] \quad \text{and} \quad \Delta_m(x) \equiv \sqrt{\left[H_{12}^{\text{eff}}(x) \right]^2 + \left[H_{22}^{\text{eff}}(x) \right]^2}. \quad (5.31)$$

In the presence of NSI, for a given matter density and neutrino energy, it is possible to choose ε_D and ε_N so that the contribution from NP cancels the standard one, resulting in $\Delta_m(x) \rightarrow 0$. It is easy to show analytically that, for such values, the adiabatic condition in Eq. (2.83) is no longer satisfied. Specifically, such cancellation takes place when:

$$\begin{aligned} \left[\xi^e + \xi^p + Y_n(x)\xi^n \right] (\chi^L + \chi^R) \varepsilon_D &\rightarrow -\frac{\Delta m_{12}^2 \cos 2\theta_{12}}{4E_\nu V(x)} + \frac{c_{13}^2}{2}, \\ \left[\xi^e + \xi^p + Y_n(x)\xi^n \right] (\chi^L + \chi^R) \varepsilon_N &\rightarrow -\frac{\Delta m_{12}^2 \sin 2\theta_{12}}{4E_\nu V(x)}, \end{aligned} \quad (5.32)$$

where $V(x) \equiv \sqrt{2}G_F N_e(x)$ is the SM matter potential. In other words, for a neutrino with a given energy E_ν at some point x along the trajectory, it is possible to find a pair of values $(\varepsilon_D, \varepsilon_N)$ for which transitions are no longer adiabatic. Note that the cancellation condition for ε_D depends on $\cos 2\theta_{12}$ and therefore will take different values for the LMA and LMA-D regions, while the corresponding value for ε_N will remain invariant under a change of octant for θ_{12} . Also, as the cancellation conditions in Eqs. (5.32) depend on the values of ξ^f , the regions will depend on whether NSI take place with electrons/protons, neutrons, or a combination of the two.

Figure 5.1 shows the regions where the transitions are not adiabatic, for NSI with protons or electrons (left panel) and for NSI with neutrons (right panel). The shaded pale blue regions show the results from a numerical computation. In contrast, the coloured lines show the points satisfying the analytic conditions in Eqs. (5.32), for neutrino energies between 1 MeV (green lines, towards the left edge of the region) and 20 MeV (blue lines, towards the right edge of the region), for $\theta_{12} = 33^\circ$ and $\Delta m_{12}^2 = 7.5 \times 10^{-5} \text{ eV}^2$. As can be seen, the agreement with the numerical computation is excellent. Also, note the very different shape of the regions in the two panels. The reason behind this is that for NSI with electrons or protons the dependence with E_ν and x comes in Eqs. (5.32) through the product $E_\nu V(x)$, while for NSI with neutrons there is an extra dependence on $Y_n(x)$. Therefore, while the regions in the left panel in Fig. 5.1 span essentially a straight line, in the right panel the dependence is more complex.

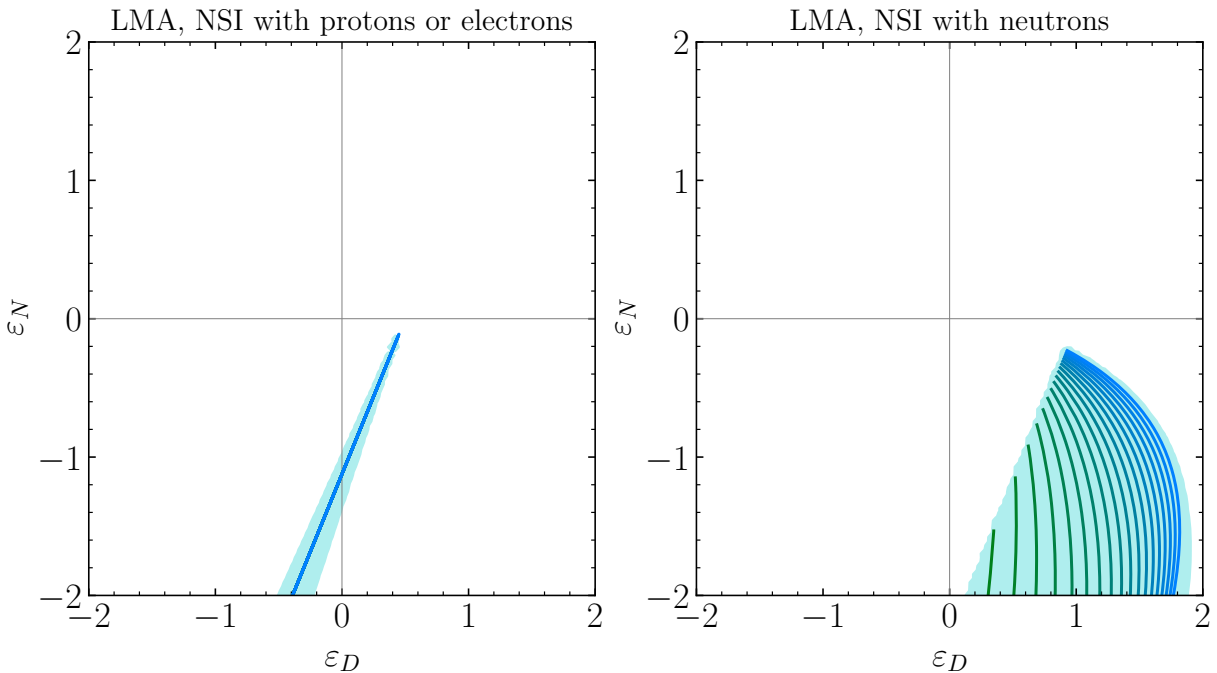


Figure 5.1: Departure from the adiabatic regime in presence of NSI, for a solar mixing angle in the LMA region. The pale blue regions show the values of NSI parameters leading to $\gamma^{-1} > 1$, obtained from a numerical computation. The coloured lines show the values of NSI parameters where Eqs. (5.32) are satisfied at some point along the neutrino trajectory, for a neutrino produced at the center of the Sun. The different lines in the right panel correspond to neutrino energies between 1 MeV (green lines, at the left edge of the region) and 20 MeV (blue lines, towards the right edge of the region).

In our past study [196], where only NSI with quarks were considered, neutrino evolution in the Sun was based on a fully numerical approach. In the present work, however, exploring the full parameter space of the most general NSI with protons, electrons, and

neutrons without assuming adiabaticity is challenging from the numerical point of view. To overcome this problem in our calculations we start by evaluating the adiabaticity index for the point in the NSI and oscillation parameter space to be surveyed. If for that point $\gamma^{-1}(x) < 1$ along the whole neutrino trajectory in the Sun we use the adiabatic approximation when computing the corresponding flavour transition probabilities and the subsequent prediction for all observables and χ^2 value. If, on the contrary, the adiabaticity condition is violated somewhere inside the Sun such point is removed from the parameter space to be surveyed. We do so because we have verified that for parameter values for which adiabaticity in the Sun is violated the predicted observables with the properly computed flavour transition probability without assuming adiabaticity never lead to good description of the data. But we also find that if one evaluates the probabilities for those parameters wrongly using the adiabatic approximation, one can find a “fake” good fit to the Solar and KamLAND data, which would lead to wrong conclusions about their acceptability. In conclusion, the adiabatic approximation can be safely used for the purposes of this work as long as one removes from the parameter space those points for which adiabaticity in the Sun is violated. Furthermore, once the data of atmospheric neutrino experiments is added to the fit, it totally disfavors the parameter regions where transitions in the Sun are not adiabatic.

5.1.2 Neutrino detection cross sections in the presence of NSI

Neutrino scattering data is also sensitive to NC NSI as they would affect the interaction rates directly [175, 206–210]. Therefore the combination of oscillation and scattering data may be used to break the LMA-D degeneracy (see for example Refs. [199, 211] for early works on this topic).

In this respect, it should be mentioned that all the atmospheric, reactor and accelerator experiments included in our fit rely on CC processes in order to detect neutrinos, so the corresponding cross-section is not affected by the NC-like NSI considered here.² This implies that the σ^{det} generalized cross-section matrix entering Eq. (5.9) is diagonal in the SM flavour basis, and its non-zero entries coincide with the usual SM cross-section, that is,

$$\sigma^{\text{det}} = \text{diag}(\sigma_e^{\text{SM}}, \sigma_\mu^{\text{SM}}, \sigma_\tau^{\text{SM}}) \quad \text{for CC processes.} \quad (5.33)$$

Some solar neutrino experiments, on the contrary, are sensitive to NC NSI in some of the detection processes involved. This is the case of Borexino and SK (and SNO, albeit with lower sensitivity) which observe neutrino-electron ES, which may be affected by electron NSI. Regarding NSI with nuclei SNO can also probe axial-vector NSI in NC events, and CE ν NS experiments are able to set important constraints on vector interactions. In the rest of this subsection we review the phenomenological implications for these three cases separately.

Neutrino-electron elastic scattering

The presence of flavour-changing effects in NSI implies that the SM flavour basis no longer coincides with the interaction eigenstates of the neutrino-electron scattering. In such case the generalized cross section σ^{det} can be obtained as the integral over the electron recoil

²It should be noted that a subleading component of NC interactions is present as background in many of these experiments, so that NSI parameter may in principle have an impact on the number of events. During my PhD, I have been studying the effects of NCNSIs using NOvA background of NC events. See more in [212].

kinetic energy T_e of the following matrix expression:

$$\frac{d\sigma^{\text{ES}}}{dT_e}(E_\nu, T_e) = \frac{2G_F^2 m_e}{\pi} \left\{ C_L^2 \left[1 + \frac{\alpha}{\pi} f_-(y) \right] + C_R^2 (1-y)^2 \left[1 + \frac{\alpha}{\pi} f_+(y) \right] - \{C_L, C_R\} \frac{m_e y}{2E_\nu} \left[1 + \frac{\alpha}{\pi} f_\pm(y) \right] \right\} \quad (5.34)$$

where $y \equiv T_e/E_\nu$ and f_+ , f_- , f_\pm are loop functions given in Ref. [213], while α stands for the fine-structure constant and m_e is the electron mass. In this formula C_L and C_R are 3×3 hermitian matrices which incorporate both SM and NSI contributions:

$$C_{\alpha\beta}^L \equiv c_{L\beta} \delta_{\alpha\beta} + \varepsilon_{\alpha\beta}^{e,L} \quad \text{and} \quad C_{\alpha\beta}^R \equiv c_{R\beta} \delta_{\alpha\beta} + \varepsilon_{\alpha\beta}^{e,R}. \quad (5.35)$$

The effective couplings $c_{L\beta}$ and $c_{R\beta}$ account for the SM part, and contain both the flavour-universal NC terms and the ν_e -only CC scattering:

$$\begin{aligned} c_{Le} &= \rho \left[\kappa_e(T_e) \sin^2 \theta_w - \frac{1}{2} \right] + 1, & c_{Re} &= \rho \kappa_e(T_e) \sin^2 \theta_w, \\ c_{L\tau} = c_{L\mu} &= \rho \left[\kappa_\mu(T_e) \sin^2 \theta_w - \frac{1}{2} \right], & c_{R\tau} = c_{R\mu} &= \rho \kappa_\mu(T_e) \sin^2 \theta_w, \end{aligned} \quad (5.36)$$

with θ_w being the weak mixing angle, and ρ and $\kappa_\beta(T_e)$ departing from 1 due to radiative corrections of the gauge boson self-energies and vertices [213]. It is immediate to see that, if the NSI terms $\varepsilon_{\alpha\beta}^{e,L}$ and $\varepsilon_{\alpha\beta}^{e,R}$ are set to zero, the matrix $d\sigma^{\text{ES}}/dT_e$ becomes diagonal. Imposing the factorization of Eq. (5.4) for the vector (+) and axial-vector (−) NSI we get:

$$\varepsilon_{\alpha\beta}^{e,V(A)} = \varepsilon_{\alpha\beta}^{e,L} \pm \varepsilon_{\alpha\beta}^{e,R} = \varepsilon_{\alpha\beta} \xi^e (\chi^L \pm \chi^R) = \sqrt{5} \cos \eta \sin \zeta (\chi^L \pm \chi^R) \varepsilon_{\alpha\beta}. \quad (5.37)$$

Let us finalize this section by discussing briefly the impact that the inclusion of NSI effects on ES could have on the generalized mass-ordering degeneracy discussed in Sec. 5.1.1. We have seen that the parameter transformations (5.12) and (5.18) lead to a complex conjugation of the neutrino density matrix, $\rho^{\text{det}} \rightarrow [\rho^{\text{det}}]^*$. As shown in Eq. (5.10), this does not affect the overall number of events (thus resulting in the appearance of the degeneracy) as long as it is accompanied by a similar transformation $\sigma^{\text{det}} \rightarrow [\sigma^{\text{det}}]^*$. The latter can be realized either as $C_L \rightarrow C_L^*$ and $C_R \rightarrow C_R^*$, which occur when both $\varepsilon_{\alpha\beta}^{e,L}$ and $\varepsilon_{\alpha\beta}^{e,R}$ undergo simple complex conjugation, or as $C_L \rightarrow -C_L^*$ and $C_R \rightarrow -C_R^*$, which require ad-hoc transformations of the diagonal entries $\varepsilon_{\alpha\alpha}^{e,L}$ and $\varepsilon_{\alpha\alpha}^{e,R}$ to compensate for the SM contribution of Eq. (5.36). While conceptually identical to the situation occurring in neutrino oscillations, where the extra freedom introduced by NSI allows to “flip the sign” of the standard matter effects, the specific transformations required to achieve a perfect symmetry of σ^{det} differ from those of Eq. (5.18). In principle one may first choose $\varepsilon_{\alpha\beta}^{e,L}$ and $\varepsilon_{\alpha\beta}^{e,R}$ accounting for Eq. (5.36) and then tune $\varepsilon_{\alpha\beta}^{p,V}$ and $\varepsilon_{\alpha\beta}^{n,V}$ to fulfill Eq. (5.18), but this procedure is incompatible with the factorization constraint of Eq. (5.4), which assumes that all NSI have the same neutrino flavour structure independently of their chirality and of the charged fermion type. The net conclusion is that, for NSI involving electrons (that is, $\zeta \neq 0$) and assuming that the factorization in Eq. (5.4) holds, ES effects *break* the generalized mass-ordering degeneracy.

SNO neutral-current cross-section

The SNO experiment observed NC interactions of solar neutrinos on deuterium, as discussed briefly in Section 3.1. At low energies, the corresponding cross section is dominated by the Gamow-Teller transition and it scales as g_A^2 where g_A is the coupling of the neutrino current to the axial isovector hadronic current which in the SM is given by $g_A \equiv g_A^u - g_A^d$ [214–216]. Using that the nuclear corrections to g_A are the same when the NSI are added, we obtain that in the presence of the NC NSI we can write

$$\sigma^{\text{det}} = \sigma_{\text{SM}} \left(\frac{G_A}{g_A} \right)^2 \quad (5.38)$$

where G_A is an hermitian matrix in flavour space

$$\frac{G_A}{g_A} = \delta_{\alpha\beta} + \varepsilon_{\alpha\beta}^{u,A} - \varepsilon_{\alpha\beta}^{d,A} = \delta_{\alpha\beta} + \varepsilon_{\alpha\beta} (\xi^u - \xi^d) (\chi^L - \chi^R), \quad (5.39)$$

Clearly for vector NSI ($\chi^L = \chi^R$), the NSI contributions vanish and σ^{det} takes just the SM value times the identity in flavour space. Conversely for axial-vector NSI one gets $\chi^L - \chi^R = 1$ and the NSI term contributes.

Coherent elastic neutrino-nucleus scattering

The generalized cross-section σ^{det} describing CE ν NS in the presence of NSI can be obtained by integrating over the recoil energy of the nucleus E_R the following expression (see Section 3.5):

$$\frac{d\sigma^{\text{coh}}(E_R, E_\nu)}{dE_R} = \frac{G_F^2}{2\pi} Q^2 F^2(q^2) m_A \left(2 - \frac{m_A E_R}{E_\nu^2} \right) \quad (5.40)$$

where m_A is the mass of the nucleus and $F(q^2)$ is its nuclear form factor evaluated at the squared momentum transfer of the process, $q^2 = 2m_A E_R$. In this formalism, the structure in flavour space which characterizes σ^{det} is encoded into the hermitian matrix \mathcal{Q} , which is just the generalization of the weak charge of the nucleus for this formalism. For a nucleus with Z protons and N neutrons, it reads:

$$\mathcal{Q}_{\alpha\beta} = Z(g_p^V \delta_{\alpha\beta} + \varepsilon_{\alpha\beta}^{p,V}) + N(g_n^V \delta_{\alpha\beta} + \varepsilon_{\alpha\beta}^{n,V}) \quad (5.41)$$

where $g_p^V = 1/2 - 2\sin^2\theta_w$ and $g_n^V = -1/2$ are the SM vector couplings to protons and neutrons, respectively. In experiments with very short baselines such as those performed so far, neutrinos have no time to oscillate and therefore the density matrix at the detector ρ^{det} is just the identity matrix. Taking this explicitly into account in Eq. (5.9) we get:

$$\rho^{\text{det}} = I \quad \Rightarrow \quad N_{\text{ev}} \propto \mathcal{Q}_\alpha^2 \quad \text{with} \quad \mathcal{Q}_\alpha^2 \equiv \left[\mathcal{Q}^2 \right]_{\alpha\alpha} = (\mathcal{Q}_{\alpha\alpha})^2 + \sum_{\beta \neq \alpha} |\mathcal{Q}_{\alpha\beta}|^2 \quad (5.42)$$

for incident neutrino flavour α , thus recovering the expressions for the ordinary weak charges \mathcal{Q}_α^2 used in our former publications. Coming back to Eq. (5.41), let us notice that it can be rewritten as:

$$\mathcal{Q}_{\alpha\beta} = Z \left[(g_p^V + Y_n^{\text{coh}} g_n^V) \delta_{\alpha\beta} + \varepsilon_{\alpha\beta}^{\text{coh}} \right] \quad \text{with} \quad \varepsilon_{\alpha\beta}^{\text{coh}} \equiv \varepsilon_{\alpha\beta}^{p,V} + Y_n^{\text{coh}} \varepsilon_{\alpha\beta}^{n,V} \quad (5.43)$$

where $Y_n^{\text{coh}} \equiv N/Z$ is the neutron/proton ratio characterizing the target of a given CE ν NS experiment. Imposing the quark-lepton factorization of Eq. (5.4) we get:

$$\varepsilon_{\alpha\beta}^{\text{coh}} = \varepsilon_{\alpha\beta} (\xi^p + Y_n^{\text{coh}} \xi^n) (\chi^L + \chi^R) = \sqrt{5} \left[\cos\eta \cos\zeta + Y_n^{\text{coh}} \sin\eta \right] (\chi^L + \chi^R) \varepsilon_{\alpha\beta}. \quad (5.44)$$

Similarly to Eq. (5.20), this expression suggests that the analysis of coherent scattering data can be performed in terms of the effective couplings $\varepsilon_{\alpha\beta}^{\text{coh}}$, whose best-fit value and allowed ranges are independent of (η, ζ) . As a consequence, the bounds on $\varepsilon_{\alpha\beta}$ simply scale as $[\cos\eta \cos\zeta + Y_n^{\text{coh}} \sin\eta]$. In analogy to Eq. (5.17), one can define an effective angle $\tan\eta'' \equiv \tan\eta / \cos\zeta$ parametrizing the direction in the (ξ^p, ξ^n) plane, such that all CE ν NS experiments depend on (η, ζ) only through the combination η'' . In particular, it is straightforward to see that a coherent scattering experiment characterized by a given Y_n^{coh} ratio will yield no bound on $\varepsilon_{\alpha\beta}$ for $\eta'' = \arctan(-1/Y_n^{\text{coh}})$, as for this value the effects of NSI on protons and neutrons cancel exactly. Such a cancellation can be obtained, for example, for models of the type proposed in Ref. [188], where the Z' associated to a new gauge symmetry also has a sizable kinetic mixing with the SM photon, which allows for arbitrary relative size of NSI with up and down quarks.

5.2 New Physics scenarios of neutrino interactions

As outlined in the preceding section, NSI can manifest in neutrino experiments through two distinct mechanisms: modifications to flavor propagation (governed by oscillation dynamics) and alterations to scattering processes (affecting both production and detection channels). In this section, we focus only on the NP effects on the interaction cross-sections at the detection stage, neglecting for simplicity its possible impact on flavor transitions during propagation. In this approach we preserve the standard oscillation framework but introduce new couplings between neutrinos and first-generation fermions (e, d, u) via the exchange of hypothetical mediators:

- Non-zero neutrino magnetic moment μ_ν ;
- Neutral scalar boson ϕ ;
- Neutral pseudoscalar boson φ ;
- Neutral vector boson Z' from $U(1)$ gauge symmetries;

A non-vanishing neutrino magnetic moment enables spin-flip interactions with charged particles, producing characteristic low-energy recoil spectra in scattering processes. In parallel, the scalar (ϕ) and pseudoscalar (φ) mediators generate Yukawa-type interactions, which modify the differential cross-section through distinct recoil energy dependencies. The vector mediator Z' introduces new current-current interactions, analogous to the SM weak force but with couplings dependent on the mediator's mass and the charge of the new gauge symmetry. Each scenario predicts unique signatures in neutrino detectors, such as deviations in event rates, spectral distortions, or anomalous scattering angles. By analysing these phenomenological consequences, we establish constraints on the parameter spaces of the mediators (coupling strengths, masses) and the neutrino magnetic moment, while distinguishing the interaction-centric aspects of this kind of NP from propagation-dependent effects. Following Ref. [2], in the rest of this section we will focus on solar experiments sensitive to ES interactions, such as Borexino.

5.2.1 Neutrino Magnetic-Moments

In the presence of a neutrino magnetic moment (μ_ν) the scattering cross sections on electrons get additional contributions which do not interfere with the SM ones. Neutrino magnetic moments arise in a variety of BSM models and, in particular, they do not

need to be flavour-universal. Therefore, in what follows we will allow different magnetic moments for the different neutrino flavours – albeit still imposing that they are flavour-diagonal. Under this assumption the ES differential cross section for either neutrinos or antineutrinos, up to order $\mathcal{O}(y^2)$, takes the form [217]

$$\frac{d\sigma_{\beta}^{\mu\nu}}{dT_e} = \frac{d\sigma_{\beta}^{\text{SM}}}{dT_e} + \left(\frac{\mu_{\nu\beta}}{\mu_B}\right)^2 \frac{\alpha^2 \pi}{m_e^2} \left[\frac{1}{T_e} - \frac{1}{E_\nu}\right]. \quad (5.45)$$

Since no flavour-changing contributions are present in this case, the expression for the number of ES interactions will be just proportional to the probability weighted total cross section.

5.2.2 Models with light scalar, pseudoscalar, and vector mediators

Concerning the scalar, the Lagrangian we consider is [218]

$$\mathcal{L}_\phi = g_\phi \phi \left(q_\phi^e \bar{e}e + \sum_\alpha q_\phi^{\nu\alpha} \bar{\nu}_{\alpha,R} \nu_{\alpha,L} + \text{h.c.} \right) - \frac{1}{2} M_\phi^2 \phi^2, \quad (5.46)$$

where q_ϕ^j are the individual scalar charges and $j = \{\nu_\alpha, e\}$. The corresponding cross section for neutrino-electron (or antineutrino-electron) scattering is

$$\frac{d\sigma_{\beta}^{\phi}}{dT_e} = \frac{d\sigma_{\beta}^{\text{SM}}}{dT_e} + \frac{g_\phi^4 (q_\phi^{\nu\beta})^2 (q_\phi^e)^2 m_e^2 T_e}{4\pi E_\nu^2 (2m_e T_e + M_\phi^2)^2} \left(1 + \frac{T_e}{2m_e}\right), \quad (5.47)$$

where we have included all orders in T_e/E_ν and T_e/m_e (beyond the leading-order terms given in Ref. [218]), since these are non-negligible for solar event rates at Borexino.

For the pseudoscalar scenario, we consider the Lagrangian

$$\mathcal{L}_\varphi = i g_\varphi \varphi \left(q_\varphi^e \bar{e} \gamma^5 e + \sum_\alpha q_\varphi^{\nu\alpha} \bar{\nu}_{\alpha,R} \gamma^5 \nu_{\alpha,L} + \text{h.c.} \right) - \frac{1}{2} M_\varphi^2 \varphi^2, \quad (5.48)$$

where q_φ^j are the individual pseudoscalar charges and $j = \{\nu_\alpha, e\}$. The corresponding cross section for neutrino-electron (or antineutrino-electron) scattering is

$$\frac{d\sigma_{\beta}^{\varphi}}{dT_e} = \frac{d\sigma_{\beta}^{\text{SM}}}{dT_e} + \frac{g_\varphi^4 (q_\varphi^{\nu\beta})^2 (q_\varphi^e)^2 m_e T_e^2}{8\pi E_\nu^2 (2m_e T_e + M_\varphi^2)^2}. \quad (5.49)$$

As for the vector mediator, our assumed Lagrangian is:

$$\mathcal{L}_V = g_{Z'} Z'_\mu \left(q_{Z'}^e \bar{e} \gamma^\mu e + \sum_\alpha q_{Z'}^{\nu\alpha} \bar{\nu}_{\alpha,L} \gamma^\mu \nu_{\alpha,L} \right) + \frac{1}{2} M_{Z'}^2 Z'^\mu Z'_\mu, \quad (5.50)$$

with the individual vector charges $q_{Z'}^j$. Unlike for the scalar and magnetic-moment cases, a neutral vector interaction interferes with the SM contribution. The differential cross section for neutrino-electron scattering reads [219]

$$\begin{aligned} \frac{d\sigma_{\beta}^{Z'}}{dT_e} = \frac{d\sigma_{\beta}^{\text{SM}}}{dT_e} + \frac{g_{Z'}^2 m_e}{2\pi} \left\{ \frac{g_{Z'}^2 (q_{Z'}^{\nu\beta})^2 (q_{Z'}^e)^2}{(2m_e T_e + M_{Z'}^2)^2} \left[1 - \frac{m_e T_e}{2 E_\nu^2} + \frac{T_e}{2 E_\nu} \left(\frac{T_e}{E_\nu} - 2 \right) \right] \right. \\ \left. + \frac{2\sqrt{2} G_F q_{Z'}^{\nu\beta} q_{Z'}^e}{(2m_e T_e + M_{Z'}^2)} \left[c_{V\beta} \left(1 - \frac{m_e T_e}{2 E_\nu^2} \right) + c_{R\beta} \frac{T_e}{E_\nu} \left(\frac{T_e}{E_\nu} - 2 \right) \right] \right\}, \quad (5.51) \end{aligned}$$

Model	q^e	$q^{\nu e}$	$q^{\nu\mu}$	$q^{\nu\tau}$
Universal/leptonic scalar (or pseudoscalar)	1	1	1	1
$B - L$ vector	-1	-1	-1	-1
$L_e - L_\mu$ vector	1	1	-1	0
$L_e - L_\tau$ vector	1	1	0	-1

Table 5.1: Charges for the vector, scalar, and pseudoscalar mediators considered in this work.

where $c_{V\beta}$ is the SM effective vector coupling, defined as $c_{L\beta} + c_{R\beta}$, such that $c_{L\beta}, c_{R\beta}$ are defined in Eq. 5.36. For the sake of simplicity, in our calculations describing the effects of light mediators, we have neglected the small SM radiative corrections to the BSM contributions. The corresponding cross section for $\bar{\nu}_\beta e^-$ ES can be obtained from Eq. (5.51) with the exchange $c_{L\beta} \leftrightarrow c_{R\beta}$.

Similarly to the SM and the magnetic moment cases, no flavour-changing contributions are considered for scalar, pseudoscalar, or vector mediators, hence the number of interactions will be just proportional to the probability-weighted total cross section.

For scalar and pseudoscalar mediators we will focus on a model in which the mediator couples universally to fermions. For vector mediators we will show the results for three anomaly-free³ models coupling to electrons, namely $B - L$, $L_e - L_\mu$ and $L_e - L_\tau$. For convenience Tab. 5.1 lists the relevant charges.

5.3 New pseudoscalar interactions in neutrino propagation

A spin-zero bosonic mediator ϕ with ultralight mass ($m_\phi \ll \text{eV}$) can interact with SM fermions ψ through two Lorentz-invariant structures: scalar couplings ($\bar{\psi}\psi\phi$), mediating spin-independent forces, and pseudoscalar couplings ($\bar{\psi}\gamma^5\psi\phi$), generating spin-dependent monopole-dipole and dipole-dipole interactions [220]. Unlike NSIs that alter local interaction cross-sections (detection/production), the ultralight ϕ does not perturb local scattering amplitudes due to its feeble couplings. Instead, its macroscopic coherence length $\sim m_\phi^{-1}$ enables cumulative phase shifts over neutrino propagation baselines, imprinting non-local effective forces on flavor transitions. For pseudoscalar couplings, the gradient $\nabla\phi$ induces an effective background magnetic field $\mathbf{B}_{\text{eff}} \propto \nabla\phi$, driving quantum spin precession in non-relativistic regimes.

In neutrino physics, the coherent superposition of ϕ -mediated long-range interactions modifies the MSW resonance mechanism (see Chapter 2) through flavor-dependent potential terms integrated over macroscopic scales. This effective force, arising from the mediator's coherence, introduces oscillatory modulations in the neutrino Hamiltonian, distinct from conventional matter effects. These dynamics fundamentally alter oscillation phenomenology [192, 221–226]. Additionally, spin-coupled interactions enable spin-flavor precession (SFP) [227, 228], resonantly enhanced in solar matter density gradients. For Dirac neutrinos, SFP converts left-handed states to undetectable right-handed counterparts, mimicking active-sterile oscillations. For Majorana neutrinos, this process generates right-handed antineutrinos, potentially producing observable solar $\bar{\nu}_e$ fluxes [229–233]. The helicity-dependent response to the coherent ϕ field provides a unique discriminant between Dirac and Majorana neutrino mass mechanisms through solar neutrino spectroscopy.

³We assume that three right-handed neutrinos are added to the SM particle content which, in addition of generating non-zero neutrino masses, cancel the anomalies in the $B - L$ case.

5.3.1 Monopole-dipole potential: Mathematical formulation

We consider the interactions of a field ϕ with scalar couplings to the nucleons $f =$ neutrons, protons, and pseudoscalar couplings to neutrinos:

$$\mathcal{L}_\phi = \sum_f g_s^f \phi \bar{f} f + i [g_p^\nu]^\alpha \beta \phi \bar{\nu}_\alpha \gamma^5 \nu_\beta, \quad (5.52)$$

where g_p^ν parametrize the pseudoscalar couplings to the spin of the neutrinos, which in its most generality is a 3×3 hermitian matrix in the neutrino flavour space.

Considering solar neutrinos, the interactions in Eq. (5.52) will generate a flavour dependent potential sourced by the nucleons in the Sun which will affect the flavour evolution of the neutrinos and can lead to observable signatures. We present in Appendix C the derivation of this potential. In brief, we find that the interactions in Eq. (5.52) generate a spin-flip potential on a neutrino of energy E_ν at position \vec{x} of the form

$$V_{\text{sp}}(\vec{x}) = -\frac{g_s^f g_p^\nu}{4E_\nu} \mathcal{E}_\perp(\vec{x}) \quad (5.53)$$

where \mathcal{E}_\perp is the size of the transverse component (with respect to the neutrino trajectory) of a vector field $\vec{\mathcal{E}}$ defined as

$$\vec{\mathcal{E}}(\vec{x}) \equiv \frac{1}{2\pi} \vec{\nabla}_x \int N_f(\vec{\rho}) \frac{e^{-m_\phi |\vec{\rho} - \vec{x}|}}{|\vec{\rho} - \vec{x}|} d^3 \vec{\rho} \equiv \frac{2}{m_\phi^2} \vec{\nabla} \hat{N}_f(\vec{x}, m_\phi). \quad (5.54)$$

In writing Eq. (5.54) we have introduced the quantity $\hat{N}_f(\vec{x}, m_\phi)$ which represents the potential-weighted matter density within a radius $\sim 1/m_\phi$ around the neutrino location [221–225]. Its normalization factor ensures that $\hat{N}_f(\vec{x}, m_\phi) \rightarrow N_f(\vec{x})$ for $m_\phi \rightarrow \infty$, because that is the limit in which one should recover the contact interaction expectation (*i.e.*, the neutrino wave packet localized at position \vec{x} should be directly sensitive to the number density distribution $N_f(\vec{x})$ of fermion f at such point).

Denoting by $r \equiv |\vec{x} - \vec{x}_\odot|$ the distance from the center of the Sun \vec{x}_\odot and taking into account the spherical symmetry of the solar matter distribution $N_f^\odot(r)$, we see that $\hat{N}_f(\vec{x}, m_\phi)$ simplifies to $\hat{N}_f(r, m_\phi)$ with:

$$\hat{N}_f(r, m_\phi) = \frac{m_\phi}{2r} \int_0^{R_\odot} \rho N_f^\odot(\rho) [e^{-m_\phi |\rho - r|} - e^{-m_\phi (\rho + r)}] d\rho. \quad (5.55)$$

Notice that since $\hat{N}_f(r, m_\phi)$ only depends on the radial distance to the center of the Sun, the direction of the vector $\vec{\mathcal{E}}(\vec{x})$ is radial. As the spin-flip potential is proportional to the component of $\vec{\mathcal{E}}$ orthogonal to the neutrino direction, it is clear that it will vanish for trajectories along the line connecting the solar center and the center of the Earth. For neutrinos at a transverse distance b from the line connecting the Earth and Sun centers, and at a radial distance r from the center of the Sun, the potential is

$$V_{\text{sp}}(r, b) = -\frac{g_s^N g_p^\nu}{2E_\nu m_\phi^2} \cdot \frac{b}{r} \cdot \frac{d\hat{N}_f(r, m_\phi)}{dr}. \quad (5.56)$$

In Fig. 5.2 we plot the value of this potential (for different values of m_ϕ) at a given position (b, z) , where b is the transverse distance to the line connecting the Sun and Earth centers, and $z = \sqrt{r^2 - b^2}$ is the distance along the Sun-Earth direction (which, as we will see below, is the variable parametrizing the neutrino trajectory). For the sake of concreteness we show the results for $g_s^{\text{proton}} = g_s^{\text{neutron}} \equiv g_s^N$.

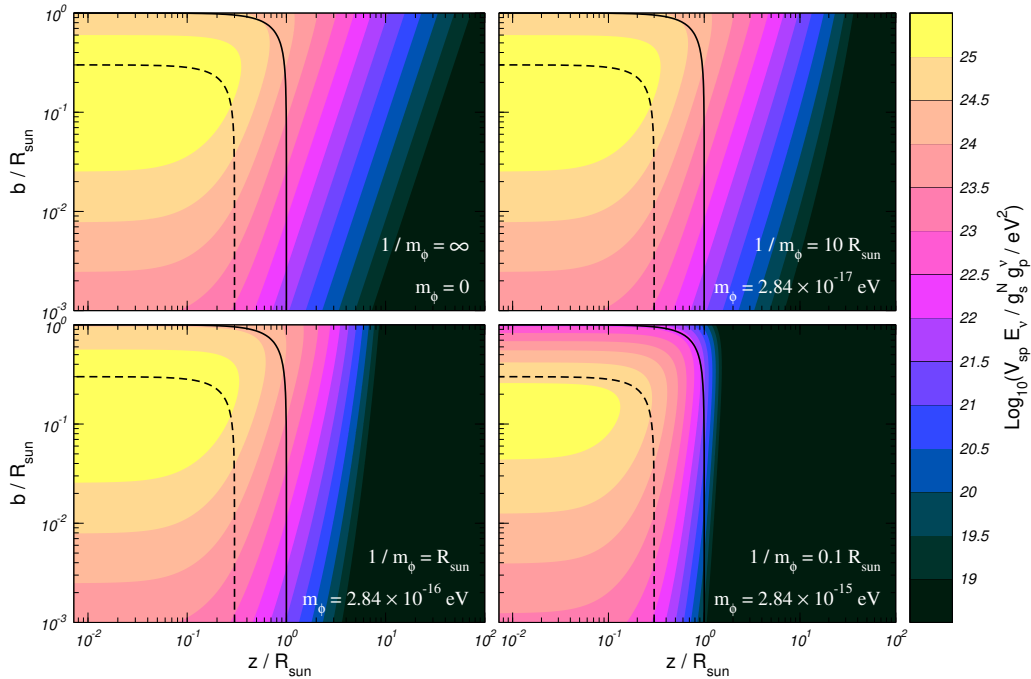


Figure 5.2: Isocontours of the potential V_{sp} sourced by nucleons with coupling g_s^N to ϕ felt by ν with coupling g_p^ν to ϕ as a function of b (its transverse distance to the line connecting the Sun and Earth centers) and z (the distance along the Sun-Earth direction characterizing its trajectory to the Earth) for several values of m_ϕ . For reference the black full and dashed lines represent the position of the edge of the Sun, $\sqrt{b^2 + z^2} = R_\odot$, and the outer edge of the solar core, $\sqrt{b^2 + z^2} = 0.3 R_\odot$, respectively.

From the figure we see that, as expected, the potential decreases as $b \rightarrow 0$. However, it increases very rapidly with b and it reaches its maximum for values of b well within the neutrino production region $b \lesssim 0.3 R_\odot$. Quantitatively we see that for the m_ϕ considered here the characteristic values of the potential inside the solar core are comparable with the inverse of the oscillation length of solar neutrinos with energy E_ν , $E_\nu/\lambda \sim \Delta m_{21}^2 \sim 10^{-4} \text{ eV}^2$ for $g_s^N g_p^\nu \sim 10^{-30}$ within the range of values of the coupling to muons proposed to account for the $(g-2)_\mu$ anomaly [234, 235].

To account for the effect of this potential in the solar neutrino observables we need to solve the evolution equation for the neutrino ensemble. Since the potential flips the helicity of the neutrino, such equation is different for Dirac and Majorana neutrinos. For a Dirac neutrino the evolution equation for its flavour components $\vec{\nu} \equiv (\nu_e, \nu_\mu, \nu_\tau)^T$ reads

$$i \frac{d}{dt} \begin{pmatrix} \vec{\nu}_L(t) \\ \vec{\nu}_R(t) \end{pmatrix} = \begin{pmatrix} H^\nu(r) & V_{sp}(r, b) \\ V_{sp}(r, b)^\dagger & H_{vac} \end{pmatrix} \begin{pmatrix} \vec{\nu}_L(t) \\ \vec{\nu}_R(t) \end{pmatrix}, \quad (5.57)$$

where, given the large distance between the Sun and the Earth, we can assume with high precision that the neutrino travels along a trajectory which runs parallel to the line connecting the Sun and Earth centers, so that its distance b from such line remains constant during propagation. Denoting by z the longitudinal position of the neutrino along its trajectory, we have that at a given time t the distance from the neutrino location to the center of the Sun is given by $r = \sqrt{b^2 + (z - z_0)^2}$ with $z = z_0 + ct$.

For a Majorana neutrino the evolution equation is

$$i \frac{d}{dt} \begin{pmatrix} \vec{\nu}_L(t) \\ \vec{\nu}_R(t) \end{pmatrix} = \begin{pmatrix} H^\nu(r) & V_{sp}(r, b) \\ V_{sp}(r, b)^\dagger & H^{\bar{\nu}}(r) \end{pmatrix} \begin{pmatrix} \vec{\nu}_L(t) \\ \vec{\nu}_R(t) \end{pmatrix}, \quad (5.58)$$

where

$$H^\nu(r) = H_{\text{vac}} + H_{\text{mat}}(r) \quad \text{and} \quad H^{\bar{\nu}}(r) = [H_{\text{vac}} - H_{\text{mat}}(r)]^*. \quad (5.59)$$

Here H_{vac} is the vacuum part which in the flavour basis is defined in Chapter 2. $H_{\text{mat}}(r)$ is the matter potential due to the SM weak interactions, which in the flavour basis takes the diagonal form

$$H_{\text{mat}}(r) = \frac{G_F}{\sqrt{2}} \text{diag} \left[2N_e(r) - N_n(r), -N_n(r), -N_n(r) \right] \quad (5.60)$$

and $N_e(r)$ and $N_n(r)$ are the electron and neutron number density at distance r from the solar center.

We numerically solve the evolution equation from the production point of the ν_{eL} in the Sun to the Earth. With our choice of variables we can characterize the production point by its radial distance r_0 from the center of the Sun, its transverse distance b from the line connecting the Sun-Earth centers, and the angle ϕ in that transverse plane, and we are left with two discrete possibilities $\vec{x}_0^\pm = (\pm\sqrt{r_0^2 - b^2}, b \cos \phi_0, b \sin \phi_0)$ where positive (negative) sign corresponds to neutrinos produced in the hemisphere of the Sun which is closer (further) from the Earth. In this way we obtain the oscillation probability into ν_α (here denoting generically either a left-handed neutrino state, or a right-handed neutrino for Dirac and a right-handed antineutrino for Majorana), $P_{e\alpha}(\vec{x}_0^\pm, E_\nu)$. In the Standard Solar Models the probability distribution of the neutrino production point only depends on the radial distance to the center of the Sun, r_0 (with different distributions for the different neutrino production reactions) so it is convenient to define

$$P_{e\alpha}(r_0, E_\nu) \equiv \frac{1}{4\pi} \int d\Omega P_{e\alpha}(\vec{x}_0, E_\nu) = \frac{1}{4\pi r_0} \int_0^{r_0} db \frac{b}{\sqrt{r_0^2 - b^2}} \int_0^{2\pi} d\phi \sum_{\pm} P_{e\alpha}(\vec{x}_0^\pm, E_\nu). \quad (5.61)$$

As mentioned above each of the eight reactions producing solar neutrinos — labeled by $i = 1 \dots 8$ for pp, ${}^7\text{Be}$, pep, ${}^{13}\text{N}$, ${}^{15}\text{O}$, ${}^{17}\text{F}$, ${}^8\text{B}$, and hep — generates neutrinos with characteristic distributions $\mathcal{R}_i(r_0)$ (normalized to one) which are energy independent. Thus we can obtain the mean survival probability for a neutrino of energy E_ν produced in reaction i as

$$P_{e\alpha}^i(E_\nu) = \int_0^{R_\odot} dr_0 \mathcal{R}_i(r_0) P_{e\alpha}(r_0, E_\nu) \quad (5.62)$$

and with those, obtain the predictions for the solar observables in our analysis.

In what follows, for the sake of concreteness, we are going to focus on four cases: three in which ϕ couples to a specific flavour γ and a fourth in which the coupling is universal in flavour space

$$[g_p^\nu]^{\alpha\beta} = g_p^{\nu\gamma} \delta^{\alpha\gamma} \delta^{\beta\gamma} \quad \text{for } \gamma \in \{e, \mu, \tau\}, \quad \text{and} \quad [g_p^\nu]^{\alpha\beta} = g_p^{\nu U} \delta^{\alpha\beta} \quad \text{for universal.} \quad (5.63)$$

As illustration we plot in Fig. 5.3 the relevant oscillation probabilities for Dirac and Majorana cases as a function of the neutrino energy. The figure is shown for the case of coupling to ν_U but the behaviour is qualitatively the same for couplings to ν_e , ν_μ or ν_τ .⁴ We assume fixed oscillation parameters $\Delta m_{21}^2 = 7.4 \times 10^{-5} \text{ eV}^2$, $\sin^2 \theta_{12} = 0.303$, $\sin^2 \theta_{13} = 0.02203$, $\Delta m_{31}^2 = 2.5 \times 10^{-3} \text{ eV}^2$, $\sin^2 \theta_{23} = 0.5$, and $\delta_{\text{CP}} = 0$, and display different values for the two model parameters (m_ϕ , $g_s^N g_p^{\nu U}$). As seen in the figure the

⁴For concreteness the probabilities shown here have been generated integrating over the production point distribution $\mathcal{R}_{s_B}(r_0)$, but the corresponding plots obtained with the distribution probabilities for the other solar fluxes are very similar.

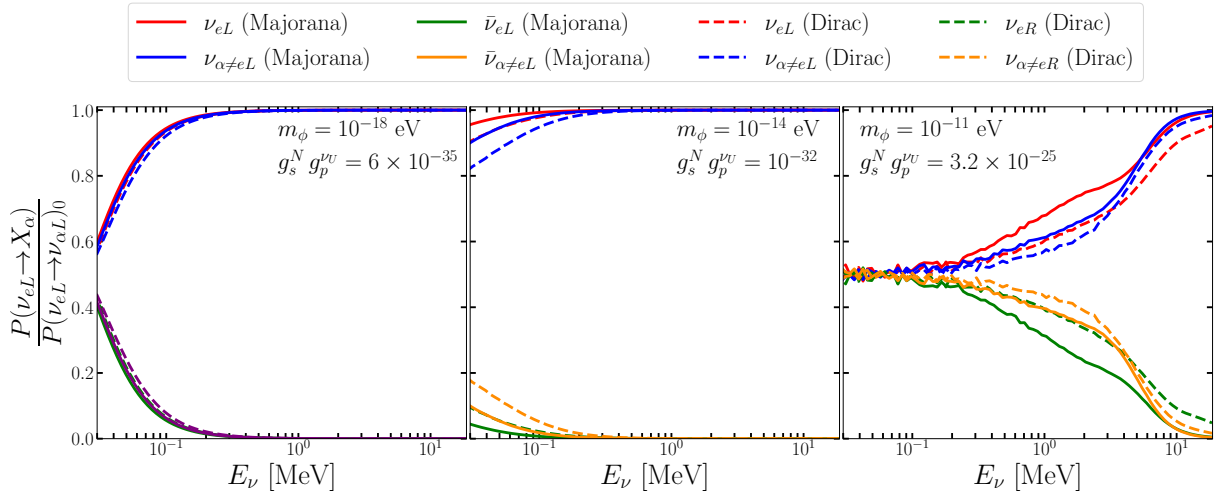


Figure 5.3: Relevant oscillation probabilities at the Earth surface of solar ν_{eL} into left and right neutrinos (antineutrinos) of flavour α divided by $P(\nu_{eL} \rightarrow \nu_{\alpha L})_0$ (the probability for zero coupling to the ϕ field) as a function of the neutrino energy for different values of model parameters as labeled in the figure. Oscillation parameters have been fixed to $\Delta m_{21}^2 = 7.4 \times 10^{-5} \text{ eV}^2$, $\sin^2 \theta_{12} = 0.303$, $\sin^2 \theta_{13} = 0.02203$, $\Delta m_{31}^2 = 2.5 \times 10^{-3} \text{ eV}^2$, $\sin^2 \theta_{23} = 0.5$, and $\delta_{\text{CP}} = 0$.

relevant probabilities are not very different for Dirac and Majorana neutrinos. Most importantly the figure shows that for moderate values of the model parameters the new interaction has the largest effect on the disappearance of ν_{eL} and the appearance of $\nu_{\alpha \neq e, L}$ and $\nu_{\alpha R}$ ($\bar{\nu}_{\alpha R}$) for Dirac (Majorana) neutrinos with the lowest energies. This is expected as the potential in Eq. (5.53) is inversely proportional to the neutrino energy, as characteristic of interactions with spin-zero mediators [223]. This is at a difference with the helicity-conserving MSW potential of Eq. (5.60) (or with any vector interaction in general [192]), and with the helicity-flip potential generated by a neutrino magnetic moment [227, 228] which are independent of the neutrino energy. We also see that for these cases the relative effect on the disappearance of ν_{eL} with $\sim \mathcal{O}(10\text{-}100)$ KeV energy is larger than the $\bar{\nu}_{eR}$ appearance at MeV. These two facts are of relevance in the derivation of the bounds from the analysis of the solar neutrino and antineutrino data as we describe next.

5.4 Summary

To begin, Section 5.1 started by describing the formalism of NSIs within the framework of neutrino oscillations and interactions for different neutrino sources. After introducing NSIs and exploring their impact on neutrino propagation by modifying matter effects in various neutrino sources, we discussed the LMA-D degeneracy.

Following this, Section 5.2 examined how non-standard scenarios can influence neutrino detection in experiments and discussed the diverse origins of New Physics (NP) scenarios. To finish, Section 5.3 established the formalism of how Monopole-Dipole interactions mediated by a very light scalar field that interacts with neutrinos and SM fermions can alter the propagation of neutrinos in the Sun.

Beyond NSI, we developed the formalism for several relevant scenarios involving interactions between quarks/leptons and neutrinos through BSM interactions, focusing in particular on the study of vector, scalar, and pseudoscalar mediators and the neutrino

magnetic moment. The last section was concentrated on an exotic BSM, a very light scalar that affects the oscillation pattern of neutrinos crossing solar matter, and interacts with charged fermions via monopole and with neutrinos via dipole interactions.

Now, we will utilize data from various experiments to analyse and determine the constraints that can be derived from a global fit for these different physical scenarios.

Chapter 6

Three neutrino oscillations with new interactions: Analysis

This chapter employs the experimental datasets outlined in Chapter 3 to impose bounds over new interactions in the three-neutrino (3ν) framework, as described theoretically in Chapter 5. Section 6.1 initiates this investigation with a detailed analysis of Borexino Phase-II solar neutrino spectral data, aiming to constrain new physics scenarios that alter neutrino matter potential or modify elastic scattering processes. These include neutrino magnetic moments, NC NSI, and simplified models with light scalar, pseudoscalar, or vector mediators.

Section 6.2 extends this work through a global analysis of neutrino data, updating and expanding upon previous studies. This analysis simultaneously accounts for NC NSI couplings to up quarks, down quarks, and electrons, treating vector and axial-vector couplings independently. The combined fit of solar, atmospheric, reactor and accelerator neutrino data introduces computational challenges, particularly in modeling NSI effects on all these experiments at the same time. Additionally, $CE\nu$ NS data from COHERENT (CsI and Ar targets) and the Dresden-II (both of them discussed in Section 3.5) reactor experiment are incorporated to resolve degeneracies in NSI parameter space, particularly those linked to the LMA-D solution.

Finally, Section 6.3 derives constraints on an exotic scenario involving a very light scalar field interacting with neutrinos via pseudoscalar couplings and with nucleons via scalar couplings. Building on the discussion in Section 5.3, which outlines how such interactions generate effective potentials altering solar neutrino oscillations, this section presents a global analysis of solar neutrino data (including KamLAND) and solar anti-neutrino flux bounds. The analysis distinguishes between Dirac and Majorana neutrino mass mechanisms, leveraging their distinct helicity-dependent responses to the scalar-mediated potential. Together, these studies demonstrate how multi-experiment synergies and novel interaction frameworks refine the boundaries of BSM physics in neutrino systems.

6.1 Confronting new interactions with electrons with Borexino data

We start by confronting the high statistics data from Borexino described in 3.1.1, with several new physics scenarios: NSI, anomalous magnetic moment, vector, pseudoscalar and scalar mediators. For illustration, we show in Fig. 6.1 the predicted event distributions for each new physics scenario. We also include the Borexino data points, after

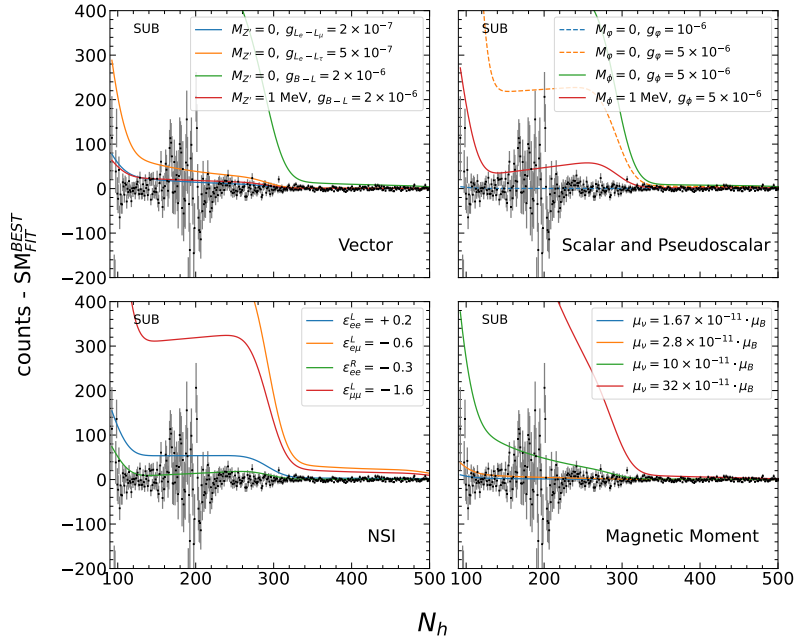


Figure 6.1: Difference between the number of events with respect to the SM expectation, as a function of N_h . For reference, the black dots are obtained for the data in the “subtracted” sample, where the error bars indicate statistical errors only. The coloured lines correspond to the predicted event rates (using the same exposure as that of the “subtracted” sample) for different BSM scenarios and parameter values, as indicated by the labels.

subtracting the best-fit background model and SM signal. For the sake of concreteness, we show the results for the subtracted event sample.

6.1.1 Non-Standard Interactions with electrons - Results

First, let us discuss the case of NSI with electrons. In this scenario Borexino is sensitive to a total of 12 operators: 6 involving left-handed electrons (with coefficients $\epsilon_{\alpha\beta}^L$) and 6 involving right-handed electrons (with coefficients $\epsilon_{\alpha\beta}^R$), see Eq. (5.2). In all generality, *a priori* all operators should be considered at once in the analysis since all of them enter at the same order in the effective theory. However, including such a large number of parameters makes the problem numerically challenging, and the extraction of meaningful conclusions is also jeopardized by the multiple interference effects between the different coefficients. Thus, here we focus on four representative cases with a reduced set of operators, depending on the type of interaction that could lead to the terms in Eq. (5.2):

- **(1)** the axial vector case, where both left-handed and right-handed NSI operators are generated with equal strength but with opposite signs;
- **(2)** the purely vector case, where both types of operators are generated with equal strength and equal sign;
- **(3)** the purely left-handed or purely right-handed cases, where only operators involving electrons of a given chirality are considered.

For each of these three benchmarks we include all operators in neutrino flavour space (both flavour-diagonal and off-diagonal operators) simultaneously in the analysis, allowing for interference and correlation effects among them.

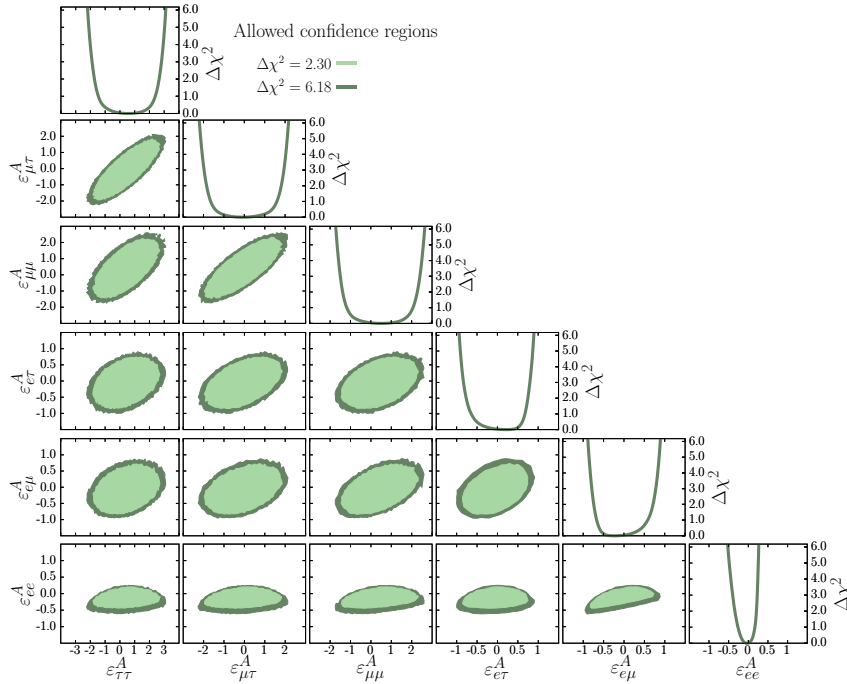


Figure 6.2: Results for axial NSI with electrons ($\varepsilon_{\alpha\beta}^L = -\varepsilon_{\alpha\beta}^R$). The central panels show the two-dimensional allowed confidence regions at 1σ and 2σ (for 2 d.o.f., using two-sided intervals $\Delta\chi^2 = 2.30, 6.18$), while the remaining panels show the profile of the $\Delta\chi^2$ for each of the parameters individually. In each panel, the results are obtained after minimization over the parameters not shown.

We start discussing the axial NSI case. For axial NSI, the effect cancels out in the matter potential, rendering neutrino oscillations insensitive to the new interactions. However, Borexino can still constrain these operators since they affect the interaction cross section in the detector. First, we notice that even allowing all 6 axial NSI coefficients to vary freely we get $\chi_{\min, \text{SM}+\text{NSI}^A}^2 = 255.7$, which is only one unit lower than the SM. So we proceed to derive the bounds on the full parameter space.

The results are presented in Fig. 6.2 where we show one-dimensional and two-dimensional projections of $\Delta\chi_{\text{SM}+\text{NSI}^A}^2$ after minimization over the parameters not shown in each panel. We notice that since the cross-section of flavour-conserving interactions receives contributions from both SM and BSM terms, which could lead to cancellations among them, the corresponding regions are generically larger than those involving only flavour-off-diagonal NSI, for which no SM term is present. From the figure we see that when all the parameters are included in the fit, Borexino is able to constrain NSI roughly only at the level of $|\varepsilon_{\alpha\alpha}^A| < \mathcal{O}(2)$ for flavour-diagonal interactions, and $|\varepsilon_{\alpha\neq\beta}^A| < \mathcal{O}(1)$ for the flavour-off-diagonal ones (see also Tab. 6.1). The only exception to this is the parameter ε_{ee}^A , for which tighter constraints are obtained, roughly at the level $|\varepsilon_{ee}^A| < \mathcal{O}(0.5)$ as it can be seen from the lowest row in the figure. The main reason behind this is that the ε_{ee}^A parameter enters the effective cross section in Eq. (5.2) multiplied by $P_{ee} \sim 0.5$, while the remaining NSI parameters are multiplied either by $P_{e\mu}, P_{e\tau} \sim 0.2 - 0.25$ or by off-diagonal elements in the density matrix (which are at most ~ 0.2).

Note also that the allowed regions for flavour-diagonal NSI are a bit asymmetric with respect to zero. In general, given the large parameter space it is difficult to identify a single reason for the specific shape of the allowed regions. Still, the origin of the asymmetry can be qualitatively understood if the generalized cross section matrix in Eq. (5.34) is

	Allowed regions at 90% CL ($\Delta\chi^2 = 2.71$)			
	Vector		Axial Vector	
	1 Parameter	Marginalized	1 Parameter	Marginalized
ε_{ee}	$[-0.09, +0.14]$	$[-1.05, +0.17]$	$[-0.05, +0.10]$	$[-0.38, +0.24]$
$\varepsilon_{\mu\mu}$	$[-0.51, +0.35]$	$[-2.38, +1.54]$	$[-0.29, +0.19] \oplus [+0.68, +1.45]$	$[-1.47, +2.37]$
$\varepsilon_{\tau\tau}$	$[-0.66, +0.52]$	$[-2.85, +2.04]$	$[-0.40, +0.36] \oplus [+0.69, +1.44]$	$[-1.82, +2.81]$
$\varepsilon_{e\mu}$	$[-0.34, +0.61]$	$[-0.83, +0.84]$	$[-0.30, +0.43]$	$[-0.79, +0.76]$
$\varepsilon_{e\tau}$	$[-0.48, +0.47]$	$[-0.90, +0.85]$	$[-0.40, +0.38]$	$[-0.81, +0.78]$
$\varepsilon_{\mu\tau}$	$[-0.25, +0.36]$	$[-2.07, +2.06]$	$[-1.10, -0.75] \oplus [-0.13, +0.22]$	$[-1.95, +1.91]$

Table 6.1: 90% CL bounds (1 d.o.f., 2-sided) on the coefficients of NSI operators with electrons, for the vector (ε^V) and axial vector (ε^A) scenarios. Results are provided separately for two cases: when only one NSI operator is included at a time (“1 Parameter”) or when the remaining NSI coefficients are allowed to float freely in the fit (“Marginalized”).

written in terms of the axial and vector coefficients, defined (in analogy to Eq. (5.35)) as

$$\begin{aligned} C_{\alpha\beta}^V &= C_{\alpha\beta}^L + C_{\alpha\beta}^R = c_{V\beta}\delta_{\alpha\beta} + \varepsilon_{\alpha\beta}^V, \\ C_{\alpha\beta}^A &= C_{\alpha\beta}^L - C_{\alpha\beta}^R = c_{A\beta}\delta_{\alpha\beta} + \varepsilon_{\alpha\beta}^A. \end{aligned} \quad (6.1)$$

In this case, the differential cross section for axial NSI, setting $\alpha = \beta$, depends on the following combination of parameters:

$$\frac{1}{2} \left(c_{V\alpha}^2 + c_{A\alpha}^2 \right) + c_{A\alpha}\varepsilon_{\alpha\alpha}^A + \frac{(\varepsilon_{\alpha\alpha}^A)^2}{2} + \mathcal{O}(y). \quad (6.2)$$

We notice that due to the interference between the SM and NSI parameters, a second *SM-like* solution appears in Eq. (6.2) with $\varepsilon_{\alpha\alpha}^A \simeq -2c_{A\alpha}$ (*i.e.*, for which $C_{\alpha\alpha}^A = -c_{A,\alpha}$). It can actually be shown that for $\alpha = \mu$ and $\alpha = \tau$ such *SM-like* solution holds also after including the full y dependence of the cross section and so it provides a fit of similar quality to the SM solution. When only one NSI parameter is considered at a time this leads to the two disconnected allowed ranges seen for $\varepsilon_{\mu\mu}^A$ and $\varepsilon_{\tau\tau}^A$ in Table 6.1. When all NSI parameters are included both allowed regions merge in a unique range which is asymmetric about zero. In the case of ε_{ee}^A , on the contrary, the y -dependent terms break such degeneracy and the second *SM-like* solution gets lifted.

From Eq. (6.2) we also see that for $\varepsilon_{\alpha\alpha}^A \simeq -c_{A\alpha}$ it is possible to reduce the cross section with respect to the SM case. This leads to a slightly better fit to the data (albeit mildly, at the level of $\Delta\chi^2 = -1$ as mentioned above) and results into the preferred solution to be at $\varepsilon_{ee}^A \lesssim 0$ (since $c_{Ae} \sim 0.5$). Conversely, for $\varepsilon_{\mu\mu}^A$ and $\varepsilon_{\tau\tau}^A$ the fit shows a mild preference for positive values since $c_{A\mu} = c_{A\tau} \sim -0.5$.

Let us now turn to the analysis of vector NSI. In this case NSI affect the matter potential felt by neutrinos in propagation and a relevant question is how sensitive the analysis is to this effect, and whether the sensitivity to NSI is still dominated by the impact on the neutrino detection cross section. We have numerically checked that the results of the analysis are rather insensitive to NSI effects in propagation. This is partly so because in the energy window relevant for Borexino the contribution from the higher-energy components (mainly 8B, but also pep neutrinos) to the event rates is subdominant, and moreover it is affected by relatively large background uncertainties. As a result we find that the impact of the matter potential on the fit is very limited and the sensitivity

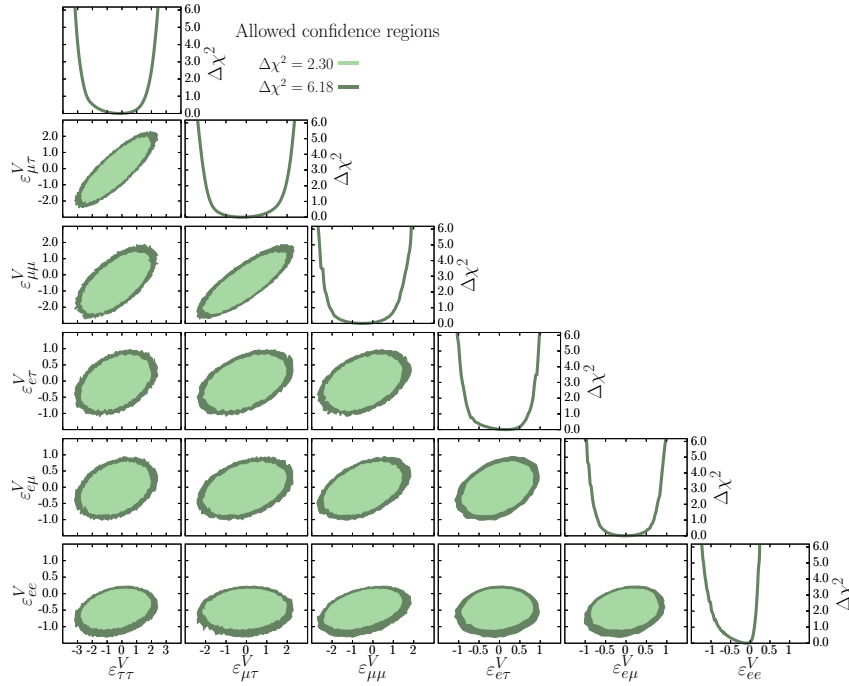


Figure 6.3: Same as Fig. 6.2, but for vector NSI with electrons ($\varepsilon_{\alpha\beta}^L = \varepsilon_{\alpha\beta}^R$).

comes dominantly from NSI effects on the detection cross section.¹ We also find that, even allowing all 6 vector NSI coefficients to vary freely in the analysis, $\chi_{\min, \text{SM}+\text{NSIV}}^2 - \chi_{\min, \text{SM}}^2$ is only -0.2 .

Our allowed regions for vector NSI are presented in Fig. 6.3, where we see that the potential of Borexino to test NSI with electrons is again limited in this multi-parameter scenario: Borexino is only able to constrain NSI at the level of $|\varepsilon_{\alpha\alpha}^V| < \mathcal{O}(2-3)$ for flavour-diagonal interactions, and $|\varepsilon_{\alpha\beta}^V| < \mathcal{O}(1)$ for the off-diagonal parameters. Precise values for the allowed regions at 90% CL are given in Tab. 6.1.

The features describing the allowed regions in the two-dimensional projections of the $\Delta\chi^2$ are qualitatively similar to the results found for the axial case, albeit with some differences. In particular the regions for $\varepsilon_{\mu\mu}^V$ and $\varepsilon_{\tau\tau}^V$ are slightly more symmetric than the axial case. Again, this can be qualitatively understood if the cross section in Eq. (5.34) is rewritten in terms of the axial and vector couplings which results in Eq. (6.2) but replacing $c_{A\alpha} \leftrightarrow c_{V\alpha}$ and $\varepsilon_{\alpha\alpha}^A \leftrightarrow \varepsilon_{\alpha\alpha}^V$. Thus, a similar interference as in the axial case takes place here; however since $c_{V\mu} = c_{V\tau} \sim -0.04$ the quasi-degenerate *SM-like* solution lies closer to the SM so the region is more symmetric about zero.

For completeness, we also provide our results for NSI involving only left-handed and right-handed electrons in Tab. 6.2, where we again show the results obtained turning on only one operator at a time, and allowing all NSI operators simultaneously in the fit. We have numerically checked that, if only a single operator is included, we recover the results of the Borexino collaboration for both left-handed and right-handed NSI (Fig. 5 in Ref. [236]) with a very good accuracy. The only difference is the secondary minimum for $\varepsilon_{ee}^L \sim -1.3$ which is outside of the range of parameters explored in Ref. [236].

	Allowed regions at 90% CL ($\Delta\chi^2 = 2.71$)			
	Left-handed		Right-handed	
	1 Parameter	Marginalized	1 Parameter	Marginalized
ε_{ee}	$[-1.37, -1.29] \oplus [-0.03, +0.06]$	$[-1.48, +0.09]$	$[-0.23, +0.07]$	$[-0.53, +0.09]$
$\varepsilon_{\mu\mu}$	$[-0.20, +0.13] \oplus [+0.58, +0.81]$	$[-1.59, +2.21]$	$[-0.36, +0.37]$	$[-1.26, +0.77]$
$\varepsilon_{\tau\tau}$	$[-0.26, +0.26] \oplus [+0.45, +0.86]$	$[-2.00, +2.60]$	$[-0.58, +0.47]$	$[-1.45, +1.04]$
$\varepsilon_{e\mu}$	$[-0.17, +0.29]$	$[-0.78, +0.75]$	$[-0.21, +0.41]$	$[-0.43, +0.42]$
$\varepsilon_{e\tau}$	$[-0.26, +0.23]$	$[-0.81, +0.79]$	$[-0.35, +0.31]$	$[-0.39, +0.43]$
$\varepsilon_{\mu\tau}$	$[-0.62, -0.52] \oplus [-0.09, +0.14]$	$[-1.95, +1.91]$	$[-0.26, +0.23]$	$[-1.10, +1.03]$

Table 6.2: Constraints at 90% CL (for 1 d.o.f., 2-sided) on the coefficients of NSI operators involving only left-handed (ε^L) or right-handed (ε^R) electrons. Results are provided separately for two cases: when only one NSI operator is included at a time (“1 Parameter”) or when the remaining NSI coefficients are allowed to float freely in the fit (“Marginalized”).

6.1.2 Neutrino magnetic moment

For the analysis with neutrino magnetic moment we find $\chi_{\min, \text{SM}+\mu\nu}^2 = 256.5$. In other words, the data do not show a statistically significant preference for a non-vanishing magnetic moment, which allows to set constraints on the parameter space for this scenario. The corresponding results are summarized in Fig. 6.4, assuming three independent parameters for the ν_e , ν_μ and ν_τ magnetic moments. In each panel, the $\Delta\chi^2$ is minimized over the undisplayed parameters. From the one-dimensional projections we can read the upper bounds at 90% CL (for 1 d.o.f., one-sided intervals, *i.e.*, $\Delta\chi^2 = 1.64$)

$$\mu_{\nu_e} < 3.7 \times 10^{-11} \mu_B, \quad \mu_{\nu_\mu} < 5.0 \times 10^{-11} \mu_B, \quad \mu_{\nu_\tau} < 5.9 \times 10^{-11} \mu_B. \quad (6.3)$$

Our results are fully compatible with those in Ref. [237], considering the different choice of oscillation parameters assumed. If we assume that all flavours carry the same value of the neutrino magnetic moment then the dependence on the oscillation parameters cancels out and we obtain the following bound (at 90 % CL for 1 d.o.f., one-sided)

$$\mu_\nu < 2.8 \times 10^{-11} \mu_B. \quad (6.4)$$

This coincides precisely with the result obtained by the collaboration in Ref. [237], and serves as validation for the χ^2 implementation and the choice of systematic uncertainties adopted in our analysis.

We notice that the Borexino bounds are stronger than those obtained by other experiments under the same flavour assumptions and CL. This is the case for the (over a decade old) experimental results of GEMMA [238, 239] ($\mu_\nu < 2.9 \times 10^{-11} \mu_B$) and TEXONO [240] ($\mu_\nu < 7.4 \times 10^{-11} \mu_B$), as well as the bounds derived from recent results such as CONUS [241] ($\mu_\nu < 7.5 \times 10^{-11} \mu_B$) and the combined analysis of Dresden-II and COHERENT [242] ($\mu_\nu < 1.8 \times 10^{-10} \mu_B$).

6.1.3 Light vector mediators

The potential of Borexino to probe simplified models with light vector mediators has been demonstrated in the literature for the $B - L$ case [243, 244], and the bound has

¹A similar finding was also reported in Ref. [236], although only on-diagonal operators were considered in that case.

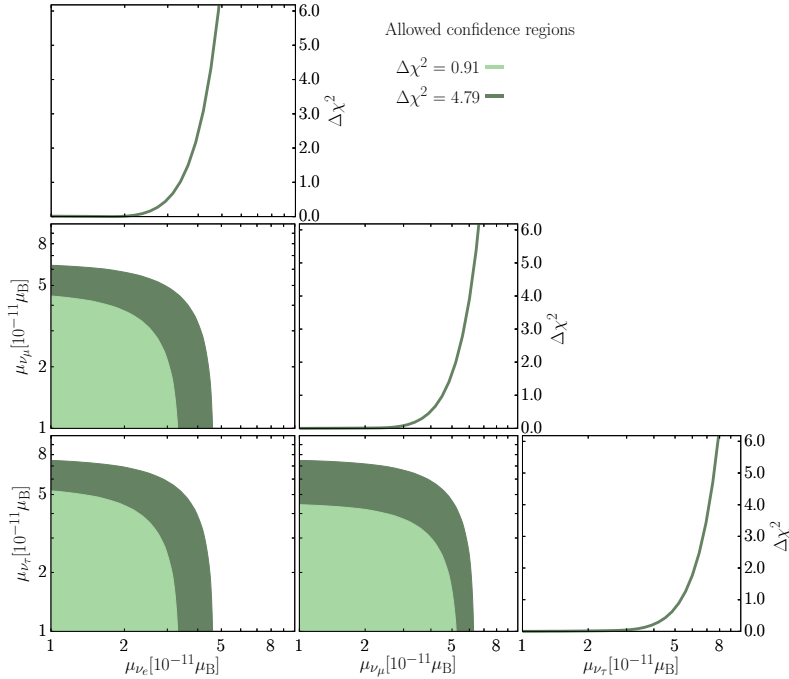


Figure 6.4: Results for the magnetic moment scenario, assuming three independent parameters (one for each of the SM neutrino flavours). Since the neutrino magnetic moment is positive definite, the cuts have been taken according to a one-sided χ^2 distribution. In the central panels, we show the allowed confidence regions (at 1σ and 2σ , for 2 d.o.f. using one-sided intervals) while in the right-most panels we show the profile of the $\Delta\chi^2$ for each of the parameters individually. In each panel, the results are obtained after minimization over the undisplayed parameters.

been later recast to other $U(1)'$ models in Refs. [245, 246]. However, Refs. [243, 244] date from 2012 and 2015 and therefore did not include Phase-II data. Furthermore, their bound was only approximate: it was derived requiring that the new physics contribution to the event rates should not exceed the SM expectation. Here we report our limits for simplified models, for our data analysis which includes full spectral information for the Phase II data and a careful implementation of systematic uncertainties.

Our results for vector mediators are shown in Fig. 6.5 for three anomaly-free models with couplings to $B - L$, $L_e - L_\mu$, or $L_e - L_\tau$. The similarity between constraints arises from the dominant interference term in Eq. (5.51), where the event rate modification

$$\Delta N_{\text{ev}} \propto P_{ee} q_{Z'}^{\nu_e} q_{Z'}^e c_{Ve} \quad (6.5)$$

dominates due to $c_{Ve} \gg c_{V\mu(\tau)}$ and $P_{ee} > P_{e\mu(\tau)}$. Identical $q_{Z'}^{\nu_e} q_{Z'}^e = 1$ values yield comparable bounds across models.

We compare Borexino constraints with previous limits from neutrino-electron scattering (GEMMA Phase-I [238], TEXONO [247]), CE ν NS measurements (COHERENT [248, 249], Dresden-II [250]), oscillation data [192], and CE ν NS/ES searches (CONNIE [251], CONUS [252]). For $B - L$, pre-2015 ‘‘Rate only’’ Borexino estimates [243, 244] are included. Technical details follow established methodologies for quenching factors [242] and confidence levels [253].

Our Borexino Phase-II analysis improves constraints by $\sim 60\%$ for light mediators and $\sim 30\%$ on $g_{Z'}/M_{Z'}$ in contact-interaction regimes. While surpassing most scattering experiment bounds, oscillation data remain dominant for $L_e - L_{\mu/\tau}$ models.

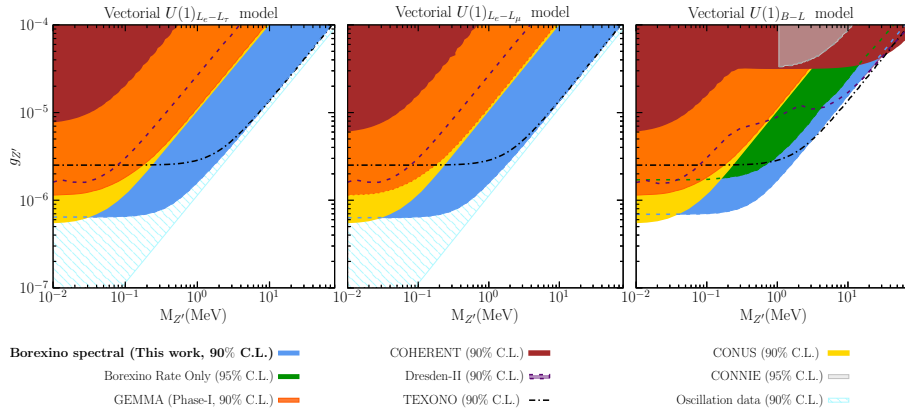


Figure 6.5: Bounds from our analysis of Borexino Phase II spectral data (at 90% CL for 1 d.o.f., using two-sided intervals, *i.e.*, $\Delta\chi^2 = 2.71$) on the vector mediators associated to a new $U(1)'$ symmetry, as indicated in the top label for each panel. Our results are compared to our derived bounds from GEMMA [192, 238], TEXONO [192, 247], COHERENT [242, 248, 249], and Dresden-II reactor experiment [242, 250], as well as those derived from a global fit to oscillation data [192], all of them obtained with the same statistical criterion. We also show the bounds from CONNIE [251] (95% CL) and CONUS [252] (90% CL) which we have obtained applying an overall rescaling factor to their published bounds on a universally coupled vector (see text for details). For the $B - L$ model, the line labelled “Borexino Rate Only” shows the approximate bound derived (at 95% CL, 1 d.o.f., for one-sided intervals) in Ref. [244] (see also Ref. [243]).

6.1.4 Light scalar and pseudoscalar mediators

Next let us discuss our results for a scalar (pseudoscalar) mediator coupled universally to the SM fermions, shown in the left (right) panel of Fig. 6.6. For comparison, we also show the bounds derived from neutrino scattering measurements, computed following (or obtained from) the same references as in Sec. 6.1.3. Our results for scalar (pseudoscalar) mediators with universal SM couplings are shown in Fig. 6.6 left (right) panel. Unlike vector mediators, scalar/pseudoscalar scenarios evade oscillation constraints. Following the methodology from Sec. 6.1.3, we compare neutrino scattering bounds which are generally weaker than vector counterparts due to: (1) quartic coupling dependence (no SM interference) versus quadratic for vectors, and (2) cross-section suppression factors $T_e m_e / E_\nu^2$ (scalar) and T_e^2 / E_ν^2 (pseudoscalar) relative to vector interactions in Eqs. (5.47)-(5.51).

For scalar mediators (left panel), Borexino Phase II improves over reactor experiments (GEMMA/TEXONO) but Dresden-II provides dominant constraints except at $M_\phi \sim 0.5$ MeV. This stems from enhanced $CE\nu NS$ sensitivity via scalar-quark couplings [242]. Conversely for pseudoscalars (right panel), Borexino leads for $M_\phi \lesssim 5$ MeV as $CE\nu NS$ contributions become negligible (spin-dependent coupling). Dresden-II limits here consider only ES contributions, while missing CONUS pseudoscalar bounds (not studied experimentally) would likely remain weaker than Borexino due to $T_e/m_e \sim 2 \times 10^{-3}$ suppression.

TEXONO provides comparable pseudoscalar constraints, though all scattering limits weaken significantly compared to vector case. The distinct suppression mechanisms and interaction topologies underscore the importance of combined spectral analyses across multiple interaction types.

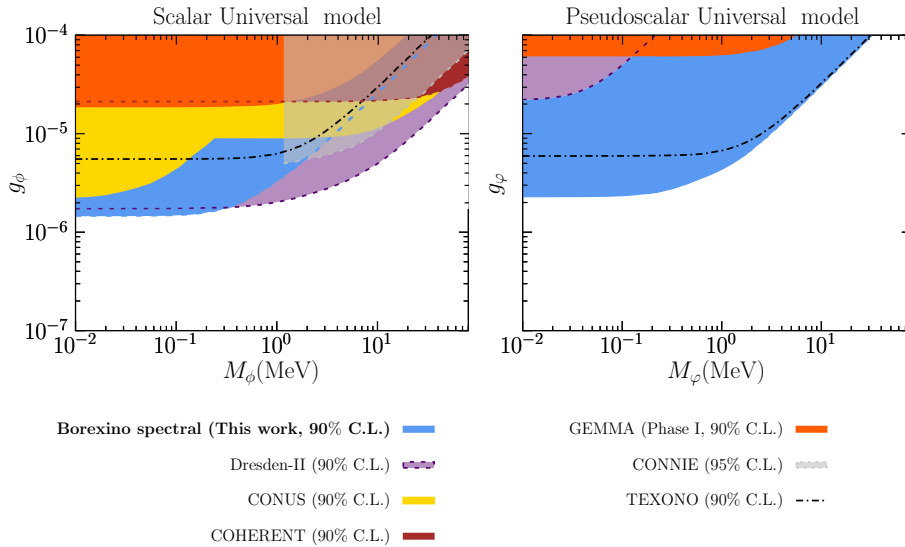


Figure 6.6: Bounds from our analysis of Borexino Phase-II spectral data on a scalar (left panel) and pseudoscalar (right panel) mediator (at 90% CL for 1 d.o.f., using two-sided intervals, *i.e.*, $\Delta\chi^2 = 2.71$) which couples universally to all fermions in the SM. Our results are compared to our derived bounds from GEMMA [192, 238], TEXONO [192, 247], COHERENT [242, 248, 249], and Dresden-II reactor experiment [242, 250], obtained using the same statistical criterion. For comparison we also show the bounds from CONNIE [251] (95 %CL) and CONUS [252] (90% CL).

6.2 Constraining NSI with electrons and quarks with global oscillation data

This section summarizes the main results of our study using global analysis to constrain NCNSIs. In Sec. 6.2.1 we first review the data included in the fit, introduce our χ^2 definition, and outline the details related to the sampling of the multi-dimensional parameter space. We then proceed to present our results for NSI with electrons (Sec. 6.2.2), with quarks (Sec. 6.2.3), and for simultaneous NSI with electrons and quarks (Sec. 6.2.4). The status of the LMA-D solution in this general case is discussed in Sec. 6.2.5.

6.2.1 Simulation details

The data samples included in our oscillation analysis mostly coincide with those in NuFIT-5.2 [254]². When combining with CE ν NS we include the results from COHER-

²In brief, in the analysis of solar neutrino data we consider the total rates from the radiochemical experiments Chlorine [147], Gallex/GNO [56], and SAGE [55], the spectral data (including day-night information) from the four phases of Super-Kamiokande in Refs. [60–62, 255], the results of the three phases of SNO in the form of the day-night spectrum data of SNO-I [256], and SNO-II [257] and the three total rates of SNO-III [258], and the spectra from Borexino Phase-I [67, 148], and Phase-II [68]. For reactor neutrinos we include the separate DS1, DS2, DS3 spectra from KamLAND [97] with Daya Bay reactor ν fluxes [259], the FD/ND spectral ratio, with 1276-day (FD), 587-day (ND) exposures of Double-Chooz [152], the 3158-day separate EH1, EH2, EH3 spectra [93] of Daya-Bay, and the 2908-day FD/ND spectral ratio of RENO [153]. For atmospheric neutrinos we use the four phases of Super-Kamiokande (up to 1775 days of SK4 [260]), the complete set of DeepCore 3-year μ -like events presented in Ref. [261] and publicly released in Ref. [262], and the results on ν_μ -induced upgoing muons reported by IceCube [263] based on one year of data taking. Finally, for LBL experiments we include the final neutrino and antineutrino spectral data on ν_e -appearance and ν_μ -disappearance in MINOS [103], the 19.7×10^{20} pot ν_μ -disappearance and 16.3×10^{20} pot $\bar{\nu}_\mu$ -disappearance data in T2K [264], and the 13.6×10^{20} pot ν_μ -disappearance and 12.5×10^{20} pot $\bar{\nu}_\mu$ -disappearance data in NO ν A [99]. Notice that to ensure full consistency with our CP-conserving parametrization we have chosen not to include in the present study the data from the

ENT data on CsI [248, 265] and Ar targets [249, 266] (see Refs. [122, 242] for details). In particular, for the analysis of COHERENT CsI data we use the quenching factor from Ref. [267] and the nuclear form factor from Ref. [268]. For the analysis of COHERENT Ar data we use the quenching factor provided by the COHERENT collaboration in Ref. [266] and Helm [269] nuclear form factor (the values of the parameters employed are the same as in Ref. [242]). For CE ν NS searches using reactor neutrinos at Dresden-II reactor experiment [250] we follow the analysis presented in Ref. [242] with YBe quenching factor [270] (the characteristic momentum-transfer in this experiment is very low so the nuclear form factor can be taken to be 1). With all this we construct the corresponding $\chi_{\text{COH,CsI}}^2(\vec{\varepsilon})$, $\chi_{\text{COH,Ar}}^2(\vec{\varepsilon})$, and $\chi_{\text{D-II,Ge}}^2(\vec{\varepsilon})$.

Our goal is to find the global minimum of the total χ^2 which, unless otherwise stated, is obtained adding the contributions from our global analysis of oscillation data («GLOB-OSC w NSI in ES») and CE ν NS data:

$$\chi^2(\vec{\omega}, \vec{\varepsilon}) = \chi_{\text{OSC}}^2(\vec{\omega}, \vec{\varepsilon}) + \chi_{\text{CE}\nu\text{NS}}^2(\vec{\varepsilon}) \quad (6.6)$$

where we have defined

$$\chi_{\text{CE}\nu\text{NS}}^2 = \chi_{\text{COH,CsI}}^2 + \chi_{\text{COH,Ar}}^2 + \chi_{\text{D-II,Ge}}^2. \quad (6.7)$$

The minimum of the total χ^2 is obtained after minimization over all the nuisance parameters, which are included as pull terms in our fit.³ Vector NSI effects in detection can be suppressed while maintaining oscillation impacts depending on mediator mass [182]. For oscillations, light mediators require $M_{\text{med}} \gtrsim \mathcal{O}(10^{-12})$ eV [192, 271]. Detection effects require momentum transfer q :

- Elastic scattering (ES): Borexino ($q \sim 500$ keV) constrains $M_{\text{med}} \ll 500$ keV («GLOB-OSC w/o NSI in ES»), while SNO/SK ($q \sim 5 - 10$ MeV) require $M_{\text{med}} \gtrsim 10$ MeV («GLOB-OSC w NSI in ES»). Intermediate masses (0.5–10 MeV) primarily affect Borexino.
- CE ν NS: COHERENT ($q \sim 30 - 50$ MeV) and Dresden-II ($q \sim 5$ MeV) constrain $M_{\text{med}} \gtrsim 50$ MeV («GLOB-OSC+CE ν NS») versus $M_{\text{med}} \ll 5$ MeV («GLOB-OSC»). Intermediate 5 – 50 MeV ranges require case-by-case analysis.

Axial-vector NSI exclusively affect detection: ES bounds follow mediator thresholds (e.g., $M_{\text{med}} \gtrsim 3$ MeV for SNO NC interactions).

Our global fit scans parameters are:

$$\theta_{12}, \theta_{23}, \Delta m_{21}^2, \Delta m_{31}^2, \varepsilon_{\oplus}, \varphi_{12}, \varphi_{23}, \varepsilon_{\mu\mu}^{\oplus}, \eta, \zeta \quad (6.8)$$

with $\delta_{\text{CP}} \in \{0, \pi\}$. Since the determination of θ_{13} is dominated by reactor data which are mostly insensitive to NSI (see Sec. 5.1.1), we fix $\sin^2 \theta_{13} = 0.022$. Atmospheric analyses are performed in the limit $\Delta m_{21}^2 \rightarrow 0$. Parameter space exploration uses MultiNest [272, 273] and Diver [274], accounting for detection-induced breaking of diagonal NSI degeneracies through $\varepsilon_{\mu\mu}^{\oplus}$.

ν_e and $\bar{\nu}_e$ appearance channels in NO ν A and T2K. With this data we construct $\chi_{\text{OSC}}^2(\vec{\omega}, \vec{\varepsilon})$ where we denote by $\vec{\omega}$ the 3 ν oscillation parameters and $\vec{\varepsilon}$ the NSI parameters considered in the analysis.

³For details on the numerical implementation of systematic uncertainties see Refs. [2, 242, 254].

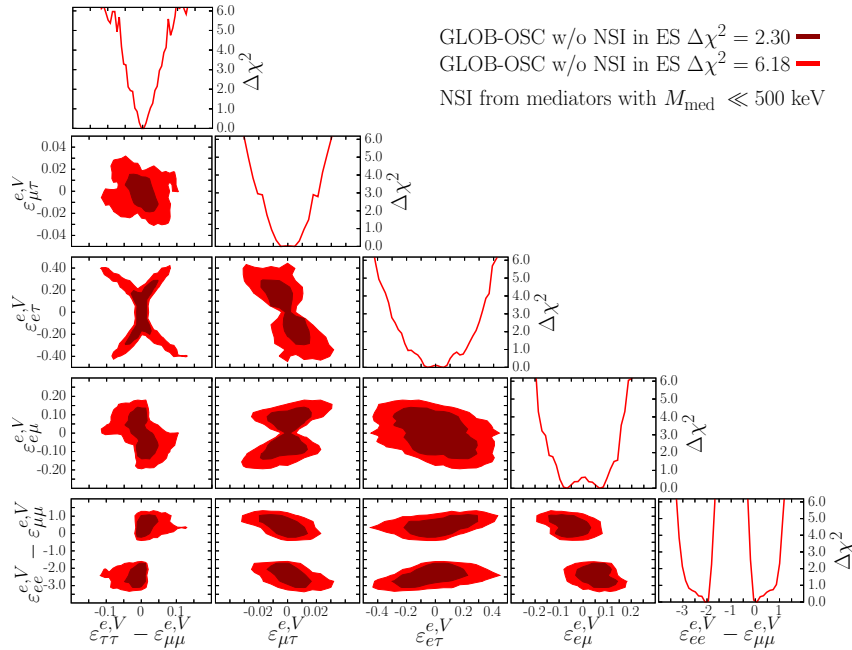


Figure 6.7: Constraints on the coefficients for vector NSI with electrons from the global analysis of oscillation data *without including the effect of NSI in the detection cross section*. Each panel shows a two-dimensional projection of the allowed multi-dimensional parameter space after minimization with respect to the undisplayed parameters. The regions correspond to 1σ and 2σ (2 d.o.f.).

6.2.2 New constraints on NSI with electrons

The global analysis of neutrino data reveals significant improvements in constraining NC NSI with electrons compared to the Borexino Phase-II spectral analysis presented in Sec. 6.1. We plot in Fig. 6.7 and 6.8 the constraints on the different coefficients for the two scenarios outlined in the previous section, without and with NSI effects in the detection cross section, respectively.⁴ The corresponding 90% CL allowed ranges are listed in Table 6.3 and on the left columns in Table 6.4 respectively.

The first thing to notice is that in the scenario «GLOB-OSC w/o NSI in ES», for the flavour diagonal coefficients, only the combinations $\varepsilon_{ee}^{e,V} - \varepsilon_{\mu\mu}^{e,V}$ and $\varepsilon_{\tau\tau}^{e,V} - \varepsilon_{\mu\mu}^{e,V}$ can be constrained, and two separate allowed ranges appear (see bottom row in Fig. 6.7): one around $\varepsilon_{ee}^{e,V} - \varepsilon_{\mu\mu}^{e,V} \sim 0$ and another around $\varepsilon_{ee}^{e,V} - \varepsilon_{\mu\mu}^{e,V} \sim -2$. This is nothing else than the result of the generalized mass-ordering degeneracy of Eq. (5.18). The two disjoint allowed solutions correspond to regions of oscillation parameters with $\theta_{12} < 45^\circ$ (with ranges labeled «LMA» in Table 6.3) and with $\theta_{12} > 45^\circ$ (with ranges labeled «LMA-D» in Table 6.3) respectively. As discussed in Sec. 5.1.1, the degeneracy is partly broken by the variation of chemical composition of the matter along the neutrino trajectory when NSI coupling to neutrons are involved. But in this case, with only coupling to electrons, the degeneracy is perfect as can be seen by the fact that $\Delta\chi^2 = 0$ in both minima of $\varepsilon_{ee}^{e,V} - \varepsilon_{\mu\mu}^{e,V}$. From the panels on the lower row we observe that the projection of the allowed regions corresponding to each of the two solutions partly overlap for $\varepsilon_{\tau\tau}^{e,V} - \varepsilon_{\mu\mu}^{e,V}$ and $\varepsilon_{\alpha\neq\beta}^{e,V}$, which leads to the non-trivial shapes of some of the corresponding two-dimensional regions for some pairs of those parameters.

⁴Notice that from the point of view of the data analysis the results from the «GLOB-OSC w/o NSI in ES» are totally equivalent to those obtained for vector NSI which couple only to protons.

	Allowed ranges at 90% CL (marginalized)	
	GLOB-OSC w/o NSI in ES	
	LMA	LMA \oplus LMA-D
$\varepsilon_{ee}^{e,V} - \varepsilon_{\mu\mu}^{e,V}$	$[-0.21, +1.0]$	$[-3.0, -1.8] \oplus [-0.21, +1.0]$
$\varepsilon_{\tau\tau}^{e,V} - \varepsilon_{\mu\mu}^{e,V}$	$[-0.015, +0.048]$	$[-0.040, +0.047]$
$\varepsilon_{e\mu}^{e,V}$	$[-0.15, +0.035]$	$[-0.15, +0.14]$
$\varepsilon_{e\tau}^{e,V}$	$[-0.21, +0.31]$	$[-0.29, +0.31]$
$\varepsilon_{\mu\tau}^{e,V}$	$[-0.020, +0.012]$	$[-0.020, +0.017]$

Table 6.3: 90% CL bounds (1 d.o.f., 2-sided) on the coefficients of NSI operators with electrons after marginalizing over all other NSI and oscillation parameters. The bounds are derived from the global analysis of oscillation data *without including the effect of NSI in the ES cross section* (NSI induced by mediators with mass $M_{\text{med}} \ll 500$ keV, see Sec. 6.2.1). The ranges in the first column (labeled «LMA») correspond to an analysis in which we restrict $\theta_{12} < 45^\circ$. In the second column (labeled «LMA \oplus LMA-D»), both $\theta_{12} < 45^\circ$ and $\theta_{12} > 45^\circ$ are allowed. The same bounds hold for vector NSI with protons.

	Allowed ranges at 90% CL (marginalized)			
	Vector ($X = V$)		Axial-vector ($X = A$)	
	Borexino	GLOB-OSC w NSI in ES	Borexino	GLOB-OSC w NSI in ES
$\varepsilon_{ee}^{e,X}$	$[-1.1, +0.17]$	$[-0.13, +0.10]$	$[-0.38, +0.24]$	$[-0.13, +0.11]$
$\varepsilon_{\mu\mu}^{e,X}$	$[-2.4, +1.5]$	$[-0.20, +0.10]$	$[-1.5, +2.4]$	$[-0.70, +1.2]$
$\varepsilon_{\tau\tau}^{e,X}$	$[-2.8, +2.1]$	$[-0.17, +0.093]$	$[-1.8, +2.8]$	$[-0.53, +1.0]$
$\varepsilon_{e\mu}^{e,X}$	$[-0.83, +0.84]$	$[-0.097, +0.011]$	$[-0.79, +0.76]$	$[-0.41, +0.40]$
$\varepsilon_{e\tau}^{e,X}$	$[-0.90, +0.85]$	$[-0.18, +0.080]$	$[-0.81, +0.78]$	$[-0.36, +0.36]$
$\varepsilon_{\mu\tau}^{e,X}$	$[-2.1, +2.1]$	$[-0.0063, +0.016]$	$[-1.9, +1.9]$	$[-0.79, +0.81]$

Table 6.4: 90% CL bounds (1 d.o.f., 2-sided) on the coefficients of vector NSI operators with electrons after marginalizing over all other NSI and oscillation parameters. The bounds are derived from the global analysis of oscillation data *including the effect of NSI in the ES cross section*. For comparison, the results obtained from the analysis of Borexino Phase-II data in Ref. [2] are also shown for comparison. Note that these bounds apply to interactions induced by mediators with masses $M_{\text{med}} \gtrsim 10$ MeV, see Sec. 6.2.1.

The results for the scenario «GLOB-OSC w NSI in ES» in Fig. 6.8, and on the left columns in Table 6.4, show that the inclusion of the effect of the vector NSI in the ES cross sections in Borexino, SNO, and SK totally lifts the degeneracy. In this scenario only the LMA solution is allowed, and $\varepsilon_{ee}^{e,V}$, $\varepsilon_{\mu\mu}^{e,V}$, and $\varepsilon_{\tau\tau}^{e,V}$ can be independently constrained. Notice also that in this case, the lifting of the LMA-D solution leads to allowed regions with more standard (close-to-elliptical) shapes. For the sake of comparison we show for this scenario the corresponding bounds derived from the analysis of Borexino spectra in Section 6.1. The comparison shows that for vector NSI with electrons the global analysis of the oscillation data reduces the allowed ranges of the NSI coefficients by factors ~ 4 –200 with respect to those derived with Borexino spectrum only. In other words, the NSI contribution to ES is important to break the LMA-D degeneracy and to impose independent bounds on the three flavour-diagonal NSI coefficients, but within the LMA solution the effect of the vector NSI on the matter potential also leads to stronger constraints. This is further illustrated by the results obtained for the analysis with axial-vector NSI which are shown in Fig. 6.9 and right columns in Table 6.4. Axial-vector NSI

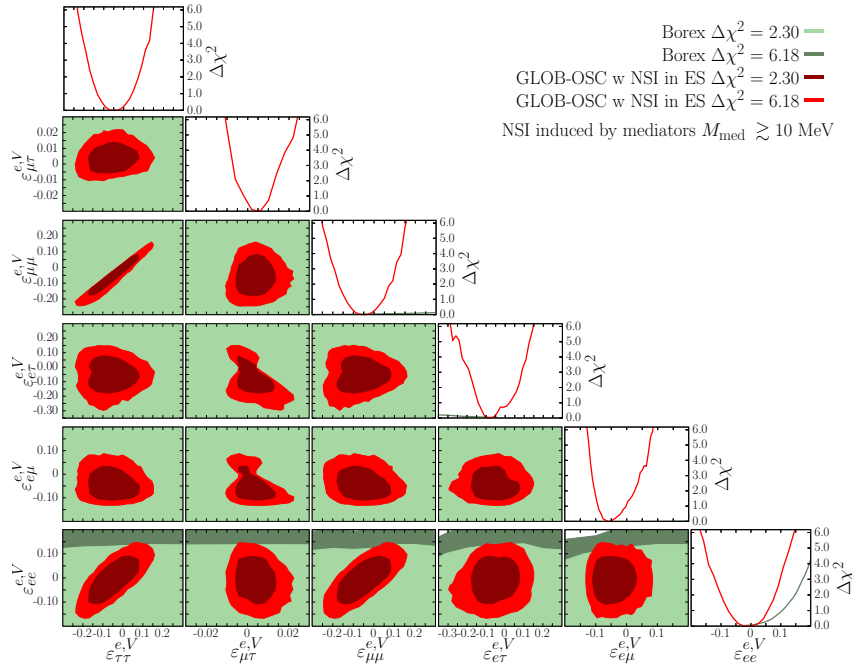


Figure 6.8: Constraints on the coefficients for vector NSI with electrons from the global analysis of oscillation data *including the effect of NSI in the ES cross section*. Each panel shows a two-dimensional projection of the allowed multi-dimensional parameter space after minimization with respect to the undisplayed parameters. The contours correspond to 1σ and 2σ (2 d.o.f.). The closed red regions correspond to the global oscillation analysis which involves the six NSI plus five oscillation parameters. For the sake of comparison we also show as green regions the constraints obtained from the analysis of full Borexino Phase-II spectrum in Figure 6.3.

do not contribute to the matter potential and therefore the difference between the results of the global oscillation and the Borexino-only analysis in this case arises solely from the effect of the axial-vector NSI on the ES cross section in SNO and SK. Comparing the red and green regions in Fig. 6.9 and the two left columns in Table 6.4 we see that for axial-vector NSI the improvement over the bounds derived with Borexino-only analysis is just a factor $\sim 2-3$.

6.2.3 Updated constraints on NSI with quarks

Next we briefly summarize the results of the analysis for the scenarios of NSI with either up or down quarks (more general combinations of couplings to quarks and electrons will be presented in the next section). For vector NSI this updates and complements the results presented in Refs. [122, 196] by accounting for the effects of increased statistics in the oscillation experiments, including the addition of new data from Borexino Phase-II. Notice also that in the present analysis, as mentioned above, the treatment of the SNO data is different than in Refs. [122, 196]. Furthermore when combining with CE ν NS we include here the results from COHERENT both on CsI [248, 265] and Ar targets [249, 266], together with the recent results from CE ν NS searches using reactor neutrinos at Dresden-II reactor experiment [242, 250].

Let us start discussing the complementary sensitivity to vector-NSI from the combined CE ν NS results with that from present oscillation data, for general models leading to NSI with quarks. With this aim we have first performed an analysis including only the effect of vector NSI on the matter potential in the neutrino oscillation experiments. The results

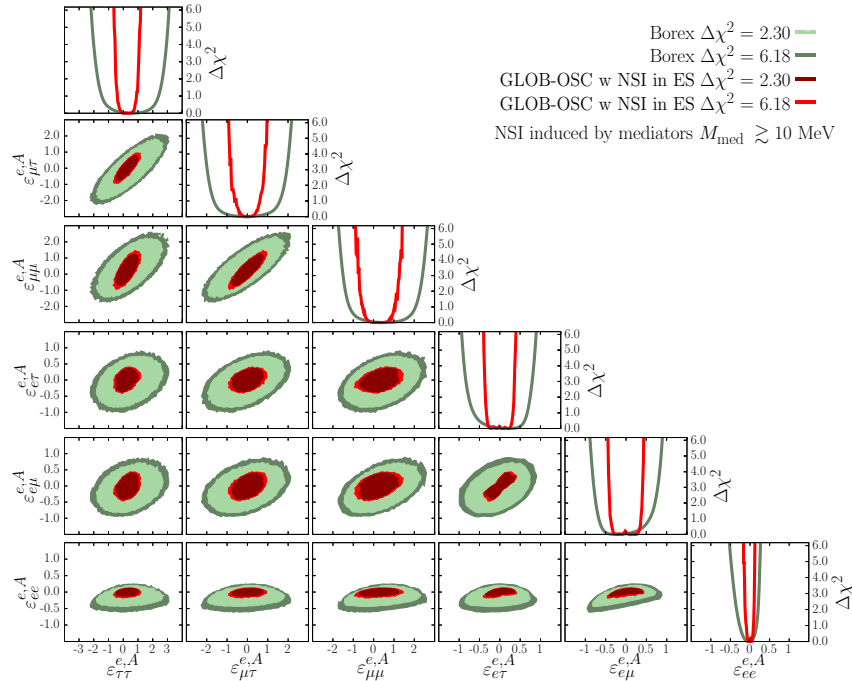


Figure 6.9: Same as Fig. 6.8 but for Axial-vector NSI, compared with Fig. 6.2.

of such analysis are given in the left column of Table 6.7 in terms of the allowed ranges of the effective NSI couplings to the Earth matter, $\varepsilon_{\alpha\beta}^{\oplus}$, defined in Eq. (5.19) (see Sec. 6.2.4 for details). Comparison with the constraints from all available CE ν NS data is illustrated in Fig. 6.10 where we plot the allowed regions in the plane $(\varepsilon_{ee}^{\oplus}, \varepsilon_{\mu\mu}^{\oplus})$. The figure shows the results obtained by the analysis of each of the two sets of data *independently*, after marginalization over the all other (including off-diagonal) NSI parameters.⁵ As discussed in Sec. 5.1.2, even when considering NSI coupling only to quarks, there is always a value of η for which the contribution of NSI to the CE ν NS cross section cancels. Consequently CE ν NS data with a single nucleus does not lead to any constraint on the $\varepsilon_{\alpha\beta}^{\oplus}$ parameters. However, the cancellation occurs at different values of η for the three nucleus considered (CsI, Ar, and Ge), and consequently, as seen in the figure, the combination of CE ν NS data with the three nuclear targets does constrain the full space of effective $\varepsilon_{\alpha\beta}^{\oplus}$, even after marginalization over η . The constraints derived from the combined CE ν NS data are independent (and complementary) to those provided by the oscillation analysis and, as seen in the figure, they are fully consistent.

The allowed ranges for vector NSI with up or down quarks are compiled in Table 6.5 and show good qualitative agreement with those of Refs. [122, 196], with the expected small deviations due to the differences in the analysis, quoted CL, and included data.

Finally for completeness we have also performed a new dedicated analysis including axial-vector NSI with up or down quarks. Axial-vector NSI with quarks do not contribute to matter effects nor to CE ν NS. They only enter the global analysis via their modification of the NC event rate in the SNO experiment (see Sec. 5.1.2), which is not able to constrain the NSI coefficients if all of them are included simultaneously due to possible cancellations between their respective contributions to the NC rate. Thus in this case we derive the bounds *assuming that only one NSI coupling is different from zero at a time*.

⁵Technically the regions for oscillations in Fig. 6.10 are obtained by performing each of the two analysis in terms of the 9 (out of the 10) basic parameters (fixing $\zeta = 0$) including the corresponding value of Y_n to each data sample. Therefore the output of each analysis is a χ^2 function of the basic 9 parameters, which is then marginalized with respect to all parameters except for the two combinations shown in the figure.

	Allowed ranges at 90% CL (marginalized)		Allowed ranges at 90% CL (marginalized)
	GLOB-OSC		
	LMA	LMA \oplus LMA-D	
$\varepsilon_{ee}^{u,V} - \varepsilon_{\mu\mu}^{u,V}$	$[-0.063, +0.36]$	$[-1.1, -0.79] \oplus [-0.063, +0.36]$	$[-0.038, +0.034] \oplus [+0.34, +0.42]$
$\varepsilon_{\tau\tau}^{u,V} - \varepsilon_{\mu\mu}^{u,V}$	$[-0.0053, +0.017]$	$[-0.021, +0.018]$	$[-0.046, +0.031] \oplus [+0.35, +0.42]$
$\varepsilon_{\tau\tau}^{u,V}$	$[-0.057, +0.013]$	$[-0.057, +0.061]$	$[-0.046, +0.033] \oplus [+0.35, +0.42]$
$\varepsilon_{\mu\mu}^{u,V}$	$[-0.076, +0.11]$	$[-0.12, +0.11]$	$[-0.044, +0.0049]$
$\varepsilon_{e\tau}^{u,V}$	$[-0.0077, +0.0042]$	$[-0.0077, +0.0083]$	$[-0.079, +0.11]$
$\varepsilon_{\mu\tau}^{u,V}$			$[-0.0064, 0.0053]$
$\varepsilon_{ee}^{d,V} - \varepsilon_{\mu\mu}^{d,V}$	$[-0.069, +0.38]$	$[-1.3, -0.91] \oplus [-0.072, +0.38]$	$[-0.036, +0.031] \oplus [+0.30, +0.39]$
$\varepsilon_{\tau\tau}^{d,V} - \varepsilon_{\mu\mu}^{d,V}$	$[-0.0058, +0.018]$	$[-0.029, +0.019]$	$[-0.040, +0.038] \oplus [+0.31, +0.39]$
$\varepsilon_{\tau\tau}^{d,V}$	$[-0.058, +0.014]$	$[-0.058, +0.098]$	$[-0.041, +0.043] \oplus [+0.31, +0.39]$
$\varepsilon_{\mu\mu}^{d,V}$	$[-0.079, +0.11]$	$[-0.16, +0.11]$	$[-0.054, +0.0045]$
$\varepsilon_{e\tau}^{d,V}$	$[-0.0087, +0.0051]$	$[-0.0087, +0.015]$	$[-0.051, +0.11]$
$\varepsilon_{\mu\tau}^{d,V}$			$[-0.0075, +0.0046]$

Table 6.5: 90% allowed ranges for the vector NSI couplings $\varepsilon_{\alpha\beta}^{u,V}$ and $\varepsilon_{\alpha\beta}^{d,V}$ as obtained from the global analysis of oscillation data (left columns, applicable to NSI induced by mediators with $M_{\text{med}} \ll 5$ MeV) and also including data from CE ν NS experiments (right columns, applicable to NSI induced by mediators with $M_{\text{med}} \gtrsim 50$ MeV). The results are obtained after marginalizing over oscillation and the other matter potential parameters either within the LMA only ($\theta_{12} < 45^\circ$) and within both LMA ($\theta_{12} < 45^\circ$) and LMA-D ($\theta_{12} > 45^\circ$) subspaces respectively (this second case is denoted as LMA \oplus LMA-D). Notice that once CE ν NS data is included the two columns become identical, since for NSI couplings with $f = u, d$ the LMA-D solution is only allowed well above 90% CL.

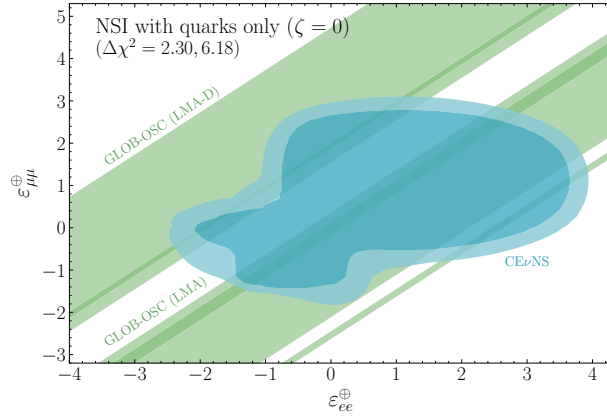


Figure 6.10: Allowed regions in the plane of $\varepsilon_{ee}^{\oplus}$ and $\varepsilon_{\mu\mu}^{\oplus}$ for vector NSI with quarks from the combinations of CE ν NS data compared with the allowed regions from the global oscillation analysis which are the two diagonal shaded bands corresponding to the LMA and LMA-D solutions. Both the green and blue regions are obtained after *independently* marginalizing over all other relevant parameters: NSI couplings (including η) for the CE ν NS region, and NSI couplings, η and oscillation parameters for the «GLOB-OSC» regions. So the values of other NSI and η in the blue and green regions are not forced to be the same.

The corresponding allowed ranges can be found in Table 6.6.

As seen in the table, for all the coefficients, the allowed range is composed of several disjoint intervals. They correspond to values of the NSI couplings for which the SNO-NC event rate is approximately the SM prediction. This can occur for either flavour diagonal or flavour non-diagonal coefficients because solar neutrinos reach the Earth as mass eigenstates, so the density matrix describing the neutrino state at the detector is diagonal in the mass basis, but not in the flavor basis. The presence of non-vanishing off-diagonal $\rho_{\alpha\neq\beta}$ elements is responsible for the sensitivity to off-diagonal $\varepsilon_{\alpha\neq\beta}$ coefficients. More quantitatively, the ranges correspond to coefficients verifying:

$$0 \simeq \text{Tr} \left[\rho^{\text{SNO}} \left(\frac{G_A}{g_A} \right)^2 \right] - 1 = \begin{cases} \rho_{\alpha\alpha}^{\text{SNO}} [(\varepsilon_{\alpha\alpha}^{q,A})^2 \pm 2\varepsilon_{\alpha\alpha}^{q,A}], \\ (\rho_{\alpha\alpha}^{\text{SNO}} + \rho_{\beta\beta}^{\text{SNO}}) (\varepsilon_{\alpha\neq\beta}^{q,A})^2 \pm 4 \text{Re}(\rho_{\alpha\neq\beta}^{\text{SNO}}) \varepsilon_{\alpha\neq\beta}^{q,A} \end{cases} \quad (6.9)$$

where the upper line holds when the NSI coefficient included is flavour diagonal, and the lower one when it is flavour-changing and the \pm sign correspond to $q = u$ and $q = d$ respectively. Thus the allowed range for flavour diagonal NSI is formed by two solutions around $\varepsilon_{\alpha\alpha}^{q,A} = 0$ and $\varepsilon_{\alpha\alpha}^{q,A} = -2$. For flavour off-diagonal NSI it is formed by solutions around $\varepsilon_{\alpha\neq\beta}^{q,A} = 0$ and $\varepsilon_{\alpha\neq\beta}^{q,A} = \mp 4 \text{Re}(\rho_{\alpha\neq\beta}^{\text{SNO}}) / (\rho_{\alpha\alpha}^{\text{SNO}} + \rho_{\beta\beta}^{\text{SNO}})$. For $\varepsilon_{e\mu}^{q,A}$ (and similarly for $\varepsilon_{e\tau}^{q,A}$) this last condition corresponds, in fact, to two distinct solutions, both around $|\varepsilon_{e\mu}^{q,A}| \neq 0$ and two possible signs, due to the two different signs of $\rho_{e\mu}^{\text{SNO}}$ for the two CP-conserving values of $\delta_{\text{CP}} \in \{0, \pi\}$. On the contrary, $\rho_{\mu\tau}^{\text{SNO}}$ takes very similar values for $\delta_{\text{CP}} \in \{0, \pi\}$, and consequently for $\varepsilon_{\mu\tau}^{q,A}$ the two non-zero solutions closely overlap around $\varepsilon_{\mu\tau}^{u,A} \sim 1.7$ ($\varepsilon_{\mu\tau}^{d,A} \sim -1.7$).

6.2.4 Constraints on NSI with quarks and electrons: effective NSI in the Earth

Let us now discuss the most general case in which NSI with quarks and electrons are considered, parametrized by the angles η and ζ introduced in Eqs. (5.7) and (5.8). We

Allowed ranges at 90% CL (1-parameter)		
GLOB-OSC		
$\varepsilon_{ee}^{u,A}$	$[-2.1, -1.8] \oplus [-0.19, +0.13]$	$-\varepsilon_{ee}^{d,A}$
$\varepsilon_{\mu\mu}^{u,A}$	$[-2.2, -1.7] \oplus [-0.26, +0.18]$	$-\varepsilon_{\mu\mu}^{d,A}$
$\varepsilon_{\tau\tau}^{u,A}$	$[-2.1, -1.8] \oplus [-0.20, +0.15]$	$-\varepsilon_{\tau\tau}^{d,A}$
$\varepsilon_{e\mu}^{u,A}$	$[-1.5, -1.2] \oplus [-0.16, +0.12] \oplus [+1.4, +1.7]$	$-\varepsilon_{e\mu}^{d,A}$
$\varepsilon_{e\tau}^{u,A}$	$[-1.5, -1.3] \oplus [-0.13, +0.10] \oplus [+1.4, +1.7]$	$-\varepsilon_{e\tau}^{d,A}$
$\varepsilon_{\mu\tau}^{u,A}$	$[-0.085, +0.11] \oplus [+1.6, +1.9]$	$-\varepsilon_{\mu\tau}^{d,A}$

Table 6.6: 90% CL bounds (1 d.o.f., 2-sided) on the effective axial-vector NSI couplings with quarks. The bounds are derived from the global analysis of oscillation data including the effect of NSI in the SNO NC cross section and *assuming only one NSI coupling different from zero at a time*. As explained in Sec. 6.2.1, these bounds apply to models with $M_{\text{med}} \gtrsim 3$ MeV.

focus on vector NSI because in this case the interplay between matter and scattering effects, and therefore the dependence on the couplings to charged fermions involved, is expected to play a most relevant role.

In this framework, it is useful to quantify the results of our analysis in terms of the effective NSI parameters which describe the generalized Earth matter potential, which are in fact the relevant quantities for the study of long-baseline and atmospheric oscillation experiments. The results are displayed in Fig. 6.11 and on the right column in Table 6.7 where we show the allowed two-dimensional regions and one-dimensional ranges of the effective NSI coefficients for the global analysis of oscillation and CE ν NS data, after marginalizing over all other parameters. Therefore what we quantify in Fig. 6.11 and the right column in Table 6.7 is our present knowledge of the matter potential for neutrino propagation in the Earth, for NSI induced by mediators heavier than $M_{\text{med}} \gtrsim 50$ MeV (as discussed in Sec. 6.2.1) and for *any unknown value* of η and ζ . Technically this is obtained by marginalizing the results of the global χ^2 with respect to η and ζ as well, and the $\Delta\chi^2$ functions plotted in the figure are defined with respect to the absolute minimum for any η and ζ which lies close to $\eta \sim -45^\circ$ and $\zeta \sim 10^\circ$.

From these results we see that the allowed ranges for the diagonal $\varepsilon_{\alpha\alpha}^\oplus$ parameters are composed of two disjoint regions. However let us stress that they both correspond to the LMA solution since neither of them falls within the LMA-D region (which requires $\varepsilon_{ee}^\oplus - \varepsilon_{\mu\mu}^\oplus = -2$). In fact, the LMA-D solution is ruled out beyond the CL shown in Fig. 6.11 and, as will be discussed in Sec. 6.2.5 in more detail, the combination of oscillation data with CE ν NS results for different nuclear targets is required to reach this sensitivity.

Conversely, for mediators with masses $M_{\text{med}} \ll 500$ keV, effects on ES and CE ν NS experiments would be suppressed even if NSI involve couplings to both quarks and electrons, and the only effect of NSI will be the modification of the matter potential in neutrino oscillations. The same holds for NSI with quarks only (*i.e.*, for $\zeta = 0$) induced by mediators with masses $M_{\text{med}} \ll 10$ MeV. Since in the matter potential the effects for protons or electrons are indistinguishable, the allowed ranges of the effective $\varepsilon_{\alpha\beta}^\oplus$ are the same in both scenarios, which are given on the left column in Table 6.7 (and included in Fig. 6.10). As discussed in Sec. 5.1.1, in this case the analysis can only constrain the differences between flavour-diagonal NSI coefficients. Furthermore, the allowed range of $\varepsilon_{ee}^\oplus - \varepsilon_{\mu\mu}^\oplus$ contains a disjoint interval around -2 (which at 90% CL further splits into two sub-intervals as seen in the table) corresponding to the LMA-D solution, which is well allowed in these scenarios. We will discuss this in more detail in Sec. 6.2.5.

Allowed ranges at $\begin{matrix} 90\% \text{ CL} \\ (99\% \text{ CL}) \end{matrix}$ marginalized	
GLOB-OSC w/o NSI in ES	GLOB-OSC w NSI in ES + CE ν NS
$\epsilon_{ee}^{\oplus} - \epsilon_{\mu\mu}^{\oplus}$	ϵ_{ee}^{\oplus}
$[-3.1, -2.8] \oplus [-2.1, -1.88] \oplus [-0.15, +0.17]$ $([-4.8, -1.6] \oplus [-0.40, +2.6])$	$[-0.19, +0.20] \oplus [+0.95, +1.3]$ $([-0.23, +0.25] \oplus [+0.81, +1.3])$
$\epsilon_{\tau\tau}^{\oplus} - \epsilon_{\mu\mu}^{\oplus}$	$\epsilon_{\mu\mu}^{\oplus}$
$[-0.0215, +0.0122]$ $([-0.075, +0.080])$	$[-0.43, +0.14] \oplus [+0.91, +1.3]$ $([-0.29, +0.20] \oplus [+0.83, +1.4])$
$\epsilon_{e\mu}^{\oplus}$	$\epsilon_{\tau\tau}^{\oplus}$
$[-0.11, -0.021] \oplus [+0.045, +0.135]$ $([-0.32, +0.40])$	$[-0.43, +0.14] \oplus [+0.91, +1.3]$ $([-0.29, +0.20] \oplus [+0.83, +1.4])$
$\epsilon_{\mu\tau}^{\oplus}$	$\epsilon_{e\mu}^{\oplus}$
$[-0.22, +0.088]$ $([-0.49, +0.45])$	$[-0.12, +0.011]$ $([-0.18, +0.08])$
$\epsilon_{\mu\tau}^{\oplus}$	$\epsilon_{e\tau}^{\oplus}$
$[-0.0063, +0.013]$ $([-0.043, +0.039])$	$[-0.16, +0.083]$ $([-0.25, +0.33])$
	$\epsilon_{\mu\tau}^{\oplus}$
	$[-0.0047, +0.012]$ $([-0.020, +0.021])$

Table 6.7: 90% and 99% CL bounds (1 d.o.f., 2-sided) on the effective NSI parameters relevant for matter effects in LBL experiments with arbitrary values of η and ζ , obtained after marginalizing over all other NSI and oscillation parameters. The bounds on the left (right) column are applicable to NSI induced by mediators with masses $M_{\text{med}} \ll 500$ keV ($M_{\text{med}} \gtrsim 50$ MeV).

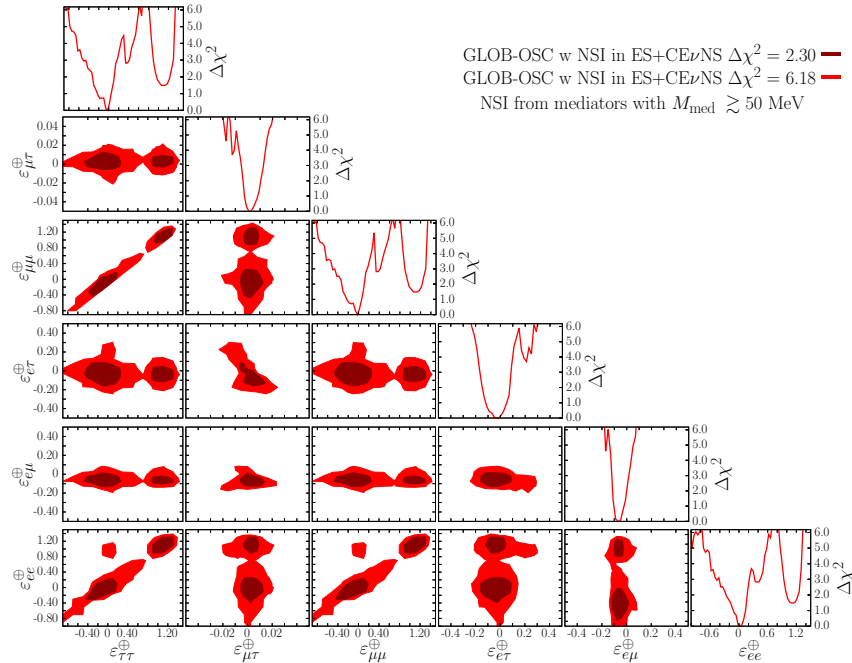


Figure 6.11: Constraints on the effective generalized NSI in the Earth matter (relevant for matter effects in LBL experiments) with arbitrary values of η and ζ . Each panel shows a two-dimensional projection of the allowed multi-dimensional parameter space after minimization with respect to the undisplayed parameters. The contours correspond to 1σ and 2σ (2 d.o.f.).

We finish this section by discussing the impact of NSI in this general framework (where we allow couplings to quarks and electrons simultaneously) on the determination of the oscillation parameters in the solar sector. This is shown in Fig. 6.12, where we see that the determination of the oscillation parameters within the LMA region, which is the region favored by the fit, is rather robust even after the inclusion of NSI couplings to both quarks and electrons. Comparing the blue and red regions in the figure we see that the inclusion of data from atmospheric and LBL experiments is important to reach such robustness. This had been previously shown in Refs. [195, 196] for NSI with quarks only; here we conclude that the same conclusions hold also in presence of NSI with electrons, as long as their impact on ES is accounted for in the fit. Also, the allowed LMA regions are not very much affected by the addition of the CE ν NS data and it is very close to that of the oscillation analysis without NSI. As also shown in the figure, the LMA-D is only allowed at 97% CL or above (for 2 d.o.f.). The current status of the LMA-D region is discussed in more detail in the next section.

6.2.5 Present status of the LMA-D solution

In this section, we discuss in more detail the present status of the LMA-D region in light of all available data, for models leading to NSI couplings to quarks and electrons simultaneously. We start by exploring the dependence of the presence of the LMA-D solution on the specific combination of couplings to the charged fermions considered. In order to do so it is convenient to introduce the functions $\chi_{\text{LMA}}^2(\eta, \zeta)$ and $\chi_{\text{LMA-D}}^2(\eta, \zeta)$ which are obtained by marginalizing the χ^2 for a given value of η and ζ over both the oscillation and the matter potential parameters within the regions $\theta_{12} < 45^\circ$ and $\theta_{12} > 45^\circ$, respectively. With this, in the left (central) panels of Fig. 6.13 we plot isocontours of the differences $\chi_{\text{LMA}}^2(\eta, \zeta) - \chi_{\text{no-NSI}}^2$ ($\chi_{\text{LMA-D}}^2(\eta, \zeta) - \chi_{\text{no-NSI}}^2$) where $\chi_{\text{no-NSI}}^2$ is the minimum χ^2 for standard

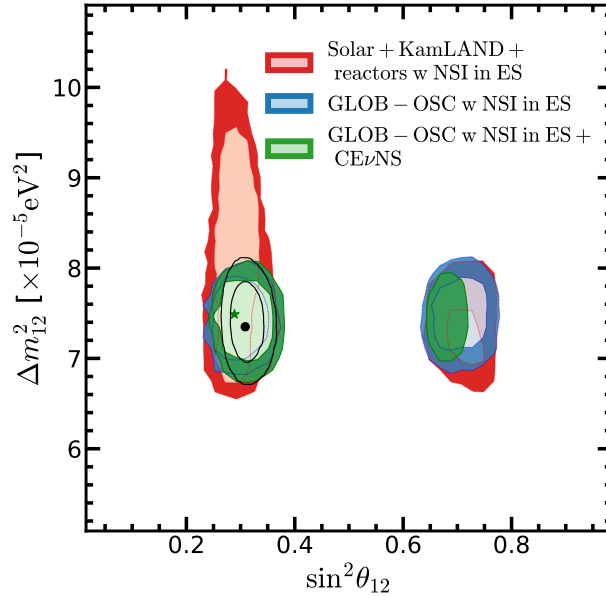


Figure 6.12: Two-dimensional projections of the allowed regions (at 90% and 3σ CL) onto Δm_{12}^2 and θ_{12} parameters, after marginalizing over all other oscillation parameters and over NSI couplings to quarks and electrons. Red regions correspond to the analysis of KamLAND and Solar data; blue regions include all oscillation data; and green regions include all oscillation and CE ν NS data. In all cases, NSI effects on ES are fully accounted for in the fit. For comparison, the empty contours (solid black lines) show the corresponding regions for the global oscillation analysis without NSI.

3ν oscillations (*i.e.*, without NSI). In the right panels we plot $\chi_{\text{LMA-D}}^2(\eta, \zeta) - \chi_{\text{LMA}}^2(\eta, \zeta)$ which quantifies the relative quality of the LMA and LMA-D solutions. In each row in this figure we include only a subset of the data as indicated by the labels.

The upper panels of Fig. 6.13 show the results when only oscillation data is analyzed accounting for the effects of NSI on the matter potential, but without including the effect of NSI in the ES cross sections in Borexino, SNO, and SK. As outlined in Sec. 6.2.1, these results would therefore apply to NSI models with very light mediators, $M_{\text{med}} \ll 500$ keV. In this scenario (as shown in Sec. 5.1.1) only the combination of NSI couplings to electrons, protons and neutrons, parametrized by the effective angle η' in Eq. (5.17), is relevant. Therefore the $\Delta\chi^2$ isocontours are curves along $\tan \eta' = \tan \eta / (\cos \zeta + \sin \zeta) = \text{constant}$. From the upper left panel we see that for most of (η, ζ) values, the inclusion of NSI leads only to a mild improvement of the global fit to oscillation data ($\chi_{\text{LMA}}^2(\eta, \zeta) - \chi_{\text{no-NSI}}^2 > -4$). As discussed in Ref. [196] (Addendum), with the updated SK4 solar data the determination of Δm_{21}^2 in solar and in KamLAND experiments are fully compatible at $\lesssim 2\sigma$ level. The inclusion of NSI only leads to an overall better fit at a CL above 2σ (but still not statistically significant in any of the different data samples) for (ζ, η) along the darker band. In particular the best fit lies along $\tan \eta' \sim -1/Y_n^\oplus \approx -0.95$ ($\eta' \approx -43.6^\circ$) for which NSI effects in the Earth matter cancel, so there is no constraint from Atmospheric and LBL experiments on the NSI which can lead to that slightly better fit to Solar + KamLAND data within the LMA solution. The central and right panels show the status of the LMA-D solution in this scenario. We find that LMA-D provides a good solution in most of the (η, ζ) plane. The LMA-D is only very disfavoured for (ζ, η) along the band with $2.75 \lesssim \tan \eta' \lesssim -1.75$. For these values the NSI contribution to the matter potential in the Sun cancels in some point inside the neutrino production area and therefore the degeneracy between NSI and the octant of θ_{12} cannot be realized.

The impact of including NSI in the ES cross section in Borexino, SNO, and SK can be seen in the middle row panels in Fig. 6.13. Since these panels include the effect of NSI in ES, they apply to NSI models with mediator masses $10 \text{ MeV} \lesssim M_{\text{med}} \lesssim 50 \text{ MeV}$. The main effect is that the ζ values for which the LMA-D solution is allowed become very restricted (in fact the best fit point for all panels are always close to $\zeta = 0$) as long as η does not approach 90° , and consequently the dependence of ζ is heavily suppressed. Thus, once the effect of NSI in the ES cross section is included, the results are not very different from those obtained for $\zeta = 0$ (no coupling to electrons) in Refs. [122, 196]. The middle and right panels in this row also illustrate how, as long as only oscillation data is included, the LMA-D solution is still allowed with a CL comparable and even slightly better than LMA.

The lower panels in Fig. 6.13 include the combination of all data available and are therefore applicable to NSI with mediators above $M_{\text{med}} \gtrsim 50 \text{ MeV}$. When comparing the LMA (LMA-D) to the SM hypothesis (*i.e.*, no NSI) we find that the global minimum of the fit is better (comparable) to that obtained in absence of NSI, as shown in the middle and left panels. However, we also see that the inclusion of the $\text{CE}\nu\text{NS}$ data in the analysis severely constrains the LMA-D solution. Quantitatively we find that LMA-D becomes disfavoured with respect to LMA with $\Delta\chi^2 > 4.7$ for any value of (η, ζ) (right panel) and it is only allowed⁶ below $\Delta\chi^2 = 9$ for very specific combinations of couplings to quarks and electrons, $-2.5^\circ \leq \zeta \leq 1.5^\circ$ and $-29^\circ \leq \eta \leq -13^\circ$.

To further illustrate the role of the different experiments in this conclusion we show in Fig. 6.14 the projection of $\chi_{\text{LMA-D}}^2(\eta, \zeta) - \chi_{\text{LMA}}^2(\eta, \zeta)$ on η after marginalizing over ζ (which, as discussed above, it is effectively not very different from fixing $\zeta = 0$). The figure illustrates the complementarity of the $\text{CE}\nu\text{NS}$ data with different targets. As discussed in Sec. 5.1.2, the effects of NSI in $\text{CE}\nu\text{NS}$ on a given target, characterized by a value of Y_n , cancel for $\eta'' = \arctan(-1/Y_n)$ (with $\tan \eta'' = \tan \eta / \cos \zeta \simeq \tan \eta$). This corresponds to $\eta \simeq -35.4^\circ$ ($Y_n^{\text{CsI}} \approx 1.407$), -39.3° ($Y_n^{\text{Ar}} \approx 1.222$), and -38.4° ($Y_n^{\text{Ge}} \approx 1.263$) for CsI, Ar, and Ge respectively. Thus, as seen in the figure, the combination of the constraints from $\text{CE}\nu\text{NS}$ with the different targets is important to disfavour the LMA-D solution.

6.3 Constraining Monopole-Dipole interactions with global oscillation data

This section summarizes our results from the global fit to solar neutrino oscillation data in the framework of three massive neutrinos including the new neutrino-matter interactions generated by the Lagrangian in Eq. (5.52) with the four choices of pseudoscalar couplings to neutrinos in Eq. (5.63).⁷ In what respect the relevant parameter space, Eqs. (5.57) and (5.58) are a set of six coupled linear differential equations whose solution

⁶Notice that this is different than what we show in Fig. 6.13, where marginalization over η, ζ has been performed.

⁷For the detailed description of the methodology we refer to our published global analysis NuFIT-5.0 [275] to which we have included the data additions in NuFIT [1]; some technical aspects of our treatment of neutrino propagation in the solar matter can be found in Sec. 2.4 of Ref. [276]. For solar neutrinos the analysis includes the total rates from the radiochemical experiments Chlorine [147], Gallex/GNO [56], and SAGE [55], the spectral and zenith data from the four phases of Super-Kamiokande (SK) in Refs. [60–62] including the latest SK4 2970-day energy and day/night spectrum [63], the results of the three phases of SNO in the form of the day-night spectrum data of SNO-I [256] and SNO-II [257] and the three total rates of SNO-III [258], and the spectra from Borexino Phase-I [67, 148] (BX1), Phase-II [68] (BX2), and Phase-III [70] (BX3). In the framework of three-neutrino mixing the oscillation probabilities for solar neutrinos dominantly depend on θ_{12} and Δm_{21}^2 , for which relevant constraints arise from the analysis of the KamLAND reactor data, hence we include in our fit the separate DS1, DS2, DS3 spectra from KamLAND [97].

depends on the two model parameters $(m_\phi, g_s^N g_p^{\nu a})$ (for $a = e, \mu, \tau$ or U) and the six oscillation parameters, $\theta_{12}, \theta_{13}, \theta_{23}, \Delta m_{21}^2, \Delta m_{32}^2$, and δ_{CP} . However, as it is well-known, the present determination of Δm_{32}^2 — derived dominantly from atmospheric, long-baseline accelerator, and medium-baseline reactor neutrino experiments — implies that the solar neutrino oscillations driven by $\Delta m_{32}^2/E_\nu$ are averaged out. Thus in our numerical evaluations we fix it to its present best-fit value, but any other value would yield the same result as long as we remain in the regime of averaged Δm_{32}^2 oscillations.⁸ In the standard 3ν oscillation scenario ν_μ and ν_τ are totally indistinguishable at the energy scale of solar and reactor experiments, hence also the dependence on θ_{23} and δ_{CP} drops out in the evaluation of the solar observables. Including the flavour dependent scalar-pseudoscalar potential reintroduces a mild dependence on θ_{23} and δ_{CP} (except for the flavour-universal case $a = U$), but quantitatively the phenomenology of solar neutrino data is still dominated by Δm_{21}^2 and θ_{21} . The dependence on θ_{13} is much weaker than its present precision from medium-baseline reactor experiments (in particular from Daya-Bay [93]), while the impact of the CP phase is very marginal. So we can safely fix θ_{13} to its current best-fit value from NuFIT $\sin^2 \theta_{13} = 0.02203$ and set $\delta_{\text{CP}} = 0$. In what respects θ_{23} , for coupling to specific flavours $a = e, \mu, \tau$ we marginalize it within the allowed range from the global oscillation analysis by adding a prior for $\sin^2 \theta_{23}$ from NuFIT [1] to the χ^2 function of the solar and KamLAND experiments.⁹ Altogether the parameter space to be explored is five-dimensional.

We perform the analysis for both Dirac and Majorana neutrinos. Besides the different ν_{eL} oscillation probabilities resulting from the evolution equations Eqs. (5.57) and (5.58), there are also differences in the evaluation of the neutrino-electron elastic scattering event rates in Borexino, SNO and SK: while for the Dirac case the produced $\nu_{\alpha R}$ does not interact in the detector, for Majorana neutrinos the $\bar{\nu}_{\alpha R}$ do interact (albeit with a different cross section than the corresponding $\nu_{\alpha L}$ neutrinos) and such interactions must be included in the evaluation of the event rates. Furthermore the CC event rate at SNO can also be different for Dirac and Majorana because the $\bar{\nu}_{eR}$ interaction will produce a positron and two neutrons which may or may not be discriminated. Lacking the details for a proper estimation, we have performed the analysis under two extreme hypothesis: either assuming that the e^+ is recognized and the whole event is rejected, or that the positron is misidentified as an electron and it contributes as a CC event *plus* two additional NC events because of the generated neutrons. We have verified that the final bounds obtained under the two assumptions are the same.

Altogether we find that the inclusion of the new interaction does not lead to any significant improvement on the description of the data, and in fact the overall best-fit χ^2 in the five-dimensional parameter space is the same as in the standard 3ν oscillation scenario. Consequently the statistical analysis results into bounds on the allowed range of the scalar-pseudoscalar model parameters.

We show in Fig. 6.15 the excluded region on the parameter space for the case of flavour-universal coupling $(m_\phi, g_s^N g_p^{\nu\nu})$ derived from the global analysis of solar neutrino and KamLAND data for Dirac and Majorana cases after marginalization over the relevant oscillation parameters $(\Delta m_{21}^2, \theta_{12})$ while keeping the other oscillation parameters fixed to their best-fit values as discussed above. We show the regions at 90% CL (2 dof, two-sided). Notice that when reporting the bounds on the model parameters one has a choice

⁸In fact this would allow for a reduction of the evolution equations to an effective 4×4 system. However from the computational point of view the reduction from a 6×6 to a 4×4 set of equations is not substantial, so in our calculations we stick to the complete 6×6 system.

⁹Our results, however, show that the difference in the bounds obtained marginalizing over θ_{23} with this prior or fixing θ_{23} to its best-fit value is very small.

on the statistical criteria to derive the constraints. The reason is that the experiment is in fact only sensitive to $|g_s^N g_p^{\nu\nu}|$: since the potential is helicity-flipping its effect does not interfere with the helicity-conserving vacuum oscillation and MSW matter potential, so the probabilities only depend on the absolute value of the couplings and on the square of the mediator mass. Therefore, accounting for the physical boundary, it is possible to report the limit on the absolute value of the coupling (and mass) as a *one-sided* limit, which at 90% CL for 1 dof (2 dof) corresponds to $\Delta\chi^2 = 1.64$ (3.22). Conversely, if this restriction is not imposed, the result obtained is what is denoted as a *two-sided* limit, which at 90%CL for 1 dof (2 dof) corresponds to $\Delta\chi^2 = 2.71$ (4.61) and results into weaker constraints. In what follows we list the bounds obtained with the least constraining two-sided criterion.

As seen in Fig. 6.15 the results are quantitatively similar for Dirac or Majorana neutrinos. In the figure we observe a change in the slope of the exclusion region for masses $m_\phi \sim 10^{-15}$ eV. For smaller mediator masses, the interaction length is larger than the Sun radius and the corresponding potential becomes saturated. Conversely for $m_\phi \gtrsim 10^{-14}$ eV the interaction range is short enough for the contact interaction approximation to hold, in which case the analysis only depends on the combination $|g_s^N g_p^{\nu\nu}| / m_\phi^2$ and the region boundary becomes a straight line of slope two in the log-log plane.

To illustrate the relevance of the different solar neutrino experiments on these results we plot in the left (central) panels in Fig. 6.16 the value of $\Delta\chi^2 \equiv \chi^2(g_s^N g_p^{\nu\nu}) - \chi^2(g_s^N g_p^{\nu\nu} = 0)$ as a function of $g_s^N g_p^{\nu\nu}$ for the Dirac (Majorana) case in the effective infinite-range interaction limit for each of the individual solar neutrino experiments, fixing all oscillation parameters (in particular Δm_{21}^2 , θ_{12} and θ_{23}) to their best-fit values. We see from the figure that the constraints are driven by the experiments sensitive to the lowest energy part of the solar neutrino spectrum (*i.e.*, to the pp flux), which correspond to the spectral data of phase-II of Borexino (BX2 in the figure) and the event rates in Gallium experiments (Ga). Conversely, those most sensitive to the higher energy part of the solar spectrum (*i.e.*, the ^8B flux), such as the spectral information of Super-Kamiokande and SNO and the total rate in Chlorine (Cl), yield weaker sensitivity to the new interaction. As a consequence the combined constraints for Majorana neutrinos are the same for both variants of the SNO CC analysis (labeled as SNO and SNO' in the figure). Furthermore, since the oscillation parameters Δm_{21}^2 and θ_{12} are dominantly determined by KamLAND reactor data as well as SNO and SK solar neutrino data, their determination is very little affected by the inclusion of the new interaction, and the allowed ranges that we found in this five-parameter analysis are exactly the same as in the standard 3ν oscillation.

The right panel illustrates the dependence of the combined bounds on the assumption for the neutrino flavour of the pseudoscalar coupling for the four choices in Eq. (5.63). As seen the variation in the bounds is below $\mathcal{O}(10)$. As expected the difference is larger between coupling to ν_e and to ν_μ (or ν_τ) because the coupling to ν_e has larger effect on P_{ee} which gives the dominant contribution to the event rates in solar neutrino experiments. We notice in passing that the small variation between the bounds for couplings to ν_μ and ν_τ is dominantly due to the non-zero value of θ_{13} .¹⁰

Finally we list in table 6.8 the 90% CL (1 dof) bounds obtained from the global analysis of solar data in the two asymptotic regimes and for the four choices of flavour dependence after marginalization over the three relevant oscillation parameters Δm_{21}^2 , θ_{12} and θ_{23} .

¹⁰In fact, it can be shown that in the limit $\theta_{13} = 0$ the χ^2 function depends on $g_s^N g_p^{\nu\mu}$, $g_s^N g_p^{\nu\tau}$ and θ_{23} only through the effective combination $g_s^N g_p^{\nu\mu} \cos^2 \theta_{23} + g_s^N g_p^{\nu\tau} \sin^2 \theta_{23}$. In the general case $\theta_{13} \neq 0$ such relation becomes only approximate.

		Global Solar ν		Solar $\bar{\nu}_e$
		Dirac	Majorana	Majorana
for $m_\phi < 10^{-16}$ eV	$a = e$	1.5×10^{-34}	1.7×10^{-34}	1.1×10^{-33}
	$a = \mu$	3.6×10^{-34}	4.3×10^{-34}	7.6×10^{-34}
	$a = \tau$	3.6×10^{-34}	6.3×10^{-34}	7.9×10^{-34}
	$a = U$	7.6×10^{-35}	9.6×10^{-35}	3.2×10^{-34}
for $m_\phi > 10^{-14}$ eV	$a = e$	1.3×10^{-31}	2.5×10^{-31}	1.9×10^{-31}
	$a = \mu$	2.0×10^{-31}	5.0×10^{-31}	2.5×10^{-31}
	$a = \tau$	2.0×10^{-31}	7.9×10^{-31}	2.5×10^{-31}
	$a = U$	6.3×10^{-32}	1.3×10^{-31}	7.0×10^{-32}

Table 6.8: Bounds from the different analysis in the two asymptotic regimes, effective infinite interaction range and contact range respectively, and for the four choices of flavour dependence. For the global solar analysis the bounds shown are obtained at 90% CL (1 dof, two-sided), $\Delta\chi^2 = 2.71$. The bounds from the antineutrino flux constraint are obtained from the 90% CL experimental constraints in Eq. (6.12). See text for details.

6.3.1 Bounds from solar antineutrino constraints

Turning now to the bounds derived from the non observation of a flux of solar antineutrinos, we plot in the left panel in Fig. 6.17 a compilation of the model-independent limits on $\bar{\nu}_e$ flux of astrophysical origin as reported by KamLAND [277], Borexino [278] and Super-Kamiokande [279–281]. In the same panel we also show the predicted flux in the presence of the helicity-flip potential for several model parameters. From the figure we see that the most stringent upper bounds on $\bar{\nu}_e$ come KamLAND [277] and Borexino [278] which constraint the $\bar{\nu}_e$ flux from the ${}^8\text{B}$ reaction by

$$\text{KamLAND:} \quad \Phi_{\bar{\nu}_e}^{\text{sB}} < 60 \text{ cm}^{-2} \text{ s}^{-1} \text{ at 90\% CL for } E_\nu > 8.3 \text{ MeV}, \quad (6.10)$$

$$\text{Borexino:} \quad \Phi_{\bar{\nu}_e}^{\text{sB}} < 138 \text{ cm}^{-2} \text{ s}^{-1} \text{ at 90\% CL for } E_\nu > 7.8 \text{ MeV} \quad (6.11)$$

which the experiments translated into a bound on the corresponding integrated oscillation probabilities

$$\begin{aligned}
P(\nu_e \rightarrow \bar{\nu}_e) &\equiv \frac{\int_{E_{\text{thres}}} \Phi_{\text{sB}}(E_\nu) \sigma(E_\nu) P_{\nu_e L \rightarrow \bar{\nu}_e R}(E_\nu) dE_\nu}{\int_{E_{\text{thres}}} \Phi_{\text{sB}}(E_\nu) \sigma(E_\nu) dE_\nu} \\
&\leq \begin{cases} 4.1 \times 10^{-5} & \text{for } E_{\text{thres}} = 8.3 \text{ MeV} \\ 7.4 \times 10^{-5} & \text{for } E_{\text{thres}} = 7.8 \text{ MeV} \end{cases} \quad (6.12)
\end{aligned}$$

where we have used the normalization of the $\Phi_{\text{sB}}(E_\nu)$ of the latest version of the SSM [146, 167] which results in the slight difference in the bounds on the probabilities in Eq. (6.12) with respect to those quoted by the experimental collaborations.

We show in the right panel of Fig. 6.17 the constraints on the model parameters obtained by the projection of the bounds in Eq. (6.12). For concreteness, in this case, we fix the oscillation parameters to their best-fit values; however, as already noted, the dependence of the bounds on the oscillation parameters is very mild within their allowed ranges from global oscillation analysis [1, 275]. We show the results for pseudoscalar coupling to ν_U , but similar bounds apply to the other cases (see Table 6.8 for the results obtained with the different flavour assumptions in Eq. (5.63)). As seen from the figure, the bounds imposed with KamLAND and Borexino constraints are very similar. In addition, we notice the expected mass independent asymptotic behaviour for effectively infinite

range interactions when $m_\phi \lesssim 10^{-16}$, as well as the dependence on $|g_s^N g_p^{\nu U}| / m_\phi^2$ in the contact interaction regime for $m_\phi \gtrsim 10^{-14}$ eV.

6.4 Summary

Using Borexino Phase II data (Section 6.1), we derived constraints on non-standard interactions (NSI), neutrino magnetic moments (NMM), and light mediators. For NSI, we accounted for flavor-diagonal and off-diagonal couplings using a density matrix formalism (Eq. (5.9)), resolving degeneracies between oscillation and interaction effects. Simultaneous inclusion of all vector/axial couplings relaxed bounds compared to single-parameter analyses (Figs. 6.2, 6.3; Tables 6.1, 6.2). Vector NSI with electrons eliminated the LMA-D solution, enabling independent determination of $\varepsilon_{\alpha\alpha}^{f,V}$.

NMM bounds (Eqs. (6.3), (6.4)) aligned with prior results, validating our χ^2 implementation. Light mediators ($M \lesssim 0.1$ MeV) yielded mass-independent 90% CL limits:

$$\begin{aligned} |g_{Z'}^{B-L}| &\leq 6.3 \times 10^{-7}, & |g_{Z'}^{L_{e^-} - L_{\mu,\tau}}| &\leq 5.8 \times 10^{-7}, \\ |g_\phi^{\text{univ}}| &\leq 1.4 \times 10^{-6}, & |g_\varphi^{\text{univ}}| &\leq 2.2 \times 10^{-6}. \end{aligned} \quad (6.13)$$

For heavy mediators ($M \gtrsim$ MeV), contact-interaction bounds scaled as $(g/M)^n$:

$$|g_{Z'}|/M_{Z'} \leq 1.4 \times 10^{-6} \text{ MeV}^{-1}, \quad |g_{\phi,\varphi}|/M \leq 2.5 \times 10^{-6} \text{ MeV}^{-1}. \quad (6.14)$$

In Section 6.2, we combined neutrino oscillation data (excluding T2K/NO ν A CPV results) with CE ν NS datasets (COHERENT, Dresden-II) and constrained vector/axial NSI couplings to e, u, d quarks. From this study, the main results can be resumed as:

- Vector NSI in matter potential allowed LMA-D solutions unless ES detection effects (Borexino, SK, SNO) were included (Fig. 6.13). CE ν NS data disfavored LMA-D beyond 2σ for quark-coupled mediators (Fig. 6.14).
- Oscillation parameters remained robust under NSI inclusion (Fig. 6.12).
- Axial NSI bounds were weaker than vector counterparts (Fig. 6.9; Table 6.4).

Earth matter potential projections for atmospheric and LBL experiments are shown in Fig. 6.11 and Table 6.7.

In Section 6.3, we discussed how global solar neutrino data provide stringent constraints on spin-zero mediators with pseudoscalar neutrino couplings (g_p^ν) and scalar nucleon couplings (g_s^N). The induced SFP potential, dominant at low neutrino energies, is constrained by global solar+KamLAND analyses (Dirac/Majorana cases) and solar $\bar{\nu}_e$ flux limits (Majorana). Our bounds (Figs. 6.15, 6.17) surpass previous constraints for ultralight mediators ($m_\phi \lesssim 10^{-12}$ eV):

- For $m_\phi < 10^{-14}$ eV: Solar bounds exceed CMB limits ($g_p^\nu \leq 7 \times 10^{-7}$ [282]).
- For $10^{-14} < m_\phi/\text{eV} < 10^{-6}$: Exceed laboratory limits ($g_p^{\nu e} \lesssim 3 \times 10^{-3}$ [283, 284]) and equivalence principle tests [285, 286].

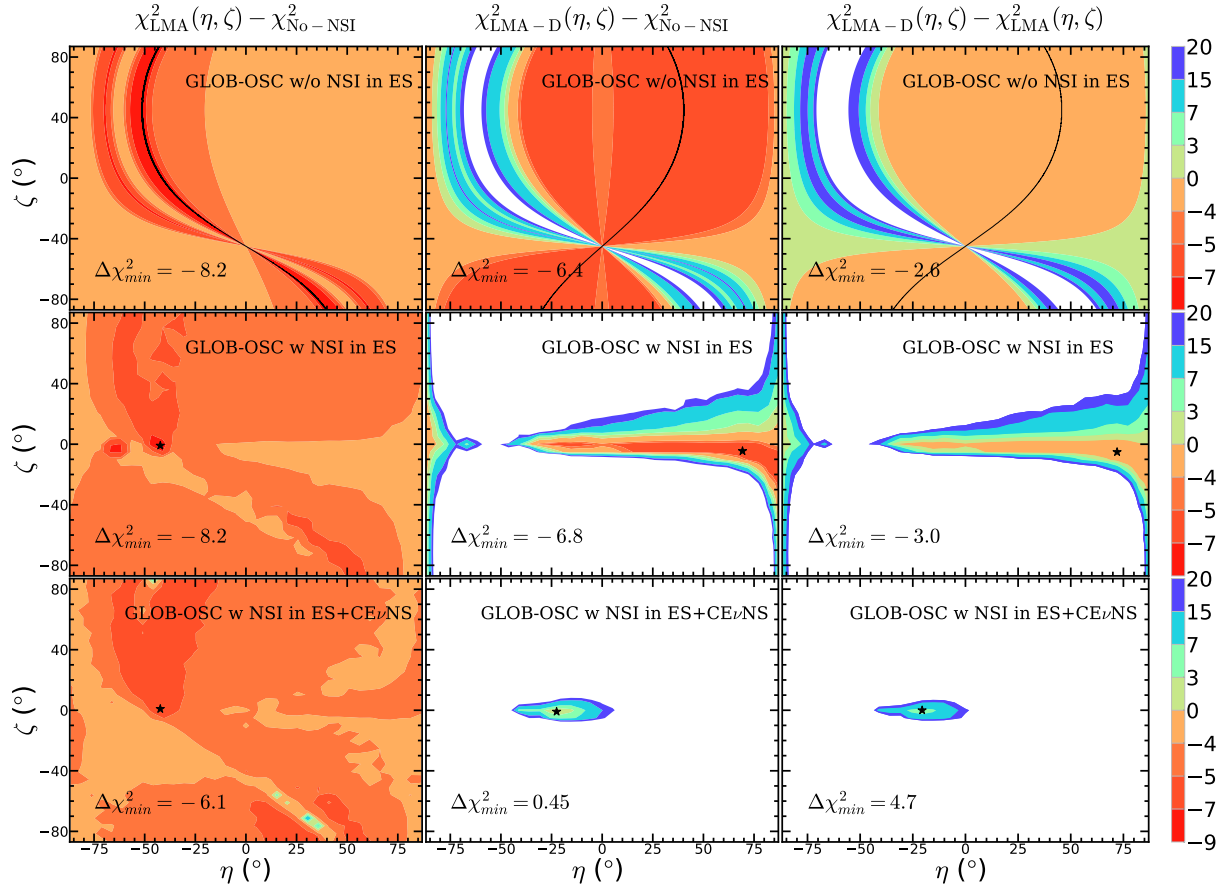


Figure 6.13: Isocontours of $\chi_{\text{LMA}}^2(\eta, \zeta) - \chi_{\text{no-NSI}}^2$, $\chi_{\text{LMA-D}}^2(\eta, \zeta) - \chi_{\text{no-NSI}}^2$ and $\chi_{\text{LMA-D}}^2(\eta, \zeta) - \chi_{\text{LMA-D}}^2(\eta, \zeta)$ of the global analysis of oscillation data without including NSI in the ES cross sections at Borexino, SNO, and SK (upper panels), and including the NSI in the ES cross sections at Borexino, SNO, and SK (middle panels). The lower panels shows of the result adding the data from CE ν NS experiments. We show projections in the plane of angles (ζ , η) (after marginalization of all other parameters) which parametrize the relative strength of the NSI couplings to up-quarks, down-quark, and electrons. The levels corresponding to the different colours are given on the color bar on the right. Contours beyond 20 are white. In each panel the best-fit point is marked with a star (middle and bottom rows) or by a solid black line (upper row). Results in the upper row are applicable to NSI induced by mediators with $M_{\text{med}} \ll 500$ keV; in the middle row, for models with $M_{\text{med}} \gtrsim 10$ MeV; and in the lower row, for models with $M_{\text{med}} \gtrsim 50$ MeV, see Sec. 6.2.1 for details.

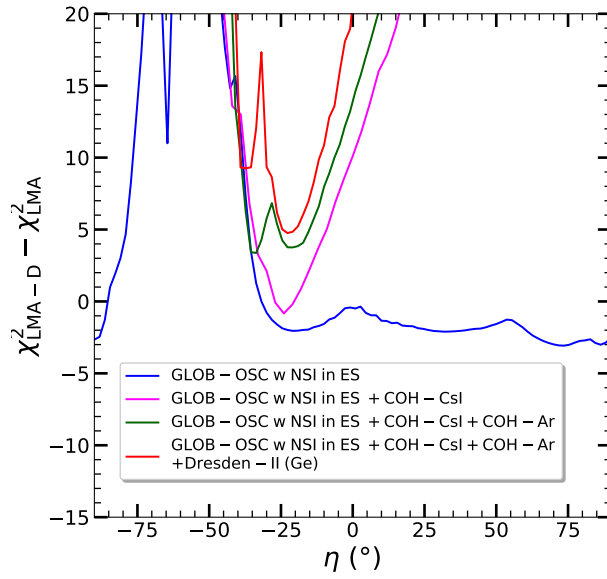


Figure 6.14: Dependence of $\chi_{\text{LMA-D}}^2(\eta, \zeta) - \chi_{\text{LMA}}^2(\eta, \zeta)$ on η after marginalizing over ζ for different combination of experiments as labeled in the figure.

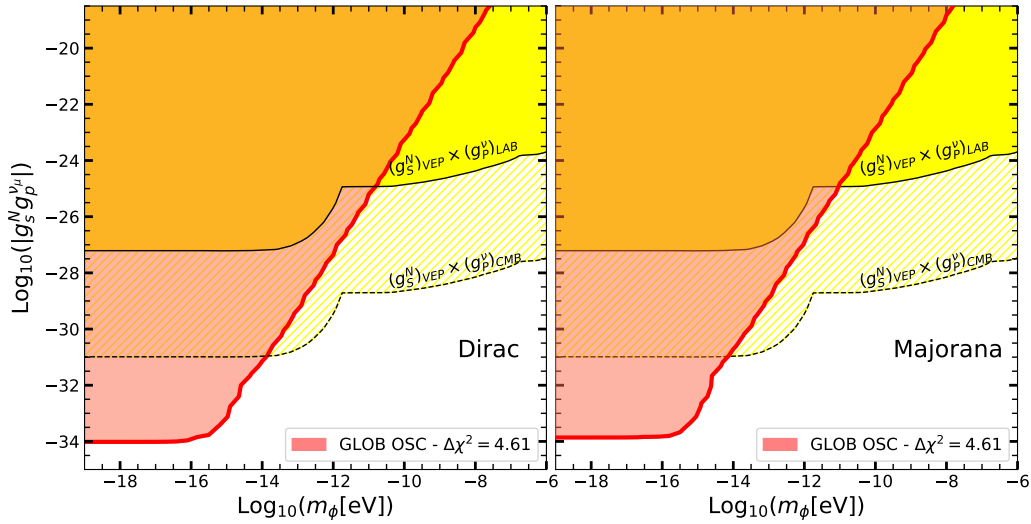


Figure 6.15: Excluded region at 90% CL in the $(m_\phi, g_s^N g_p^{\nu U})$ plane by the global analysis of solar neutrino data after marginalization over the relevant oscillation parameters ($\Delta m_{21}^2, \theta_{12}$) while keeping the other oscillation parameters fixed as described in the text. Left (right) panel corresponds to Dirac (Majorana) neutrinos. For comparison we show as yellow region the bounds on the product of couplings from the product of the bound on g_s^N from violation of weak equivalent (VEP) principle and the bounds on g_p^{ν} from either kinematic and rare effects in weak decays in laboratory experiments (LAB) or cosmology bounds from cosmic microwave background (CMB).

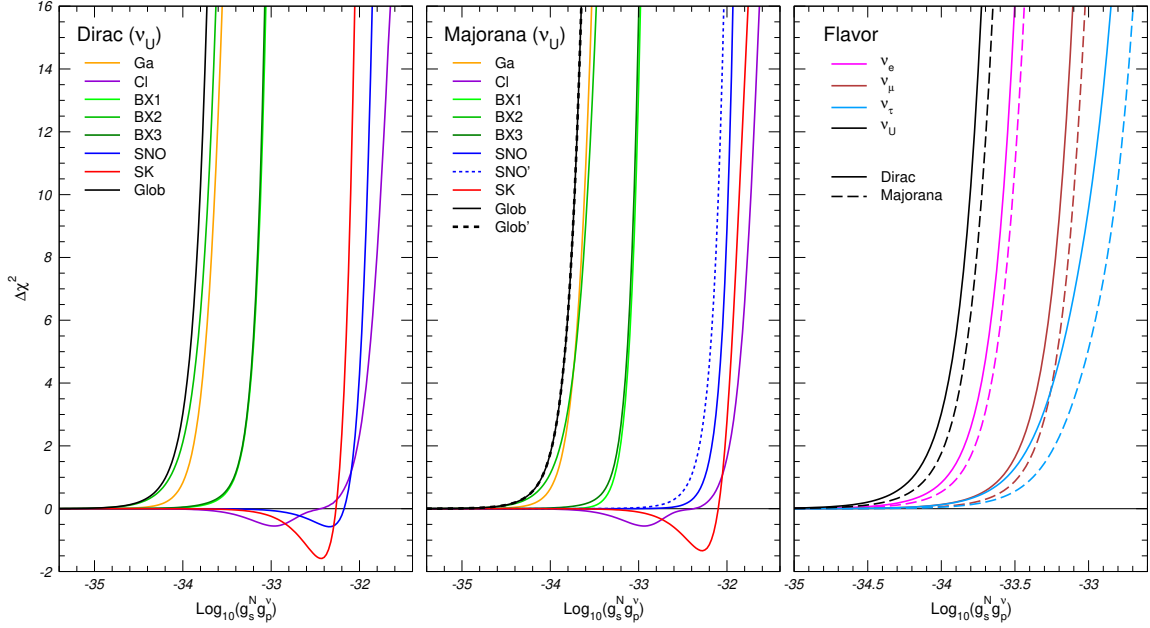


Figure 6.16: $\Delta\chi^2 \equiv \chi^2(g_s^N g_p^{\nu U}) - \chi^2(g_s^N g_p^{\nu U} = 0)$ as a function of $g_s^N g_p^{\nu U}$ for $m_\phi \ll 10^{-15}$ eV fixing all oscillation parameters (in particular Δm_{21}^2 , θ_{12} and θ_{23}) to their best-fit values. The left (central) panel show $\Delta\chi^2$ for each of the individual solar neutrino experiments for Dirac (Majorana) neutrinos and for the case of coupling to ν_U . In the central panel SNO and SNO' label the two variants of the SNO CC analysis for Majorana neutrinos (see text for details). The right panel show the global $\Delta\chi^2$ for four choices of the flavour dependence of the pseudoscalar-neutrino couplings; in particular, the black lines (coupling to ν_U) for Dirac and Majorana cases coincide with the corresponding ‘‘Glob’’ ones in left and central panels, respectively.

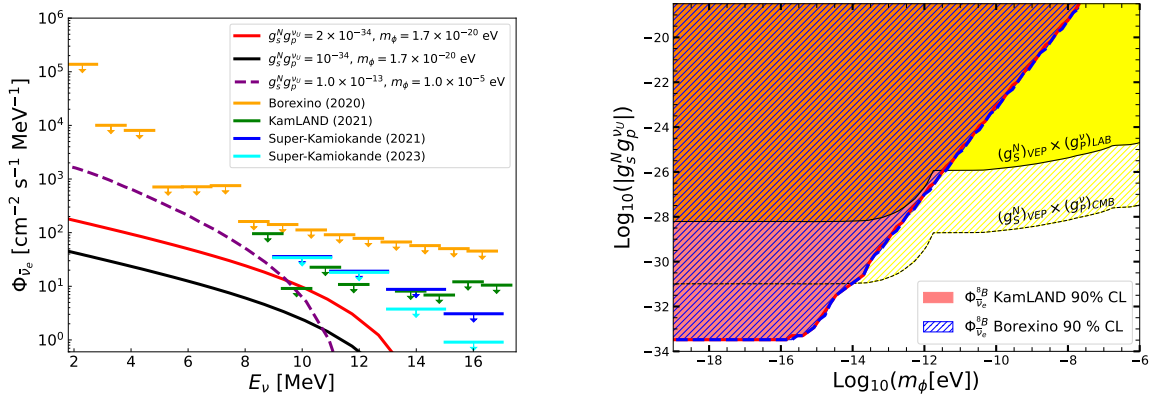


Figure 6.17: Left: Limits on $\bar{\nu}_e$ flux of astrophysical origin, as reported by KamLAND [277], Borexino [278] and Super-Kamiokande [279–281]. For comparison, we show the expected solar $\bar{\nu}_e$ flux for several values of the model parameters as labeled in the figure. Right: Excluded region on the $(m_\phi, g_s^N g_p^{\nu U})$ plane obtained for Majorana neutrinos obtained from the 90% CL constraint reported by KamLAND [277] and Borexino [278], Eqs. (6.10) and (6.11) (see text for details). For comparison we show as yellow region the bounds on the product of couplings from the product of the bound on g_s^N from violation of weak equivalent (VEP) principle and the bounds on g_p^{ν} from either kinematic and rare effects in weak decays in laboratory experiments (LAB) or cosmology bounds from cosmic microwave background (CMB).

Chapter 7

Determination of the Solar Neutrino Fluxes and addressing Gallium Anomaly

In Chapter 3, we discussed briefly solar neutrinos and what their main mechanisms of production are, pp-chain and CNO cycle. In this chapter, we will dig deep into the understanding of solar neutrino fluxes and how we can use neutrino data to determine them and incorporate the latest results from both solar and non-solar neutrino experiments. Specifically, in Sec. 7.1 we work in the context of three-neutrino oscillations and present the results of a SSM independent analysis where the normalization of the various neutrino-producing nuclear reactions is determined solely from experimental data, with no other theoretical input than the imposition of the luminosity constraint which links together the neutrino fluxes and the thermal energy produced by each nuclear reaction in the Sun (and accounts for the fact that the overall amount of generated thermal energy must match the observed solar radiated luminosity). We then relax also such constraint and check it against neutrino data, finding that there is indeed excellent experimental agreement between the observed luminosity and its neutrino-inferred value. In Sec. 7.2 we extend our analysis to sterile neutrino models and address the issue of the *Gallium anomaly* as described in Section 3.6, performing consistency tests to assess the level of incompatibility between the 3+1 neutrino scenario invoked to explain the results from Gallium source experiments and the strong constraints for light-sterile neutrinos that come from solar data. In the end of such section we also comment on the implications that assuming at face value the sterile solution of the Gallium anomaly would have on the mechanism for energy production in the Sun.

7.1 Determination of solar neutrino fluxes

7.1.1 Solar Neutrino Fluxes: State of the Art

Following the discussion in Section 3.1, the pp-chain five fusion reactions among elements lighter than $A = 8$ produce neutrinos which are labeled by the parent reaction as pp, ${}^7\text{Be}$, pep, ${}^8\text{B}$, and hep neutrinos. In the CNO-cycle the abundance of C and N acts as a catalyst, and the ${}^{13}\text{N}$ and ${}^{15}\text{O}$ beta decays provide the primary source of neutrinos, while ${}^{17}\text{F}$ beta decay produces a subdominant flux. For each of these eight processes the spectral energy shapes of the produced neutrinos is known, but the calculation of the rate of neutrinos produced in each reaction requires dedicated modeling of the Sun.

The detection of solar neutrinos, with their extremely small interaction cross sections,

enables us to see into the solar interior and verify directly our understanding of the Sun [287] – provided, of course, that one counts with an established model of the physics effects relevant to their production, interaction, and propagation. The SM was thought to be such an established framework, but it badly failed at the first attempt of this task giving rise to the so-called “solar neutrino problem” [288, 289]. Fortunately, we stand here, almost fifty years after that first realization of the problem, with a different but well established framework for the relevant effects in solar neutrino propagation. A framework in which the three flavour neutrinos (ν_e, ν_μ, ν_τ) of the Standard Model are mixed quantum superpositions of three massive states ν_i ($i = 1, 2, 3$) with different masses. This allows for the flavour of the neutrino to oscillate from production to detection [290, 291], and for non-trivial effects (the so-called LMA-MSW [193, 194] flavour transitions) to take place when crossing dense regions of matter. Furthermore, due to the wealth of experiments exploring neutrino oscillations, the value of the neutrino properties governing the propagation of solar neutrinos, mass differences, and mixing angles, are now precisely and independently known.

Armed with this robust particle physics framework for neutrino production, propagation, and detection, it is possible to turn to the observation of solar neutrino experiments to test and refine the SSM. Unfortunately soon after the particle physics side of the exercise was clarified, the construction of the SSM run into a new puzzle: the so called “solar composition problem”. In brief, SSMs built in the 1990’s using the abundances of heavy elements on the surface of the Sun from Ref. [163] (GS98) had notable successes in predicting other observations, in particular helioseismology measurements such as the radial distributions of sound speed and density [43, 48–50]. But in the 2000’s new determinations of these abundances became available and pointed towards substantially lower values, as summarized in Ref. [164] (AGSS09). The SSMs built incorporating such lower metallicities failed at explaining the helioseismic observations [292]. For almost two decades there was no successful solution of this puzzle as changes in the modeling of the Sun did not seem able to account for this discrepancy [52, 293, 294]. Consequently two different sets of SSMs were built, each based on the corresponding set of solar abundances [52, 53, 165].

With this in mind, in Refs. [69, 295] we performed solar model independent analysis of the solar and terrestrial neutrino data available at the time, in the framework of three-neutrino masses and mixing, where the flavour parameters and all the solar neutrino fluxes were simultaneously determined with a minimum set of theoretical priors. The results were compared with the two variants of the SSM, but they were not precise enough to provide a significant discrimination.

Since then there have been a number of developments. First of all, a substantial amount of relevant data has been accumulated, in particular the full spectral information of the Phase-II [68] and Phase-III [70] of Borexino and their results based on the correlated integrated directionality (CID) method [73]. All of them have resulted into the first positive observation of the neutrino fluxes produced in the CNO-cycle which are particularly relevant for discrimination among the SSMs.

On the model front, an update of the AGSS09 results was recently presented by the same group (AAG21) [166], though leading only to a slight revision upwards of the solar metallicity. Most interestingly, almost simultaneously a new set of results (MB22) [167], based on similar methodologies and techniques but with different atomic input data for the critical oxygen lines among other differences, led to a substantial change in solar elemental abundances with respect to AGSS09 (see the original reference for details). The outcome is a set of solar abundances based on three-dimensional radiation hydrodynamic solar atmosphere models and line formation treated under non-local thermodynamic equi-

librium that yields a total solar metallicity comparable to those of the “high-metallicity” results by GS98.

Another issue which has come up in the interpretation of the solar neutrino results is the appearance of the so-called “gallium anomaly”. In brief, it accounts for the deficit of the rate of events observed in Gallium source experiments with respect to the expectation. It was originally observed in the calibration of the gallium solar-neutrino detectors GALLEX [56, 128] and SAGE [129, 130] with radioactive ^{51}Cr and ^{37}Ar sources, and it has been recently confirmed by the BEST collaboration with a dedicated source experiment using a ^{51}Cr source with high statistical significance [132, 133].

The solution of this puzzle is an open question in neutrino physics (see Ref. [140] and reference therein for a recent discussion of – mostly unsuccessful – attempts at explanations in terms of standard and non-standard physics scenarios). In particular, in the framework of 3ν oscillations, the attempts at explanation (or at least alleviation) of the anomaly invoke the uncertainties of the capture cross section [134, 135, 137]. With this motivation, in this work we have studied the (in)sensitivity of our results to the intrinsic uncertainty on the observed neutrino rates in the Gallium source experiments posed by possible modification of the capture cross section in Gallium, or equivalently, of the detection efficiency of the Gallium solar neutrino experiments.

All these developments motivate the new analysis which we present in this section with the following outline. In Sec. 7.1.2 we describe the assumptions and methodology followed in our study of the neutrino data. As mentioned above, this work builds upon our previous solar flux determination in Refs. [69, 295]. Thus in Sec. 7.1.2, for convenience, we summarize the most prominent elements common to those analyses, but most importantly, we detail the relevant points in which the present analysis method deviates from them. The new determination of the solar fluxes is presented in Sec. 7.1.3 where we also discuss and quantify the role of the Gallium source experiments and address their robustness with respect to the Gallium anomaly. In Sec. 7.1.4 we have a closer look at the determination of the neutrino fluxes from the CNO-cycle and its dependence on the assumptions on the relative normalization of the fluxes produced in the three relevant reactions. In Sec. 7.1.5 we compare our determined fluxes with the predictions of the SSMs in the form of a *parameter goodness of fit* test, and quantify the output of the test for the assumptions in the analysis.

7.1.2 Analysis framework

In the analysis of solar neutrino experiments we include the total rates from the radiochemical experiments Chlorine [147], Gallex/GNO [56], and SAGE [55], the spectral and day-night data from the four phases of Super-Kamiokande [60–62, 255], the results of the three phases of SNO in terms of the parametrization given in their combined analysis [64], and the full spectra from Borexino Phase-I [67], Phase-II [68], and Phase-III [70], together with their latest results based on the correlated integrated directionality (CID) method [73]. In the framework of three neutrino masses and mixing the expected values for these solar neutrino observables depend on the parameters Δm_{21}^2 , θ_{12} , and θ_{13} as well as on the normalizations of the eight solar fluxes. Thus besides solar experiments, we also include in the analysis the separate DS1, DS2, DS3 spectra from KamLAND [97] which in the framework of three neutrino mixing also yield information on the parameters Δm_{21}^2 , θ_{12} , and θ_{13} .

In what follows we will use as normalization parameters for the solar fluxes the reduced

Flux	Φ_i^{ref} [$\text{cm}^{-2} \text{s}^{-1}$]	α_i [MeV]	β_i
pp	5.960×10^{10}	13.099	9.1864×10^{-1}
${}^7\text{Be}$	4.854×10^9	12.552	7.1693×10^{-2}
pep	1.425×10^8	11.920	1.9987×10^{-3}
${}^{13}\text{N}$	2.795×10^8	12.658	4.1630×10^{-3}
${}^{15}\text{O}$	2.067×10^8	12.368	3.0082×10^{-3}
${}^{17}\text{F}$	5.350×10^6	12.365	7.7841×10^{-5}
${}^8\text{B}$	5.025×10^6	6.6305	3.9205×10^{-5}
hep	7.950×10^3	3.7355	3.4944×10^{-8}

Table 7.1: The reference neutrino fluxes Φ_i^{ref} used for normalization (from Ref. [146, 167]), the energy α_i provided to the star by nuclear fusion reactions associated with the i^{th} neutrino flux (taken from Ref. [296]), and the fractional contribution β_i of the i^{th} nuclear reaction to the total solar luminosity.

quantities:

$$f_i = \frac{\Phi_i}{\Phi_i^{\text{ref}}} \quad (7.1)$$

with $i = \text{pp}, {}^7\text{Be}, \text{pep}, {}^{13}\text{N}, {}^{15}\text{O}, {}^{17}\text{F}, {}^8\text{B}$, and hep. In this work the numerical values of Φ_i^{ref} are set to the predictions of the latest GS98 solar model, described in Ref. [146, 167]. They are listed in Table 7.1. The methodology of the analysis presented in this work builds upon our previous solar flux determination in Refs. [69, 295], which we briefly summarize here for convenience, but it also exhibits a number of differences besides the additional data included as described next.

The theoretical predictions for the solar and KamLAND observables depend on eleven parameters: the eight reduced solar fluxes $f_{\text{pp}}, \dots, f_{\text{hep}}$, and the three relevant oscillation parameters $\Delta m_{21}^2, \theta_{12}, \theta_{13}$. In our analysis we include as well the complementary information on θ_{13} obtained after marginalizing over $\Delta m_{3\ell}^2, \theta_{23}$ and δ_{CP} the results of all the other oscillation experiments considered in NuFIT-5.2 [254]. This results into a prior $\sin^2 \theta_{13} = 0.0223 \pm 0.0006$, *i.e.*, $\theta_{13} = 8.59^\circ (1 \pm 0.014)$. Given the weak dependence of the solar and KamLAND observables on θ_{13} , including such prior yields results which are indistinguishable from just fixing the value of $\bar{\theta}_{13} = 8.59^\circ$.

Throughout this work, we follow a frequentist approach in order to determine the allowed confidence regions for these parameters (unlike in our former works [69, 295] where we used instead a Bayesian analysis to reconstruct their posterior probability distribution function). To this end we make use of the experimental data from the various solar and KamLAND samples (D_{solar} and D_{KamLAND} , respectively) as well as the corresponding theoretical predictions (which depends on ten free parameters, as explained above) to build the χ^2 statistical function

$$\chi_{\text{global}}^2(\vec{\omega}_{\text{flux}}, \vec{\omega}_{\text{osc}}) \equiv \chi_{\text{solar}}^2(D_{\text{solar}} | \vec{\omega}_{\text{flux}}, \vec{\omega}_{\text{osc}}) + \chi_{\text{KamLAND}}^2(D_{\text{KamLAND}} | \vec{\omega}_{\text{osc}}), \quad (7.2)$$

with $\vec{\omega}_{\text{flux}} \equiv (f_{\text{pp}}, \dots, f_{\text{hep}})$ and $\vec{\omega}_{\text{osc}} \equiv (\Delta m_{21}^2, \theta_{12}, \bar{\theta}_{13})$. In order to scan this multi-dimensional parameter space efficiently, we make use of the MultiNest [272, 273] and Diver [274] algorithms.

The allowed range for the solar fluxes is further reduced when imposing the so-called ‘‘luminosity constraint’’, *i.e.*, the requirement that the overall sum of the thermal energy generated together with each solar neutrino flux coincides with the solar luminosity [297]:

$$\frac{L_{\odot}}{4\pi (\text{A.U.})^2} = \sum_{i=1}^8 \alpha_i \Phi_i. \quad (7.3)$$

Here the constant α_i is the energy released into the star by the nuclear fusion reactions associated with the i^{th} neutrino flux; its numerical value is independent of details of the solar model to an accuracy of one part in 10^4 or better [298]. A detailed derivation of this equation and the numerical values of the coefficients α_i is presented in Ref. [298], with some refinement and correction following in [296].¹ The coefficients employed in this work are listed in Table 7.1. In terms of the reduced fluxes Eq. (7.3) can be written as:

$$1 = \sum_{i=1}^8 \beta_i f_i \quad \text{with} \quad \beta_i \equiv \frac{\alpha_i \Phi_i^{\text{ref}}}{L_\odot / [4\pi (\text{A.U.})^2]} \quad (7.4)$$

where β_i is the fractional contribution to the total solar luminosity of the nuclear reactions responsible for the production of the Φ_i^{ref} neutrino flux. In Refs. [69, 295] we adopted the best-estimate value for the solar luminosity $L_\odot / [4\pi (\text{A.U.})^2] = 8.5272 \times 10^{11} \text{ MeV cm}^{-2} \text{ s}^{-1}$ given in Ref. [298], which was obtained from all the available satellite data [299]. This value was revised in Ref. [300] using an updated catalog and calibration methodology (see Ref. [301] for a detailed comparative discussion), yielding a slightly lower result which is now the reference value listed by the PDG [302] and leads to $L_\odot / [4\pi (\text{A.U.})^2] = 8.4984 \times 10^{11} \text{ MeV cm}^{-2} \text{ s}^{-1}$. In this work we adopt this new value when evaluating the β_i coefficients listed in Table 7.1. Furthermore, in order to account for the systematics in the extraction of the solar luminosity we now assign an uncertainty of 0.34% to the constraint in Eq. (7.4), which we conservatively derive from the range of variation of the estimates of L_\odot . In what follows we will present results with and without imposing the luminosity constraint. For the analysis including the luminosity constraint we add a prior

$$\chi_{\text{LC}}^2(\vec{\omega}_{\text{flux}}) = \frac{\left(1 - \sum_{i=1}^8 \beta_i f_i\right)^2}{(0.0034)^2} \quad (7.5)$$

Besides the imposition of the luminosity constraint in some of the analysis, the flux normalizations are allowed to vary freely within a set of physical constraints. In particular:

- The fluxes must be positive:

$$\Phi_i \geq 0 \quad \Rightarrow \quad f_i \geq 0. \quad (7.6)$$

- Consistency in the pp-chain implies that the number of nuclear reactions terminating the pp-chain should not exceed the number of nuclear reactions which initiate it [298, 303]:

$$\begin{aligned} \Phi_{7\text{Be}} + \Phi_{8\text{B}} &\leq \Phi_{\text{pp}} + \Phi_{\text{pep}} \\ \Rightarrow \quad 8.12 \times 10^{-2} f_{7\text{Be}} + 8.42 \times 10^{-5} f_{8\text{B}} &\leq f_{\text{pp}} + 2.38 \times 10^{-3} f_{\text{pep}}. \end{aligned} \quad (7.7)$$

- The ratio of the pep neutrino flux to the pp neutrino flux is fixed to high accuracy because they have the same nuclear matrix element. We have constrained this ratio to match the average of the values in the five B23 SSMs (Sec. 7.1.5), with 1σ Gaussian uncertainty given by the difference between the values in the five models

$$\frac{f_{\text{pep}}}{f_{\text{pp}}} = 1.004 \pm 0.018. \quad (7.8)$$

¹We have explicitly verified that the numerical differences between the results of the analysis performed using the original α_i coefficients in Ref. [298] and those in Ref. [296] are below the quoted precision.

Technically we implement this constraint by adding a Gaussian prior

$$\chi_{\text{pep/pp}}^2(f_{\text{pp}}, f_{\text{pep}}) \equiv \left(\frac{f_{\text{pep}}/f_{\text{pp}} - 1.004}{0.018} \right)^2. \quad (7.9)$$

- For the CNO fluxes ($f\Phi_{^{13}\text{N}}$, $\Phi_{^{15}\text{O}}$, and $\Phi_{^{17}\text{F}}$) a minimum set of assumptions required by consistency are:
 - The $^{14}\text{N}(p, \gamma)^{15}\text{O}$ reaction must be the slowest process in the main branch of the CNO-cycle [303]:

$$\Phi_{^{15}\text{O}} \leq \Phi_{^{13}\text{N}} \quad \Rightarrow \quad f_{^{15}\text{O}} \leq 1.35 f_{^{13}\text{N}} \quad (7.10)$$

- the CNO-II branch must be subdominant:

$$\Phi_{^{17}\text{F}} \leq \Phi_{^{15}\text{O}} \quad \Rightarrow \quad f_{^{17}\text{F}} \leq 40 f_{^{15}\text{O}}. \quad (7.11)$$

The conditions quoted above are all dictated by solar physics. However, more practical reasons require that the CNO fluxes are treated with a special care. As discussed in detail in Appendix B, the analysis of the Borexino Phase-III spectra in Ref. [66] (which we closely reproduce) has been optimized by the collaboration to maximize the sensitivity to the overall CNO production rate, and therefore it may not be directly applicable to a situation where the three ^{13}N , ^{15}O and ^{17}F flux normalizations are left totally free, subject only to the conditions in Eqs. (7.10) and (7.11). Hence, following the approach of the Borexino collaboration in Ref. [66], we first perform an analysis where the three CNO components are all scaled simultaneously by a unique normalization parameter while their ratios are kept fixed as predicted by the SSMs. In order to avoid a bias towards one of the different versions of the SSM we have constrained the two ratios to match the average of the five B23 SSMs values

$$\frac{\Phi_{^{15}\text{O}}}{\Phi_{^{13}\text{N}}} = 0.73 \quad \text{and} \quad \frac{\Phi_{^{17}\text{F}}}{\Phi_{^{13}\text{N}}} = 0.016 \quad \Rightarrow \quad \frac{f_{^{15}\text{O}}}{f_{^{13}\text{N}}} = 0.98 \quad \text{and} \quad \frac{f_{^{17}\text{F}}}{f_{^{13}\text{N}}} = 0.85. \quad (7.12)$$

In these analysis, which we label «CNO-Rfixed», the conditions in Eq. (7.12) effectively reduces the number of free parameters from ten to eight, namely the two oscillation parameters in $\vec{\omega}_{\text{osc}}$ and six flux normalizations in

$$\vec{\omega}_{\text{flux}}^{\text{CNO-Rfixed}} \equiv (f_{\text{pp}}, f_{^{7}\text{Be}}, f_{\text{pep}}, f_{^{13}\text{N}}, f_{^{15}\text{O}} = 0.98 f_{^{13}\text{N}}, f_{^{17}\text{F}} = 0.85 f_{^{13}\text{N}}, f_{^8\text{B}}, f_{\text{hep}}).$$

In Sec. 7.1.4 we will discuss and quantify the effect of relaxing the condition of fixed CNO ratios.

7.1.3 New determination of solar neutrino fluxes

We present first the results of our analysis with the luminosity constraint and the ratios of the CNO fluxes fixed by the relations in Eq. (7.12), so that altogether for this case we construct the χ^2 function

$$\chi_{\text{wLC,CNO-Rfixed}}^2 \equiv \chi_{\text{global}}^2(\vec{\omega}_{\text{osc}}, \vec{\omega}_{\text{flux}}^{\text{CNO-Rfixed}}) + \chi_{\text{pep/pp}}^2(f_{\text{pp}}, f_{\text{pep}}) + \chi_{\text{LC}}^2(\vec{\omega}_{\text{flux}}^{\text{CNO-Rfixed}}). \quad (7.13)$$

The results of this analysis are displayed in Fig. 7.1, where we show the two- and one-dimensional projections of $\Delta\chi_{\text{wLC,CNO-Rfixed}}^2$. From these results one reads that the ranges at 1σ (and at the 99% CL in square brackets) for the two oscillation parameters are:

$$\begin{aligned} \Delta m_{21}^2 &= 7.43_{-0.30}^{+0.30} [_{-0.49}^{+0.44}] \times 10^{-5} \text{eV}^2, \\ \sin^2 \theta_{12} &= 0.300_{-0.017}^{+0.020} [_{-0.027}^{+0.031}], \end{aligned} \quad (7.14)$$

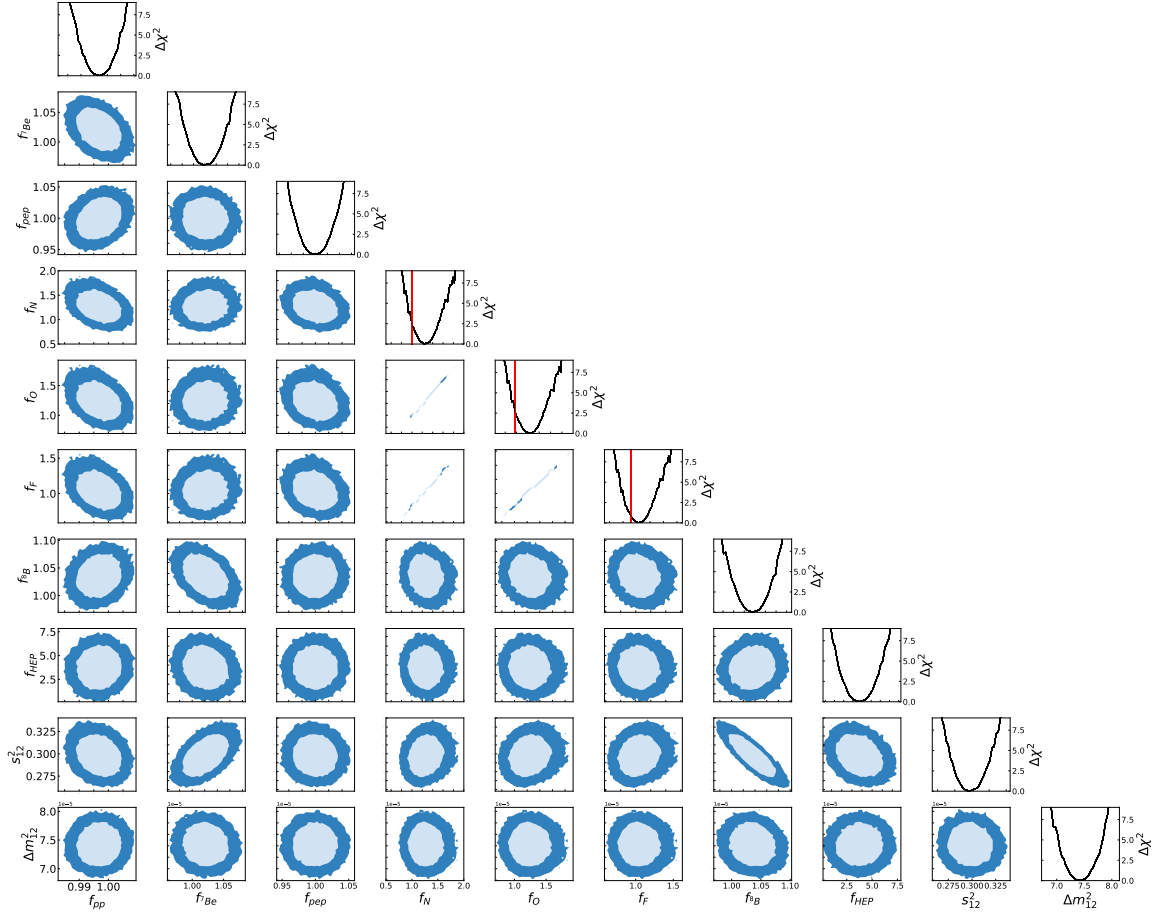


Figure 7.1: Constraints from our global analysis on the solar neutrino fluxes for the analysis with luminosity constraint and fixed ratios of the CNO fluxes (see Eq. (7.13)). Each panel shows a two-dimensional projection of the allowed multidimensional parameter space after minimization with respect to the undisplayed parameters. The regions correspond to 90% and 99% CL (2 d.o.f.). The curves in the rightmost panels show the marginalized one-dimensional $\Delta\chi_{\text{wLC,CNO-Rfixed}}^2$ for each of the parameters.

which are very similar to the results of NuFIT-5.2 [254] with the expected slight enlargement of the allowed ranges. In other words, within the 3ν scenario the data is precise enough to simultaneously constraint the oscillation parameters and the normalizations of the solar flux components without resulting into a substantial degradation of the former. As for the solar fluxes, the corresponding ranges read:

$$\begin{aligned}
 f_{\text{pp}} &= 0.9969_{-0.0039}^{+0.0041} [_{-0.0092}^{+0.0095}], & \Phi_{\text{pp}} &= 5.941_{-0.023}^{+0.024} [_{-0.055}^{+0.057}] \times 10^{10} \text{ cm}^{-2} \text{ s}^{-1}, \\
 f_{7\text{Be}} &= 1.019_{-0.017}^{+0.020} [_{-0.041}^{+0.047}], & \Phi_{7\text{Be}} &= 4.93_{-0.08}^{+0.10} [_{-0.20}^{+0.23}] \times 10^9 \text{ cm}^{-2} \text{ s}^{-1}, \\
 f_{\text{pep}} &= 1.000_{-0.018}^{+0.016} [_{-0.042}^{+0.041}], & \Phi_{\text{pep}} &= 1.421_{-0.026}^{+0.023} [_{-0.060}^{+0.058}] \times 10^8 \text{ cm}^{-2} \text{ s}^{-1}, \\
 f_{13\text{N}} &= 1.25_{-0.14}^{+0.17} [_{-0.40}^{+0.47}], & \Phi_{13\text{N}} &= 3.48_{-0.40}^{+0.47} [_{-1.10}^{+1.30}] \times 10^8 \text{ cm}^{-2} \text{ s}^{-1}, \\
 f_{15\text{O}} &= 1.22_{-0.14}^{+0.17} [_{-0.39}^{+0.46}], & \Phi_{15\text{O}} &= 2.53_{-0.29}^{+0.34} [_{-0.80}^{+0.94}] \times 10^8 \text{ cm}^{-2} \text{ s}^{-1}, \\
 f_{17\text{F}} &= 1.03_{-0.20}^{+0.20} [_{-0.48}^{+0.47}], & \Phi_{17\text{F}} &= 5.51_{-0.63}^{+0.75} [_{-1.75}^{+2.06}] \times 10^7 \text{ cm}^{-2} \text{ s}^{-1}, \\
 f_{8\text{B}} &= 1.036_{-0.020}^{+0.020} [_{-0.048}^{+0.047}], & \Phi_{8\text{B}} &= 5.20_{-0.10}^{+0.10} [_{-0.24}^{+0.24}] \times 10^6 \text{ cm}^{-2} \text{ s}^{-1}, \\
 f_{\text{hep}} &= 3.8_{-1.2}^{+1.1} [_{-2.7}^{+2.7}], & \Phi_{\text{hep}} &= 3.0_{-1.0}^{+0.9} [_{-2.1}^{+2.2}] \times 10^4 \text{ cm}^{-2} \text{ s}^{-1}.
 \end{aligned} \tag{7.15}$$

Notice that in Fig. 7.1 we separately plot the ranges for the three CNO flux normalization parameters, however they are fully correlated since their ratios are fixed, which explains

the thin straight-line shape of the regions as seen in the three corresponding panels. Compared to the results from our previous analysis we now find that all the fluxes are clearly determined to be non-zero, while in Refs. [69, 295] only an upper bound for the CNO fluxes was found. This is a direct consequence of the positive evidence of neutrinos produced in the CNO cycle provided by Borexino Phase-III spectral data, which is here confirmed in a fully consistent global analysis. We will discuss this point in more detail in Sec. 7.1.4. We also observe that the inclusion of the full statistics of Borexino has improved the determination of $f_{7\text{Be}}$ by a factor $\mathcal{O}(3)$.

Figure 7.1 exhibits the expected correlation between the allowed ranges of the pp and pep fluxes, which is a consequence of the relation (7.8). This correlation is somewhat weaker than what observed in the corresponding analysis in Ref. [295] because the spectral information from Borexino Phase-II and Phase-III provides now some independent information on f_{pep} . We also observe the presence of anticorrelation between the allowed ranges of the two most intense fluxes, pp and ${}^7\text{Be}$, as dictated by the luminosity constraint (see comparison with Fig. 7.2). Finally we notice that the allowed ranges of $f_{7\text{Be}}$ and $f_{s\text{B}}$ – the two most precise directly determined flux normalizations irrespective of the luminosity constraint (see Fig. 7.2) – are anticorrelated. This is a direct consequence of the different dependence of the survival probability with $\sin^2 \theta_{12}$ in their respective energy ranges. ${}^8\text{B}$ neutrinos have energies of the order of several MeV for which the flavour transition occurs in the MSW regime and the survival probability $P_{ee} \propto \sin^2 \theta_{12}$. Hence an increase in $\sin^2 \theta_{12}$ must be compensated by a decrease of $f_{s\text{B}}$ to get the correct number of events, which leads to the anticorrelation between the $\sin^2 \theta_{12}$ and $f_{s\text{B}}$ seen in the corresponding panel in Fig. 7.1. On the contrary, most ${}^7\text{Be}$ neutrinos have 0.86 MeV (some have 0.38 MeV) and for that energy the flavour transition occurs in the transition regime between MSW and vacuum average oscillations for which P_{ee} decreases with $\sin^2 \theta_{12}$. Hence the correlation between $\sin^2 \theta_{12}$ and $f_{7\text{Be}}$ seen in the corresponding panel. Altogether, this leads to the anticorrelation observed between $f_{7\text{Be}}$ and $f_{s\text{B}}$. This was already mildly present in the results in Ref. [295] but it is now a more prominent feature because of the most precise determination of $f_{7\text{Be}}$.

All these results imply the following share of the energy production between the pp-chain and the CNO-cycle

$$\frac{L_{\text{pp-chain}}}{L_{\odot}} = 0.9919_{-0.0030}^{+0.0035} \left[\begin{array}{c} +0.0082 \\ -0.0077 \end{array} \right] \iff \frac{L_{\text{CNO}}}{L_{\odot}} = 0.0079_{-0.0011}^{+0.0009} \left[\begin{array}{c} +0.0028 \\ -0.0026 \end{array} \right] \quad (7.16)$$

in perfect agreement with the SSMs which predict $L_{\text{CNO}}/L_{\odot} \leq 1\%$ at the 3σ level. Once again we notice that in the present analysis the evidence for $L_{\text{CNO}} \neq 0$ clearly stands well above 99% CL.

We next show in Fig. 7.2 the results of the analysis performed without imposing the luminosity constraint – but still with the ratios of the CNO fluxes fixed by the relations in Eq. (7.12) – for which we employ

$$\chi_{\text{woLC,CNO-Rfixed}}^2 \equiv \chi_{\text{global}}^2(\vec{\omega}_{\text{osc}}, \vec{\omega}_{\text{flux}}^{\text{CNO-Rfixed}}) + \chi_{\text{pep/pp}}^2(f_{\text{pp}}, f_{\text{pep}}). \quad (7.17)$$

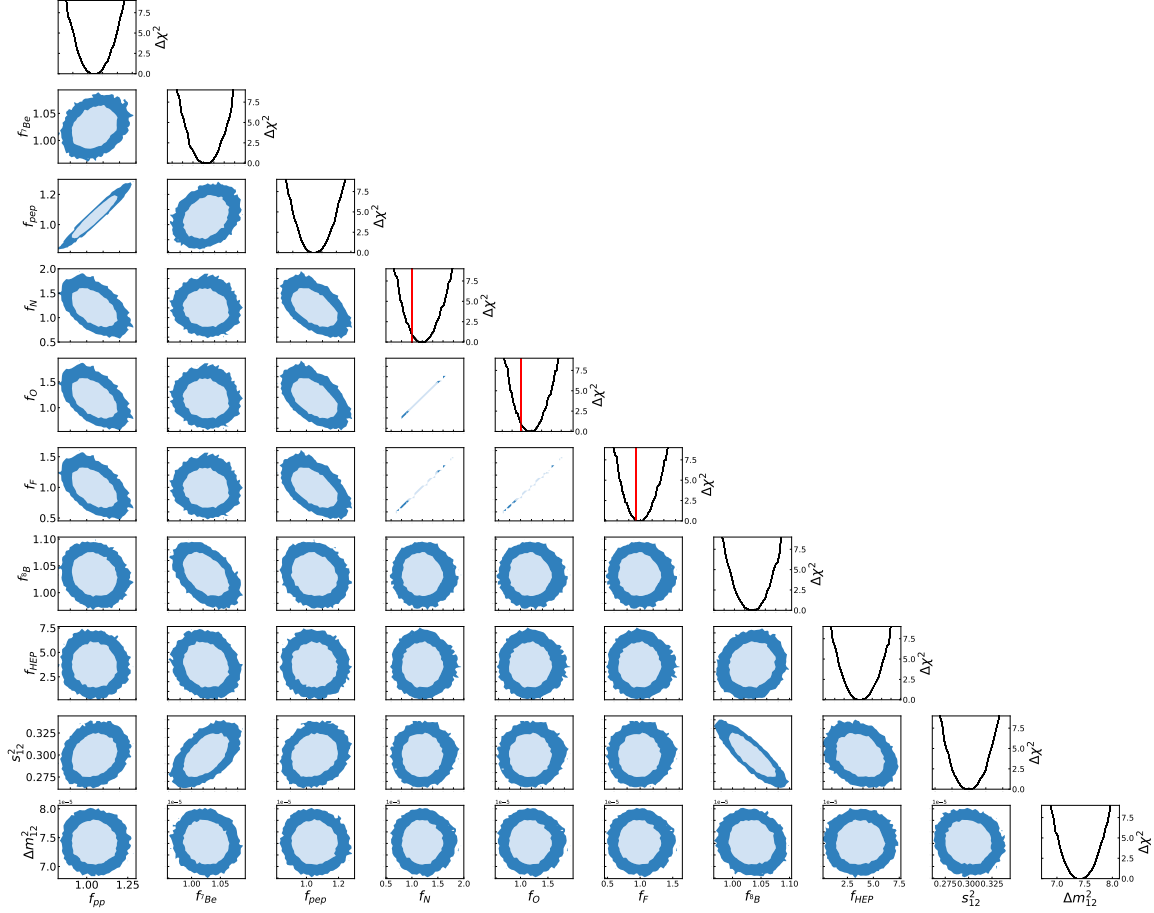


Figure 7.2: Same as Fig. 7.1 but without imposing the luminosity constraint (see Eq. (7.17)).

The allowed ranges for the fluxes in this case are:

$$\begin{aligned}
 f_{\text{pp}} &= 1.038_{-0.066}^{+0.076} \left[\begin{smallmatrix} +0.18 \\ -0.16 \end{smallmatrix} \right], & \Phi_{\text{pp}} &= 6.19_{-0.39}^{+0.45} \left[\begin{smallmatrix} +1.1 \\ -1.0 \end{smallmatrix} \right] \times 10^{10} \text{ cm}^{-2} \text{ s}^{-1}, \\
 f_{7\text{Be}} &= 1.022_{-0.018}^{+0.022} \left[\begin{smallmatrix} +0.051 \\ -0.042 \end{smallmatrix} \right], & \Phi_{7\text{Be}} &= 4.95_{-0.089}^{+0.11} \left[\begin{smallmatrix} +0.25 \\ -0.22 \end{smallmatrix} \right] \times 10^9 \text{ cm}^{-2} \text{ s}^{-1}, \\
 f_{\text{pep}} &= 1.039_{-0.065}^{+0.082} \left[\begin{smallmatrix} +0.19 \\ -0.16 \end{smallmatrix} \right], & \Phi_{\text{pep}} &= 1.48_{-0.09}^{+0.11} \left[\begin{smallmatrix} +0.26 \\ -0.22 \end{smallmatrix} \right] \times 10^8 \text{ cm}^{-2} \text{ s}^{-1}, \\
 f_{13\text{N}} &= 1.16_{-0.19}^{+0.19} \left[\begin{smallmatrix} +0.50 \\ -0.45 \end{smallmatrix} \right], & \Phi_{13\text{N}} &= 3.32_{-0.54}^{+0.53} \left[\begin{smallmatrix} +1.40 \\ -1.24 \end{smallmatrix} \right] \times 10^8 \text{ cm}^{-2} \text{ s}^{-1}, \\
 f_{15\text{O}} &= 1.16_{-0.19}^{+0.19} \left[\begin{smallmatrix} +0.49 \\ -0.44 \end{smallmatrix} \right], & \Phi_{15\text{O}} &= 2.41_{-0.39}^{+0.38} \left[\begin{smallmatrix} +1.02 \\ -0.90 \end{smallmatrix} \right] \times 10^8 \text{ cm}^{-2} \text{ s}^{-1}, \\
 f_{17\text{F}} &= 1.01_{-0.16}^{+0.16} \left[\begin{smallmatrix} +0.45 \\ -0.38 \end{smallmatrix} \right], & \Phi_{17\text{F}} &= 5.25_{-0.85}^{+0.84} \left[\begin{smallmatrix} +2.21 \\ -1.97 \end{smallmatrix} \right] \times 10^6 \text{ cm}^{-2} \text{ s}^{-1}, \\
 f_{8\text{B}} &= 1.034_{-0.021}^{+0.020} \left[\begin{smallmatrix} +0.052 \\ -0.051 \end{smallmatrix} \right], & \Phi_{8\text{B}} &= 5.192_{-0.11}^{+0.10} \left[\begin{smallmatrix} +0.26 \\ -0.26 \end{smallmatrix} \right] \times 10^6 \text{ cm}^{-2} \text{ s}^{-1}, \\
 f_{\text{hep}} &= 3.6_{-1.1}^{+1.2} \left[\begin{smallmatrix} +3.0 \\ -2.6 \end{smallmatrix} \right], & \Phi_{\text{hep}} &= 2.9_{-0.9}^{+1.0} \left[\begin{smallmatrix} +2.4 \\ -2.1 \end{smallmatrix} \right] \times 10^4 \text{ cm}^{-2} \text{ s}^{-1}.
 \end{aligned} \tag{7.18}$$

As expected, the pp flux is the most affected by the release of the luminosity constraint as it is this reaction which gives the largest contribution to the solar energy production and therefore its associated neutrino flux is the one more strongly bounded when imposing the luminosity constraint. The pep flux is also affected due to its strong correlation with the pp flux, Eq. (7.8). The CNO fluxes are mildly affected in an indirect way due to the modified contribution of the pep fluxes to the Borexino spectra.

Thus we find that the energy production in the pp-chain and the CNO-cycle without imposing the luminosity constraint are given by:

$$\frac{L_{\text{pp-chain}}}{L_{\odot}} = 1.030_{-0.061}^{+0.070} \left[\begin{smallmatrix} +0.17 \\ -0.15 \end{smallmatrix} \right] \quad \text{and} \quad \frac{L_{\text{CNO}}}{L_{\odot}} = 0.0075_{-0.0013}^{+0.0013} \left[\begin{smallmatrix} +0.0030 \\ -0.0029 \end{smallmatrix} \right]. \tag{7.19}$$

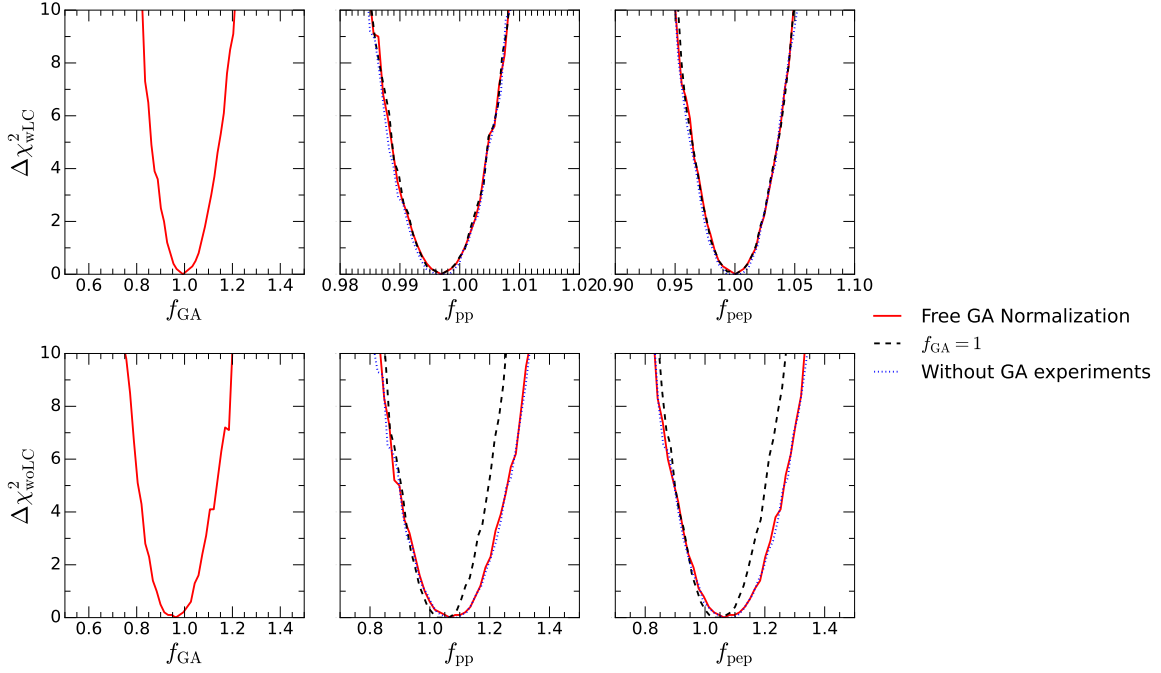


Figure 7.3: Dependence of the determination of the pp and pep fluxes on the assumptions about the Gallium source experiments included in the analysis. The upper (lower) panels show the results of different variants of the analysis «CNO-Rfixed» with (without) luminosity constraint. See text for details.

Comparing Eqs. (7.16) and (7.19) we see that while the amount of energy produced in the CNO cycle is about the same in both analysis, releasing the luminosity constraint allows for larger production of energy in the pp-chain. So in this case we find that the present value of the ratio of the neutrino-inferred solar luminosity, $L_{\odot}(\text{neutrino-inferred})$, to the photon measured luminosity L_{\odot} is:

$$\frac{L_{\odot}(\text{neutrino-inferred})}{L_{\odot}} = 1.038^{+0.069}_{-0.060} \begin{matrix} [+0.17] \\ [-0.15] \end{matrix}. \quad (7.20)$$

The neutrino-inferred luminosity is in good agreement with the one measured in photons, with a 1σ uncertainty of $\sim 6\%$. This represents only a very small variation with respect to the previous best determination [295]. Such result is expected because the determination of the pp flux, which, as mentioned above gives the largest contribution to the neutrino-inferred solar luminosity, has not improved sensibly with the inclusion of the full statistics of the phases II and III of Borexino.

We finish this section by discussing the role of the Gallium experiments in these results with the aim of addressing the possible impact of the Gallium anomaly [127, 304, 305]. As described in Section 3.6, this anomaly consists in a deficit of the event rate observed in Gallium source experiments with respect to the expectation, which represents an obvious puzzle for the interpretation of the results of the solar neutrino Gallium measurements. In this work we assume the well established standard 3ν oscillation scenario and in this context the attempts at explanation (or at least alleviation) of the anomaly invoke the uncertainties of the capture cross section [134, 135, 137]. Thus the open question posed by the Gallium anomaly is the possible impact of such modification of the cross section in the results of our fit.

In order to quantify this we performed two additional variants of our analysis. In the first one we introduce an additional parameter, f_{GA} , which multiplies the predicted event

rates from all solar fluxes in the Gallium solar experiments. This parameter is left free to vary in the fits and would mimic an energy independent modification of the capture cross section (or equivalently of the detection efficiency). In the second variant we simply drop Gallium solar experiments from our global fit.

The results of these explorations are shown in Fig. 7.3 where we plot the most relevant marginalized one-dimensional projections of $\Delta\chi^2$ for these two variants. The upper (lower) panels correspond to analysis performed with (without) the luminosity constraint. The left panel shows the projection over the normalization parameter f_{GA} obtained in the variant of the analysis which makes use of this parameter. As seen from the figure, the results of the fit favour f_{GA} close to one, or, in other words, the global analysis of the solar experiments do *not* support a modification of the neutrino capture cross section in Gallium (or any other effect inducing an energy-independent reduction of the detection efficiency in the Gallium source experiments). This is so because, within the 3ν oscillation scenario, the global fit implies a rate of pp and ${}^7\text{Be}$ neutrinos in the Gallium experiment which is in good agreement with the luminosity constraint as well as with the rates observed in Borexino.

On the central and right panel of the figure we show the corresponding modification of marginalized one-dimensional projections of $\Delta\chi^2$ on the pp and pep flux normalizations which are those mostly affected in these variants. For the sake of comparison, in the upper and lower panels we also plot the results for the $f_{\text{GA}} = 1$ analysis (also visible in the corresponding windows in Figs. 7.1 and 7.2, respectively). The figure illustrates that once the luminosity constraint is imposed, the determination of the solar fluxes is totally unaffected by the assumptions about the capture rate in Gallium. As seen in the lower panels, even without the luminosity constraint the impact on the pp and pep determination is marginal, which emphasizes the robustness of the flux determination in Eqs. (7.15) and (7.18). This is the case thanks to the independent precise determination of the pp flux in the phases I and II in Borexino. Furthermore, the small modification is the same irrespective of whether the Gallium capture rate is left free or completely removed from the analysis; this is due to the lack of spectral and day-night capabilities in Gallium experiments, which prevents them from providing further information beyond the overall normalization scale of the signal.

7.1.4 Examination of the determination of the CNO fluxes

As mentioned above, one of the most important developments in the experimental determination of the solar neutrino fluxes in the last years have been the evidence of neutrinos produced in the CNO cycle reported by Borexino [66, 70, 73]. The detection was made possible thanks to a novel method to constrain the rate of the ${}^{210}\text{Bi}$ background. In Ref. [66], using a partial sample of their Phase-III data, the collaboration found a 5.1σ significance of the CNO flux observation, which increased to 7σ with the full Phase-III statistics [70], and to about 8σ when combined with the CID method [73].

Key ingredients in the analysis performed by the collaboration in Refs. [66, 70, 73] (and therefore in the derivation of these results) are the assumptions about the relative contribution of the three reactions producing neutrinos in the CNO cycle, as well as those about other solar fluxes in the same energy range, in particular the pep neutrinos. In a nutshell, as mentioned above, the collaboration assumes a common shift of the normalization of the CNO fluxes with respect to that of the SSM, and it is the evidence of a non-zero value of such normalization which is quantified in Refs. [66, 70, 73]. In what respects the rate from the pep flux, the SSM expectation was assumed because the Phase-III data by itself does not allow to constraint simultaneously the CNO and pep

flux normalizations.

In this respect, the global analysis presented in the previous section are performed under the same paradigm of a common shift normalization of the CNO fluxes, but being global, the pep flux normalization is also simultaneously fitted. For the sake of comparison we reproduce in Fig. 7.4 the projection of the marginalized $\Delta\chi_{\text{woLC,CNO-Rfixed}}^2$ (7.13) and $\Delta\chi_{\text{woLC,CNO-Rfixed}}^2$ (7.13) on the normalization parameters for the three CNO fluxes. For convenience we also show the projections as a function of the total neutrino flux produced in the CNO cycle. As seen in the figure the results of the analysis (either with or without luminosity constraint) yield a value of $\Delta\chi^2$ well beyond 3σ for $\Phi_{\text{CNO}} = 0$. A dedicated run for this no-CNO scenario case gives $\Delta\chi^2 = 54$ (33) for the analysis with (without) luminosity constraints, and it is therefore excluded at 7.3σ (5.7σ) CL.

In order to study the dependence of the results on the assumption of a unique common shift of the normalization of three CNO fluxes we explored the possibility of making a global analysis in which the three normalization parameters are varied independently. As mentioned above, a priori the three normalizations only have to be subject to a minimum set of consistency relations in Eqs. (7.10) and (7.11). However, as discussed in detail in Sec. B, the background model in Refs. [66, 70, 73] only assumes an upper bound on the amount of ^{210}Bi and cannot be reliably employed to such general analysis because of the larger degeneracy between the ^{210}Bi background and the ^{13}N flux spectra.

With this limitation in mind, we proceed to perform two alternative analysis (with and without imposing the luminosity constraints) in which the normalization of the three CNO fluxes are left free to vary independently but with ratios constrained within a range broad enough to generously account for all variants of the B23 SSM, but not to extend into regions of the parameter space where the assumptions on the background model may not be applicable. Conservatively neglecting correlations between their theoretical uncertainties, the neutrino fluxes of SSMs presented in Ref. [167] and available publicly through a public repository [146] verify

$$\frac{f_{^{15}\text{O}}}{f_{^{13}\text{N}}} = \begin{cases} 1.00 (1 \pm 0.24) \\ 0.95 (1 \pm 0.22) \\ 0.96 (1 \pm 0.21) \\ 1.01 (1 \pm 0.23) \\ 1.00 (1 \pm 0.23) \end{cases} \quad \frac{f_{^{17}\text{F}}}{f_{^{13}\text{N}}} = \begin{cases} 1.00 (1 \pm 0.25) & \text{B23-GS98} \\ 0.84 (1 \pm 0.23) & \text{B23-AGSS09-met} \\ 0.80 (1 \pm 0.20) & \text{B23-AAG21} \\ 0.79 (1 \pm 0.22) & \text{B23-MB22-met} \\ 0.79 (1 \pm 0.22) & \text{B23-MB22-phot} \end{cases} \quad (7.21)$$

Thus in these analyses, here onward labeled «CNO-Rbound», we introduce two pulls ξ_1 and ξ_2 for these two ratios. Notice, however, that we could have equally defined the priors with respect to the reciprocal of the ratios in Eq. (7.21). Hence, in order to avoid a bias towards larger fluxes in the numerator versus the denominator introduced by either choice, we resort instead to logarithmic priors for the ratios:

$$\vec{\omega}_{\text{flux}}^{\text{CNO-Rbound}} \equiv (f_{\text{pp}}, f_{^{7}\text{Be}}, f_{\text{pep}}, f_{^{13}\text{N}}, f_{^{15}\text{O}} = 0.98 \exp(\xi_1) f_{^{13}\text{N}}, f_{^{17}\text{F}} = 0.85 \exp(\xi_2) f_{^{13}\text{N}}, f_{^8\text{B}}, f_{\text{hep}}) \quad (7.22)$$

and add two Gaussian penalty factors for these pulls, so that the corresponding χ^2 function without the luminosity constraint is:

$$\chi_{\text{woLC,CNO-Rbound}}^2 \equiv \chi_{\text{global}}^2(\vec{\omega}_{\text{osc}}, \vec{\omega}_{\text{flux}}^{\text{CNO-Rbound}}) + \chi_{\text{pep/pp}}^2(f_{\text{pp}}, f_{\text{pep}}) + \frac{\xi_1^2}{\sigma_{\xi_1}^2} + \frac{\xi_2^2}{\sigma_{\xi_2}^2} \quad (7.23)$$

with $\sigma_{\xi_1} = 0.26$ and $\sigma_{\xi_2} = 0.48$, chosen to cover the ranges in Eq. (7.21). In addition $f_{^{13}\text{N}}$, $f_{^{15}\text{O}}$, and $f_{^{17}\text{F}}$ are required to verify the consistency relations in Eqs. (7.10) and (7.11).

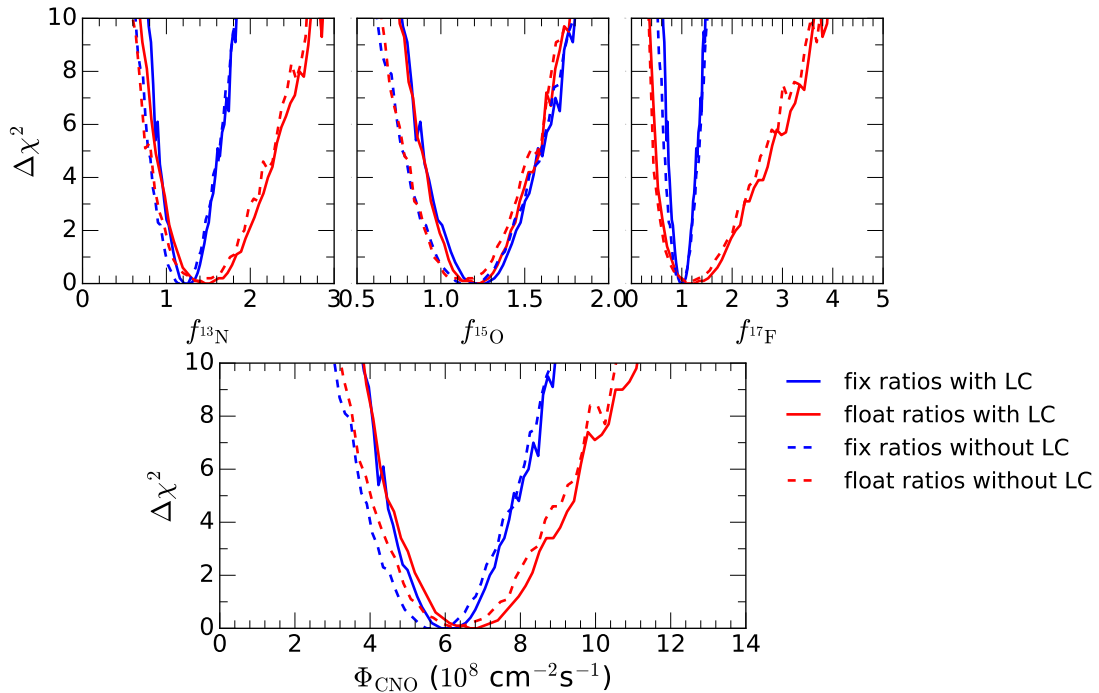


Figure 7.4: One dimensional projections of the global $\Delta\chi^2$ of the for the three neutrino fluxes produced in the CNO-cycle for different assumptions as labeled in the figure. See text for details.

The χ^2 function with the luminosity constraint is obtained by further including the χ_{LC}^2 prior of Eq. (7.5):

$$\chi_{\text{wLC,CNO-Rbound}}^2 \equiv \chi_{\text{woLC,CNO-Rbound}}^2 + \chi_{\text{LC}}^2(\vec{\omega}_{\text{flux}}^{\text{CNO-Rbound}}). \quad (7.24)$$

We plot in Fig. 7.4 the projection of the marginalized $\Delta\chi_{\text{wLC,CNO-Rbound}}^2$ (7.24) and $\Delta\chi_{\text{woLC,CNO-Rbound}}^2$ (7.24) on the normalization parameters for the three CNO fluxes as well as on the total neutrino flux produced in the CNO cycle. As seen in the figure, allowing for the ratios of the CNO normalizations to vary within the intervals (7.21) has little impact on the allowed range of the ^{15}O flux and on the lower limit of the ^{13}N and ^{17}F fluxes. As a consequence, the CL at which the no-CNO scenario can be ruled out is unaffected. On the contrary, we see in Fig. 7.4 that the upper bound on the ^{13}N and ^{17}F fluxes, and therefore of the total neutrino flux produced in the CNO-cycle, is relaxed.² This is a consequence of the strong degeneracy between the spectrum of events from these fluxes and those from the ^{210}Bi background mentioned above, see Fig. B.3 and discussion in Appendix B. Conversely the fact that the range of the ^{15}O flux is robust under the relaxation of the constraints on the CNO flux ratios, means that the high statistics spectral data of the Phase-III of Borexino holds the potential to differentiate the event rates from ^{15}O ν 's from those from ^{13}N and ^{17}F ν 's. The reliable quantification of this possibility, however, requires the knowledge of the minimum allowed value of the ^{210}Bi background which so far has not been presented by the collaboration.

So, let us emphasize that our «CNO-Rbound» analysis have been performed with the aim of testing the effect of relaxing the severe constrains on the CNO fluxes in the studies

²The allowed ranges for the fluxes produced in the pp-chain are not substantially modified with respect to the ones obtained from the «CNO-Rfixed» fits, Eqs. (7.15) and (7.18).

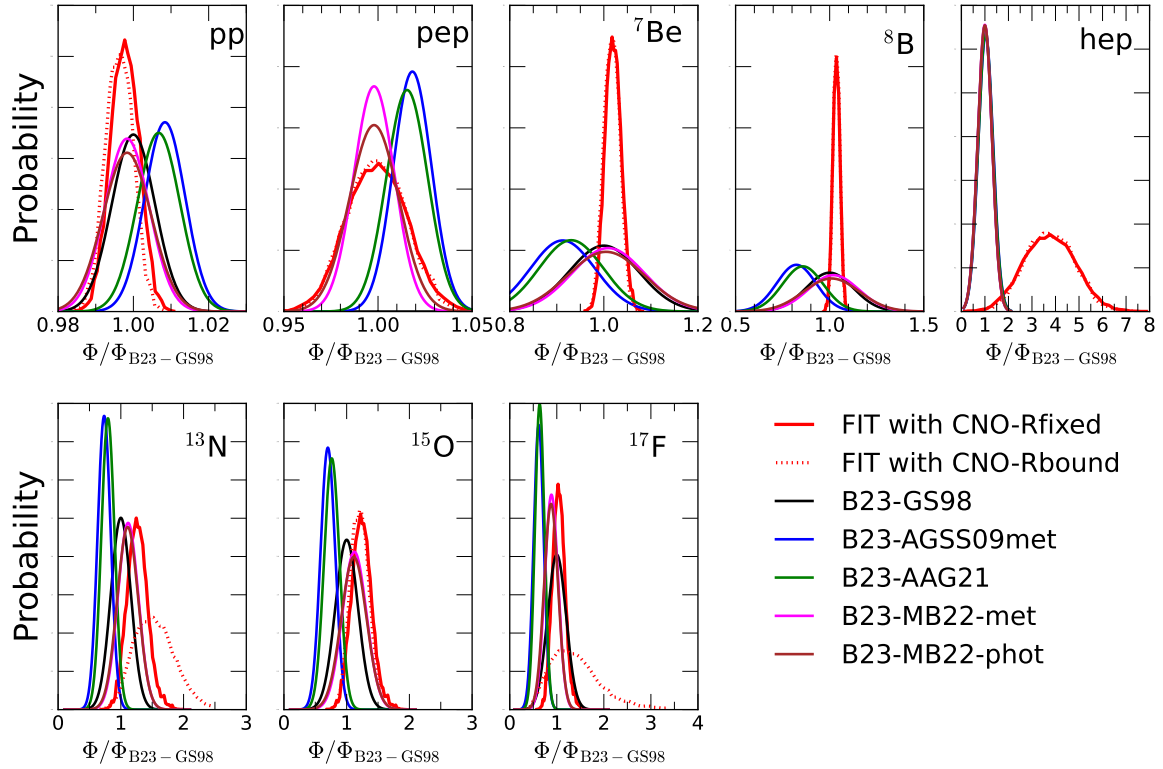


Figure 7.5: Marginalized one-dimensional probability distributions for the best determined solar fluxes in our analysis as compared to the predictions for the five SSMs in Ref. [146, 167].

of the Borexino collaboration. Our conclusion is that the statistical significance of the evidence of detection of events produced by neutrinos from the CNO-cycle is affected very little by the relaxation of the constraint on their relative ratios. However, their allowed range is, and this can have an impact when confronting the results of the fit with the predictions of the SSM as we discuss next.

7.1.5 Comparison with Standard Solar Models

Next we compare the results of our determination of the solar fluxes with the expectations from the five B23 solar models: SSMs computed with the abundances compiled in table 5 of [167] based on the photospheric and meteoritic solar mixtures (MB22-phot and MB22-met models, respectively), and with the [166] (AAG21), the meteoritic scale from [164] (AGSS09-met), and [163] (GS98) compositions. We use both MB22-phot and MB22-met for completeness, although the abundances are very similar in both scales, as clearly reflected by the results in this section. A similar agreement would be found using both the meteoritic and photospheric scales from AAG21, and therefore we use only one scale in this case.³

SSMs predict that nuclear energy accounts for all the solar luminosity (barred about a few parts in 10^4 that are of gravothermal origin) so for all practical matters the neutrino fluxes predicted by SSMs satisfy the luminosity constraint. Therefore we compare the expectations of the various SSM models with the results of our analysis performed with such constraint. In what respects the assumptions on the CNO fluxes, in order to explore the dependence of our conclusions on the specific choice of flux ratios we quantify

³The structures of these models, as well as the total neutrino fluxes and internal distributions are available at [146].

the results obtained in both the «FIT=CNO-Rfixed» analysis (with χ_{FIT}^2 in Eq. (7.13)) and the «FIT=CNO-Rbounded» one (with χ_{FIT}^2 in Eq. (7.24)). For illustration we plot in Fig. 7.5 the marginalized one-dimensional probability distributions for the best determined solar fluxes in such two cases as compared to the predictions for the five B23 SSMs. The probability distributions for our fits are obtained from the one-dimensional marginalized $\Delta\chi_{\text{FIT}}^2(f_i)$ of the corresponding analysis as $P_{\text{FIT}}(f_i) \propto \exp[-\Delta\chi_{\text{FIT}}^2(f_i)/2]$ normalized to unity. To construct the analogous distributions for each of the SSMs we use the predictions $\langle f_i^{\text{SSM}} \rangle$ for the fluxes, the relative uncertainties σ_i^{SSM} and their correlations ρ_{ij}^{SSM} as obtained from Refs. [146], and also assume gaussianity so to build the corresponding $\chi_{\text{SSM}}^2(\vec{\omega}_{\text{flux}})$

$$\chi_{\text{SSM}}^2(\vec{\omega}_{\text{flux}}) = \sum_{i,j} (f_i - f_i^{\text{SSM}}) C_{ij}^{-1} (f_i - f_i^{\text{SSM}}) \quad \text{with} \quad C_{ab} = \sigma_a^{\text{SSM}} \sigma_b^{\text{SSM}} \rho_{ab}, \quad (7.25)$$

from which it is trivial to obtain the marginalized one-dimensional $\Delta\chi_{\text{SSM}}^2(f_i)$ and construct the probability $P_{\text{SSM}}(f_i) \propto \exp[-\Delta\chi_{\text{SSM}}^2(f_i)/2]$.

In the frequentist statistical approach, quantitative comparison of a model prediction for a set of fluxes with the results from the data analysis can be obtained using the *parameter goodness of fit* (PG) criterion introduced in Ref. [158], by comparing the minimum value of χ^2 function for the analysis of the data with that obtained for the same analysis adding the prior imposed by the model.⁴ Thus, following Ref. [158], we construct the test statistics

$$\Delta\chi_{\text{FIT,SSM,SET}}^2 = \left[\chi_{\text{FIT}}^2(\vec{\omega}_{\text{osc}}, \vec{\omega}_{\text{flux}}^{\text{FIT}}) + \chi_{\text{SSM,SET}}^2(\vec{\omega}_{\text{flux}}^{\text{FIT}}) \right]_{\min} - \chi_{\text{FIT}}^2(\vec{\omega}_{\text{osc}}, \vec{\omega}_{\text{flux}}^{\text{FIT}})_{\min} - \chi_{\text{SSM,SET}}^2(\vec{\omega}_{\text{flux}}^{\text{FIT}})_{\min} \quad (7.26)$$

where $\chi_{\text{SSM,SET}}^2(\vec{\omega}_{\text{flux}})$ is obtained as Eq. (7.25) with i, j (and a, b) fluxes restricted to a specific subset as specified by “SET”. The minimization of each of the terms in Eq. (7.26) is performed independently in the corresponding parameter space. $\Delta\chi_{\text{FIT,SSM,SET}}^2$ follows a χ^2 distribution with n degrees of freedom, which, in the present case, coincides with the number of free parameters in common between $\chi_{\text{FIT}}^2(\vec{\omega}_{\text{osc}}, \vec{\omega}_{\text{flux}}^{\text{FIT}})$ and $\chi_{\text{SSM,SET}}^2(\vec{\omega}_{\text{flux}}^{\text{FIT}})$. Notice that, by construction, the result of the test depends on the number of fluxes to be compared, *i.e.*, on the fluxes in “SET”, both because of the actual comparison between the measured and predicted values for those specific fluxes, and because of the change in n with which the p -value of the model is to be computed. This is illustrated in Table 7.2 where we list the values of $\Delta\chi_{\text{FIT,SSM,SET}}^2$ for different choices of “SET” which we have labeled as:

SET	constrained fluxes	
FULL	$(f_{\text{pp}}, f_{7\text{Be}}, f_{\text{pep}}, f_{13\text{N}}, f_{15\text{O}}, f_{17\text{F}}, f_{8\text{B}}, f_{\text{hep}})$	(7.27)
Be+B+CNO	$(f_{7\text{Be}}, f_{13\text{N}}, f_{15\text{O}}, f_{17\text{F}}, f_{8\text{B}})$	
CNO	$(f_{13\text{N}}, f_{15\text{O}}, f_{17\text{F}})$	

Upon analyzing the data in the Table 7.2, it becomes evident that the B23-MB22 models (both the meteoritic and photospheric variations) exhibit a significantly higher level of compatibility with the observed data, even slightly better the B23-GS98 model. On the contrary the B23-AGSS09met and B23-AAG21 models exhibits a lower level of

⁴In this respect it is important to notice that, in order to avoid any bias towards one of the models in the data analysis, in both «CNO-Rfixed» and «CNO-Rbounded» cases the assumptions on the ratios of the three CNO fluxes have been chosen to be “model-democratic”, *i.e.*, centered at the average of the predictions of the models (and, in the case of «CNO-Rbound», with 1σ uncertainties covering the 1σ range allowed by all SSM models).

FIT	B23-SSM	FULL			Be+B+CNO			CNO		
		n=6			n=3			n=1		
		$\Delta\chi^2$	p_{GF}	CL [σ]	$\Delta\chi^2$	p_{GF}	CL [σ]	$\Delta\chi^2$	p_{GF}	CL [σ]
CNO-Rfixed	AGSS09-met	14.5	0.024	2.3	9.8	0.020	2.3	7.2	0.0073	2.7
	GS98	8.1	0.24	1.2	3.0	0.39	0.86	2.4	0.12	1.5
	AAG21	12.5	0.052	1.9	7.8	0.05	2.0	6.2	0.013	2.5
	MB22-met/phot	7.1	0.31	1.0	2.2	0.53	0.62	2.0	0.16	1.4
CNO-Rbound		n=8			n=5			n=3		
		$\Delta\chi^2$	p_{GF}	CL [σ]	$\Delta\chi^2$	p_{GF}	CL [σ]	$\Delta\chi^2$	p_{GF}	CL [σ]
	AGSS09-met	14.1	0.079	1.8	9.3	0.098	1.7	7.2	0.066	1.8
	GS98	6.7	0.57	0.57	1.7	0.88	0.14	1.6	0.66	0.44
	AAG21	11.7	0.16	1.4	6.8	0.24	1.2	5.7	0.13	1.5
MB22-met/phot	5.9	0.66	0.44	1.1	0.95	0.06	1.0	0.80	0.25	

Table 7.2: Results of the PG test for the different models and data samples considered. Within the given accuracy the results for MB22-met and MB22-phot models are the same.

compatibility with observations, with B23-AAG21 model slightly better aligned with the data. Maximum discrimination is provided by comparing mainly the CNO fluxes for which the prediction of both models is mostly different. On the other hand, including all the fluxes from the pp-chain in the comparison tends to dilute the discriminating power of the test. The table also illustrates how allowing for the three CNO fluxes normalizations to vary in the fit tends to relax the CL at which the models are compatible with the observations.

Let us remember that our previously determined fluxes in Ref [295] when confronted with the GS98 and AGSS09 models of the time [52] showed *absolutely* no preference for either model. This was driven by the fact that the most precisely measured ^8B flux (and also of ^7Be) laid right in the middle of the prediction of both models. The new B16-GS98 model in Ref. [53] predicted a slightly lower value for ^8B flux in slightly better agreement with the extracted fluxes of Ref [295], but the conclusion was still that there was no significant preference for either model. Compared to those results, both the most precisely determined ^7Be flux and, most importantly, the newly observed rate of CNO events in Borexino have consistently moved towards the prediction of the models with higher metallicity abundances.

Let us finish commenting on the relative weight of the experimental precision versus the theoretical model uncertainties in the results in Table 7.2. To this end one can envision an ideal experiment which measures f_i to match precisely the values predicted by one of the models with infinite accuracy. Assuming the measurements to coincide with the predictions of B23-GS98, one gets $\Delta\chi_{\text{SSM,SET}}^2 = 17.1$ and 16.7 for SSM=B23-AGSS09-met and SSM=B23-AAG21 with SET=FULL, which means that the maximum CL at which these two SSM can be disfavoured is 2.2σ and 2.1σ . Choosing instead SET=CNO these numbers become $\Delta\chi_{\text{SSM,SET}}^2 = 15.0$ and 14.1 for SSM=B23-AGSS09-met and SSM=B23-AAG21, respectively, corresponding to a 3.1σ and 3.0σ maximum rejection. This stresses the importance of reducing the uncertainties in the model predictions to boost the discrimination between the models.

7.2 Confronting the gallium anomaly with solar neutrino data

The analysis presented in Section 7.1 was performed in the framework of 3ν oscillations, but the same methodology can be applied in the presence of mixing with a fourth sterile neutrino state, thus determining the constraints on the sterile interpretation of the Gallium anomaly in a way which is completely independent of the modeling of the Sun.

As mentioned in Section 3.6, an attempt to alleviate the Gallium anomaly invokes the uncertainties of the capture cross section [134, 135, 137]. This raises the issue of whether the estimated rate of solar neutrino events in Gallium source experiments is really robust. To quantify the impact of such possibility, we performed two variants of our solar neutrino data analysis. In the first one we include the results of the solar Gallium source experiments at their nominal values as provided by the collaboration. In the second one we introduce an additional parameter, f_{Ga} , which is varied freely in the fits and accounts for an overall scaling of the predicted event rates in the solar Gallium source experiments. Statistically this is equivalent to removing the Gallium source experiments from the solar analysis, but done in this way it allows us to quantify the range of f_{Ga} favoured by the solar data. We will return to this point in the next section.

Concerning KamLAND, we include in the analysis the separate DS1, DS2, DS3 spectral data [97] (69 data points). Since KamLAND has no near detector, the theoretical uncertainties in the calculations of the reactor neutrino spectra should be carefully taken into account. Here we will consider two limiting cases. In the first one we will assume some theoretically calculated reactor fluxes which will be used as input in the analysis of the KamLAND data. We will label this analysis as «reactor flux constrained», or «KamLAND-RFC» in short. For concreteness we use as *theoretical reactor fluxes* those predicted by an ad-hoc model adjusted to perfectly reproduce the spectrum observed in Daya-Bay experiment [94] (and their uncertainties) in the absence of sterile oscillations. Similar results would be obtained with any of the reactor flux models in the literature as long as they are consistent with the Daya-Bay measurements in the framework of 3ν mixing. By construction this is the most limiting scenario. Alternatively one can use the Daya-Bay reactor spectra as a truly experimental input, taking into account that at the moment of their detection the suppression induced by the $\Delta m^2 \sim \mathcal{O}(\text{eV}^2)$ oscillations has already taken place (so that the neutrino flux generated by the reactor cores must be proportionally larger). This is a more conservative scenario in which nothing is assumed about the theoretical prediction of the reactor flux normalization. We label this analysis as «reactor flux free», or «KamLAND-RFF» in short.

In what respects the relevant survival probabilities, we focus here on a 3+1 scenario where $\{\nu_1, \nu_2, \nu_3\}$ (with mass-squared splittings Δm_{21}^2 and Δm_{31}^2 as determined by the standard 3ν oscillation analysis) are dominantly admixtures of the left-handed states $\{\nu_e, \nu_\mu, \nu_\tau\}$, and a fourth massive state ν_4 (with a mass-squared splitting $\Delta m_{41}^2 \simeq \Delta m_{42}^2 \simeq \Delta m_{43}^2 \sim \mathcal{O}(\text{eV}^2)$) is mostly sterile (*i.e.*, not coupled to the weak currents) but has some non-vanishing projection over the left-handed states (see appendix C of Ref. [306] for details). We obtain the oscillation probabilities for solar neutrinos by numerically solving the evolution equation for the neutrino ensemble from the neutrino production point to the detector including matter effects both in the Sun and in the Earth, with no other approximation than the assumption that the evolution in the Sun is adiabatic. We parametrize the mixing matrix as in Ref. [306, 307]:

$$U = V_{34}V_{24}V_{14}V_{23}V_{13}V_{12}, \quad (7.28)$$

where V_{ij} is a rotation in the ij plane by an angle θ_{ij} , which in general can also contain a complex phase (see appendix A of [306] for a discussion). Following Ref. [138] we make use of the fact that that bounds from ν_μ disappearance in atmospheric and long-baseline neutral-current measurements render the solar neutrino data effectively insensitive to θ_{34}

and θ_{24} , hence in what follows we set $\theta_{34} = \theta_{24} = 0$ and obtain:

$$U = \begin{pmatrix} c_{14}c_{13}c_{12} & c_{14}c_{13}s_{12} & c_{14}s_{13} & s_{14} \\ \cdot & \cdot & \cdot & 0 \\ \cdot & \cdot & \cdot & 0 \\ -s_{14}c_{13}c_{12} & -s_{14}c_{13}s_{12} & -s_{14}s_{13} & c_{14} \end{pmatrix}. \quad (7.29)$$

Under these approximations and taking into account that for the distance and energies of solar and KamLAND neutrinos the oscillations driven by Δm_{31}^2 and Δm_{4i}^2 are averaged out, the relevant probabilities depend only on the three angles θ_{12} , θ_{13} , θ_{14} as well as Δm_{21}^2 . Furthermore in [306] it has been shown that the determination of θ_{13} is basically unaffected by the presence of a sterile neutrino, so we can fix it to the best fit value $s_{13}^2 = 0.02224$ obtained in the 3ν scenario and safely neglect its current uncertainty. Altogether the relevant probabilities depend on three parameters: Δm_{21}^2 , $\sin^2 \theta_{12}$, and $\sin^2 \theta_{14}$.

Finally, in the analysis of the Gallium source experiments one can set $\Delta m_{21}^2 = \Delta m_{31}^2 = 0$, so that the corresponding ν_e survival probability reduces to the well-known 2ν vacuum oscillation formula and involves only two parameters, namely the large mass-squared splitting $\Delta m_{41}^2 = \Delta m_{42}^2 = \Delta m_{43}^2$ and the mixing angle θ_{14} :

$$P_{ee}^{\text{Ga-source}} = 1 - \sin^2(2\theta_{14}) \sin^2\left(\frac{\Delta m_{41}^2 L}{4E}\right). \quad (7.30)$$

Hence the only common parameter between the Gallium-source experiments and the solar and KamLAND experiments is θ_{14} . In what follows we will perform several compatibility tests of the oscillation parameters allowed by solar data (both alone and in combination with KamLAND) and those implied by the analysis of the Gallium source experiments. To this aim we will make use of a $\Delta\chi_{\text{Ga-source}}^2(\theta_{14})$ function inferred from the combined fit of the Gallium source experiments presented in Ref. [133].

7.2.1 Results

Updated bounds with SSM fluxes

In the first round of analyses we present the results of our fits to solar data in the framework of four different versions of the B23 standard solar models. Concretely, we consider the SSMs computed with the abundances compiled in table 5 of [167] based on the photospheric solar mixtures (MB-phot; the results obtained with meteoritic solar mixtures are totally equivalent), as well as models with the solar composition taken from Ref. [166] (AAG21), from the meteoritic scale of Ref. [164] (AGSS09-met), and from Ref. [163] (GS98).

The results of the SSM constrained analysis are presented in Fig. 7.6 where we plot $\Delta\chi^2(\theta_{14})$ for different choices of the solar fluxes and of the KamLAND analysis. For sake of comparison we also show $\Delta\chi_{\text{Ga-source}}^2(\theta_{14})$ as inferred from the combined fit of the Gallium source experiments presented in Ref. [133]. As can be seen all variants of the solar (+KamLAND) data analysis favour $\theta_{14} = 0$, so that the fit always results into an upper bound on the allowed range of $\sin^2 \theta_{14}$ which is in clear tension with the values required to explain the Gallium anomaly. Comparing the upper and lower panels we also see that relaxing the constraint on the normalization parameter f_{Ga} does not lead to any significant difference in the outcome. Let us notice that f_{Ga} is a factor introduced only in the fit of solar neutrinos, without affecting the analysis of the Gallium source experiments, because in here we are interested in testing if relaxing some assumptions in

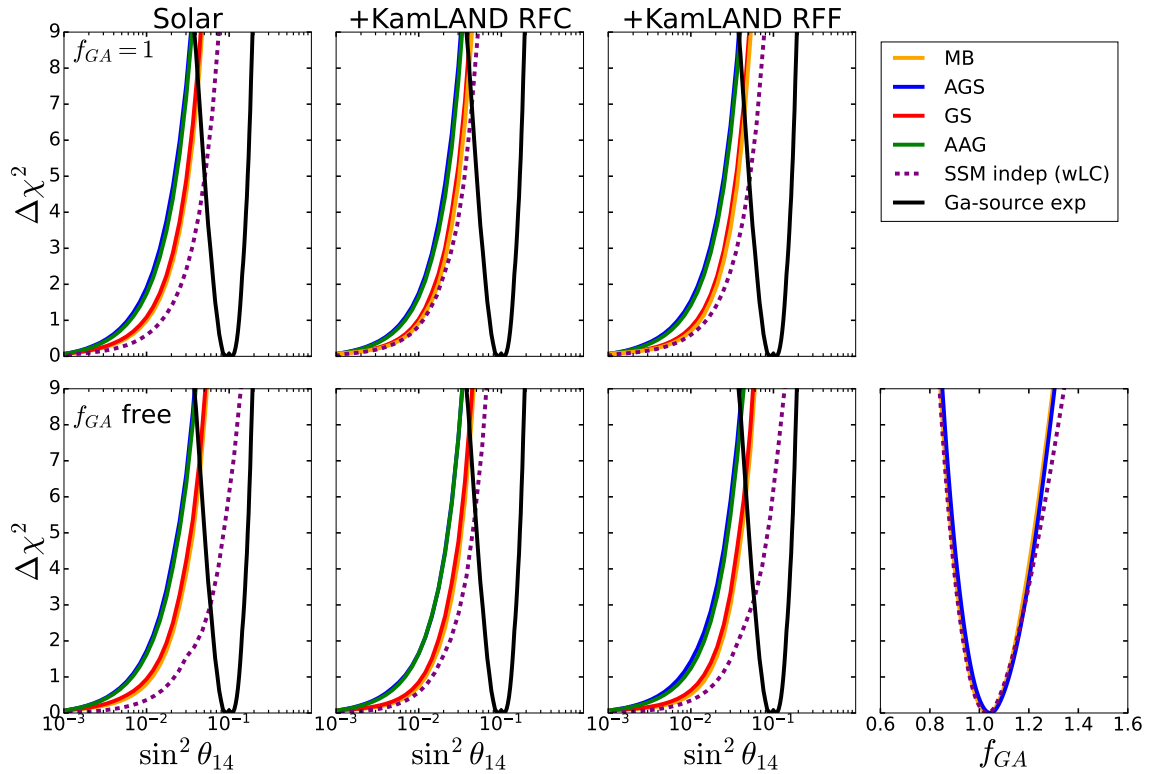


Figure 7.6: One-dimensional projection of the global $\Delta\chi^2$ on the mixing angle θ_{14} after marginalization over the undisplayed parameters, for different assumptions on the solar neutrino fluxes as labelled in the legend. The first (second) [third] column corresponds to the analysis including solar-only (solar+KamLAND-RFC) [solar+KamLAND-RFF] data. The upper (lower) panels show the results with $f_{\text{Ga}} = 1$ (free f_{Ga}). In all panels the black parabola is $\Delta\chi_{\text{Ga-source}}^2(\theta_{14})$ as inferred from the combined analysis of the Gallium source experiments presented in Ref. [133]. In the rightmost lower panel we show the dependence of $\Delta\chi^2$ on the normalization parameter f_{Ga} .

the solar and KamLAND analysis can lead to a better agreement with the sterile neutrino interpretation of the results of Gallium source experiments. Studies of correlated effects affecting the Gallium capture rate in both solar and source experiments, such as variations of the capture cross sections, have been presented in various works (see, *e.g.*, Refs. [131, 134, 135, 308–311]). Statistically, allowing f_{Ga} to be free in the solar and KamLAND analysis is equivalent to removing the solar Gallium source experiments from the fit, as clearly visible in Fig. 7.3 where both approaches have been explicitly implemented. As explained at the end of Sec. 7.1.3, this is due to the lack of spectral and day-night capabilities in Gallium data, which prevents them from providing further information beyond the overall normalization scale of the signal. The advantage of performing the analysis introducing the unconstrained f_{Ga} factor, is that one can quantify the range of f_{Ga} favoured by the fit. Interestingly from the bottom-right panel we see that the solar and KamLAND data always favours f_{Ga} close to one with 1σ uncertainty of about 7%. In comparison, the prediction of the neutrino capture cross section in Gallium in the different models can vary up to about 15% [131, 134, 135, 308–311]. This means that the global analyses of solar experiments do not support a significant modification of the neutrino capture cross section in Gallium, or any other effect inducing an energy independent reduction of the detection efficiency in the solar experiments.

The quantitative question to address is the level of (in)compatibility of these results

		$f_{\text{Ga}} = 1$			$f_{\text{Ga}} \text{ free}$		
	SSM	χ_{PG}^2/n	$p\text{-value} (\times 10^{-3})$	$\#\sigma$	χ_{PG}^2/n	$p\text{-value} (\times 10^{-3})$	$\#\sigma$
Solar	MB-phot/GS98	14.9	0.11	3.9	13.1	0.3	3.6
	AAG21/AGSS09	18.7	0.2	4.3	17.3	0.03	4.2
	SSM indep (wLC)	9.1	2.6	3.0	4.9	27	2.2
Solar + KL-RFC	MB-phot/GS98	15.9	0.07	4.0	15.1	0.1	3.9
	AAG21/AGSS09	19.4	0.1	4.4	18.7	0.01	4.3
	SSM indep (wLC)	13.5	0.23	3.7	10.5	1.2	3.2
Solar + KL-RFF	MB-phot/GS98	13.2	0.28	3.6	11.7	0.64	3.4
	AAG21/AGSS09	17.3	0.03	4.2	16.0	0.06	4.0
	SSM indep (wLC)	8.7	3.1	2.9	4.8	29	2.2

Table 7.3: Results of the PG test for the different solar flux model assumptions and the different analysis variants.

from the solar (+KamLAND) analysis with those from the Gallium source experiments in the context of the 3+1 scenario.⁵ Consistency among different data sets can be quantified with the parameter goodness-of-fit (PG) test [158]. For a number N of uncorrelated data sets i , each one depending on n_i model parameters and collectively depending on n_{glob} parameters, it can be shown that the test statistic

$$\chi_{\text{PG}}^2 \equiv \chi_{\text{min, glob}}^2 - \sum_i^N \chi_{\text{min, } i}^2 = \min \left[\sum_i^N \chi_i^2 \right] - \sum_i \min \chi_i^2 \quad (7.31)$$

follows a χ^2 distribution with $n_{\text{PG}} \equiv \sum_i n_i - n_{\text{glob}}$ degrees of freedom [158]. In this section we have $N = 2$, and the relevant number of parameters are $n_{\text{solar}(+\text{KamLAND})} = 3$ (or 4 for analysis with f_{Ga} free), $n_{\text{Ga-source}} = 2$ and $n_{\text{global}} = 4$ (or 5 for analysis with f_{Ga} free). So for all tests $n_{\text{PG}} = 1$, reflecting the fact that the only parameter in common between the solar (+KamLAND) and the Gallium-source data sets is θ_{14} . We list in table 7.3 the results of applying the PG test to the different variants of the analysis. As can be seen, from the results in the lines labeled MB-phot/GS98 (AAG21/AGSS09) in the ‘‘Solar’’ case, the analysis of the solar neutrino data performed in the framework of the SSM’s with higher (lower) metallicity are incompatible with the Gallium source experiments at the 3.6σ (4.2σ) level even when allowing for a free f_{Ga} . Looking at the corresponding lines for the ‘‘Solar+KL-RFC’’ and ‘‘Solar+KL-RFF’’ fits we see that combination with KamLAND data results into a slight improvement or weakening of the incompatibility depending on the assumption on the reactor fluxes.

To further illustrate the interplay between solar and KamLAND data we show in Fig. 7.7 the two-dimensional projection of the global $\Delta\chi^2$ for the separate analysis of solar-only and KamLAND-only results under different assumptions for the corresponding input fluxes. From the upper left panel, as expected, we see that the determination of Δm_{21}^2 in KamLAND is robust irrespective of the presence of sterile neutrinos or the assumptions on the reactor flux normalization, since both occurrences only affect the overall scale of the signal whereas Δm_{21}^2 is determined by the distortions of the energy spectral shape. As it is well known from the results of the 3ν analysis, the Δm_{21}^2 values

⁵Prof. Thomas Schwetz did a simple calculation assuming the same cross-section rescaling would hit both types of experiments equally, and found about a 2.8σ disagreement between solar gallium and gallium source results.

favoured by KamLAND lie in the upper 2σ allowed range of the solar neutrino fit. From the upper right panel we see that the dependence of $\Delta\chi_{\text{solar}}^2$ on θ_{14} within the Δm_{21}^2 interval favoured by KamLAND is flatter than at the lower Δm_{21}^2 values preferred by the solar-only analysis, which means that the solar-only bound on θ_{14} becomes weaker when Δm_{21}^2 is constrained to the KamLAND range. In addition, the lower panel shows that in the «KamLAND-RFF» analysis (for which no information on the absolute reactor flux normalization is included) there is a degeneracy between θ_{12} and θ_{14} . Such degeneracy is expected as the KamLAND survival probability in vacuum reads

$$P_{ee}^{\text{KamLAND}} \simeq \cos^4 \theta_{14} (\cos^4 \theta_{13} + \sin^4 \theta_{13}) + \sin^4 \theta_{14} - \cos^4 \theta_{14} \cos^4 \theta_{13} \sin^2(2\theta_{12}) \sin^2(\Delta m_{21}^2 L/E) \quad (7.32)$$

so the spectral shape of the signal only provides information on the ratio of the energy-dependent and energy-independent pieces

$$\frac{\cos^4 \theta_{14} \cos^4 \theta_{13} \sin^2(2\theta_{12})}{\cos^4 \theta_{14} (\cos^4 \theta_{13} + \sin^4 \theta_{13}) + \sin^4 \theta_{14}} \quad (7.33)$$

whose isocontours precisely trace the magenta lines in the $(\sin^2 \theta_{12}, \sin^2 \theta_{14})$ plane observed in the lower panel. As a consequence of all this, the combination of solar+KamLAND-RFF data leads to a slight weakening of the bounds on θ_{14} compared to the solar-only analysis, as can be seen comparing the left and right panels in Fig. 7.6 as well as the corresponding values of the PG test in Table 7.3. On the contrary the analysis of KamLAND with constrained reactor fluxes can independently bound both the numerator and denominator in Eq. (7.33) and therefore provides an additional constraint on θ_{14} , as illustrated by the filled green regions in the lower panel of Fig. 7.7. In the end when combining solar and KamLAND-RFC this second effect overcompensates the weakening of the solar bound associated with the larger Δm_{21}^2 value, so that the solar+KamLAND-RFC analysis results in a stronger θ_{14} bound than the solar-only fit.

Bounds from solar model independent analysis

Let us now discuss the results of fits performed without the assumption of standard solar model fluxes (but still retaining the condition of consistency with the observed solar luminosity). As mentioned in Section 7.1, the combined analysis of present solar neutrino experiments and KamLAND reactor data allows for the simultaneous determination of the relevant oscillation parameters together with the normalizations Φ_i of the eight solar neutrino fluxes — five produced in the reactions of the pp-chain, $i \in \{\text{pp}, {}^7\text{Be}, \text{pep}, {}^8\text{B}, \text{hep}\}$, and three originating from the CNO-cycle, $i \in \{{}^{13}\text{N}, {}^{15}\text{O}, {}^{17}\text{F}\}$. In Section 7.1 we presented such determination in the framework of 3ν oscillations (Eqs. (7.3-7.12)).

In Fig. 7.7 we show as void black contours the constraints on the oscillation parameters from our SSM independent analysis of solar data (labeled as “SSM indep (wLC)” in short), as obtained after marginalization over the various flux normalizations. Comparing these contours with the full red regions (corresponding to the analysis with solar fluxes as predicted by the MB-phot SSM) we see that the determination of the oscillation parameters is only slightly loosened in the SSM independent fit, and in particular the analysis still yields a strong bound on θ_{14} . The corresponding one-dimensional projections $\Delta\chi^2(\theta_{14})$ (both for solar-only and in combination with the two variants of the KamLAND fit) are shown as dotted lines in the various panels of Fig. 7.6, and the values of the PG tests are given in Table 7.3. From the table we read that, as long as the normalization

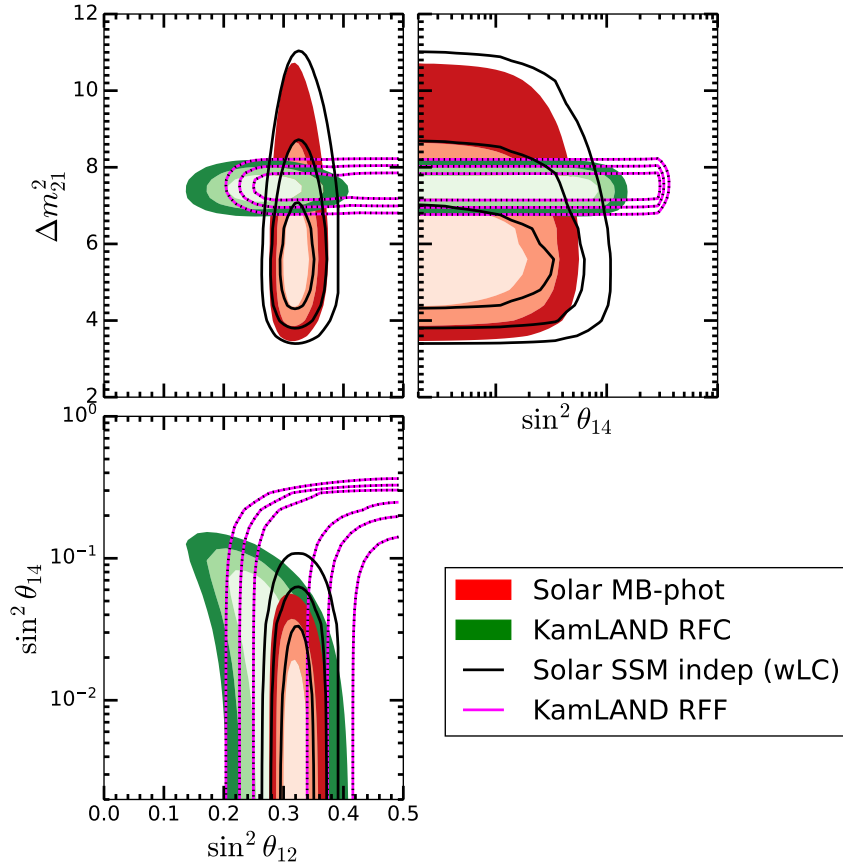


Figure 7.7: Two-dimensional projection of the global $\Delta\chi^2$ (for $f_{\text{GA}} = 1$) on the relevant oscillation parameters at 1σ , 2σ and 3σ after marginalization over the undisplayed parameters. The full red regions (void black contours) correspond to the analysis of solar data with MB-phot (free) fluxes, while the full green regions (void magenta contours) correspond to the KamLAND-RFC (KamLAND-RFF) fit.

parameter f_{Ga} is kept to its nominal value $f_{\text{Ga}} = 1$, the level of (in)compatibility between the solar (+KamLAND) data and the Gallium source experiments is at a level $\gtrsim 3\sigma$. The tension can only be relaxed to the $\sim 2.2\sigma$ level when allowing the value of f_{Ga} to float freely.

Implications for the ν -inferred Sun Luminosity

We finish by exploring the implications that assuming at face value the sterile solution of the Gallium anomaly would have on the mechanism for energy production in the Sun as inferred from neutrino data. As mentioned above, pp neutrinos yield the largest contribution both to $L_{\odot}(\nu\text{-inferred})$ ($\gtrsim 90\%$) and to the event rate of the Gallium solar experiments ($\gtrsim 55\%$), which poses the question of what should be the deviation from the relation in Eq. (7.3) required for solar observations to be compatible with the Gallium source experimental results. In order to quantitatively answer this question we have performed a SSM independent analysis similar to the one described above, but without imposing the prior in Eq. (7.5). This allows us to determine the level of compatibility between solar+KamLAND data and Gallium source experiments as a function of the ν -inferred solar luminosity, by comparing the $\sin^2\theta_{14}$ range preferred by each data set. The results are shown in Fig. 7.8. In this analysis we have kept $f_{\text{Ga}} = 1$ because of the strong correlation (induced by Φ_{pp}) between the solar luminosity and the event rate in

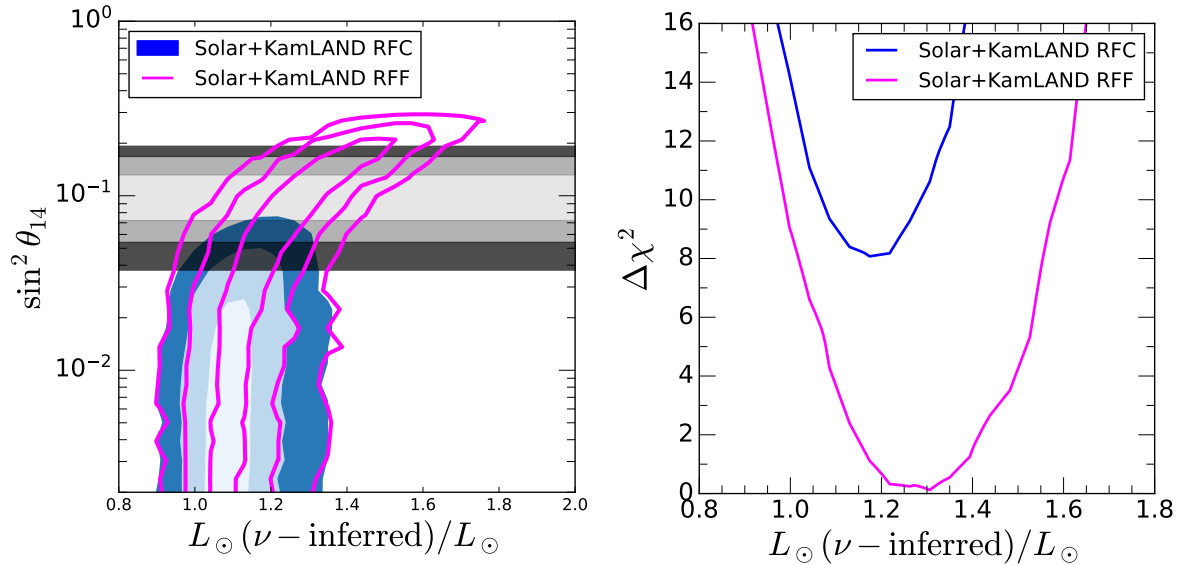


Figure 7.8: Left: dependence of the 1σ , 2σ , 3σ ranges of $\sin^2 \theta_{14}$ from the analysis of solar+KamLAND without imposing the constraint in Eq. (7.5) on the resulting neutrino-inferred solar luminosity. Fill (void) regions correspond to solar+KamLAND-RFC (solar+KamLAND-RFF) analysis. The horizontal grey regions illustrate the 1σ , 2σ , 3σ ranges required to explain the Gallium source results. Right: value of $\Delta\chi^2$ from the joint analysis of solar+KamLAND and Ga-source data, defined with respect to the sum of the two separate best-fit χ^2_{\min} , as a function of the neutrino-inferred solar luminosity. In these analysis we keep $f_{\text{GA}} = 1$ (see text for details).

the Gallium source experiments, which results in an almost complete degeneracy if both $L_{\odot}(\nu\text{-inferred})$ and f_{Ga} are left free to vary at the same time. In the left panel we plot the 1σ , 2σ , 3σ (1 dof) ranges for θ_{14} (defined with respect to the global minimum) allowed by the combined fit of solar and KamLAND data (for both variants of the KamLAND analysis) as a function of the ν -inferred solar luminosity in units of the directly observed L_{\odot} . For comparison we show as horizontal grey bands the corresponding required ranges to explain the Gallium anomaly. As seen in the figure, for either analysis, compatibility requires a substantial deviation of the luminosity inferred from the solar neutrino observations with respect to its value as directly determined. This is further quantified in the right panel, which shows the increase in χ^2 when combining together solar+KamLAND and Ga-source data (as a function of the aforesaid luminosity ratio) with respect to the sum of the two separate best-fits (so that by construction the minimum of each curve yields the χ^2_{PG} value defined in Eq. (7.31)). As seen in the figure, for the KamLAND-RFC case the level of compatibility is always higher than 2.8σ , while in the KamLAND-RFF case the compatibility only drops below the 2σ level if one allows $L_{\odot}(\nu\text{-inferred})$ to deviate by more than 10% from the directly determined solar luminosity. In other words, to accommodate the sterile neutrino interpretation of the Gallium anomaly within the present observation of solar and KamLAND neutrinos at better than the 2σ level, it is necessary to (a) make no assumption on the normalization of the reactor antineutrino fluxes, and (b) accept that more than 10% of the energy produced in the nuclear reactions in the Sun does *not* result into observed radiation — despite the fact that, as mentioned before, the solar radiated luminosity is directly determined with 0.34% precision.

7.3 Summary

In this chapter, we have updated our former determination of solar neutrino fluxes from neutrino data as presented in Refs. [69, 295], by incorporating into the analysis the latest results from both solar and non-solar neutrino experiments. In particular, this includes the full data from the three phases of the Borexino experiments, which have provided us with the first direct evidence of neutrinos produced in the CNO-cycle.

In Section 7.1, we have derived the best neutrino oscillation parameters and solar fluxes constraints using a frequentist analysis with and without imposing nuclear physics as the only source of energy generation (luminosity constraint). Compared to the results from previous analysis, we find that the determination of the ${}^7\text{Be}$ flux has improved by a factor $\mathcal{O}(3)$, but most importantly, we now find that the three fluxes produced in the CNO-cycle are clearly determined to be non-zero, with 1σ precision ranges between 20% to $\sim 100\%$ depending on the assumptions in the analysis about their relative normalization. Conversely, in Refs. [69, 295] only an upper bound for the CNO fluxes was found. This also implies that it is solidly established that at 99% CL, the solar energy produced in the CNO-cycle is between 0.46% and 1.05% of the total solar luminosity.

The observation of the CNO neutrinos is also paramount to discriminate among the different versions of the SSMs built with different inputs for the solar abundances, since the CNO fluxes are the most sensitive to the solar composition. In this work we confront for the first time the neutrino fluxes determined on a purely experimental basis with the predictions of the latest generation of SSM obtained in Ref. [146, 167]. Our results show that the SSMs built incorporating lower metallicities are less compatible with the solar neutrino observations.

In Section 7.2, we have applied our global analyses of solar neutrino data in the framework of the 3+1 neutrino mixing scenario commonly invoked to explain the results from Gallium source experiments. With these fits at hand, we have performed consistency tests to assess the level of (in)compatibility between the range of the sterile neutrino mixing preferred by each data set, and we have studied the dependence of the results on the different assumptions entering in the analysis. All the fits considered here have shown compatibility (as measured by the parameter goodness-of-fit) only at the 3σ level or higher. This conclusion holds for analyses assuming solar neutrino fluxes as predicted by any of the last generation Standard Solar Models, and irrespective of the assumptions on the KamLAND reactor flux normalization and on the gallium capture rate. Relaxing the SSM constraints on the solar fluxes — while still enforcing the relation between the observed value of the solar radiated luminosity and the total amount of thermal energy generated by the various neutrino-emitting nuclear reactions — only improves the compatibility to levels below 3σ when no prior knowledge in either the gallium capture rate or the normalization of reactor neutrino fluxes is assumed. If the luminosity constraint is also dropped, then it is formally possible to achieve a compatibility level below 2σ as long as the flux of reactor antineutrinos is left free, but such solution unavoidably requires that more than 10% of the energy produced together with neutrinos in the nuclear reactions of the Sun does not result into observable radiation.

Chapter 8

Conclusion

In the quest of understanding the fundamental nature of neutrinos, this thesis has explored multidirectional approaches to address some intriguing puzzles surrounding these ghostly particles. Neutrinos represent one of the most compelling subjects in present particle physics due to their observed properties diverging from SM predictions (at least the original content of the SM). The established non-zero neutrino mass necessitates modifications to the traditional particle physics framework, as evidenced by experimental results discussed throughout this work. This requirement has stimulated extensive experimental and theoretical research aimed at uncovering the mechanisms governing neutrino behavior and nature, leading to significant insights into physics beyond the SM.

The experimental foundation of three-neutrino mixing has been robustly confirmed through analyses of solar, atmospheric, reactor, and accelerator-based neutrino experiments, as detailed in Chapter 3. Sections 3.1, 3.2, 3.3, and 3.4 presented comprehensive examinations of these experimental setups, solidifying the three-flavor oscillation paradigm. However, persistent discrepancies in gallium-based experiments (Section 3.6) and novel measurements of coherent elastic neutrino-nucleus scattering ($\text{CE}\nu\text{NS}$, Section 3.5) challenge the standard formalism, prompting investigations into new physics scenarios.

Chapter 4 presented an updated global analysis of neutrino oscillation data through September 2024, employing two dataset variants: «IC19 w/o SK-atm» (independent detailed fits) and «IC24 with SK-atm» (incorporating collaboration-provided χ^2 tables). Key parameters θ_{12} , θ_{13} , Δm_{21}^2 , and $|\Delta m_{3\ell}^2|$ exhibit strong constraints with relative uncertainties of 13%, 8%, 16%, and 5–6% at 3σ , respectively. The mixing angle θ_{23} remains least constrained (20% uncertainty at 3σ), maintaining persistent octant ambiguity with $\Delta\chi^2 < 4$ between solutions. CP-violation analyses reveal $\delta_{\text{CP}} \approx 180^\circ$ (NO) favoring CP conservation, while IO favors $\delta_{\text{CP}} \approx 270^\circ$ with 3.6σ – 4σ rejection of CP conservation. Mass ordering preferences show $\Delta\chi_{\text{IO,NO}}^2 = -0.6$ (IC19) versus 6.1 (IC24), reflecting competing experimental trends and atmospheric data impacts.

Theoretical extensions beyond the SM were systematically explored in Chapter 5. Section 5.1 established Non-Standard Interaction (NSI) formalism for neutrino oscillations and matter effects, including discussion of LMA-D degeneracy. Section 5.2 examined detection-level modifications from new physics scenarios, while Section 5.3 developed monopole-dipole interaction formalisms for light scalar mediators. These frameworks enable comprehensive analysis of vector, scalar, and pseudoscalar mediators affecting neutrino propagation and detection.

Experimental constraints on beyond-SM scenarios were rigorously derived in Chapter 6. Borexino Phase II data (Section 6.1) yielded NC NSI with electrons bounds through density matrix formalism (Eq. (5.9)), resolving oscillation-interaction degeneracies. In

particular, the LMA-D solution arising in the presence of vector NSI was eliminated, enabling independent $\varepsilon_{\alpha\alpha}^{f,V}$ determination. Neutrino magnetic moment (NMM) constraints (Eqs. (6.3), (6.4)) aligned with prior results, while light mediator analyses produced mass-dependent limits:

$$\begin{aligned} |g_{Z'}^{B-L}| &\leq 6.3 \times 10^{-7}, & |g_{Z'}^{L_{e^{-}L_{\mu,\tau}}}| &\leq 5.8 \times 10^{-7}, \\ |g_{\phi}^{\text{univ}}| &\leq 1.4 \times 10^{-6}, & |g_{\phi}^{\text{univ}}| &\leq 2.2 \times 10^{-6} \end{aligned} \quad (8.1)$$

for $M \lesssim 0.1$ MeV. Heavy mediator constraints scaled as $(g/M)^n$, with $|g_{Z'}|/M_{Z'} \leq 1.4 \times 10^{-6} \text{ MeV}^{-1}$. Global fits combining oscillation and CEvNS data (Section 6.2) excluded LMA-D beyond 2σ for quark-coupled mediators, while maintaining oscillation parameter robustness. Axial NSI bounds proved weaker than vector counterparts (Fig. 6.9), with Earth matter effects quantified for atmospheric/LBL experiments (Fig. 6.11). Solar neutrino analyses constrained spin-zero mediators (Section 6.3), surpassing previous limits for $m_{\phi} \lesssim 10^{-12}$ eV through SFP potential constraints.

Chapter 7 advanced solar neutrino flux determinations by incorporating Borexino's CNO-cycle neutrino observations. Section 7.1 achieved $\mathcal{O}(3)$ improvement in ${}^7\text{Be}$ flux precision, establishing non-zero CNO fluxes (20%–100% uncertainties) and constraining CNO energy contribution to 0.46%–1.05% of solar luminosity at 99% CL. Confrontation with SSM predictions revealed incompatibilities with low-metallicity models. Section 7.2 analyzed 3+1 neutrino mixing scenarios for gallium anomalies, finding $> 3\sigma$ incompatibility across SSM assumptions, only reaching $< 2\sigma$ compatibility when relaxing luminosity constraints and reactor flux normalizations.

In summary, this thesis has pursued a multidimensional investigation into the present limits of the standard neutrino parameters, reinforcing the robustness of the three-flavor oscillation framework and the investigation of BSM scenarios over the most up-to-date experimental data. Starting with a rigorous analysis of the three-neutrino oscillation framework, this work systematically probed current limits on beyond-SM physics while utilizing neutrino flux data to test solar models and address the unresolved gallium anomaly. From Pauli's hypothetical particle to current precision experiments, neutrino physics continues to illuminate BSM phenomena while guiding our understanding of astronomical objects. The field's future promises continued surprises, building upon the rigorous methodologies and insights presented throughout this work.

Acknowledgements

Agora que a tese está finalizada, tenho a sensação de dever cumprido. Eu não consigo me ver de outra forma, a não ser como um físico (espero ser ao menos um razoável agora, com certeza muito melhor que há 4 anos atrás...). Ainda me lembro do dia em que resolvi escolher a física como carreira. Num ato de impulsividade, uma escolha em 2014 que mudou o rumo da minha vida. A minha amada avó Eudália me ajudou desde o princípio. Fui estudar em outro estado, com a ajuda dos meus tios Tércio e Áurea me cedendo por uns meses um espaço em seu apartamento, e contando com o suporte financeiro da minha avó. Os agradeço muito por todo o suporte, sem vocês eu não estaria aqui. Porém, tenho que agradecer principalmente aos meus pais, Ednólia e José que sempre mostraram apoio, independente das minhas escolhas, e me ensinaram o que é o certo e o errado, o que é moral e imoral, e o valor do trabalho duro e consistente. Meus pais me ensinaram (e continuam me ensinando) o valor da família e do amor. À minha irmã, Paula, com quem sempre compartilhamos o que sentíamos e que durante esse período de Doutorado me ajudou inúmeras vezes financeiramente e psicologicamente, e que quando eu fui morar na Espanha, cuidou da minha cadelinha Liana. Também, agradeço a todos os meus outros familiares que me ajudaram nesse processo. Mãe Santana, Marcelo, Ariane, Adnorah e Netinho.

Gostaria de agradecer aos meus amigos de infância que continuaram a me apoiar a todo momento. Sávio, uma pessoa excepcional e com quem mantemos contato sempre. A Samuel, que sempre foi próximo a mim, e não importa o nosso contato diário, sempre parece que nos falamos ontem. Sem vocês para dividir conquistas e dores durante esse período, minha vida seria muito ruim. E a Raick, que nos motivamos a continuar a carreira acadêmica desde o ensino médio. Sem vocês, dificilmente eu teria concluído todo esse trajeto.

Sair de uma cidade interiorana como Petrolina, e ir para uma capital como João Pessoa, não foi uma transição fácil. Ainda mais sendo uma pessoa difícil como eu, num período de formação aos 18 anos de idade. Na Universidade Federal da Paraíba me formei físico, e carrego todos os seus pontos fortes e fracos tatuados em mim. Nesse período, duas pessoas foram essenciais: os professores Carlos Pires e Paulo Sérgio. Paulo me acolheu durante a graduação como seu estudante de Iniciação Científica. Carlos foi essencial para a minha formação e continua sendo. Ele foi o responsável por colocar a ideia de fazer um doutorado fora do Brasil na minha cabeça e depois disso segui esse objetivo. Carlos é e continua sendo peça chave no meu processo formativo.

Durante o meu período na universidade, tive amigos que me ajudaram a seguir em frente. Vinícius, que sempre foi uma referência para mim e um amigo com quem eu sempre pude compartilhar tudo. Foi a primeira pessoa a saber que eu era pai. Espero levar a nossa amizade para sempre. E também foi a única pessoa que compartilhou esse sonho louco comigo de ir fazer um doutorado fora do país. Ver seus passos a cada dia me enche de orgulho. Também quero agradecer a Jefferson, William, Jacinto e Leandro, que sempre foram bons amigos durante esse período no Brasil.

Porém, a pessoa que mais devo no meu processo formativo como um todo se chama Concha. Concha basicamente pegou a minha mão e me ensinou como se eu fosse um estudante do jardim de infância. Te dei muita dor de cabeça nesses 4 anos. Coisas básicas que somente consegui entender ao adquirir mais maturidade, depois de refletir melhor sobre as coisas. Conceitos de ética, rigor, análise estatística, programação, fenomenologia... Muito do que sei foi apenas um fragmento que extraí da senhora, que é um mar de conhecimento vivo.

Mi período en España ha sido rico en todos los sentidos. He conocido una lengua distinta, con costumbres distintas. He conocido la comunidad de neutrinos de Europa, he conocido el mundo. Sin Concha y la Universitat de Barcelona, esto sería imposible para mí. En estos 4 años aquí he madurado mucho, y también vivido muchas experiencias. He conocido excelentes personas, como el grande Michele, una persona extremadamente agradable e inteligente. Me ha enseñado todo de programación, con sus consejos, códigos y longos correos. Muchas gracias por siempre ayudarme. Ahora, siempre que escribo un código pienso antes: ¿Cómo Michele lo haría? Muchas gracias por todo. A Jordi, por siempre estar con sus puertas abiertas para hablar de todo, desde física hasta sobre la vida en general. También a Salva, mi gran amigo que conocí antes de llegar a España y ha sido un gran profesor. Siempre me enseña algo nuevo. Muchas gracias. A Toni y David, que empezamos juntos y compartimos muchos momentos, nuestras angustias, dolores, dudas y momentos de felicidad. A Stefan, Pol e Iñigo, por siempre poder hablar, beber un café, almorzar, beber unas cañas, hablar de todo lo que sea. Muchas gracias. Agradezco a todos los que han pasado por mi vida en este momento de formación, muchas gracias.

During my PhD, I had the privilege of traveling to many different places around the world. I am deeply grateful to all those who welcomed me so warmly during my secondments and research visits. Throughout this journey, I met an incredible number of wonderful people: Jaime, Jay, Xavi, Stefan, Rasmi, Federica, Miguel, Federico, Sandra, Antonio, Gustavo, Alejandro, Androniki, Ushak, Giacomo, Gioaccino, Mario, Ana, Daniel, Joachim, Salva, Maria, Arturo, Christoph, and Michele (my apologies if I have forgotten anyone).

I extend my gratitude to Olcyr, Damir, and Asmaa for all their help and support and a very nice reception in Orsay. Pedro, você é um cara excepcional e espero sempre poder trabalhar contigo, me recepcionou muito bem durante a minha estadia curta no Fermilab. Tao, thank you for your exceptional hospitality in Pittsburgh. I would like to express my sincere appreciation to Renata and Oscar for their warm reception in São Paulo. I am also grateful to all my research collaborators: Pilar, Thomas, Ivan M, Saeed, Julia, Aldo, Adriano, and Patrício. Special thanks go to Ivan E, who provided tremendous assistance in helping me understand and simulate NOvA, as discussed in Chapter 4. I look forward to continued fruitful collaboration in the years ahead.

Finally, I would like to acknowledge the Hidden Network, which provided me with the financial support necessary to travel to different continents, disseminate my research, present my findings, and engage with a diverse community of outstanding researchers. I must give special recognition to Sheila, a dedicated staff member at the Universitat de Barcelona working with the Bosch i Gimpera Foundation, who handled all the bureaucratic processes related to reimbursements. Her diligent work and patience in managing these administrative tasks were invaluable throughout the first three years of my PhD journey.

I am also grateful to the Universitat de Barcelona, which, like any institution, has both its strengths and challenges. The university is home to exceptional students and faculty, and Barcelona's favorable climate creates an environment where people tend to be more

friendly and relaxed, fostering genuine human connections that made my experience truly memorable. However, I must admit that navigating the bureaucratic processes was not always straightforward. Despite these administrative challenges, the overall atmosphere and the quality of people I encountered made this journey worthwhile. Only a place like Barcelona could offer such a unique blend of academic rigor and Mediterranean charm.

My deepest thanks go to everyone who has enriched my life and contributed positively to my journey thus far.

Appendix A

A.1 Assumed true values for the MO test

As mentioned in Sec. 4.2.3, the values of T_0^o — and therefore the distribution of T — depend on the unknown true value of the oscillation parameters. In principle, one needs to consider the distribution of T for all possible values of θ^{true} and the final p -value of a MO hypothesis will be given by the largest one among all choices of θ^{true} , *i.e.*, by the weakest rejection (see the discussion in Ref. [161]). In the main text, we have assumed that the best fit of the real data is representative of the T -distribution at the unknown true value of θ . Indeed, given the allowed regions of the oscillation parameters, we do not expect T_0 to change significantly if we vary θ^{true} within the allowed regions at reasonable confidence level. The only exception may be the sensitivity of LBL data as a function of δ_{CP} , which is known to affect the MO sensitivity, especially for NOvA as shown in Fig. 4.4.

For IO, the global fit constrains δ_{CP} reasonably well, so that we do not expect strong variations of T_0^{IO} for true values of δ_{CP} in its allowed range for IO. However, for NO, a significantly larger range of δ_{CP} is allowed, in particular in correlation with θ_{23} , see Fig. 4.7. Therefore, the question arises, whether the MO test would give largely different results when considering true values for δ_{CP} and θ_{23} within the allowed region for NO.

From Fig. 4.4, we see that for $\delta_{\text{CP}} \approx 270^\circ$ and NO, the number of ν_e events in NOvA is maximal, and its value cannot be obtained by any parameter choice in IO. Therefore, we expect best sensitivity to NO for this value of δ_{CP} . In contrast, values around 0 or 180° can be easily accommodated within IO, and we expect that the sensitivity to NO is weakest around CP-conserving values. We have confirmed this expectation, as we obtain

$$T_0^{\text{NO}}(\delta_{\text{CP}}^{\text{true}} = 270^\circ, \sin^2 \theta_{23}^{\text{true}} = 0.46) = 12.38, \quad (\text{A.1})$$

with all other oscillation parameters kept at their best-fit values. Actually, for the value in Eq. (A.1) the observed value $T_{\text{obs}} = -0.6$ would imply a p -value for NO of 3.2%. Since values of δ_{CP} around 90° are significantly disfavored also for NO, we do not consider them relevant for the MO test.

To summarize, for relevant choices of the oscillation parameters, the sensitivity to the NO is weakest for values of δ_{CP} around 180° . In turn, for IO, δ_{CP} is sufficiently constrained, and we expect only minor variations of T_0 within the relevant range around 270° . Therefore, it is appropriate to consider the current best fit points to quote the final p -values for both orderings.

Appendix B

B.1 Allowing free normalizations for the three CNO fluxes

In their analysis of the different phases, the Borexino collaboration always considers a common shift in the normalization for the three fluxes of neutrinos produced in the CNO cycle with respect to their values in the SSM. On the contrary the normalization of the fluxes produced in the pp-chain are fitted independently.

In principle, once one departs from the constraints imposed by the SSM, the normalization of the three CNO fluxes could be shifted independently, subject only to the minimum set of consistency relations in Eqs. (7.10) and (7.11). In fact in our previous works [69, 295] we could perform such general analysis. At the time there was no evidence of CNO neutrinos and therefore those analysis resulted into a more general set of upper bounds on their allowed values compared to those obtained assuming a common shift. With this as motivation, one can attempt to perform an analysis of the present BXIII spectra under the same assumption of free normalization. However, within the present modelling of the backgrounds in the Borexino analysis, optimized to provide maximum sensitivity to a positive evidence of CNO neutrinos, such generalized analysis runs into trouble as we illustrate in Fig. B.2. As expected, allowing three free CNO flux normalizations results in a weaker constraints on each of the three parameters. This is particularly the case for the smaller ^{17}F flux which is allowed to take values as large as ~ 40 times the value predicted by the SSM without however yielding substantial χ^2 improvements over the standard $f_{17\text{F}} = 1$ value. In the same way $f_{15\text{O}}$ is compatible with the prediction of the SSM, $\Delta\chi^2(f_{15\text{O}} = 1) \simeq 0$, with an upper bound $f_{15\text{O}} \lesssim 2$.¹ On the contrary the fit results into a favoured range for ^{13}N which, if taken at face value, would imply an incompatibility with the SSM at large CL: $\Delta\chi^2(f_{13\text{N}} = 1) \gtrsim 6$. This large ^{13}N flux comes at a price of a very low value of the ^{210}Bi normalization, which as seen in the figure is more strongly correlated with ^{13}N than with ^{15}O and ^{17}F .

To illustrate further this point we show in Fig. B.3 our best fitted spectra of the “subtracted” sample for the analysis where one common normalization for the three CNO fluxes is used (left, in what follows “CNO” fit) and the one where all the three normalizations are varied independently (right, in what follows “N” fit). Thus the spectra in the left panel of Fig. B.3 are the same as the right panel of Fig. B.1, except that now, for convenience, we plot separately the events from each of the CNO fluxes. This highlights clearly the different shape of the spectra of ^{15}O and ^{13}N , with ^{15}O extending to larger energies. It is also evident that ^{13}N is the one mostly affected by degeneracies with the ^{210}Bi background. Comparing the two panels we see by naked eye that both spectra

¹It is interesting to notice that the Borexino bound on $\Phi_{17\text{F}}$ is about one-half that on $\Phi_{15\text{O}}$. This is no surprise since the energy spectra of ^{17}F and ^{15}O neutrinos are extremely similar hence neither Borexino nor any other experiment can separate them and what is actually constrained is their *sum*. This is reflected in the clear anticorrelation visible in Fig. B.2, while the factor of two stems from the consistency condition in Eq. (7.11).

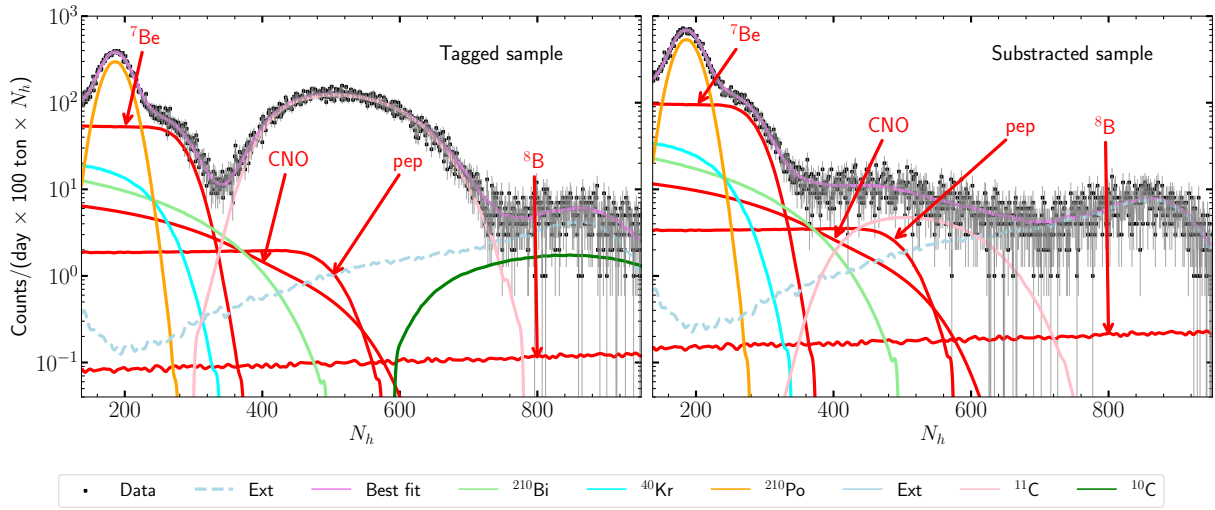


Figure B.1: Spectrum for the best-fit normalizations of the different components obtained from our fit to the Borexino Phase-III data for TFC-tagged (left) and TFC-subtracted (right) events. In this figure “CNO” labels the events produced by sum of the three fluxes produced in the CNO-cycle, $\Phi_{13\text{N}} + \Phi_{15\text{O}} + \Phi_{13\text{F}}$.

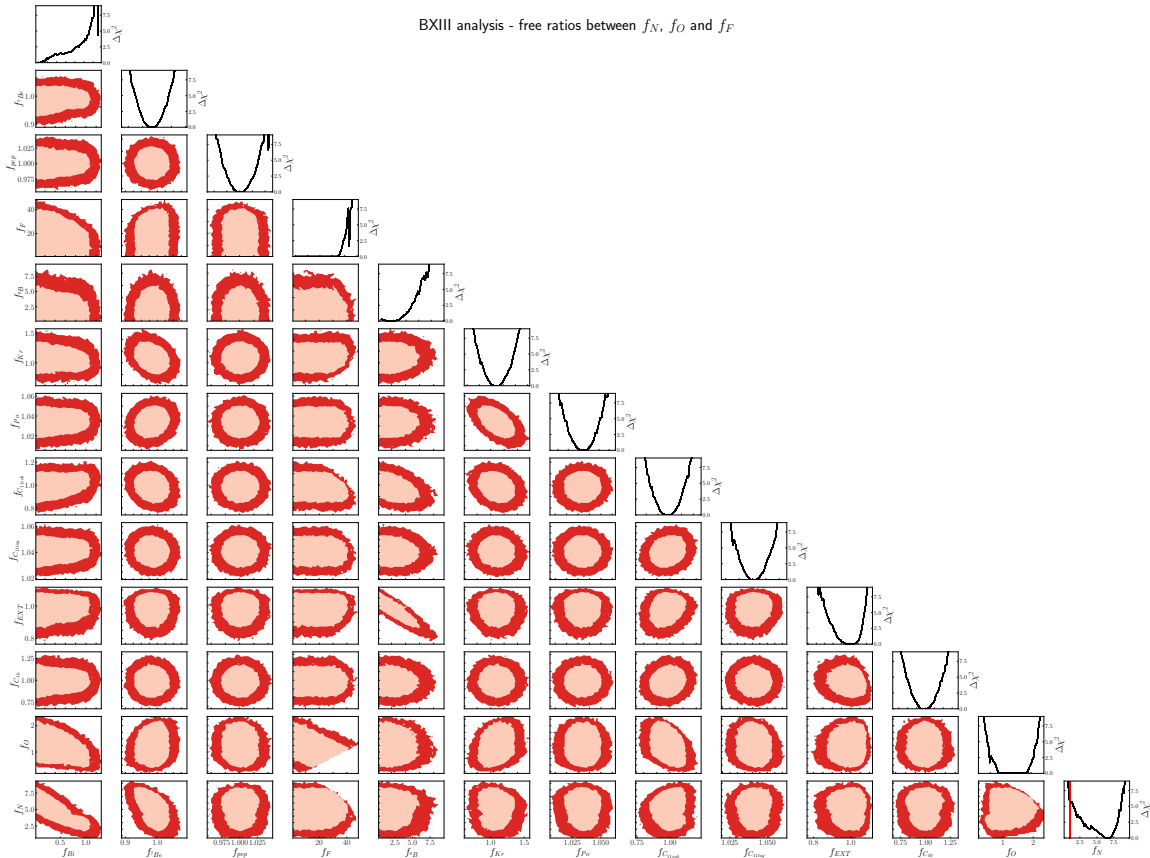


Figure B.2: Same as Fig. 3.5 but but allowing independent variation of the normalizations of the three CNO fluxes, only subject to the consistency conditions in Eqs. (7.10) and (7.11).

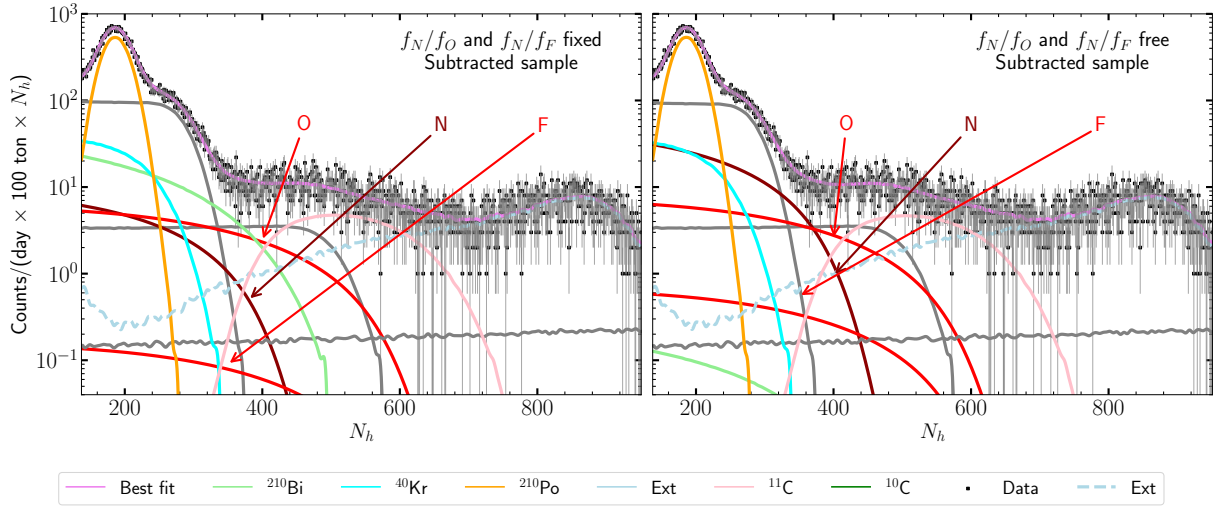


Figure B.3: Spectrum of events in the TFC-subtracted sample for the best-fit normalizations of the different components obtained from two fits to the Borexino Phase-III data. In the left panel the fit is performed assuming a common normalization shift for the 3 CNO fluxes, while on the right panel the three normalizations are allowed to vary free subject only the conditions Eqs. (7.10) and (7.11).

describe well the data: in fact, the event rates for ^{15}O are comparable in both panels. But in the right panel the normalization of the ^{13}N events is considerably enhanced while the ^{210}Bi background is suppressed: this is the option favoured by the fit.

Upon closer examination we find that in the range of N_h spanning between 300 and 400 photon hits, an increase in the value of $f_{^{13}\text{N}}$ better fits the data while driving $f_{^{210}\text{Bi}}$ towards 0. In Fig. B.4 we show a blow-up of the spectra in this N_h window. To quantify the difference in the quality of the fit for those two solutions and the relevant range of N_h we plot in the right panel the cumulative difference of $\chi_{\text{BIII, test}}^2$ for the best fits of the “CNO” and “N” fits as a function of the maximum N_h bin included in the fit.

Clearly, this anomalously large ^{13}N solution is possible only because the sole information included in the fit for the ^{210}Bi background is the upper bound provided by the collaboration. Such upper bound is enough to ensure a lower bound on the amount of CNO neutrinos, and indeed it results in a positive evidence of CNO fluxes (in good agreement with at least some of the SSMs) when a common normalization for the three CNO fluxes is enforced, as reported by the collaboration in Refs. [66, 70] (and properly reproduced by us, as described in the previous section). Our results show that this is the case because the spectrum of ^{210}Bi and ^{15}O are sufficiently different. However, once the normalization of the three CNO fluxes are not linked together, the degeneracy between the spectral shape of ^{13}N and ^{210}Bi – together with the lack of a proper estimate for a lower bound on ^{210}Bi which is not quantified in Refs. [66, 70] – pushes the best-fit of ^{13}N towards unnaturally large values. In other words, the background model proposed in Refs. [66, 70] cannot be reliably employed for fits with independent ^{13}N and ^{15}O normalizations.

We finish by noticing that this also implies that the high quality data of Borexino Phase-III, besides having been able to yield the first evidence of the presence of the CNO neutrinos, also holds the potential to discriminate between the contributions from ^{13}N and ^{15}O , a potential which may be interesting to explore by the collaboration.

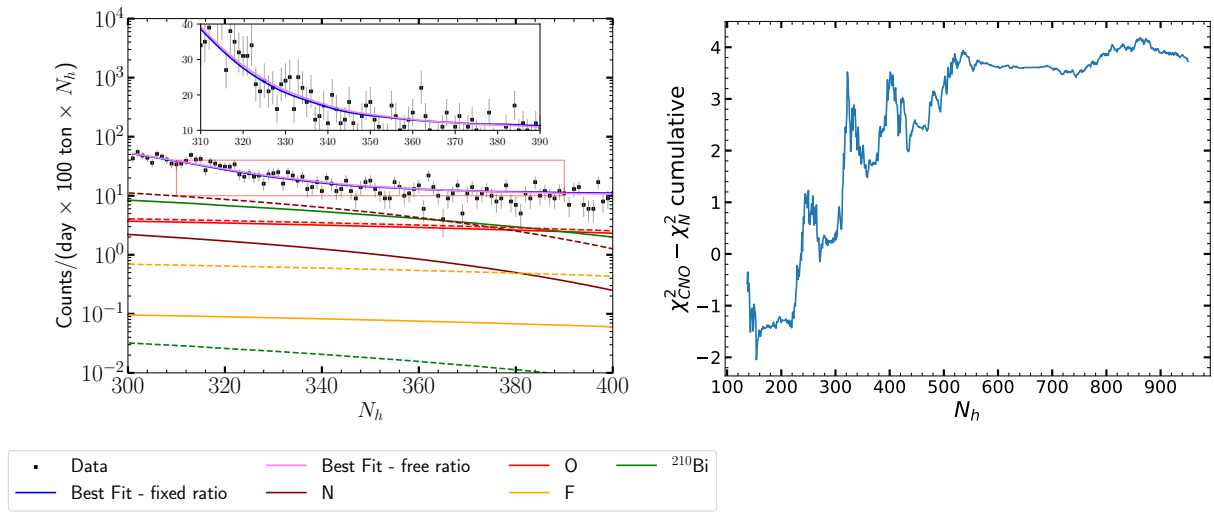


Figure B.4: Left: Spectra of subtracted event rates from best fit CNO fluxes and ^{210}Bi background in the range of $300 \leq N_h \leq 400$ for the “CNO” fit (fit with a common normalization factor for the three CNO fluxes, full lines) and the “N” fit (fit with three independent normalizations, dashed lines). We also show the best fit spectra for both fits compared to the data as labeled in the figure. Right: Difference of the value of χ^2 in both fits as a function of the maximum N_h bin included in the fit.

Appendix C

C.1 Derivation of the scalar-pseudoscalar potential

Our starting point is the well-known relation between the static potential generated by a non-relativistic source particle — here a nucleon f located at $\vec{\rho}$ — felt by a probe particle — here a neutrino ν at position \vec{x} — to the elastic scattering amplitude \mathcal{M} of the process $\nu + f \rightarrow \nu + f$ as computed in QFT in momentum space

$$V(\vec{r} \equiv \vec{x} - \vec{\rho}) = - \int \frac{d^3\vec{q}}{(2\pi)^3} e^{i\vec{q}\cdot\vec{r}} \mathcal{M}(\vec{q}) \quad (\text{C.1})$$

with four-momentum transfer between the source particle and the neutrino given by $q \equiv (0, \vec{q}) \equiv p' - p$ where p and p' are the neutrino four-momenta before and after the elastic scattering, which for a scalar-pseudoscalar interaction of a neutrino with mass m

$$\mathcal{L} = g_s^f \phi \bar{f} f + i g_p^\nu \phi \bar{\nu} \gamma^5 \nu \quad (\text{C.2})$$

reads

$$i\mathcal{M} = \frac{i(g_s^f)(-g_p^\nu)}{q^2 - m_\phi^2} \left[\bar{u}_{r'}^f(k) u_r^f(k) \right] \left[\bar{u}_{\lambda'}^\nu(p') \gamma^5 u_\lambda^\nu(p) \right]. \quad (\text{C.3})$$

In writing Eq. (C.1) we are implicitly assuming the normalization of the spinors to be one particle per unit volume for both nucleons and neutrinos. Explicitly, in the Dirac representation of the gamma matrices our choice for the spinor of fermion with four-momentum (E, \vec{p}) and spin state s is

$$u_s(p) = \sqrt{\frac{E+m}{2E}} \begin{pmatrix} \chi_s \\ \frac{\vec{\sigma}\cdot\vec{p}}{E+m} \chi_s \end{pmatrix} \quad (\text{C.4})$$

where χ_s are 2-spinors normalized as $\chi_{s'}^\dagger \chi_s = \delta_{ss'}$. With this choice, for the non-relativistic nucleons $\bar{u}_{r'}^f(k) u_r^f(k) = \delta_{rr'}$, while for the neutrinos we can write

$$\bar{u}_{\lambda'}^\nu(p') \gamma^5 u_\lambda^\nu(p) = \sqrt{\frac{E'+m}{2E'}} \sqrt{\frac{E+m}{2E}} \left(\chi_{\lambda'}^\dagger \vec{\sigma} \chi_\lambda \right) \cdot \left(\frac{\vec{p}'}{E'+m} - \frac{\vec{p}}{E+m} \right). \quad (\text{C.5})$$

Expanding to the lowest non-vanishing order in \vec{q} we find

$$\bar{u}_{\lambda'}^\nu(p') \gamma^5 u_\lambda^\nu(p) = \frac{\chi_{\lambda'}^\dagger \vec{\sigma} \chi_\lambda}{2E} \cdot \left[\vec{q} - \left(1 - \frac{m}{E} \right) (\hat{n} \cdot \vec{q}) \hat{n} \right], \quad (\text{C.6})$$

where \hat{n} denotes the neutrino direction. Introducing Eq. (C.6) in Eq. (C.3) and evaluating the \vec{q} integral in Eq. (C.1) one finds

$$V(\vec{r}) = - \frac{g_s^f g_p^\nu}{8\pi E} \left[\vec{S}_{\lambda\lambda'} - \left(1 - \frac{m}{E} \right) (\vec{S}_{\lambda\lambda'} \cdot \hat{n}) \hat{n} \right] \cdot \vec{\nabla}_r \left(\frac{e^{-m_\phi r}}{r} \right), \quad (\text{C.7})$$

where we have defined $\vec{S}_{\lambda\lambda'} \equiv \chi_{\lambda'}^\dagger \vec{\sigma} \chi_\lambda$ as a spin-like vector quantity. In the non-relativistic limit $\vec{S}_{\lambda\lambda'}$ corresponds to the spin of the neutrino, and Eq. (C.7) reduces to the well-known monopole-dipole potential [220]

$$V(r) = g_s^f g_p^\nu \frac{\hat{\sigma}_\nu \cdot \hat{r}}{8\pi m_\nu} \left[\frac{m_\phi}{r} + \frac{1}{r^2} \right] e^{-m_\phi r} \quad (\text{C.8})$$

where $\hat{\sigma}_\nu$ is the direction of the neutrino spin. Conversely for relativistic neutrinos one can identify λ with the helicity of the neutrino and using the explicit form of the spinors:

$$\vec{S}_{++} = -\vec{S}_{--} = \hat{n}, \quad \vec{S}_{+-} = \vec{S}_{-+}^* = \hat{u} + i\hat{v}, \quad (\text{with } \hat{n} \perp \hat{u} \perp \hat{v}) \quad (\text{C.9})$$

we get

$$V(\vec{r}) = -\frac{g_s^f g_p^\nu}{8\pi E} \left[\delta_{\lambda \neq \lambda'} (\vec{\nabla}_r)_\perp \pm \delta_{\lambda \lambda'} \frac{m}{E} (\vec{\nabla}_r)_\parallel \right] \left(\frac{e^{-m_\phi r}}{r} \right) \quad (\text{C.10})$$

where

$$(\vec{\nabla}_r)_\parallel \equiv \hat{n} \cdot \vec{\nabla}_r \quad \text{and} \quad (\vec{\nabla}_r)_\perp \equiv (\hat{u} + i\hat{v}) \cdot \vec{\nabla}_r \quad (\text{C.11})$$

are the gradient operators along and perpendicular to the neutrino direction respectively. We notice that Eq. (C.10) displays the relativistic $1/\gamma = m/E$ factor suppression of the helicity-conserving potential in analogy with the well-known results for the potential generated by a magnetic field in the presence of a neutrino magnetic moment [312, 313]. Conversely the scalar-pseudoscalar interaction produces a helicity-flip potential which is proportional to the variation of the potential in the direction perpendicular to that of the neutrino propagation.

We are interested in taking the Sun as a source of the potential and for that we integrate Eq. (C.10) with the number density of nucleon f at position $\vec{\rho}$ to obtain the potential at neutrino position \vec{x} to be

$$V(\vec{x}) = -\frac{g_s^f g_p^\nu}{8\pi E} \left[\delta_{\lambda \neq \lambda'} (\vec{\nabla}_x)_\perp \pm \delta_{\lambda \lambda'} \frac{m}{E} (\vec{\nabla}_x)_\parallel \right] \int N_f(\vec{\rho}) \frac{e^{-m_\phi |\vec{\rho} - \vec{x}|}}{|\vec{\rho} - \vec{x}|} d^3 \vec{\rho}. \quad (\text{C.12})$$

where we have replaced $\vec{\nabla}_r$ with $-\vec{\nabla}_\rho = \vec{\nabla}_x$ because the position of the neutrino is fixed in the integral.

List of Figures

2.1	Convention for the numbering of mass eigenstates and possible orderings (NO in left, IO in right). The colours indicate the amount of mixing between mass and flavour eigenstates as obtained from the global analysis of neutrino oscillation experiments as we will describe and quantify in Chapters 3 and 4	14
3.1	Neutrino fluxes predicted by the SSM[43] as a function of the neutrino energy. Figure extracted from [44].	25
3.2	Left: our choice of the energy resolution function, based on the relation between σ_h and \bar{N}_h inferred from the upper panel of Fig. 22 of Ref.[68]. Right: our reconstruction of solar spectra after the optimization of the energy scale function.	30
3.3	Spectrum for the best-fit normalizations of the different components obtained from our fit to the (upper panel) Borexino Phase II data for TFC-subtracted (left) and TFC-tagged events and (lower panel) Borexino Phase III data for TFC-subtracted (left) and TFC-tagged events.	31
3.4	Dependence of our $\Delta\chi^2$ for the fit to the Borexino phase-II spectra on the normalization of the solar fluxes and the dominant backgrounds (normalized to the corresponding best fit normalizations of the fit of the Borexino collaboration in Ref.[68]). For comparison we show as light blue curves the corresponding results of the determination of solar fluxes in Ref.[68]) (see text for details).	32
3.5	Constraints from our analysis of Borexino Phase-III spectra obtained with $\chi^2_{\text{BXIII, test}}$ in Eq. (3.15). Each panel shows a two-dimensional projection of the allowed multi-dimensional parameter space after minimization with respect to the undisplayed parameters. The regions correspond to 90% and 99% CL (2 d.o.f.). The curves in the right-most panels show the marginalized one-dimensional $\Delta\chi^2_{\text{BXIII, test}}$ for each of the parameters.	33
3.6	Dependence of $\Delta\chi^2$ of our fit to the Borexino Phase-III spectra on the common normalization of the CNO fluxes (red line). For comparison we plot (black dot-dashed line) the corresponding results in figure 2(b) of [70] for their “Fit w/ Systematics”, divided by the central value of the predicted CNO- ν rate of the B16-GS98 mode.	33
3.7	Left: CID posterior probabilities for the number for Phase-I and Phase-II+III of CNO- ν events after constraining pep and ^8B neutrino events to their SSM expectation. Right: Dependence of $\Delta\chi^2$ on the CNO flux normalization from our fit to the Borexino Phase-III spectra combined with the CID constraint (blue line) compared to that obtained by the Borexino collaboration (dotted black line). For comparison we also show the result without CID information (dashed black line).	35

3.8	Atmospheric neutrino flux at the Super-Kamiokande site, averaged over all directions and over one year. Extracted from Ref. [74].	37
3.9	Zenith-angle distribution of Super-Kamiokande neutrino events, comparing data (points) to expectations without (blue) and with (red) oscillations. A clear $\nu_\mu/\bar{\nu}_\mu$ disappearance is observed, enhanced for upward-going neutrinos. Events are categorized as Sub-GeV (< 1.33 GeV), Multi-GeV (> 1.33 GeV), or up-going muons (“UpStop”/“UpThrough” from rock interactions, the latter involving higher-energy neutrinos). Figure extracted from [79].	38
3.10	Reactor $\bar{\nu}_e$ spectrum, as measured by the Daya Bay collaboration [82]. . .	39
3.11	NOvA results as of June 2024 on ν_μ and $\bar{\nu}_\mu$ disappearance (upper panels) and ν_e and $\bar{\nu}_e$ appearance. The appearance events are classified in three bins from lowest to highest purity: Peripheral, Low PID, and High PID. Extracted from Ref.[98]	42
3.12	Validation of our simulation of NOvA. Each figure represents in green the information released by the collaboration in Ref. [98] while in black the corresponding results obtained with our simulations.	44
4.1	Global 3ν oscillation analysis. We show $\Delta\chi^2$ profiles minimized with respect to all undisplayed parameters. The red (blue) curves correspond to Normal (Inverted) Ordering. Solid and dashed curves correspond to the two variants of the analysis as described in the labels.	50
4.2	Global 3ν oscillation analysis. Each panel shows the two-dimensional projection of the allowed six-dimensional region after minimization with respect to the undisplayed parameters. The regions in the four lower panels are obtained from $\Delta\chi^2$ minimized with respect to the mass ordering. The different contours correspond to 1σ , 90%, 2σ , 99%, 3σ CL (2 dof). Colored regions (black contours) correspond to the variant with IC19 and without SK-atm (with IC24 and with SK-atm).	51
4.3	Dependence of the global $\Delta\chi^2$ function on the Jarlskog invariant. The red (blue) curves are for NO (IO). Solid (dashed) curves are for the «IC19 w/o SK-atm» («IC24 with SK-atm») $\Delta\chi^2$	52
4.4	Predicted number of events as a function of δ_{CP} for the T2K (left) and NOvA (right) appearance data sets. $\sin^2\theta_{23}$ varies between 0.44 and 0.58, where the lower-light (upper-dark) bound of the colored bands corresponds to 0.44 (0.58). Red (blue) bands correspond to NO (IO). For the other oscillation parameters we have adopted $\sin^2\theta_{13} = 0.0222$, $ \Delta m_{3\ell}^2 = 2.5 \times 10^{-3}$ eV ² , $\sin^2\theta_{12} = 0.32$, $\Delta m_{21}^2 = 7.5 \times 10^{-5}$ eV ² . The horizontal dashed lines show the observed number of events, with the $\pm 1\sigma$ statistical error indicated by the gray shaded band.	53
4.5	$\Delta\chi^2$ profiles as a function of δ_{CP} for different data sets and combinations as labeled in the figure. In the curves where the reactors R are not included in the combination we have fixed $\sin^2\theta_{13} = 0.0222$ as well as the solar parameters and minimized with respect to θ_{23} and $ \Delta m_{3\ell}^2 $. When the reactors are included θ_{13} is also marginalized. Left (right) panels are for IO (NO) and $\Delta\chi^2$ is shown with respect to the global best-fit point for each curve. Upper panels are for the NuFIT 5.0 data set, whereas lower panels correspond to the current update.	55

- 4.6 1σ and 2σ allowed regions (2 dof) for T2K (red shading), NOvA (blue shading) and their combination (black curves). Contours are defined with respect to the local minimum for IO (left) or NO (right). We fix $\sin^2 \theta_{13} = 0.0222$, $\sin^2 \theta_{12} = 0.31$, $\Delta m_{21}^2 = 7.5 \times 10^{-5} \text{ eV}^2$ and minimize with respect to $|\Delta m_{3\ell}^2|$ 57
- 4.7 Two-dimensional projection of the allowed six-dimensional region from global data in the plane of $(\delta_{\text{CP}}, \sin^2 \theta_{23})$ for IO (left) and NO (right) after minimization with respect to the undisplayed parameters. Regions for both orderings are defined with respect to the global best-fit point. The different contours correspond to 1σ , 90%, 2σ , 99%, 3σ CL (2 dof). Colored regions (black contours) correspond to the variant with IC19 and without SK-atm (with IC24 and with SK-atm). 57
- 4.8 Confidence regions at 95.45% CL (2 dof) in the plane of $\sin^2 \theta_{23}$ ($\sin^2 \theta_{13}$) and $\Delta m_{3\ell}^2$ in the left (right) panels. For the left panels we use both appearance and disappearance data from MINOS (green), NOvA (purple) and T2K (red), as well as atmospheric data from IC (orange) and Super-Kamiokande (light-brown); the colored region corresponds to the combination of these accelerator data with IC19, whereas the black-dashed contour corresponds to the combination with IC24 and Super-Kamiokande. A prior on θ_{13} is included to account for the reactor constraint. The right panels show regions using data from Daya-Bay (pink), Double-Chooz (magenta), RENO (violet), and their combination (black regions). In all panels solar, KamLAND and SNO+ data are included to constrain Δm_{21}^2 and θ_{12} . Contours are defined with respect to the global minimum of the two orderings for each data set. 59
- 4.9 $\Delta\chi^2$ profiles as a function of $\Delta m_{3\ell}^2$ for different data sets and combinations as labeled in the figures. In the curves where the reactors R are not included in the combination we have fixed $\sin^2 \theta_{13} = 0.0222$ as well as the solar parameters and minimized with respect to θ_{23} and δ_{CP} . When the reactors are included θ_{13} is also marginalized. $\Delta\chi^2$ is shown with respect to the global best-fit point (IO or NO) for each curve. The left set of panels visualizes the reactor/LBL combination, whereas in the right set of panels we are illustrating the impact of the IC19 or IC24 data sets. 60
- 4.10 p -values (top) and distributions (bottom) for the test statistic $T = \chi_{\text{IO},\text{min}}^2 - \chi_{\text{NO},\text{min}}^2$ corresponding to the «IC19 w/o SK-atm» analysis, assuming true NO (red) or true IO (blue). The observed value $T_{\text{obs}} = -0.6$ is shown by the solid vertical black line. The corresponding median values are shown by the dashed vertical lines. The green and yellow bands in the top panel—vertically displaced to avoid graphical overlap—correspond to the 1σ and 2σ intervals for T assuming NO (upwards displaced bands) and IO (downwards displaced bands). 61

- 4.11 Left: Allowed parameter regions (at 1σ , 90%, 2σ , 99%, and 3σ CL for 2 dof) from the combined analysis of solar data for MB22-met model (full regions with best fit marked by black star) and AAG21 model (dashed void contours with best fit marked by a white dot), and for the analysis of the combination of KamLAND and SNO+ data (solid green contours with best fit marked by a green star) for fixed $\sin^2 \theta_{13} = 0.0222$. For comparison we also show as orange contours the results obtained with the MB22-met model without including the results of the day-night variation in SK. Right: $\Delta\chi^2$ dependence on Δm_{21}^2 for the same four analyses after marginalizing over θ_{12} . In addition we show separately the results from KamLAND and SNO+. 62
- 4.12 Upper: 95% CL allowed ranges of the three probes of the absolute neutrino mass $\sum m_\nu$, m_{ν_e} , m_{ee} as a function of the mass of the lightest neutrino obtained from projecting the results of the global analysis of oscillation data. The regions are defined with respect to the minimum for each ordering. Lower: Corresponding 95% CL allowed regions (for 2 dof) in the planes $(m_{\nu_e}, \sum m_\nu)$, $(m_{ee}, \sum m_\nu)$, and (m_{ν_e}, m_{ee}) 63
- 5.1 Departure from the adiabatic regime in presence of NSI, for a solar mixing angle in the LMA region. The pale blue regions show the values of NSI parameters leading to $\gamma^{-1} > 1$, obtained from a numerical computation. The coloured lines show the values of NSI parameters where Eqs. (5.32) are satisfied at some point along the neutrino trajectory, for a neutrino produced at the center of the Sun. The different lines in the right panel correspond to neutrino energies between 1 MeV (green lines, at the left edge of the region) and 20 MeV (blue lines, towards the right edge). . . . 75
- 5.2 Isocontours of the potential V_{sp} sourced by nucleons with coupling g_s^N to ϕ felt by ν with coupling g_p^ν to ϕ as a function of b (its transverse distance to the line connecting the Sun and Earth centers) and z (the distance along the Sun-Earth direction characterizing its trajectory to the Earth) for several values of m_ϕ . For reference the black full and dashed lines represent the position of the edge of the Sun, $\sqrt{b^2 + z^2} = R_\odot$, and the outer edge of the solar core, $\sqrt{b^2 + z^2} = 0.3 R_\odot$, respectively. 83
- 5.3 Relevant oscillation probabilities at the Earth surface of solar ν_{eL} into left and right neutrinos (antineutrinos) of flavour α divided by $P(\nu_{eL} \rightarrow \nu_{\alpha L})_0$ (the probability for zero coupling to the ϕ field) as a function of the neutrino energy for different values of model parameters as labeled in the figure. Oscillation parameters have been fixed to $\Delta m_{21}^2 = 7.4 \times 10^{-5} \text{ eV}^2$, $\sin^2 \theta_{12} = 0.303$, $\sin^2 \theta_{13} = 0.02203$, $\Delta m_{31}^2 = 2.5 \times 10^{-3} \text{ eV}^2$, $\sin^2 \theta_{23} = 0.5$, and $\delta_{CP} = 0$ 85
- 6.1 Difference between the number of events with respect to the SM expectation, as a function of N_h . For reference, the black dots are obtained for the data in the “subtracted” sample, where the error bars indicate statistical errors only. The coloured lines correspond to the predicted event rates (using the same exposure as that of the “subtracted” sample) for different BSM scenarios and parameter values, as indicated by the labels. 88

6.2 Results for axial NSI with electrons ($\varepsilon_{\alpha\beta}^L = -\varepsilon_{\alpha\beta}^R$). The central panels show the two-dimensional allowed confidence regions at 1σ and 2σ (for 2 d.o.f., using two-sided intervals $\Delta\chi^2 = 2.30, 6.18$), while the remaining panels show the profile of the $\Delta\chi^2$ for each of the parameters individually. In each panel, the results are obtained after minimization over the parameters not shown. 89

6.3 Same as Fig. 6.2, but for vector NSI with electrons ($\varepsilon_{\alpha\beta}^L = \varepsilon_{\alpha\beta}^R$). 91

6.4 Results for the magnetic moment scenario, assuming three independent parameters (one for each of the SM neutrino flavours). Since the neutrino magnetic moment is positive definite, the cuts have been taken according to a one-sided χ^2 distribution. In the central panels, we show the allowed confidence regions (at 1σ and 2σ , for 2 d.o.f. using one-sided intervals) while in the right-most panels we show the profile of the $\Delta\chi^2$ for each of the parameters individually. In each panel, the results are obtained after minimization over the undisplayed parameters. 93

6.5 Bounds from our analysis of Borexino Phase II spectral data (at 90% CL for 1 d.o.f., using two-sided intervals, *i.e.*, $\Delta\chi^2 = 2.71$) on the vector mediators associated to a new $U(1)'$ symmetry, as indicated in the top label for each panel. Our results are compared to our derived bounds from GEMMA [192, 238], TEXONO [192, 247], COHERENT [242, 248, 249], and Dresden-II reactor experiment [242, 250], as well as those derived from a global fit to oscillation data [192], all of them obtained with the same statistical criterion. We also show the bounds from CONNIE [251] (95% CL) and CONUS [252] (90% CL) which we have obtained applying an overall rescaling factor to their published bounds on a universally coupled vector (see text for details). For the $B - L$ model, the line labelled “Borexino Rate Only” shows the approximate bound derived (at 95% CL, 1 d.o.f., for one-sided intervals) in Ref. [244] (see also Ref. [243]). 94

6.6 Bounds from our analysis of Borexino Phase-II spectral data on a scalar (left panel) and pseudoscalar (right panel) mediator (at 90% CL for 1 d.o.f., using two-sided intervals, *i.e.*, $\Delta\chi^2 = 2.71$) which couples universally to all fermions in the SM. Our results are compared to our derived bounds from GEMMA [192, 238], TEXONO [192, 247], COHERENT [242, 248, 249], and Dresden-II reactor experiment [242, 250], obtained using the same statistical criterion. For comparison we also show the bounds from CONNIE [251] (95 %CL) and CONUS [252] (90% CL). 95

6.7 Constraints on the coefficients for vector NSI with electrons from the global analysis of oscillation data *without including the effect of NSI in the detection cross section*. Each panel shows a two-dimensional projection of the allowed multi-dimensional parameter space after minimization with respect to the undisplayed parameters. The regions correspond to 1σ and 2σ (2 d.o.f.). 97

- 6.8 Constraints on the coefficients for vector NSI with electrons from the global analysis of oscillation data *including the effect of NSI in the ES cross section*. Each panel shows a two-dimensional projection of the allowed multi-dimensional parameter space after minimization with respect to the undisplayed parameters. The contours correspond to 1σ and 2σ (2 d.o.f.). The closed red regions correspond to the global oscillation analysis which involves the six NSI plus five oscillation parameters. For the sake of comparison we also show as green regions the constraints obtained from the analysis of full Borexino Phase-II spectrum in Figure 6.3. 99
- 6.9 Same as Fig. 6.8 but for Axial-vector NSI, compared with Fig. 6.2. . . . 100
- 6.10 Allowed regions in the plane of $\varepsilon_{ee}^{\oplus}$ and $\varepsilon_{\mu\mu}^{\oplus}$ for vector NSI with quarks from the combinations of CE ν NS data compared with the allowed regions from the global oscillation analysis which are the two diagonal shaded bands corresponding to the LMA and LMA-D solutions. Both the green and blue regions are obtained after *independently* marginalizing over all other relevant parameters: NSI couplings (including η) for the CE ν NS region, and NSI couplings, η and oscillation parameters for the «GLOB-OSC» regions. So the values of other NSI and η in the blue and green regions are not forced to be the same. 102
- 6.11 Constraints on the effective generalized NSI in the Earth matter (relevant for matter effects in LBL experiments) with arbitrary values of η and ζ . Each panel shows a two-dimensional projection of the allowed multi-dimensional parameter space after minimization with respect to the undisplayed parameters. The contours correspond to 1σ and 2σ (2 d.o.f.). . . . 105
- 6.12 Two-dimensional projections of the allowed regions (at 90% and 3σ CL) onto Δm_{12}^2 and θ_{12} parameters, after marginalizing over all other oscillation parameters and over NSI couplings to quarks and electrons. Red regions correspond to the analysis of KamLAND and Solar data; blue regions include all oscillation data; and green regions include all oscillation and CE ν NS data. In all cases, NSI effects on ES are fully accounted for in the fit. For comparison, the empty contours (solid black lines) show the corresponding regions for the global oscillation analysis without NSI. . . 106
- 6.13 Isocontours of $\chi_{\text{LMA}}^2(\eta, \zeta) - \chi_{\text{no-NSI}}^2$, $\chi_{\text{LMA-D}}^2(\eta, \zeta) - \chi_{\text{no-NSI}}^2$ and $\chi_{\text{LMA-D}}^2(\eta, \zeta) - \chi_{\text{LMA-D}}^2(\eta, \zeta)$ of the global analysis of oscillation data without including NSI in the ES cross sections at Borexino, SNO, and SK (upper panels), and including the NSI in the ES cross sections at Borexino, SNO, and SK (middle panels). The lower panels shows of the result adding the data from CE ν NS experiments. We show projections in the plane of angles (ζ, η) (after marginalization of all other parameters) which parametrize the relative strength of the NSI couplings to up-quarks, down-quark, and electrons. The levels corresponding to the different colours are given on the color bar on the right. Contours beyond 20 are white. In each panel the best-fit point is marked with a star (middle and bottom rows) or by a solid black line (upper row). Results in the upper row are applicable to NSI induced by mediators with $M_{\text{med}} \ll 500$ keV; in the middle row, for models with $M_{\text{med}} \gtrsim 10$ MeV; and in the lower row, for models with $M_{\text{med}} \gtrsim 50$ MeV, see Sec. 6.2.1 for details. 112
- 6.14 Dependence of $\chi_{\text{LMA-D}}^2(\eta, \zeta) - \chi_{\text{LMA}}^2(\eta, \zeta)$ on η after marginalizing over ζ for different combination of experiments as labeled in the figure. 113

- 6.15 Excluded region at 90% CL in the $(m_\phi, g_s^N g_p^{\nu\nu})$ plane by the global analysis of solar neutrino data after marginalization over the relevant oscillation parameters $(\Delta m_{21}^2, \theta_{12})$ while keeping the other oscillation parameters fixed as described in the text. Left (right) panel corresponds to Dirac (Majorana) neutrinos. For comparison we show as yellow region the bounds on the product of couplings from the product of the bound on g_s^N from violation of weak equivalent (VEP) principle and the bounds on g_p^ν from either kinematic and rare effects in weak decays in laboratory experiments (LAB) or cosmology bounds from cosmic microwave background (CMB). 113
- 6.16 $\Delta\chi^2 \equiv \chi^2(g_s^N g_p^{\nu\nu}) - \chi^2(g_s^N g_p^{\nu\nu} = 0)$ as a function of $g_s^N g_p^{\nu\nu}$ for $m_\phi \ll 10^{-15}$ eV fixing all oscillation parameters (in particular $\Delta m_{21}^2, \theta_{12}$ and θ_{23}) to their best-fit values. The left (central) panel show $\Delta\chi^2$ for each of the individual solar neutrino experiments for Dirac (Majorana) neutrinos and for the case of coupling to ν_U . In the central panel SNO and SNO' label the two variants of the SNO CC analysis for Majorana neutrinos (see text for details). The right panel show the global $\Delta\chi^2$ for four choices of the flavour dependence of the pseudoscalar-neutrino couplings; in particular, the black lines (coupling to ν_U) for Dirac and Majorana cases coincide with the corresponding "Glob" ones in left and central panels, respectively. . . 114
- 6.17 Left: Limits on $\bar{\nu}_e$ flux of astrophysical origin, as reported by KamLAND [277], Borexino [278] and Super-Kamiokande [279–281]. For comparison, we show the expected solar $\bar{\nu}_e$ flux for several values of the model parameters as labeled in the figure. Right: Excluded region on the $(m_\phi, g_s^N g_p^{\nu\nu})$ plane obtained for Majorana neutrinos obtained from the 90% CL constraint reported by KamLAND [277] and Borexino [278], Eqs. (6.10) and (6.11) (see text for details). For comparison we show as yellow region the bounds on the product of couplings from the product of the bound on g_s^N from violation of weak equivalent (VEP) principle and the bounds on g_p^ν from either kinematic and rare effects in weak decays in laboratory experiments (LAB) or cosmology bounds from cosmic microwave background (CMB). 114
- 7.1 Constraints from our global analysis on the solar neutrino fluxes for the analysis with luminosity constraint and fixed ratios of the CNO fluxes (see Eq. (7.13)). Each panel shows a two-dimensional projection of the allowed multidimensional parameter space after minimization with respect to the undisplayed parameters. The regions correspond to 90% and 99% CL (2 d.o.f.). The curves in the rightmost panels show the marginalized one-dimensional $\Delta\chi_{\text{wLC,CNO-Rfixed}}^2$ for each of the parameters. 121
- 7.2 Same as Fig. 7.1 but without imposing the luminosity constraint (see Eq. (7.17)). 123
- 7.3 Dependence of the determination of the pp and pep fluxes on the assumptions about the Gallium source experiments included in the analysis. The upper (lower) panels show the results of different variants of the analysis «CNO-Rfixed» with (without) luminosity constraint. See text for details. 124
- 7.4 One dimensional projections of the global $\Delta\chi^2$ of the for the three neutrino fluxes produced in the CNO-cycle for different assumptions as labeled in the figure. See text for details. 127
- 7.5 Marginalized one-dimensional probability distributions for the best determined solar fluxes in our analysis as compared to the predictions for the five SSMs in Ref. [146, 167]. 128

- 7.6 One-dimensional projection of the global $\Delta\chi^2$ on the mixing angle θ_{14} after marginalization over the undisplayed parameters, for different assumptions on the solar neutrino fluxes as labelled in the legend. The first (second) [third] column corresponds to the analysis including solar-only (solar+KamLAND-RFC) [solar+KamLAND-RFF] data. The upper (lower) panels show the results with $f_{\text{Ga}} = 1$ (free f_{Ga}). In all panels the black parabola is $\Delta\chi_{\text{Ga-source}}^2(\theta_{14})$ as inferred from the combined analysis of the Gallium source experiments presented in Ref. [133]. In the right-most lower panel we show the dependence of $\Delta\chi^2$ on the normalization parameter f_{Ga} 133
- 7.7 Two-dimensional projection of the global $\Delta\chi^2$ (for $f_{\text{GA}} = 1$) on the relevant oscillation parameters at 1σ , 2σ and 3σ after marginalization over the undisplayed parameters. The full red regions (void black contours) correspond to the analysis of solar data with MB-phot (free) fluxes, while the full green regions (void magenta contours) correspond to the KamLAND-RFC (KamLAND-RFF) fit. 136
- 7.8 Left: dependence of the 1σ , 2σ , 3σ ranges of $\sin^2\theta_{14}$ from the analysis of solar+KamLAND without imposing the constraint in Eq. (7.5) on the resulting neutrino-inferred solar luminosity. Fill (void) regions correspond to solar+KamLAND-RFC (solar+KamLAND-RFF) analysis. The horizontal grey regions illustrate the 1σ , 2σ , 3σ ranges required to explain the Gallium source results. Right: value of $\Delta\chi^2$ from the joint analysis of solar+KamLAND and Ga-source data, defined with respect to the sum of the two separate best-fit χ_{min}^2 , as a function of the neutrino-inferred solar luminosity. In these analysis we keep $f_{\text{GA}} = 1$ (see text for details). . . . 137
- B.1 Spectrum for the best-fit normalizations of the different components obtained from our fit to the Borexino Phase-III data for TFC-tagged (left) and TFC-subtracted (right) events. In this figure ‘‘CNO’’ labels the events produced by sum of the three fluxes produced in the CNO-cycle, $\Phi_{13\text{N}} + \Phi_{15\text{O}} + \Phi_{13\text{F}}$ 146
- B.2 Same as Fig. 3.5 but but allowing independent variation of the normalizations of the three CNO fluxes, only subject to the consistency conditions in Eqs. (7.10) and (7.11). 146
- B.3 Spectrum of events in the TFC-subtracted sample for the best-fit normalizations of the different components obtained from two fits to the Borexino Phase-III data. In the left panel the fit is performed assuming a common normalization shift for the 3 CNO fluxes, while on the right panel the three normalizations are allowed to vary free subject only the conditions Eqs. (7.10) and (7.11). 147
- B.4 Left: Spectra of subtracted event rates from best fit CNO fluxes and ^{210}Bi background in the range of $300 \leq N_h \leq 400$ for the ‘‘CNO’’ fit (fit with a common normalization factor for the three CNO fluxes, full lines) and the ‘‘N’’ fit (fit with three independent normalizations, dashed lines). We also show the best fit spectra for both fits compared to the data as labeled in the figure. Right: Difference of the value of χ^2 in both fits as a function of the maximum N_h bin included in the fit. 148

List of Tables

2.1	Quantum numbers for the different representations of the gauge group, associated to the Higgs boson and the fermions belonging to each family in the SM. Fermion families are ordered attending to their masses: the third one is the most massive, while the first one contains the lightest fermions.	5
3.1	Summary of experiments contributing to the present determination of the oscillation parameters in the 3ν framework (table taken from Ref. [79]). .	47
4.1	Three-flavor oscillation parameters from our fit to global data for the two variants of the analysis described in the text. The numbers in the 1st (2nd) column are obtained assuming NO (IO), i.e., relative to the respective local minimum. Note that $\Delta m_{3\ell}^2 \equiv \Delta m_{31}^2 > 0$ for NO and $\Delta m_{3\ell}^2 \equiv \Delta m_{32}^2 < 0$ for IO.	49
4.2	Normalization coefficients \mathcal{N}_ν and $\mathcal{N}_{\bar{\nu}}$ for T2K and NOvA appearance samples. Numbers in parentheses correspond to NuFIT 5.0.	54
4.3	Consistency test among different data sets, shown in the first column, assuming either normal or inverted ordering. “React” includes Daya-Bay, RENO and Double-Chooz. In the analyses above the horizontal line, θ_{13} is a free parameter, whereas below the line we have fixed $\sin^2 \theta_{13} = 0.0222$. See text for more details.	56
5.1	Charges for the vector, scalar, and pseudoscalar mediators considered in this work.	81
6.1	90% CL bounds (1 d.o.f., 2-sided) on the coefficients of NSI operators with electrons, for the vector (ε^V) and axial vector (ε^A) scenarios. Results are provided separately for two cases: when only one NSI operator is included at at time (“1 Parameter”) or when the remaining NSI coefficients are allowed to float freely in the fit (“Marginalized”).	90
6.2	Constraints at 90% CL (for 1 d.o.f., 2-sided) on the coefficients of NSI operators involving only left-handed (ε^L) or right-handed (ε^R) electrons. Results are provided separately for two cases: when only one NSI operator is included at at time (“1 Parameter”) or when the remaining NSI coefficients are allowed to float freely in the fit (“Marginalized”).	92

- 6.3 90% CL bounds (1 d.o.f., 2-sided) on the coefficients of NSI operators with electrons after marginalizing over all other NSI and oscillation parameters. The bounds are derived from the global analysis of oscillation data *without including the effect of NSI in the ES cross section* (NSI induced by mediators with mass $M_{\text{med}} \ll 500$ keV, see Sec. 6.2.1). The ranges in the first column (labeled «LMA») correspond to an analysis in which we restrict $\theta_{12} < 45^\circ$. In the second column (labeled «LMA \oplus LMA-D»), both $\theta_{12} < 45^\circ$ and $\theta_{12} > 45^\circ$ are allowed. The same bounds hold for vector NSI with protons. 98
- 6.4 90% CL bounds (1 d.o.f., 2-sided) on the coefficients of vector NSI operators with electrons after marginalizing over all other NSI and oscillation parameters. The bounds are derived from the global analysis of oscillation data *including the effect of NSI in the ES cross section*. For comparison, the results obtained from the analysis of Borexino Phase-II data in Ref. [2] are also shown for comparison. Note that these bounds apply to interactions induced by mediators with masses $M_{\text{med}} \gtrsim 10$ MeV, see Sec. 6.2.1. 98
- 6.5 90% allowed ranges for the vector NSI couplings $\varepsilon_{\alpha\beta}^{u,V}$ and $\varepsilon_{\alpha\beta}^{d,V}$ as obtained from the global analysis of oscillation data (left columns, applicable to NSI induced by mediators with $M_{\text{med}} \ll 5$ MeV) and also including data from CE ν NS experiments (right columns, applicable to NSI induced by mediators with $M_{\text{med}} \gtrsim 50$ MeV). The results are obtained after marginalizing over oscillation and the other matter potential parameters either within the LMA only ($\theta_{12} < 45^\circ$) and within both LMA ($\theta_{12} < 45^\circ$) and LMA-D ($\theta_{12} > 45^\circ$) subspaces respectively (this second case is denoted as LMA \oplus LMA-D). Notice that once CE ν NS data is included the two columns become identical, since for NSI couplings with $f = u, d$ the LMA-D solution is only allowed well above 90% CL. 101
- 6.6 90% CL bounds (1 d.o.f., 2-sided) on the effective axial-vector NSI couplings with quarks. The bounds are derived from the global analysis of oscillation data including the effect of NSI in the SNO NC cross section and *assuming only one NSI coupling different from zero at a time*. As explained in Sec. 6.2.1, these bounds apply to models with $M_{\text{med}} \gtrsim 3$ MeV. 103
- 6.7 90% and 99% CL bounds (1 d.o.f., 2-sided) on the effective NSI parameters relevant for matter effects in LBL experiments with arbitrary values of η and ζ , obtained after marginalizing over all other NSI and oscillation parameters. The bounds on the left (right) column are applicable to NSI induced by mediators with masses $M_{\text{med}} \ll 500$ keV ($M_{\text{med}} \gtrsim 50$ MeV). 104
- 6.8 Bounds from the different analysis in the two asymptotic regimes, effective infinite interaction range and contact range respectively, and for the four choices of flavour dependence. For the global solar analysis the bounds shown are obtained at 90% CL (1 dof, two-sided), $\Delta\chi^2 = 2.71$. The bounds from the antineutrino flux constraint are obtained from the 90% CL experimental constraints in Eq. (6.12). See text for details. 110
- 7.1 The reference neutrino fluxes Φ_i^{ref} used for normalization (from Ref. [146, 167]), the energy α_i provided to the star by nuclear fusion reactions associated with the i^{th} neutrino flux (taken from Ref. [296]), and the fractional contribution β_i of the i^{th} nuclear reaction to the total solar luminosity. 118

7.2	Results of the PG test for the different models and data samples considered. Within the given accuracy the results for MB22-met and MB22-phot models are the same.	130
7.3	Results of the PG test for the different solar flux model assumptions and the different analysis variants.	134

Bibliography

- [1] NuFit webpage. <http://www.nu-fit.org>.
- [2] Pilar Coloma, Pilar Coloma, M. C. Gonzalez-Garcia, M. C. Gonzalez-Garcia, Michele Maltoni, Michele Maltoni, João Paulo Pinheiro, João Paulo Pinheiro, Salvador Urrea, and Salvador Urrea. Constraining new physics with Borexino Phase-II spectral data. *JHEP*, 07:138, 2022. [Erratum: *JHEP* 11, 138 (2022)].
- [3] Pilar Coloma, M. C. Gonzalez-Garcia, Michele Maltoni, João Paulo Pinheiro, and Salvador Urrea. Global constraints on non-standard neutrino interactions with quarks and electrons. *JHEP*, 08:032, 2023.
- [4] Saeed Ansarifard, M. C. Gonzalez-Garcia, Michele Maltoni, and Joao Paulo Pinheiro. Solar neutrinos and leptonic spin forces. *JHEP*, 07:172, 2024.
- [5] M. C. Gonzalez-Garcia, Michele Maltoni, João Paulo Pinheiro, and Aldo M. Serenelli. Status of direct determination of solar neutrino fluxes after Borexino. *JHEP*, 02:064, 2024.
- [6] M. C. Gonzalez-Garcia, Michele Maltoni, and João Paulo Pinheiro. Solar model independent constraints on the sterile neutrino interpretation of the Gallium Anomaly. *Phys. Lett. B*, 862:139297, 2025.
- [7] Institute of Physics. Henri becquerel discovers radioactivity, 2024. Accessed: 2024-12-08.
- [8] Emilio Segrè. *From X-rays to Quarks: The Story of Atomic Physics*. W. H. Freeman and Company, San Francisco, 1980.
- [9] Klaus Winter, editor. *Neutrino Physics*. Cambridge University Press, Cambridge, UK, 2nd edition, 2000.
- [10] Rabindra N. Mohapatra and Palash B. Pal. *Massive Neutrinos in Physics and Astrophysics*, volume 72 of *World Scientific Lecture Notes in Physics*. World Scientific Publishing, Singapore, 3rd edition, 2004.
- [11] C. L. Cowan, F. Reines, F. B. Harrison, H. W. Kruse, and A. D. McGuire. Detection of the free neutrino: A Confirmation. *Science*, 124:103–104, 1956.
- [12] C. S. Wu, E. Ambler, R. W. Hayward, D. D. Hoppes, and R. P. Hudson. Experimental Test of Parity Conservation in β Decay. *Phys. Rev.*, 105:1413–1414, 1957.
- [13] Steven Weinberg. A model of leptons. *Physical Review Letters*, 19(21):1264–1266, 1967.

- [14] Abdus Salam. Elementary particle theory. *Nobel Symposium*, 8:367–377, 1968.
- [15] Sheldon L. Glashow. Partial-symmetries of weak interactions. *Nuclear Physics*, 22(4):579–588, 1961.
- [16] C. Patrignani and others (Particle Data Group). Review of particle physics. *Chinese Physics C*, 40(10):100001, 2016.
- [17] Ta-Pei Cheng and Ling-Fong Li. *Gauge theory of elementary particle physics*. Oxford University Press, 1984.
- [18] C. S. Wu, E. Ambler, R. W. Hayward, D. D. Hoppes, and R. P. Hudson. Experimental test of parity conservation in beta decay. *Physical Review*, 105(4):1413–1414, 1957.
- [19] T. D. Lee and C. N. Yang. Question of parity conservation in weak interactions. *Physical Review*, 104(1):254–258, 1956.
- [20] Murray Gell-Mann. Symmetries of baryons and mesons. *Physical Review*, 125(3):1067–1084, 1962.
- [21] Sheldon L. Glashow, John Iliopoulos, and Luciano Maiani. Weak interactions and quantum numbers. *Physical Review D*, 2(7):1285–1292, 1970.
- [22] Francis Halzen and Alan D. Martin. *Quarks and leptons: An introductory course in modern particle physics*. John Wiley & Sons, 1984.
- [23] Y. Fukuda et al. Evidence for oscillation of atmospheric neutrinos. *Phys. Rev. Lett.*, 81:1562–1567, 1998.
- [24] ALEPH Collaboration. Precision Electroweak Measurements on the Z Resonance. *Phys. Rept.*, 427:257–454, 2006.
- [25] ALEPH; DELPHI; L3; OPAL Collaborations and LEP EW Working Group. A Combination of Preliminary Electroweak Measurements and Constraints on the Standard Model. 2006.
- [26] C. Patrignani et al. Review of Particle Physics. *Chin. Phys. C*, 40:100001, 2016.
- [27] Ivan Esteban, M. C. Gonzalez-Garcia, Michele Maltoni, Ivan Martinez-Soler, João Paulo Pinheiro, and Thomas Schwetz. NuFit-6.0: Updated global analysis of three-flavor neutrino oscillations. 10 2024.
- [28] J. Schechter and J. W. F. Valle. Neutrino Masses in SU(2) x U(1) Theories. *Phys. Rev. D*, 22:2227, 1980.
- [29] M. Magg and C. Wetterich. Neutrino Mass Problem and Gauge Hierarchy. *Phys. Lett. B*, 94:61–64, 1980.
- [30] Rabindra N. Mohapatra and Goran Senjanovic. Neutrino Mass and Spontaneous Parity Nonconservation. *Phys. Rev. Lett.*, 44:912, 1980.
- [31] Steven Weinberg. Baryon and Lepton Nonconserving Processes. *Phys. Rev. Lett.*, 43:1566–1570, 1979.
- [32] Carlo Giunti and Chung W. Kim. *Fundamentals of Neutrino Physics and Astrophysics*. 2007.

- [33] M. C. Gonzalez-Garcia and Yosef Nir. Neutrino Masses and Mixing: Evidence and Implications. *Rev. Mod. Phys.*, 75:345–402, 2003.
- [34] L. Wolfenstein. Neutrino oscillations in matter. *Phys. Rev. D*, 17:2369, 1978.
- [35] S. P. Mikheev and A. Yu. Smirnov. Resonant Oscillations of Neutrinos in Matter and the Solar-Neutrino Problem. *Sov. Phys. JETP*, 64:4, 1986.
- [36] H. A. Bethe. A Possible Explanation of the Solar Neutrino Puzzle. *Phys. Rev. Lett.*, 56:1305, 1986.
- [37] M. Aker et al. Direct neutrino-mass measurement based on 259 days of KATRIN data. 6 2024.
- [38] M. Agostini et al. Final Results of GERDA on the Search for Neutrinoless Double- β Decay. *Phys. Rev. Lett.*, 125(25):252502, 2020.
- [39] S. Abe et al. Search for Majorana Neutrinos with the Complete KamLAND-Zen Dataset. 6 2024.
- [40] Jun-Qian Jiang, William Giarè, Stefano Gariazzo, Maria Giovanna Dainotti, Eleonora Di Valentino, Olga Mena, Davide Pedrotti, Simony Santos da Costa, and Sunny Vagnozzi. Neutrino cosmology after DESI: tightest mass upper limits, preference for the normal ordering, and tension with terrestrial observations. 7 2024.
- [41] Daniel Naredo-Tuero, Miguel Escudero, Enrique Fernández-Martínez, Xabier Marciano, and Vivian Poulin. Living at the Edge: A Critical Look at the Cosmological Neutrino Mass Bound. 7 2024.
- [42] A. G. Adame et al. DESI 2024 VI: Cosmological Constraints from the Measurements of Baryon Acoustic Oscillations. 4 2024.
- [43] John N. Bahcall, Aldo M. Serenelli, and Sarbani Basu. New solar opacities, abundances, helioseismology, and neutrino fluxes. *Astrophys. J. Lett.*, 621:L85–L88, 2005.
- [44] M. C. Gonzalez-Garcia and Michele Maltoni. Phenomenology with Massive Neutrinos. *Phys. Rept.*, 460:1–129, 2008.
- [45] Steen Hannestad, Rasmus Sloth Hansen, and Thomas Tram. How Self-Interactions can Reconcile Sterile Neutrinos with Cosmology. *Phys. Rev. Lett.*, 112(3):031802, 2014.
- [46] John N. Bahcall and Roger K. Ulrich. Solar Models, Neutrino Experiments and Helioseismology. *Rev. Mod. Phys.*, 60:297–372, 1988.
- [47] Sylvaine Turck-Chieze, S. Cahen, M. Casse, and C. Doom. Revisiting the standard solar model. *Astrophys. J.*, 335:415–424, 1988.
- [48] John N. Bahcall and M. H. Pinsonneault. Standard solar models, with and without helium diffusion and the solar neutrino problem. *Rev. Mod. Phys.*, 64:885–926, 1992.
- [49] John N. Bahcall and M. H. Pinsonneault. Solar models with helium and heavy element diffusion. *Rev. Mod. Phys.*, 67:781–808, 1995.

- [50] John N. Bahcall, M. H. Pinsonneault, and Sarbani Basu. Solar models: Current epoch and time dependences, neutrinos, and helioseismological properties. *Astrophys. J.*, 555:990–1012, 2001.
- [51] Carlos Pena-Garay and Aldo Serenelli. Solar neutrinos and the solar composition problem. 2008.
- [52] Aldo M. Serenelli, W. C. Haxton, and Carlos Pena-Garay. Solar models with accretion. I. Application to the solar abundance problem. *Astrophys. J.*, 743:24, 2011.
- [53] Núria Vinyoles, Aldo M. Serenelli, Francesco L. Villante, Sarbani Basu, Johannes Bergström, M. C. Gonzalez-Garcia, Michele Maltoni, Carlos Peña-Garay, and Ningqiang Song. A new Generation of Standard Solar Models. *Astrophys. J.*, 835(2):202, 2017.
- [54] Raymond Davis, Jr., Don S. Harmer, and Kenneth C. Hoffman. Search for neutrinos from the sun. *Phys. Rev. Lett.*, 20:1205–1209, 1968.
- [55] J. N. Abdurashitov et al. Measurement of the solar neutrino capture rate with gallium metal. III: Results for the 2002–2007 data-taking period. *Phys. Rev.*, C80:015807, 2009.
- [56] F. Kaether, W. Hampel, G. Heusser, J. Kiko, and T. Kirsten. Reanalysis of the GALLEX solar neutrino flux and source experiments. *Phys. Lett.*, B685:47–54, 2010.
- [57] K. S. Hirata et al. Observation of a small atmospheric muon-neutrino / electron-neutrino ratio in Kamiokande. *Phys. Lett. B*, 280:146–152, 1992.
- [58] K. S. Hirata et al. Observation of B-8 Solar Neutrinos in the Kamiokande-II Detector. *Phys. Rev. Lett.*, 63:16, 1989.
- [59] K. S. Hirata et al. Real time, directional measurement of B-8 solar neutrinos in the Kamiokande-II detector. *Phys. Rev. D*, 44:2241, 1991. [Erratum: *Phys.Rev.D* 45, 2170 (1992)].
- [60] J. Hosaka et al. Solar neutrino measurements in Super-Kamiokande-I. *Phys. Rev.*, D73:112001, 2006.
- [61] J.P. Cravens et al. Solar neutrino measurements in Super-Kamiokande-II. *Phys. Rev.*, D78:032002, 2008.
- [62] K. Abe et al. Solar neutrino results in Super-Kamiokande-III. *Phys. Rev.*, D83:052010, 2011.
- [63] K. Abe et al. Solar neutrino measurements using the full data period of Super-Kamiokande-IV. 12 2023.
- [64] B. Aharmim et al. Combined Analysis of all Three Phases of Solar Neutrino Data from the Sudbury Neutrino Observatory. 2011.
- [65] G. Bellini et al. Measurement of the solar 8B neutrino rate with a liquid scintillator target and 3 MeV energy threshold in the Borexino detector. *Phys. Rev. D*, 82:033006, 2010.

- [66] M. Agostini et al. Experimental evidence of neutrinos produced in the CNO fusion cycle in the Sun. *Nature*, 587:577–582, 2020.
- [67] G. Bellini et al. Precision measurement of the ^7Be solar neutrino interaction rate in Borexino. *Phys. Rev. Lett.*, 107:141302, 2011.
- [68] M. Agostini et al. First Simultaneous Precision Spectroscopy of pp , ^7Be , and pep Solar Neutrinos with Borexino Phase-II. *Phys. Rev. D*, 100(8):082004, 2019.
- [69] M. C. Gonzalez-Garcia, Michele Maltoni, and Jordi Salvado. Direct determination of the solar neutrino fluxes from solar neutrino data. *JHEP*, 05:072, 2010.
- [70] S. Appel et al. Improved Measurement of Solar Neutrinos from the Carbon-Nitrogen-Oxygen Cycle by Borexino and Its Implications for the Standard Solar Model. *Phys. Rev. Lett.*, 129(25):252701, 2022.
- [71] N. Rossi. Private communication, n.d.
- [72] BOREXINO collaboration. Improved measurement of solar neutrinos from the carbon-nitrogen-oxygen cycle by borexino and its implications for the standard solar model. <https://borex.lngs.infn.it/category/opendata/>. Accessed: August of 2023.
- [73] D. Basilico et al. Final results of Borexino on CNO solar neutrinos. *Phys. Rev. D*, 108(10):102005, 2023.
- [74] M. Honda, M. Sajjad Athar, T. Kajita, K. Kasahara, and S. Midorikawa. Atmospheric neutrino flux calculation using the NRLMSISE-00 atmospheric model. *Phys. Rev.*, D92(2):023004, 2015.
- [75] T. Wester et al. Atmospheric neutrino oscillation analysis with neutron tagging and an expanded fiducial volume in Super-Kamiokande I-V. 11 2023.
- [76] Atmospheric neutrino oscillation analysis with neutron tagging and an expanded fiducial volume in Super-Kamiokande I-V, 2024. ZENODO.
- [77] M. G. Aartsen et al. Measurement of Atmospheric Tau Neutrino Appearance with IceCube DeepCore. *Phys. Rev. D*, 99(3):032007, 2019.
- [78] M. G. Aartsen et al. Development of an analysis to probe the neutrino mass ordering with atmospheric neutrinos using three years of IceCube DeepCore data. *Eur. Phys. J. C*, 80(1):9, 2020.
- [79] S. Navas et al. Review of particle physics. *Phys. Rev. D*, 110(3):030001, 2024.
- [80] R. Abbasi et al. Measurement of atmospheric neutrino oscillation parameters using convolutional neural networks with 9.3 years of data in IceCube DeepCore. 5 2024.
- [81] Data release for neutrino oscillation parameters using convolutional neural networks with 9.3 years of data in icecube deepcore, 2024. .
- [82] Feng Peng An et al. Measurement of the Reactor Antineutrino Flux and Spectrum at Daya Bay. *Phys. Rev. Lett.*, 116(6):061801, 2016. [Erratum: *Phys.Rev.Lett.* 118, 099902 (2017)].

- [83] Y. Declais, J. Favier, A. Metref, H. Pessard, B. Achkar, et al. Search for neutrino oscillations at 15-meters, 40-meters, and 95-meters from a nuclear power reactor at Bugey. *Nucl.Phys.*, B434:503–534, 1995.
- [84] G. Zacek et al. Neutrino Oscillation Experiments at the Gosgen Nuclear Power Reactor. *Phys. Rev. D*, 34:2621–2636, 1986.
- [85] H. Kwon, F. Boehm, A.A. Hahn, H.E. Henrikson, J.L. Vuilleumier, et al. Search for neutrino oscillations at a fission reactor. *Phys.Rev.*, D24:1097–1111, 1981.
- [86] Y. J. Ko et al. Sterile Neutrino Search at the NEOS Experiment. *Phys. Rev. Lett.*, 118:121802, 2017.
- [87] I. Alekseev et al. Search for sterile neutrinos at the DANSS experiment. *Phys. Lett. B*, 787:56–63, 2018.
- [88] J. Ashenfelter et al. First search for short-baseline neutrino oscillations at HFIR with PROSPECT. *Phys. Rev. Lett.*, 121:251802, 2018.
- [89] H. Almazan Molina et al. Sterile Neutrino Constraints from the STEREO Experiment with 66 Days of Reactor-On Data. *Phys. Rev. Lett.*, 121:161801, 2019.
- [90] M. Apollonio et al. Limits on Neutrino Oscillations from the CHOOZ Experiment. *Phys. Lett.*, B466:415–430, 1999.
- [91] F. Boehm et al. Final results from the Palo Verde neutrino oscillation experiment. *Phys. Rev. D*, 64:112001, 2001.
- [92] F. P. An et al. Observation of electron-antineutrino disappearance at Daya Bay. *Phys. Rev. Lett.*, 108:171803, 2012.
- [93] F. P. An et al. Precision measurement of reactor antineutrino oscillation at kilometer-scale baselines by Daya Bay. 11 2022.
- [94] F. P. An et al. Antineutrino energy spectrum unfolding based on the Daya Bay measurement and its applications. *Chin. Phys. C*, 45(7):073001, 2021.
- [95] J. K. Ahn et al. Observation of Reactor Electron Antineutrino Disappearance in the RENO Experiment. *Phys. Rev. Lett.*, 108:191802, 2012.
- [96] Y. Abe et al. Indication of Reactor ν -e Disappearance in the Double Chooz Experiment. *Phys. Rev. Lett.*, 108:131801, 2012.
- [97] A. Gando et al. Reactor On-Off Antineutrino Measurement with KamLAND. *Phys. Rev.*, D88(3):033001, 2013.
- [98] Jeremy Wolcott. New NOvA Results with 10 Years of Data.
- [99] A. Himmel. New Oscillation Results from the NOvA Experiment. Talk given at the *XXIX International Conference on Neutrino Physics and Astrophysics*, Chicago, USA, June 22–July 2, 2020 (online conference).
- [100] Claudio Giganti. T2K experiment status and plans. Talk given at the *XXXI International Conference on Neutrino Physics and Astrophysics*, Milan, Italy, June 16–22, 2024.

- [101] K. Abe et al. Updated T2K measurements of muon neutrino and antineutrino disappearance using 3.6×10^{21} protons on target. *Phys. Rev. D*, 108(7):072011, 2023.
- [102] K. Abe et al. Measurements of neutrino oscillation parameters from the T2K experiment using 3.6×10^{21} protons on target. *Eur. Phys. J. C*, 83(9):782, 2023.
- [103] P. Adamson et al. Measurement of Neutrino and Antineutrino Oscillations Using Beam and Atmospheric Data in MINOS. *Phys. Rev. Lett.*, 110:251801, 2013.
- [104] P. Adamson et al. Electron neutrino and antineutrino appearance in the full MINOS data sample. *Phys. Rev. Lett.*, 2013.
- [105] F. Feroz and M. P. Hobson. Multinest: an efficient and robust bayesian inference tool for cosmology and particle physics. *Mon. Not. R. Astron. Soc.*, 398:1601–1614, 2009.
- [106] F. Feroz, M. P. Hobson, E. Cameron, and A. N. Pettitt. Importance nested sampling and the multinest algorithm. *arXiv preprint*, 2013.
- [107] M. Galassi et al. *GNU Scientific Library Reference Manual*. 3rd edition, 2009.
- [108] D. Akimov et al. Observation of Coherent Elastic Neutrino-Nucleus Scattering. *Science*, 357(6356):1123–1126, 2017.
- [109] Daniel Z. Freedman. Coherent effects of a weak neutral current. *Phys. Rev. D*, 9:1389–1392, 1974.
- [110] H. T. Wong and TEXONO Collaboration. The TEXONO research program on neutrino and astroparticle physics. *Mod. Phys. Lett. A*, 19:1207, 2004.
- [111] V. Belov et al. The GeN experiment at the kalinin nuclear power plant. *JINST*, 10:P12011, 2015.
- [112] A. Aguilar-Arevalo et al. The CONNIE experiment. *J. Phys. Conf. Ser.*, 761:012057, 2016.
- [113] G. Agnolet et al. Background studies for the MINER coherent neutrino scattering reactor experiment. *Nucl. Instrum. Meth. A*, 853:53, 2017.
- [114] J. Billard et al. Coherent neutrino scattering with low-temperature bolometers at Chooz reactor complex. *J. Phys. G*, 44:105101, 2017.
- [115] R. Strauss et al. The ν -cleus experiment: A gram-scale fiducial-volume cryogenic detector for the first detection of coherent neutrino-nucleus scattering. *Eur. Phys. J. C*, 77:506, 2017.
- [116] D. Y. Akimov et al. First ground-level laboratory test of the two-phase xenon emission detector RED-100. *JINST*, 15:P02020, 2020.
- [117] J. J. Choi. Neutrino elastic-scattering observation with NaI[Tl] (NEON). *PoS, NuFact2019:047*, 2020.
- [118] H. Bonet et al. Constraints on elastic neutrino nucleus scattering in the fully coherent regime from the CONUS experiment. *Phys. Rev. Lett.*, 126:041804, 2021.

- [119] J. Colaresi et al. First results from a search for coherent elastic neutrino-nucleus scattering at a reactor site. *Phys. Rev. D*, 104:072003, 2021.
- [120] NCC-1701 Collaboration. Improved constraints on $\bar{\nu}_{e\nu}$ s at the dresden-ii reactor with increased exposure. *Phys. Rev. D*, 107, 2023. Update with DOI/arXiv when available.
- [121] T. W. Donnelly and I. Sick. Nuclear structure from electron scattering. *Rev. Mod. Phys.*, 56:461, 1984.
- [122] Pilar Coloma, Ivan Esteban, M. C. Gonzalez-Garcia, and Michele Maltoni. Improved global fit to Non-Standard neutrino Interactions using COHERENT energy and timing data. *JHEP*, 02:023, 2020. [Addendum: *JHEP* 12, 071 (2020)].
- [123] D. K. Papoulias and T. S. Kosmas. Neutrino electromagnetic properties and $\bar{\nu}_{e\nu}$ s. *Phys. Rev. D*, 97:033003, 2018.
- [124] C. et al. Giunti. Sterile neutrinos and $\bar{\nu}_{e\nu}$ s anomalies. *Phys. Rev. D*, 101:035025, 2020.
- [125] D. Baxter et al. Coherent Elastic Neutrino-Nucleus Scattering at the European Spallation Source. 2019.
- [126] Carlo Giunti and Marco Laveder. Short-Baseline Active-Sterile Neutrino Oscillations? *Mod. Phys. Lett. A*, 22:2499–2509, 2007.
- [127] Marco Laveder. Unbound neutrino roadmaps. *Nucl. Phys. B Proc. Suppl.*, 168:344–346, 2007.
- [128] W. Hampel et al. Final results of the Cr-51 neutrino source experiments in GALLEX. *Phys. Lett. B*, 420:114–126, 1998.
- [129] J. N. Abdurashitov et al. Measurement of the response of the Russian-American gallium experiment to neutrinos from a Cr-51 source. *Phys. Rev. C*, 59:2246–2263, 1999.
- [130] J. N. Abdurashitov et al. Measurement of the response of a Ga solar neutrino experiment to neutrinos from an Ar-37 source. *Phys. Rev. C*, 73:045805, 2006.
- [131] J. N. Bahcall. Gallium solar neutrino experiments: Absorption cross-sections, neutrino spectra, and predicted event rates. *Phys. Rev. C*, 56:3391–3409, 1997.
- [132] V. V. Barinov et al. Results from the Baksan Experiment on Sterile Transitions (BEST). *Phys. Rev. Lett.*, 128(23):232501, 2022.
- [133] V. V. Barinov et al. Search for electron-neutrino transitions to sterile states in the BEST experiment. *Phys. Rev. C*, 105(6):065502, 2022.
- [134] S. R. Elliott, V. N. Gavrin, W. C. Haxton, T. V. Ibragimova, and E. J. Rule. Gallium neutrino absorption cross section and its uncertainty. *Phys. Rev. C*, 108(3):035502, 2023.
- [135] C. Giunti, Y. F. Li, C. A. Ternes, and Z. Xin. Inspection of the detection cross section dependence of the Gallium Anomaly. *Phys. Lett. B*, 842:137983, 2023.
- [136] S. Navas et al. Review of particle physics. *Phys. Rev. D*, 110(3):030001, 2024.

- [137] Jeffrey M. Berryman, Pilar Coloma, Patrick Huber, Thomas Schwetz, and Albert Zhou. Statistical significance of the sterile-neutrino hypothesis in the context of reactor and gallium data. *JHEP*, 02:055, 2022.
- [138] K. Goldhagen, M. Maltoni, S. E. Reichard, and T. Schwetz. Testing sterile neutrino mixing with present and future solar neutrino data. *Eur. Phys. J. C*, 82(2):116, 2022.
- [139] C. Giunti, Y. F. Li, C. A. Ternes, O. Tyagi, and Z. Xin. Gallium anomaly: critical view from the global picture of ν_e and $\bar{\nu}_e$ disappearance. *JHEP*, 10:164, 2022.
- [140] Vedran Brdar, Julia Gehrlein, and Joachim Kopp. Towards resolving the gallium anomaly. *JHEP*, 05:143, 2023.
- [141] Y. Farzan and T. Schwetz. A decoherence explanation of the gallium neutrino anomaly. *SciPost Phys.*, 15(4):172, 2023.
- [142] C. A. Argüelles, T. Bertólez-Martínez, and J. Salvado. Impact of wave packet separation in low-energy sterile neutrino searches. *Phys. Rev. D*, 107(3):036004, 2023.
- [143] J. M. Hardin, I. Martinez-Soler, A. Diaz, M. Jin, N. W. Kamp, C. A. Argüelles, J. M. Conrad, and M. H. Shaevitz. New clues about light sterile neutrinos: preference for models with damping effects in global fits. *JHEP*, 09:058, 2023.
- [144] H. Banks, K. J. Kelly, M. McCullough, and T. Zhou. Broad sterile neutrinos & the reactor/gallium tension. *JHEP*, 04:096, 2024.
- [145] C. Giunti and C. A. Ternes. Confronting solutions of the gallium anomaly with reactor rate data. *Phys. Lett. B*, 849:138436, 2024.
- [146] Y. Herrera and A. Serenelli. Standard Solar Models B23 / SF-III, 2023. ZENODO.
- [147] B. T. Cleveland et al. Measurement of the solar electron neutrino flux with the Homestake chlorine detector. *Astrophys. J.*, 496:505–526, 1998.
- [148] G. Bellini et al. Measurement of the solar 8B neutrino rate with a liquid scintillator target and 3 MeV energy threshold in the Borexino detector. *Phys. Rev.*, D82:033006, 2010.
- [149] A. Allega et al. Initial measurement of reactor antineutrino oscillation at SNO+. 5 2024.
- [150] Sofia Andringa. Reactor Antineutrino Oscillations and Geoneutrinos in SNO+. Poster 525 at the *XXXI International Conference on Neutrino Physics and Astrophysics*, Milan, Italy, June 16–22, 2024.
- [151] Jose Maneira. Solar Neutrinos: Recent Results and Prospects. Talk given at the *XXXI International Conference on Neutrino Physics and Astrophysics*, Milan, Italy, June 16–22, 2024.
- [152] T. Bezerra. New Results from the Double Chooz Experiment. Talk given at the *XXIX International Conference on Neutrino Physics and Astrophysics*, Chicago, USA, June 22–July 2, 2020 (online conference).

- [153] J. Yoo. RENO. Talk given at the *XXIX International Conference on Neutrino Physics and Astrophysics*, Chicago, USA, June 22–July 2, 2020 (online conference).
- [154] Ivan Esteban, M. C. Gonzalez-Garcia, Alvaro Hernandez-Cabezudo, Michele Maltoni, and Thomas Schwetz. Global analysis of three-flavour neutrino oscillations: synergies and tensions in the determination of θ_{23} , δ_{CP} , and the mass ordering. *JHEP*, 01:106, 2019.
- [155] M. C. Gonzalez-Garcia and Carlos Pena-Garay. Three neutrino mixing after the first results from K2K and KamLAND. *Phys. Rev.*, D68:093003, 2003.
- [156] C. Jarlskog. Commutator of the Quark Mass Matrices in the Standard Electroweak Model and a Measure of Maximal CP Violation. *Phys.Rev.Lett.*, 55:1039, 1985.
- [157] Jessica Elevant and Thomas Schwetz. On the determination of the leptonic CP phase. *JHEP*, 09:016, 2015.
- [158] M. Maltoni and T. Schwetz. Testing the Statistical Compatibility of Independent Data Sets. *Phys. Rev.*, D68:033020, 2003.
- [159] Hiroshi Nunokawa, Stephen J. Parke, and Renata Zukanovich Funchal. Another possible way to determine the neutrino mass hierarchy. *Phys. Rev.*, D72:013009, 2005.
- [160] H. Minakata, H. Nunokawa, Stephen J. Parke, and R. Zukanovich Funchal. Determining Neutrino Mass Hierarchy by Precision Measurements in Electron and Muon Neutrino Disappearance Experiments. *Phys. Rev.*, D74:053008, 2006.
- [161] Mattias Blennow, Pilar Coloma, Patrick Huber, and Thomas Schwetz. Quantifying the sensitivity of oscillation experiments to the neutrino mass ordering. *JHEP*, 03:028, 2014.
- [162] X. Qian, A. Tan, W. Wang, J. J. Ling, R. D. McKeown, and C. Zhang. Statistical Evaluation of Experimental Determinations of Neutrino Mass Hierarchy. *Phys. Rev. D*, 86:113011, 2012.
- [163] N. Grevesse and A. J. Sauval. Standard Solar Composition. *Space Sci. Rev.*, 85:161–174, May 1998.
- [164] Martin Asplund, Nicolas Grevesse, A. Jacques Sauval, and Pat Scott. The Chemical Composition of the Sun. *ARA&A*, 47(1):481–522, September 2009.
- [165] Aldo Serenelli, Sarbani Basu, Jason W. Ferguson, and Martin Asplund. New Solar Composition: The Problem With Solar Models Revisited. *Astrophys. J.*, 705:L123–L127, 2009.
- [166] M. Asplund, A. M. Amarsi, and N. Grevesse. The chemical make-up of the Sun: A 2020 vision. *arXiv e-prints*, page arXiv:2105.01661, May 2021.
- [167] Ekaterina Magg et al. Observational constraints on the origin of the elements - IV. Standard composition of the Sun. *Astron. Astrophys.*, 661:A140, 2023.
- [168] G. L. Fogli, E. Lisi, A. Marrone, A. Melchiorri, A. Palazzo, P. Serra, and J. Silk. Observables sensitive to absolute neutrino masses: Constraints and correlations from world neutrino data. *Phys. Rev.*, D70:113003, 2004.

- [169] S. Pascoli, S. T. Petcov, and T. Schwetz. The Absolute Neutrino Mass Scale, Neutrino Mass Spectrum, Majorana Cp-Violation and Neutrinoless Double-Beta Decay. *Nucl. Phys.*, B734:24–49, 2006.
- [170] Stefano Gariazzo et al. Neutrino mass and mass ordering: no conclusive evidence for normal ordering. *JCAP*, 10:010, 2022.
- [171] Adam Falkowski, Martín González-Alonso, Joachim Kopp, Yotam Soreq, and Zahra Tabrizi. EFT at FASER ν . *JHEP*, 10:086, 2021.
- [172] Víctor Bresó-Pla, Adam Falkowski, Martín González-Alonso, and Kevin Monsálvez-Pozo. EFT analysis of New Physics at COHERENT. 1 2023.
- [173] Adam Falkowski, Martín González-Alonso, and Zahra Tabrizi. Consistent QFT description of non-standard neutrino interactions. *JHEP*, 11:048, 2020.
- [174] Adam Falkowski, Martín González-Alonso, and Zahra Tabrizi. Reactor neutrino oscillations as constraints on Effective Field Theory. *JHEP*, 05:173, 2019.
- [175] S. Davidson, C. Pena-Garay, N. Rius, and A. Santamaria. Present and future bounds on nonstandard neutrino interactions. *JHEP*, 03:011, 2003.
- [176] Carla Biggio, Mattias Blennow, and Enrique Fernandez-Martinez. General bounds on non-standard neutrino interactions. *JHEP*, 08:090, 2009.
- [177] Carla Biggio, Mattias Blennow, and Enrique Fernandez-Martinez. Loop bounds on non-standard neutrino interactions. *JHEP*, 03:139, 2009.
- [178] M. B. Gavela, D. Hernandez, T. Ota, and W. Winter. Large gauge invariant non-standard neutrino interactions. *Phys. Rev.*, D79:013007, 2009.
- [179] Stefan Antusch, Jochen P. Baumann, and Enrique Fernandez-Martinez. Non-Standard Neutrino Interactions with Matter from Physics Beyond the Standard Model. *Nucl. Phys.*, B810:369–388, 2009.
- [180] P. S. Bhupal Dev et al. Neutrino Non-Standard Interactions: A Status Report. In *NTN Workshop on Neutrino Non-Standard Interactions St Louis, MO, USA, May 29-31, 2019*, 2019.
- [181] K. S. Babu, A. Friedland, P. A. N. Machado, and I. Mocioiu. Flavor Gauge Models Below the Fermi Scale. *JHEP*, 12:096, 2017.
- [182] Yasaman Farzan. A model for large non-standard interactions of neutrinos leading to the LMA-Dark solution. *Phys. Lett. B*, 748:311–315, 2015.
- [183] Yasaman Farzan and Julian Heck. Neutrinophilic nonstandard interactions. *Phys. Rev. D*, 94(5):053010, 2016.
- [184] Yasaman Farzan and Ian M. Shoemaker. Lepton Flavor Violating Non-Standard Interactions via Light Mediators. *JHEP*, 07:033, 2016.
- [185] Admir Greljo, Peter Stangl, Anders Eller Thomsen, and Jure Zupan. On $(g - 2)_\mu$ from gauged $U(1)_X$. *JHEP*, 07:098, 2022.
- [186] Julian Heck, Manfred Lindner, Werner Rodejohann, and Stefan Vogl. Non-Standard Neutrino Interactions and Neutral Gauge Bosons. *SciPost Phys.*, 6(3):038, 2019.

- [187] Y. Farzan. A model for lepton flavor violating non-standard neutrino interactions. *Phys. Lett. B*, 803:135349, 2020.
- [188] Nicolás Bernal and Yasaman Farzan. Neutrino nonstandard interactions with arbitrary couplings to u and d quarks. *Phys. Rev. D*, 107(3):035007, 2023.
- [189] K. S. Babu, P. S. Bhupal Dev, Sudip Jana, and Anil Thapa. Non-Standard Interactions in Radiative Neutrino Mass Models. *JHEP*, 03:006, 2020.
- [190] Mark B. Wise and Yue Zhang. Effective Theory and Simple Completions for Neutrino Interactions. *Phys. Rev. D*, 90(5):053005, 2014.
- [191] Admir Greljo, Yotam Soreq, Peter Stangl, Anders Eller Thomsen, and Jure Zupan. Muonic force behind flavor anomalies. *JHEP*, 04:151, 2022.
- [192] Pilar Coloma, M. C. Gonzalez-Garcia, and Michele Maltoni. Neutrino oscillation constraints on $U(1)'$ models: from non-standard interactions to long-range forces. *JHEP*, 01:114, 2021. [Erratum: *JHEP* 11, 115 (2022)].
- [193] L. Wolfenstein. Neutrino Oscillations in Matter. *Phys. Rev.*, D17:2369–2374, 1978.
- [194] S. P. Mikheev and A. Yu. Smirnov. Resonance enhancement of oscillations in matter and solar neutrino spectroscopy. *Sov. J. Nucl. Phys.*, 42:913–917, 1985.
- [195] M. C. Gonzalez-Garcia and Michele Maltoni. Determination of matter potential from global analysis of neutrino oscillation data. *JHEP*, 09:152, 2013.
- [196] Ivan Esteban, M. C. Gonzalez-Garcia, Michele Maltoni, Ivan Martinez-Soler, and Jordi Salvado. Updated constraints on non-standard interactions from global analysis of oscillation data. *JHEP*, 08:180, 2018. [Addendum: *JHEP* 12, 152 (2020)].
- [197] J. W. F. Valle. Resonant Oscillations of Massless Neutrinos in Matter. *Phys. Lett.*, B199:432–436, 1987.
- [198] M. M. Guzzo, A. Masiero, and S. T. Petcov. On the MSW effect with massless neutrinos and no mixing in the vacuum. *Phys. Lett.*, B260:154–160, 1991.
- [199] O. G. Miranda, M. A. Tortola, and J. W. F. Valle. Are solar neutrino oscillations robust? *JHEP*, 10:008, 2006.
- [200] M. C. Gonzalez-Garcia, Michele Maltoni, and Jordi Salvado. Testing matter effects in propagation of atmospheric and long-baseline neutrinos. *JHEP*, 05:075, 2011.
- [201] Pouya Bakhti and Yasaman Farzan. Shedding light on LMA-Dark solar neutrino solution by medium baseline reactor experiments: JUNO and RENO-50. *JHEP*, 07:064, 2014.
- [202] Pilar Coloma and Thomas Schwetz. Generalized mass ordering degeneracy in neutrino oscillation experiments. *Phys. Rev.*, D94(5):055005, 2016.
- [203] Dorian W. P. Amaral, David Cerdeno, Andrew Cheek, and Patrick Foldenauer. A direct detection view of the neutrino NSI landscape. 2 2023.
- [204] A.M. Dziewonski and D.L. Anderson. Preliminary reference earth model. *Phys. Earth Planet. Interiors*, 25:297–356, 1981.

- [205] Alexander Friedland, Cecilia Lunardini, and Michele Maltoni. Atmospheric neutrinos as probes of neutrino-matter interactions. *Phys.Rev.*, D70:111301, 2004.
- [206] Kate Scholberg. Prospects for measuring coherent neutrino-nucleus elastic scattering at a stopped-pion neutrino source. *Phys. Rev. D*, 73:033005, 2006.
- [207] J. Barranco, O. G. Miranda, C. A. Moura, and J. W. F. Valle. Constraining non-standard interactions in $\nu(e)e$ or $\bar{\nu}(e)e$ scattering. *Phys. Rev. D*, 73:113001, 2006.
- [208] J. Barranco, O. G. Miranda, and T. I. Rashba. Probing New Physics with Coherent Neutrino Scattering Off Nuclei. *JHEP*, 12:021, 2005.
- [209] J. Barranco, O. G. Miranda, C. A. Moura, and J. W. F. Valle. Constraining non-standard neutrino-electron interactions. *Phys. Rev. D*, 77:093014, 2008.
- [210] A. Bolanos, O. G. Miranda, A. Palazzo, M. A. Tortola, and J. W. F. Valle. Probing non-standard neutrino-electron interactions with solar and reactor neutrinos. *Phys. Rev. D*, 79:113012, 2009.
- [211] F. J. Escrivuela, O. G. Miranda, M. A. Tortola, and J. W. F. Valle. Constraining nonstandard neutrino-quark interactions with solar, reactor and accelerator data. *Phys. Rev.*, D80:105009, 2009. [Erratum: *Phys. Rev.*D80,129908(2009)].
- [212] Julia Gehrlein, Pedro A. N. Machado, and João Paulo Pinheiro. Constraining non-standard neutrino interactions with neutral current events at long-baseline oscillation experiments. 12 2024.
- [213] John N. Bahcall, Marc Kamionkowski, and Alberto Sirlin. Solar neutrinos: Radiative corrections in neutrino - electron scattering experiments. *Phys. Rev. D*, 51:6146–6158, 1995.
- [214] John N. Bahcall, K. Kubodera, and S. Nozawa. Neutral Current Reactions of Solar and Supernova Neutrinos on Deuterium. *Phys. Rev. D*, 38:1030, 1988.
- [215] J. Bernabeu, Torleif Erik Oskar Ericson, E. Hernandez, and J. Ros. Effects of the axial isoscalar neutral current for solar neutrino detection. *Nucl. Phys. B*, 378:131–149, 1992.
- [216] Jiunn-Wei Chen, Karsten M. Heeger, and R. G. Hamish Robertson. Constraining the leading weak axial two-body current by SNO and super-K. *Phys. Rev. C*, 67:025801, 2003.
- [217] P. Vogel and J. Engel. Neutrino electromagnetic form-factors. *Phys. Rev. D*, 39:3378, 1989.
- [218] David G. Cerdeño, Malcolm Fairbairn, Thomas Jubb, Pedro A. N. Machado, Aaron C. Vincent, and Céline Boehm. Physics from solar neutrinos in dark matter direct detection experiments. *JHEP*, 05:118, 2016. [Erratum: *JHEP* 09, 048 (2016)].
- [219] Manfred Lindner, Farinaldo S. Queiroz, Werner Rodejohann, and Xun-Jie Xu. Neutrino-electron scattering: general constraints on Z' and dark photon models. *JHEP*, 05:098, 2018.
- [220] J. E. Moody and F. Wilczek. New macroscopic forces? *Phys. Rev. D*, 30:130, 1984.

- [221] J. A. Grifols and E. Masso. Long range forces from pseudoscalar exchange. *Phys. Lett. B*, 579:123, 2004.
- [222] A. S. Joshipura and S. Mohanty. Long range leptonic forces and neutrino oscillations. *Phys. Rev. D*, 69:033006, 2004.
- [223] M. C. Gonzalez-Garcia, M. Maltoni, et al. Atmospheric neutrino oscillations and new physics. *Phys. Rev. D*, 75:033007, 2007.
- [224] H. Davoudiasl et al. Neutrino masses from a pseudo-nambu-goldstone boson. *Phys. Rev. D*, 84:095019, 2011.
- [225] M. B. Wise and Y. Zhang. Effective field theory approach to transient phenomena. *Phys. Rev. D*, 98:036006, 2018.
- [226] A. Yu. Smirnov et al. Neutrino flavor conversions in astrophysical environments. *Rev. Mod. Phys.*, 91:045004, 2019.
- [227] E. Kh. Akhmedov. Resonant amplification of neutrino spin rotation in matter. *Phys. Lett. B*, 213:64, 1988.
- [228] C. S. Lim and W. J. Marciano. Resonant Spin - Flavor Precession of Solar and Supernova Neutrinos. *Phys. Rev. D*, 37:1368, 1988.
- [229] A. Cisneros. Effect of neutrino magnetic moment on solar neutrino observations. *Astrophys. Space Sci.*, 10:87, 1971.
- [230] L. B. Okun et al. Neutrino electrodynamics and possible effects for solar neutrinos. *Sov. Phys. JETP*, 65:214, 1987.
- [231] L. B. Okun, M. B. Voloshin, and M. I. Vysotsky. Neutrino Electrodynamics and Possible Effects for Solar Neutrinos. *Sov. Phys. JETP*, 64:446, 1986. [*Zh. Eksp. Teor. Fiz.* 91 (1986) 754].
- [232] L. B. Okun et al. Neutrino spin rotation in matter. *Sov. Phys. JETP*, 65:221, 1987.
- [233] M. B. Voloshin et al. Neutrino magnetic moment and time variation of solar neutrino flux. *Sov. J. Nucl. Phys.*, 44:440, 1986.
- [234] P. Agrawal et al. Probing the muon $g-2$ anomaly with polarized electron scattering. *Phys. Rev. D*, 106:115017, 2022.
- [235] H. Davoudiasl et al. Muon $g-2$ and relic dark matter with pseudoscalar-mediated interactions. *Phys. Rev. D*, 106:035025, 2022.
- [236] S. K. Agarwalla et al. Constraints on flavor-diagonal non-standard neutrino interactions from Borexino Phase-II. *JHEP*, 02:038, 2020.
- [237] Borexino Collaboration. Limits on neutrino magnetic moments from borexino phase-ii. *Phys. Rev. D*, 96:091103, 2017.
- [238] A.G. Beda, V.B. Brudanin, V.G. Egorov, D.V. Medvedev, V.S. Pogosov, M.V. Shirchenko, and A.S. Starostin. Upper limit on the neutrino magnetic moment from three years of data from the GEMMA spectrometer. 5 2010.

- [239] A. G. Beda, V. B. Brudanin, V. G. Egorov, D. V. Medvedev, V. S. Pogosov, M. V. Shirchenko, and A. S. Starostin. The results of search for the neutrino magnetic moment in GEMMA experiment. *Adv. High Energy Phys.*, 2012:350150, 2012.
- [240] TEXONO Collaboration. Measurement of $\bar{\nu}_e$ - e^- scattering cross section with a csi(tl) scintillating crystal array at the kuo-sheng nuclear power reactor. *Phys. Rev. D*, 81:072001, 2010.
- [241] H. Bonet et al. First limits on neutrino electromagnetic properties from the CONUS experiment. 1 2022.
- [242] Pilar Coloma, Ivan Esteban, M. C. Gonzalez-Garcia, Leire Larizgoitia, Francesc Monrabal, and Sergio Palomares-Ruiz. Bounds on new physics with data of the Dresden-II reactor experiment and COHERENT. 2 2022.
- [243] R. Harnik et al. Neutrino mixing and neutrino oscillations in non-standard interactions. *JHEP*, 11:111, 2012.
- [244] S. Bilmis et al. Constraints on neutrino electromagnetic properties from neutrino-electron scattering. *Phys. Rev. D*, 92:033009, 2015.
- [245] Yuya Kaneta and Takashi Shimomura. On the possibility of a search for the $L_\mu - L_\tau$ gauge boson at Belle-II and neutrino beam experiments. *PTEP*, 2017(5):053B04, 2017.
- [246] Martin Bauer, Patrick Foldenauer, and Joerg Jaeckel. Hunting All the Hidden Photons. *JHEP*, 07:094, 2018.
- [247] M. Deniz et al. Measurement of $\text{Nu}(e)\text{-bar}$ -Electron Scattering Cross-Section with a CsI(Tl) Scintillating Crystal Array at the Kuo-Sheng Nuclear Power Reactor. *Phys. Rev. D*, 81:072001, 2010.
- [248] D. Akimov et al. Observation of Coherent Elastic Neutrino-Nucleus Scattering. *Science*, 357(6356):1123–1126, 2017.
- [249] D. Akimov et al. First Measurement of Coherent Elastic Neutrino-Nucleus Scattering on Argon. *Phys. Rev. Lett.*, 126(1):012002, 2021.
- [250] J. Colaresi, J. I. Collar, T. W. Hossbach, C. M. Lewis, and K. M. Yocum. Suggestive evidence for Coherent Elastic Neutrino-Nucleus Scattering from reactor antineutrinos. 2 2022.
- [251] CONNIE Collaboration. Results from the connie experiment. *J. Phys. Conf. Ser.*, 1468:012142, 2020.
- [252] H. Bonet et al. Novel constraints on neutrino physics beyond the standard model from the CONUS experiment. 10 2021.
- [253] M. Rink and others (CONUS Collaboration). Improved constraints on neutrino electromagnetic properties from conus. 2022.
- [254] Ivan Esteban, M. C. Gonzalez-Garcia, Michele Maltoni, Thomas Schwetz, and Albert Zhou. NuFIT 5.2 (2022). <http://www.nu-fit.org>.
- [255] Y. Nakajima. Recent results and future prospects from Super-Kamiokande. Talk given at the *XXIX International Conference on Neutrino Physics and Astrophysics*, Chicago, USA, June 22–July 2, 2020 (online conference).

- [256] B. Aharmim et al. Measurement of the ν/e and total B-8 solar neutrino fluxes with the Sudbury Neutrino Observatory phase I data set. *Phys. Rev.*, C75:045502, 2007.
- [257] B. Aharmim et al. Electron energy spectra, fluxes, and day-night asymmetries of B-8 solar neutrinos from the 391-day salt phase SNO data set. *Phys. Rev.*, C72:055502, 2005.
- [258] B. Aharmim et al. An Independent Measurement of the Total Active 8B Solar Neutrino Flux Using an Array of ^3He Proportional Counters at the Sudbury Neutrino Observatory. *Phys. Rev. Lett.*, 101:111301, 2008.
- [259] Feng Peng An et al. Improved Measurement of the Reactor Antineutrino Flux and Spectrum at Daya Bay. *Chin. Phys.*, C41(1):013002, 2017.
- [260] Roger Wendell. Atmospheric Results from Super-Kamiokande. *AIP Conf. Proc.*, 1666:100001, 2015. slides available at <https://indico.fnal.gov/event/8022/other-view?view=standard>.
- [261] M. G. Aartsen et al. Determining neutrino oscillation parameters from atmospheric muon neutrino disappearance with three years of IceCube DeepCore data. *Phys. Rev.*, D91(7):072004, 2015.
- [262] J. P. Yañez et al. IceCube Oscillations: 3 years muon neutrino disappearance data. http://icecube.wisc.edu/science/data/nu_osc.
- [263] M. G. Aartsen et al. Searches for Sterile Neutrinos with the IceCube Detector. *Phys. Rev. Lett.*, 117(7):071801, 2016.
- [264] P. Dunne. Latest Neutrino Oscillation Results from T2K. Talk given at the *XXIX International Conference on Neutrino Physics and Astrophysics*, Chicago, USA, June 22–July 2, 2020 (online conference) doi.org/10.5281/zenodo.3959558.
- [265] D. Akimov et al. COHERENT Collaboration data release from the first observation of coherent elastic neutrino-nucleus scattering. 4 2018.
- [266] D. Akimov et al. COHERENT Collaboration data release from the first detection of coherent elastic neutrino-nucleus scattering on Argon. 6 2020.
- [267] J. I. Collar, A. R. L. Kavner, and C. M. Lewis. Response of CsI[Na] to Nuclear Recoils: Impact on Coherent Elastic Neutrino-Nucleus Scattering ($\text{CE}\nu\text{NS}$). *Phys. Rev. D*, 100(3):033003, 2019.
- [268] P. Klos, J. Menéndez, D. Gazit, and A. Schwenk. Large-scale nuclear structure calculations for spin-dependent WIMP scattering with chiral effective field theory currents. *Phys. Rev. D*, 88(8):083516, 2013. [Erratum: *Phys.Rev.D* 89, 029901 (2014)].
- [269] Richard H. Helm. Inelastic and Elastic Scattering of 187-Mev Electrons from Selected Even-Even Nuclei. *Phys. Rev.*, 104:1466–1475, 1956.
- [270] J. I. Collar, A. R. L. Kavner, and C. M. Lewis. Germanium response to sub-keV nuclear recoils: a multipronged experimental characterization. *Phys. Rev. D*, 103(12):122003, 2021.

- [271] M. C. Gonzalez-Garcia, P. C. de Holanda, E. Masso, and R. Zukanovich Funchal. Probing long-range leptonic forces with solar and reactor neutrinos. *JCAP*, 01:005, 2007.
- [272] F. Feroz, M. P. Hobson, E. Cameron, and A. N. Pettitt. Importance Nested Sampling and the MultiNest Algorithm. *Open J. Astrophys.*, 2(1):10, 2019.
- [273] F. Feroz, M. P. Hobson, and M. Bridges. MultiNest: an efficient and robust Bayesian inference tool for cosmology and particle physics. *Mon. Not. Roy. Astron. Soc.*, 398:1601–1614, 2009.
- [274] Gregory D. Martinez, James McKay, Ben Farmer, Pat Scott, Elinore Roebber, Antje Putze, and Jan Conrad. Comparison of statistical sampling methods with ScannerBit, the GAMBIT scanning module. *Eur. Phys. J. C*, 77(11):761, 2017.
- [275] Ivan Esteban, M. C. Gonzalez-Garcia, Michele Maltoni, Thomas Schwetz, and Albert Zhou. The fate of hints: updated global analysis of three-flavor neutrino oscillations. *JHEP*, 09:178, 2020.
- [276] Michele Maltoni. From ray to spray: augmenting amplitudes and taming fast oscillations in fully numerical neutrino codes. *JHEP*, 11:033, 2023.
- [277] S. Abe et al. Limits on Astrophysical Antineutrinos with the KamLAND Experiment. *Astrophys. J.*, 925(1):14, 2022.
- [278] M. Agostini et al. Search for low-energy neutrinos from astrophysical sources with Borexino. *Astropart. Phys.*, 125:102509, 2021.
- [279] K. Abe et al. Search for solar electron anti-neutrinos due to spin-flavor precession in the Sun with Super-Kamiokande-IV. 12 2020.
- [280] K. Abe et al. Diffuse supernova neutrino background search at Super-Kamiokande. *Phys. Rev. D*, 104(12):122002, 2021.
- [281] M. Harada et al. Search for Astrophysical Electron Antineutrinos in Super-Kamiokande with 0.01% Gadolinium-loaded Water. *Astrophys. J. Lett.*, 951(2):L27, 2023.
- [282] F. Forastieri et al. Cosmic microwave background constraints on secret interactions among sterile neutrinos. *JCAP*, 07:038, 2019.
- [283] A. M. Lessa et al. Constraints on pseudoscalar couplings to neutrinos from meson decays. *Phys. Rev. D*, 76:075001, 2007.
- [284] P. S. Pasquini et al. Pseudoscalar neutrino couplings from higgs boson decays. *Phys. Rev. D*, 92:113012, 2015.
- [285] MICROSCOPE Collaboration. Microscope final results: Testing the equivalence principle in space. *Phys. Rev. Lett.*, 129:121102, 2022.
- [286] S. Schlamminger et al. Test of the equivalence principle using a rotating torsion balance. *Phys. Rev. Lett.*, 100:041101, 2008.
- [287] John N. Bahcall. Solar neutrinos. I: Theoretical. *Phys. Rev. Lett.*, 12:300–302, 1964.

- [288] John N. Bahcall, Neta A. Bahcall, and G. Shaviv. Present status of the theoretical predictions for the Cl-36 solar neutrino experiment. *Phys. Rev. Lett.*, 20:1209–1212, 1968.
- [289] John N. Bahcall and R. Davis. Solar Neutrinos - a Scientific Puzzle. *Science*, 191:264–267, 1976.
- [290] B. Pontecorvo. Neutrino Experiments and the Problem of Conservation of Leptonic Charge. *Sov. Phys. JETP*, 26:984–988, 1968. [Zh. Eksp. Teor. Fiz.53,1717(1967)].
- [291] V. N. Gribov and B. Pontecorvo. Neutrino astronomy and lepton charge. *Phys. Lett.*, B28:493, 1969.
- [292] John N. Bahcall, Sarbani Basu, Marc Pinsonneault, and Aldo M. Serenelli. Helioseismological implications of recent solar abundance determinations. *Astrophys. J.*, 618:1049–1056, 2005.
- [293] M. Castro, S. Vauclair, and O. Richard. Low abundances of heavy elements in the solar outer layers: comparisons of solar models with helioseismic inversions. *Astron. & Astrophys.*, 463:755–758, February 2007.
- [294] J. A. Guzik and K. Mussack. Exploring Mass Loss, Low-Z Accretion, and Convective Overshoot in Solar Models to Mitigate the Solar Abundance Problem. *Astrophys. J.*, 713:1108–1119, April 2010.
- [295] Johannes Bergstrom, M. C. Gonzalez-Garcia, Michele Maltoni, Carlos Pena-Garay, Aldo M. Serenelli, and Ningqiang Song. Updated determination of the solar neutrino fluxes from solar neutrino data. *JHEP*, 03:132, 2016.
- [296] Diego Vescovi, Carlo Mascaretti, Francesco Vissani, Luciano Piersanti, and Oscar Straniero. The luminosity constraint in the era of precision solar physics. *Journal of Physics G Nuclear Physics*, 48(1):015201, January 2021.
- [297] M. Spiro and D. Vignaud. Solar Model Independent Neutrino Oscillation Signals in the Forthcoming Solar Neutrino Experiments? *Phys. Lett.*, B242:279–284, 1990. [609(1990)].
- [298] John N. Bahcall. The Luminosity constraint on solar neutrino fluxes. *Phys. Rev.*, C65:025801, 2002.
- [299] Lean J. Frohlich C. The Sun’s total irradiance: cycles,trends and related climate change uncertainties since 1978. *Geophys. Res. Lett.*, 25:4377–4380, 1998.
- [300] Lean J. Kopp G. A New, Lower Value of Total Solar Irradiance: Evidence and Climate Significance. *Geophys. Res. Lett.*, 38:L01706, 2011.
- [301] Nicola Scafetta and Richard C. Willson. ACRIM total solar irradiance satellite composite validation versus TSI proxy models. *Astrophysics and Space Science*, 350(2):421–442, jan 2014.
- [302] R. L. Workman and Others. Review of Particle Physics. *PTEP*, 2022:083C01, 2022.
- [303] John N. Bahcall and P. I. Krastev. How well do we (and will we) know solar neutrino fluxes and oscillation parameters? *Phys. Rev.*, D53:4211–4225, 1996.

- [304] Mario A. Acero, Carlo Giunti, and Marco Laveder. Limits on $\nu(e)$ and anti- $\nu(e)$ disappearance from Gallium and reactor experiments. *Phys. Rev. D*, 78:073009, 2008.
- [305] Carlo Giunti and Marco Laveder. Statistical Significance of the Gallium Anomaly. *Phys. Rev. C*, 83:065504, 2011.
- [306] Joachim Kopp, Pedro A. N. Machado, Michele Maltoni, and Thomas Schwetz. Sterile Neutrino Oscillations: The Global Picture. *JHEP*, 1305:050, 2013.
- [307] Mona Dentler, Álvaro Hernández-Cabezudo, Joachim Kopp, Pedro A. N. Machado, Michele Maltoni, Ivan Martinez-Soler, and Thomas Schwetz. Updated Global Analysis of Neutrino Oscillations in the Presence of eV-Scale Sterile Neutrinos. *JHEP*, 08:010, 2018.
- [308] W. C. Haxton. Cross-section uncertainties in the gallium neutrino source experiments. *Phys. Lett. B*, 431:110–118, 1998.
- [309] D. Frekers et al. Precision evaluation of the ^{71}Ga solar neutrino capture rate from the $(^3\text{He},t)$ charge exchange reaction. *Phys. Rev. C*, 91(3):034608, 2015. [Erratum: *Phys.Rev.C* 100, 049901 (2019)].
- [310] Joel Kostensalo, Jouni Suhonen, Carlo Giunti, and Praveen C. Srivastava. The gallium anomaly revisited. *Phys. Lett. B*, 795:542–547, 2019.
- [311] S. V. Semenov. Cross Section of Neutrino Absorption by the Gallium-71 Nucleus. *Phys. Atom. Nucl.*, 83(11):1549–1552, 2020.
- [312] Evgeny K. Akhmedov and M. Yu. Khlopov. Resonant Amplification of Neutrino Oscillations in Longitudinal Magnetic Field. *Mod. Phys. Lett. A*, 3:451–457, 1988.
- [313] Evgeny K. Akhmedov and M. Yu. Khlopov. Resonant Enhancement of Neutrino Oscillations in Longitudinal Magnetic Field. *Sov. J. Nucl. Phys.*, 47:689–691, 1988.